©2019

Zeynep Aygüzer Yaşar

ALL RIGHTS RESERVED

PRODUCING SILICON CARBIDE BORON CARBIDE COMPOSITES BY SPARK PLASMA SINTERING

by

ZEYNEP AYGÜZER YAŞAR

A dissertation submitted to the

School of Graduate Studies

Rutgers, The State University of New Jersey

In partial fulfillment of the requirements

For the degree of

Doctor of Philosophy

Graduate Program in Materials Science and Engineering

Written under the direction of

Dr. Richard A. Haber

And approved by

_____

_____

_____

_____

_____

New Brunswick, New Jersey

January, 2019

ABSTRACT OF THE DISSERTATION

Producing Silicon Carbide Boron Carbide Composites by Spark Plasma Sintering

By ZEYNEP AYGÜZER YAŞAR

Dissertation Director:

Richard A. Haber

Silicon carbide has a high melting point, high mechanical and elastic properties and excellent chemical stability. Boron carbide is a non-metallic material with exceptional physical and chemical properties. Boron carbide is third hardest material after diamond and cubic boron nitride. Besides a high hardness, boron carbide also has a high melting point, high strength, high neutron cross-section, and low density. Due to the their outstanding properties both materials can be used in spray nozzles, turbine engines, heat conducting tubes, and in the defense industry as armor plates. Since silicon carbide and boron carbide are both strongly covalent bonded, the densification of these materials is extremely difficult. High sintering temperature and fine powder sizes are critical to achieve a high density. Fine starting powders also add the presence of oxygen. The residual oxide layer forms as SiO_2 on the SiC surfaces and as B_2O_3 on the B_4C surfaces. These oxide layers inhibit high density and cause grain coarsening.

The goals of this thesis were to produce high density SiC-B_4C composites, optimize the mechanical properties of SiC-B_4C composites, and understand the role of excess oxygen content on sinterability. To achieve these goals, the oxygen content was managed using two methods; a safe and effective laboratory scale acid etching process developed to reduce the oxygen content of SiC and additional carbon used to remove the residual oxide layer. Then, SiC- B_4C composites with varying amounts of C powders were mixed and sintered by spark plasma sintering method (SPS).

The dense composites were characterized to evaluate the effect of the oxygen content and residual carbon on the microstructure and mechanical properties. The composite samples' microstructure was characterized using The Zeiss Sigma emission scanning electron microscopy. The phase of the composites was determined using X-ray diffraction. Poisson's ratio, Young's modulus, shear modulus, and bulk modulus were measured by ultrasound analyses. Since the densification of a ceramic affects the mechanical properties, the Archimedes method was used to determine the density of the sintered composite samples. Polished samples were used for hardness testing using a Vickers diamond tipped (9.8 N load) LECO-M-400-G3 and Berkovich nano-hardness (100 mN-500 mN load).

The results showed that the oxygen content and the addition of carbon should be matched to achieve high density and high mechanical properties. Carbon also played a role on the mechanical properties as well as the oxygen since modifying the oxygen content by adding varying amounts of carbon caused surplus carbon. The presence of excess carbon decreased the elastic modulus and hardness of the composites.

Acknowledgements

I would like to thank everyone who has helped me throughout my time at Rutgers University. Firstly, I would like to express my sincere gratitude to my advisor Dr. Richard A. Haber, for all his continuous support, help, guidance, and patience through the years. I would also like to thank my committee members, Dr. Richard Lehman, Dr. William Rafaniello, and Dr. Dunbar Birnie for their advice and help.

A special thanks to Michelle Sole, who means everything to Haber group. Nothing can be done without you. I would also like to thank Dr. Lisa Klein for her understanding and help through the years, she made my life easier as an international student.

Also, I would like to thank the Ministry of National Education, the Republic of Turkey and CCOMC for financially supporting me during my study here.

Thanks to the past and current members of the Haber group. I would like to specially thank to Mert, Metin, Kanak, Berra, and Hulya for their close friendship and always being available for me all the time. You guys became my family in here.

I would like to thank my parents and my brother for their support, love, and help since I was born. I could not have made it without your encouragement. Thank you for always being by my side listening to me and believing in me. I am very proud of being part of this family.

I would like to thank my two daughters Arya Deren and Alin Deniz. I did not know how beautiful life could be before meeting you. You brought spring to me every day, even at a very hard time. I have learned how I was lazy before you and, thanks to you, I have

learned a lot. You are the most beautiful being in my life. Thank you for letting me be your mother.

I would like to give a final thanks to my husband Burak. Since I met you, you have been my favorite person and the strongest support in my life. I may not have even graduated from college without you. You always pushed me to do my best. I cannot forget how you watched me while I was studying to make sure I studied enough when we were at university. Thank you for letting us grow together. I love you!

Dedication

I dedicate this thesis to my mother Senem, and my father Muzaffer. I am so proud of being your daughter. I love you so much!

Table of Content

List of Figures

List of Tables

1. Introduction

Whether composites are metal, organic, or inorganic, combining two or more materials results in higher mechanical and physical properties than their individual components. Components of composites different are usually chemically and do not dissolve in each other [1, 2]. Some material properties can be improved by creating composite materials, such as toughness, corrosion resistance, wear resistance, elastic properties, density, fatigue, temperature-dependent behavior, heat insulation, and thermal conductivity [1, 3]

Since boron and silicon are in the same group on the periodic table, both SiC and B_4C have similar physical and chemical properties. For instance, they have high covalent bonding, a high melting point, high hardness, high mechanical strength, high Young's modulus, low thermal expansion, and excellent chemical stability [4, 5]. Since silicon carbide and boron carbide are both strongly covalent bonded, the densification of these materials is extremely difficult. High sintering temperature and fine powders sizes are critical to achieve a high density. Fine starting powders also add the presence of oxygen.

Non-oxide high temperature structural materials such as SiC and B_4C will develop an oxide layer on their surface when they are exposed to oxygen. The amount of silica layer (SiO_2) on the SiC particles depends on the particle size of SiC [6, 7]. Boron carbide may also develop a B_2O_3 oxide layer during processing. This layer causes grain coarsening at low temperatures and prevents high density [8].

The goals of this thesis were to produce high density SiC-B_4C composites, optimize the mechanical properties of SiC-B_4C composites, and understand the role of excess

oxygen content on sinterability. To achieve these goals, the oxygen content was managed using two methods: a safe and effective laboratory scale acid etching process developed to reduce the oxygen content of SiC and additional carbon used to remove the residual oxide layer. Then, SiC- B_4C composites with varying amounts of C powders were mixed and sintered by spark plasma sintering method (SPS).

The dense composites were characterized to evaluate the effect of the oxygen content and residual carbon on the microstructure and mechanical properties using SEM, XRD, ultrasound analysis, Vickers micro hardness, and Berkovich nano-hardness techniques.

2. Background

2.1. Silicon Carbide

At the end of the 1800's, SiC had started to be used in the industry [9]. In 1885, Cowless had launched synthesis of SiC methods, however, in 1892, Acheson was the first person who understood the importance of SiC as a hard material and produced SiC on a large scale. SiC is an important industrial material due to its excellent properties such as high oxidation resistance, high wear resistance, high thermal conductivity, and good thermal shock resistance [9-12].

2.1.1. Crystal Structure

Today, more than 200 SiC polytypes have been identified. Grain orientation causes the formation of these polytypes, and this was proved by researchers [13, 14]. A silicon carbide crystal consists of Si and C atoms. In all SiC polytypes, the bond length between Si contiguous atoms is 0.308 nm. The C atom is located at the center of the tetrahedral; it has an equal 0.189nm distance to the four neighbor Si atoms with bonding energy of 4.53eV [15-19].

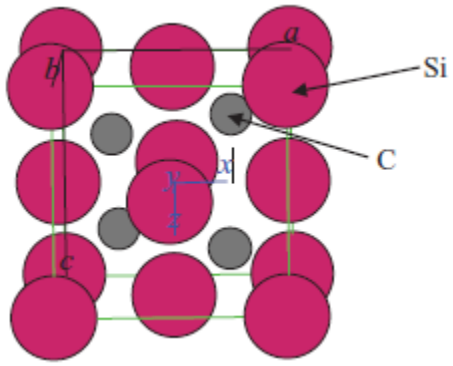

Figure 1. SiC crystal structure is showing tetrahedral coordination [20].

The common polytypes are 3C (Cubic), 4H, 6H (hexagonal) and 15R (rhombohedral) [21].

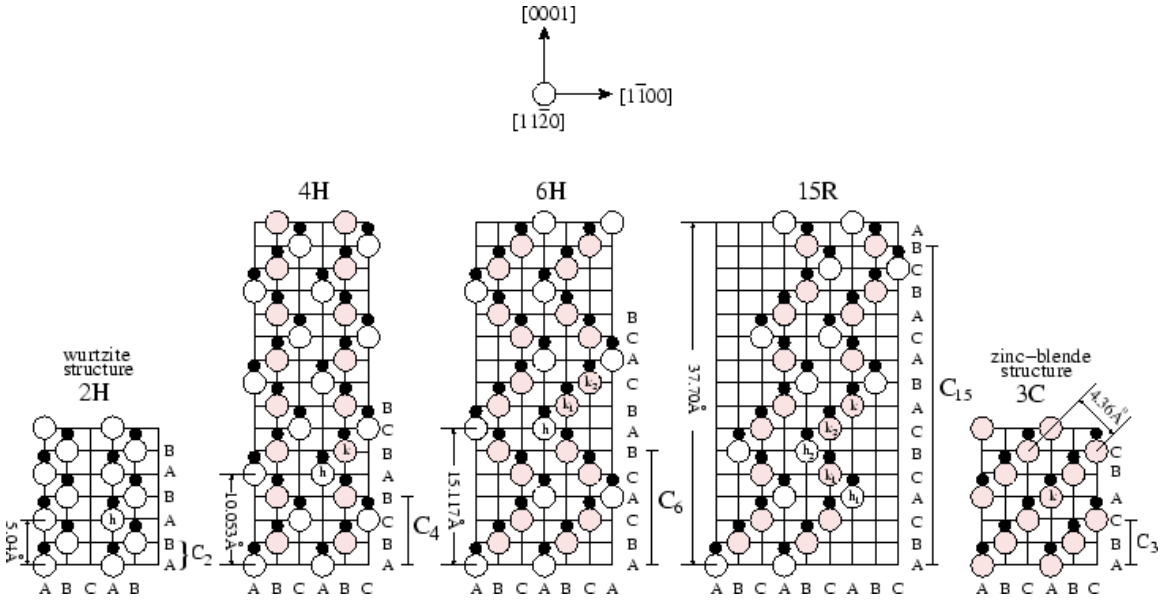

Figure 2. Popular polytypes of SiC [21]

The cubic and hexagonal crystal structures are most often seen within many polytypes [22]. The cubic form of SiC (3C) has a sequences of ABCABC, and hexagonal form of SiC (α-SiC) has a sequence of ABAB [23].

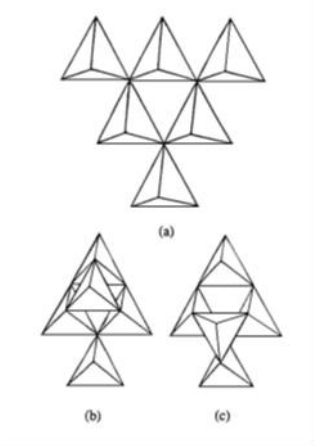

Figure 3. (a) Two-dimensional arrangement of tetrahedral, (b) parallel arrangement of tetrahedral planes and (c) anti-parallel arrangement of tetrahedral planes [23]

2.1.2. The Si-C System

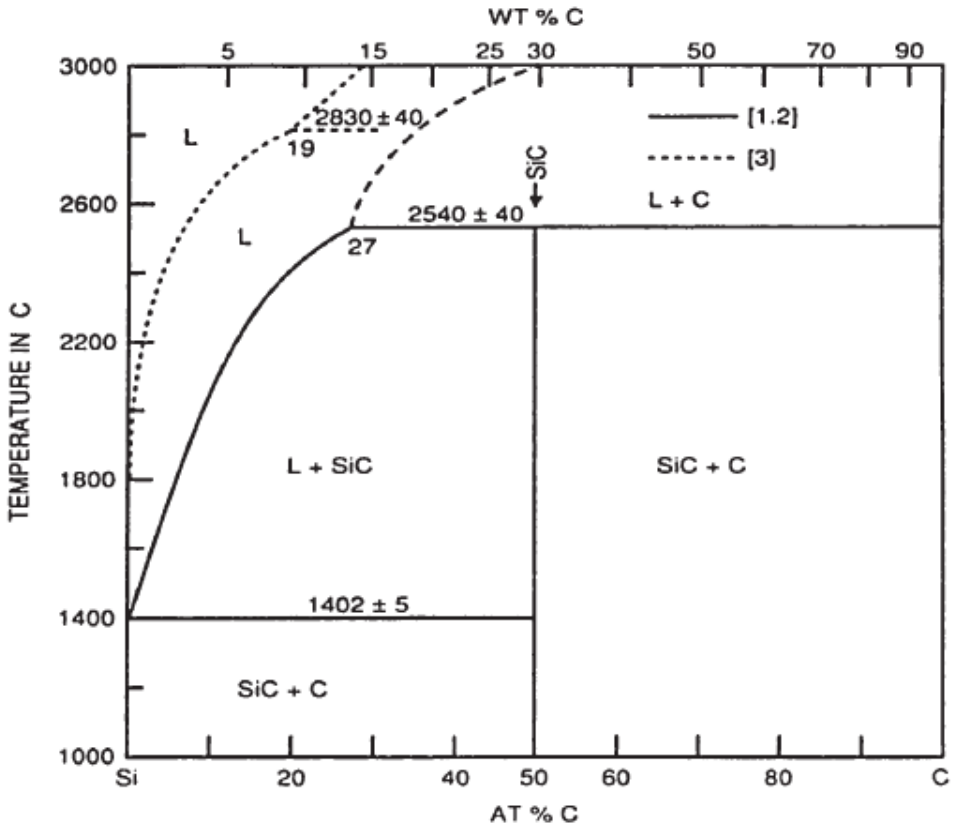

Figure 4.Silicon carbide phase diagram [24]

The Si-C phase diagram is shown in Figure 4. The reaction between Si and C occurs under the melting temperature of Si to form SiC. It can be seen that a eutectic point between Si and C lies at 1402°C with 0.75 at%C. A peritectic point occurs around 2540°C with 27 at%C. The liquid form between Si and SiC can be seen at 2600°C [24-26].

2.1.3. Mechanical Properties

SiC has a relatively low theoretical density of 3.21g/cm^3 and consisted 70.05 wt % Si and 29.95 wt % C [27, 28]. Silicon carbide has a high hardness and a high elastic modulus. It is noted for fourth hardest material after diamond, cubic boron nitride and boron carbide [29, 30].

SiC has these properties due to the strong covalent bonding between Si and C. The covalency is measured approximately 87%, which also causes its high melting point and minimal-high-temperature induced creep [12, 27, 28].

The mechanical properties for SiC differ depending on the sintering method, and the different types of SiC that can form are seen in Table 1 [28].

Table 1. Silicon carbide's mechanical properties for different crystal types and densification method[28].

Type of SiC	Young's modulus (GPa)	Shear modulus (GPa)	Flexural strength (MPa)	Knoop hardness (HK0.1)
α-SiC, hot-pressed	440	177	530	3100
α -SiC, sintered	410		460	2800
β -SiC, sintered	410	140-190	650	

Additionally, silicon carbide property values include: a tensile strength of 600 MPa, the compressive strength of 2.48 GPa, and fracture toughness of 5.2 MPa.m ^{½} [28].

2.1.4. Thermal and Electrical Properties

Silicon carbide has a higher thermal conductivity compared to other ceramic materials. Thermal conductivity has been reported to be 150 W/m·K at 20°C and 54 W/m·K at 1400°C. The SiC thermal expansion coefficient is 4.7 x10^{-6} between 20°C and 1400°C.These two properties provide the basis for SiC having a high thermal shock resistance [10]. Silicon carbide is a semiconductor material with a wide band gap. The band

gap can be form 2.4 to 3.3 eV with different polytypes. The band gap is 3.26eV for 4H-SiC and 3.03eV for 6H-SiC [11, 27].

2.2. Synthesis of Silicon Carbide Powders

The manufacture of high-quality SiC ceramics requires the use of high purity, small-sizes (average particle size <1μm), and high specific surface area powders [31]. Silicon carbide is generally synthesized on a large scale by the Acheson process [25, 32].

In this method (Figure 5), two large graphite electrodes are connected with graphite powder, a mixture of silica and coke is filled in the enclosed region, and the entire is heated electrically until 2500° C to synthesize SiC. The high synthesis temperature produces the alpha form of SiC [24, 33].

The equation of reaction [32, 33];

$$SiO_2+3C \rightarrow SiC+2CO \quad (1)$$

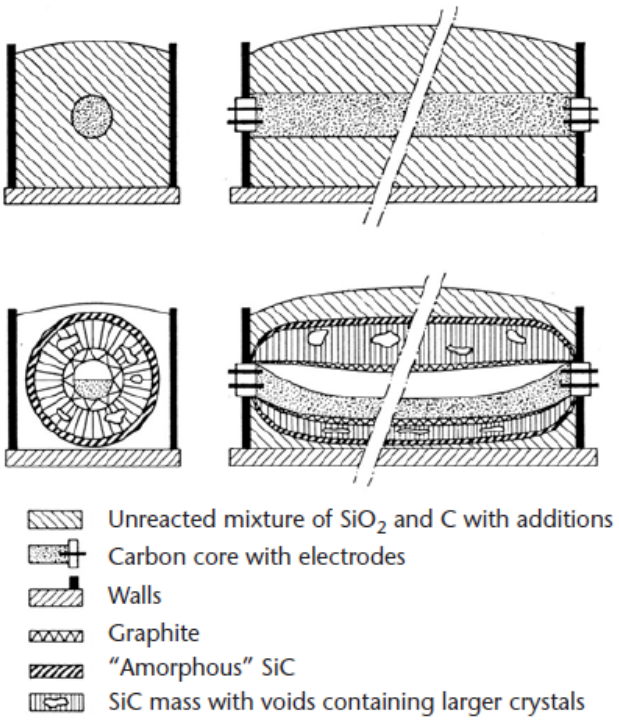

Figure 5. The Acheson process [11]

The product of prepared SiC blocks are then ground, refined and classified to produce SiC powders. With this process, SiC has a coarse grain size and an average particle size of 5 µm [33].

Fine grain β-SiC can be produced using the Acheson process at a lower temperature (1500-1800°C) or by vapor-phase reaction [33, 34]. With the vapor-phase method less than 0.1 µm, high purity powder can be achieved [33]. Vapor-phase methods use the reaction of SiH_4 or $SiCl_4$ with hydrocarbons like CH_4 and C_3H_8 or the thermal decomposition of CH_3SiCl_3, $(CH_3)4Si$, or polycarbosilane to synthesis β –SiC [33, 34]. Steps of vapor-phase methods can be shown as follows [34];

$$SiH_4 + CH_4 \xrightarrow{1400℃} SiC + 4H_2 \quad (2)$$

$$CH_3\ SiCl_3 \xrightarrow{plasma} SiC + 3HCl \quad (3)$$

$$Si\ (CH_3)_4 \xrightarrow{950-1400℃} SiC + 3CH_4 \quad (4)$$

$$(CH_3)_2SiCl_2 \xrightarrow{1200℃} SiC + CH_4 + 2HCl \quad (5)$$

Average grain size and ratio depend on reaction heat, gas density, and gas rate of flow [34].

2.3. Industrial Uses

More than 700,000 tons of silicon carbide is produced every year, half of which solely goes towards use in the abrasives industry [10]. Silicon carbide's extremely high hardness makes it especially useful for grinding and polishing a wide range of materials. In loose particle form, silicon carbide is an excellent lapping agent and when mixed with a binder, can be made into abrasive sticks or applied as a coating for cutoff wheels [35]. It may also be formed into grinding wheels and whetstones, or bonded to cloth and sheets for use as abrasive papers and belts [10]. Due to its high-temperature properties, SiC is used for furnace components, nozzles, aerospace applications, and high-temperature strength testing apparatuses [15].

2.4. Boron Carbide

Boron carbide is a non-metallic material with outstanding physical and chemical properties [36]. In 1883, boron carbide was first synthesized by Joly and, in 1934, the chemical formula B_4C was assigned. Boron carbide is third hardest material after diamond and cubic boron nitride. Beside high hardness, boron carbide also has a high melting point, high strength, high neutron cross-section, and low density [12, 37, 38].

2.4.1.Phase Diagram and Crystal Structure

Many disputable phase diagrams have been suggested for B-C between1955-1960. The most widely accepted standard diagram for this binary system was introduced by Elliott and Kieffer in 1961 and is shown in Figure 6 [39].

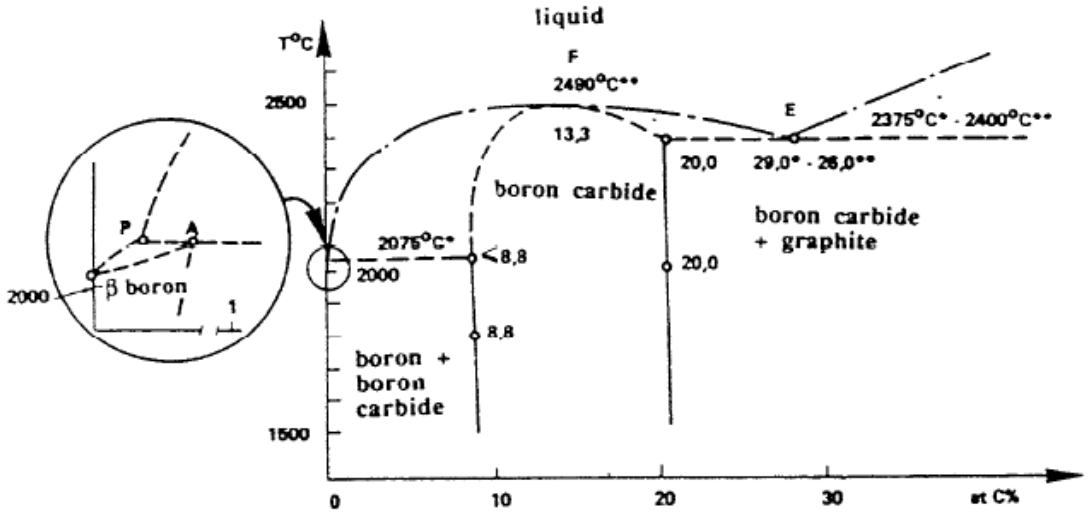

Figure 6. Boron carbide phase diagram [39]

According to the phase diagram, boron carbide's carbon concentration ranges from almost 8.8 at% to 20 at.%. A eutectic point between B_4C and C at 26 at.% C and 2400°C can also be seen from the binary phase diagram given in Figure 6 [39, 40].

B_4C has a unique crystal structure; it consists of a rhombohedral unit cell that contains fifteen atoms (one twelve atom icosahedra and three-atom chain linking the icosahedra along the c-axis) [8, 36, 37, 41, 42]. In Figure 7, the unit cell of B_4C and the crystal structure can be seen [37]. The twelve atom icosahedra consist of polar and equatorial sites. The polar side has three atoms at the top and bottom (totaling six atoms) to link to the icosahedron, and the equatorial side has six atoms [43]. The highly covalent bonding B_4C lattice belongs to the $D3_{d5}$ –R_3m space group [39, 44]. Rhombohedral lattice

constants a = 5.19 Å and α = 66°18’; the corresponding hexagonal lattice constants are a = 5.61 Å and c = 12.07 Å [45, 46].

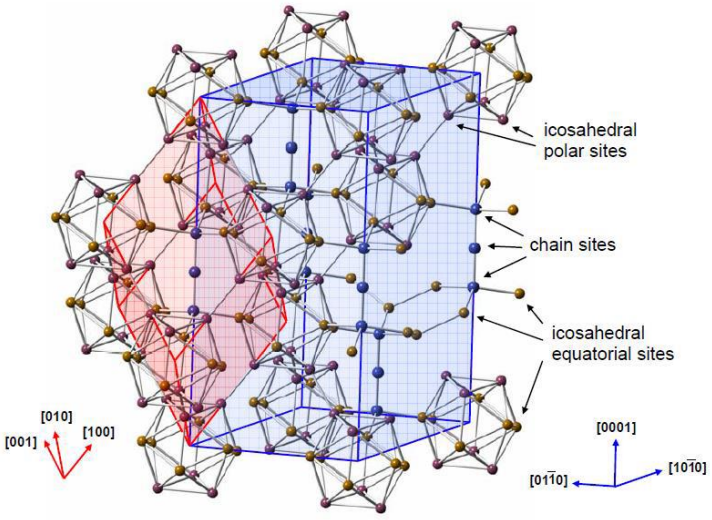

Figure 7.Rhombohedral unit cell of B_4C [47]

B_4C (20% carbon) has been reported as B_{12} icosahedral with C-C-C intericosahedral chains and as $B_{11}C$ icosahedral with C-B- C intericosahedral chains.For $B_{13}C_2$ (13.3% carbon) has been reported as B_{12} icosahedra with C-B- C chains and as $B_{11}C$ icosahedra with C-B-B chains [40, 48]. Common boron carbide atomic configurations can be seen in Figure 8 [49].

Figure 8. Common boron carbide atomic configurations [49]

2.4.2. Physical Properties

Boron carbide has a low-density material of 2.52 g/cm^3 [46, 50]. The density of boron carbide increases with increasing carbon content within homogeneity range of the phase. The relationship can be described by the following equation:

$$d\ (g/cm^{3}) = 2.422 + 0.0048\ [C] \quad (6)$$

at. % ($r = 0.998$) with 8.8 at. % < [C] < 20-0 at.% from the phase diagram. According to the equation, the density measured for B_4C is 2.52 g/cm^3, for $B_{13}C_2$ is 2.488 g/cm^3, for $B_{10.4}C$ is 2.465 g/cm^3 [39]. The density of boron-rich side is 2.465 g/cm^3 and the carbon-rich side is 2.52 g/cm^3 [51].

The nature of the rhombohedral crystal for boron carbide results in extremely anisotropic elastic properties. However, most reported values are averaged: Young's modulus of B_4C is reported around 450GPa, Shear modulus (G) is approximately 197GPa, Bulk modulus (K) is about 243GPa, and Poisson's ratio changes from 0.14 to 0.18 [20, 44].

All elastic properties have some dependency on carbon content and crystal orientation, as shown in Table 2 [39] and 3 [44] respectively.

Table 2. Elastic properties of B_4C with different carbon content [39]

Carbon %	E (GPa)	G (GPa)	ν	B (GPa)
20.0	471	200	0.18	245
18.2	465	197	0.18	243
15.4	466	197	0.18	245
13.3	450	189	0.19	241
11.5	351	150	0.17	178
10.0	348	150	0.16	170
10.0	323	132	0.22	194

Table 3. Anisotropic elastic constant for different B_4C [44]

C_{ij}(GPa)	$B_{5.6}C$	$B_{6.5}C$	B_4C
11	542.8	500.4	561.8
33	534.5	430.2	517.7
44	164.8		
12	130.6	125.3	123.6
13	63.6	73.9	69.6
14		7.7	17.8

Boron carbide is third hardest material after diamond and cubic boron nitride [52-54]. Generally, Knoop hardness testing is used to measure hardness values. 100 gram load hardness values(HK100) range from 2900 to 3100kg/mm^2 [44]. Hardness increases with increasing carbon content in homogeneity regions [39]. Flexural strength increases with increasing carbon content within the phase homogeneity range. After this region, free carbon decreas the strength. Flexural strength also decreases with increasing porosity and grain size [37].

Besides these good properties, boron carbide has low fracture toughness. K_{IC} values were reported to be from 3.1 to 4.1 MPam$^{1/2}$ [44, 55-58].

2.4.3.Synthesis of Boron Carbide

2.4.3.1. Carbothermic Reduction of Boric Acid

Elemental boron and carbon can be used to produce boron carbide powder. Due to the high cost of elemental starting materials, this method is not economically sustainable. Metallothermic and carbothermic methods are generally used to synthesize boron carbide powder. Inexpensive boric acid (H_3BO_3) and boron oxide (B_2O_3) are used as starting materials and reduced by adding carbon to synthesize boron carbide. The powder

synthesized by this method can be sintered with hot pressing and hot isostatic pressing. The carbothermic reaction can be summarized by the following equations [59, 60];

$$2B_2O_3 + 7C \rightarrow B_4C + 6CO \quad (7)$$

Or

$$4\ H_3B0_3 + 7C \rightarrow B_4C + 6CO + 6H_2O \quad (8)$$

This reaction proceeds in three steps [61]:

$$4\ H_3BO_3 \rightarrow 2B_2O_3 + 6H_2O \quad (9)$$

$$B_2O_3 + 3CO \rightarrow 2B + 3CO_2 \quad (10)$$

$$4B + C \rightarrow B_4C \quad (11)$$

The reaction between B_2O_3 and CO is thermodynamically possible after 1400℃, however, the reaction temperature is maintained above 2000℃ to increases the reaction rate [61].

Boron carbide synthesizes using an electric arc furnace process was patented by Schroll in 1939 [62].

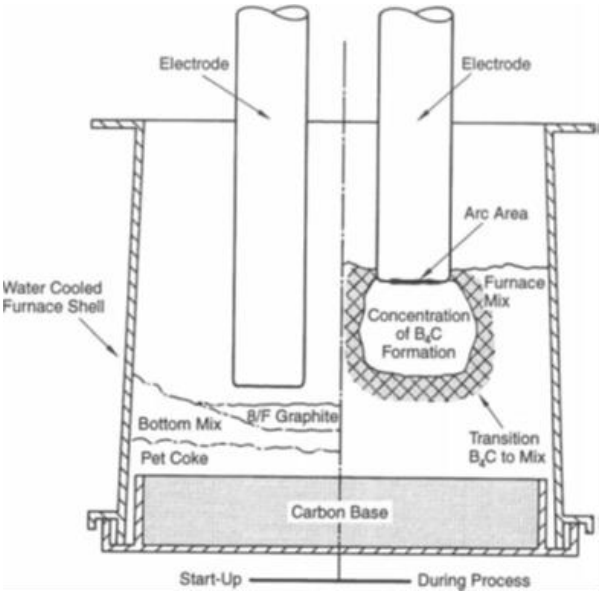

Figure 9. Electric arc furnace [59]

Boric acid and petroleum coke are mixed and melted in an arc furnace. Then the product is crushed and mixed with the same amount of boric acid and remelted again. The processing temperature is usually very high because of localized electric arcs [43]. In Figure 10, the giant ingot can be seen to can be several meters diameter and have several zones. Since it has high viscosity and thermal properties, the mixtures cannot be reacted completely. Materials closer to the electrodes will be well reacted, high purity and fully formed boron carbide [44]. After that, the product needs to be crushed and grinded [43].

Figure 10. An ingot of boron carbide Sections (a) unreacted material while (b) well-reacted crystalline boron carbide with some possible graphitization [44]

2.4.3.2. The Rapid Carbothermal Reduction

Rafaniello et al. first launched the synthesis of boron carbide by rapid carbothermal reduction in 1989 [63]. A customized Thermal Technologies furnace was used to perform this process [64]. Since electric arc furnace has a slow heating rate, the rapid carbothermal reduction has fast heating rate [63, 65]. As shown in Figure 11, cold finger (a water cooler) is fitted from the top of the furnace. It has a connection with screw feed and sealed hopper. The precursor is fed from the cold finger; the cold finger lets the precursor get into the furnace's hot zone below the boron oxide melting point. Since the precursor gets into the hot region, it will have a very fast heating rate of 10^3-$l0^5$ K/s. This furnace has two types of feeding mechanism. In the first type, a certain amount of precursor can be dropped from sealed hooper gate into the hot zone. By increasing loading size, the heating rate will be decreased. In the second type, using screw feed, the furnace can be fed continuously with precursor [64]. Overall, the rapid carbothermal reduction method has a decreased reaction

time to produce boron carbide, and a decreased particle size since it does not involve an ingot [63].

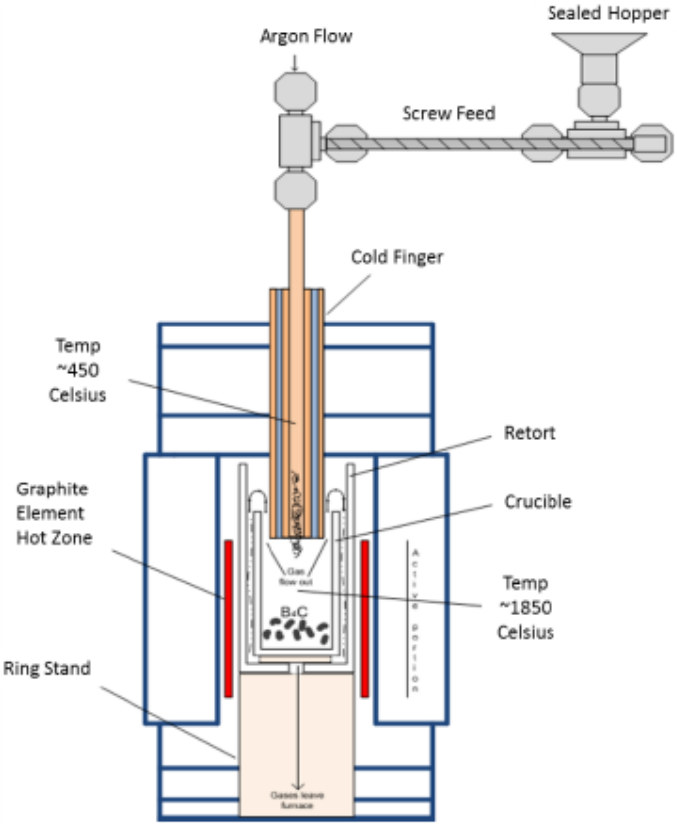

Figure 11. Rapid carbothermal reduction furnace schematic [64].

2.4.3.3. Other Synthesis Methods

Many different synthesis methods have been reported in the literature. These include the synthesis of elements, magnesiothermic reduction, vapor phase reactions, and synthesis from polymer precursor [43].

Due to the expensive starting materials, synthesis of boron carbide from elements is not economically sustainable. This method is only used for special research, such as B_{10} enrich or the synthesis of very pure boron carbide.

The magnesiothermic reduction method is an alternative method to carbothermal reduction to produce boron carbide. In this method, boron oxide, carbon, and magnesium are used. The magnesiothermic reduction reaction can be seen in the following equations:

$$2B_2O_3+6Mg+C\rightarrow B_4C+6MgO \quad (12)$$

This reaction takes place in two steps:

$$2B_2O_3+6Mg\rightarrow 4B+6MgO \quad (13)$$

$$4B+C\rightarrow B_4C \quad (14)$$

The reaction is naturally exothermic with $\Delta H=1812 kJ\ mol^{-1}$. The product of the magnesiothermic reaction has residual magnesium oxide and magnesium borides. Magnesium oxide can be easily washed away from the product using the aqueous method, however, the magnesium borides will be remain.

Vapor phase reaction is used to make boron carbide coating, thin films, and whiskers in submicron particle sizes. Typical vapor phase reactions can be seen in following equations:

$$4BCl_3+CCl_4+8H_2\rightarrow B_4C+16HCl \quad (15)$$

$$4BCl_3+C+6H_2\rightarrow B_4C+12HCl \quad (16)$$

$$4BCl_3+CH_4+4H_2\rightarrow B_4C+12HCl \quad (17)$$

Unlike other synthesis methods, by polymer precursors, boron carbide can be synthesized at a relatively low temperature of around 1000-1500℃. However, the final product powder may have free carbon or boron oxide as impurities [43].

2.4.4. Industrial Applications

Boron carbide has been commonly used for many applications because of its remarkable properties such as high hardness, wear resistance, low specific gravity, and high chemical stability [56, 66-69].

The primary application of boron carbide is abrasive grit powder. Boron carbide particle (particle size from 1-10 mm) can be used for lapping, polishing, grinding and water jet cutting [39, 70]. Boron carbide can be used as a coating material for different alloys like brass, stainless steel, titanium alloys, aluminum alloys, or cast iron [71]. It can also be used in refractor applications of high melting point and thermal stability. Boron carbide is durable material in extreme conditions: it can be used as lightweight armor, blasting nozzle, neutron absorber. Since boron carbide is a high-temperature semiconductor, it can be used electronic applications as well [42, 47, 50, 52, 58, 72-74].

2.5. Oxidation

Non-oxide high temperature structural materials such as SiC, B_4C, and TiB_2 will have an oxide layer on their surface when they are exposed to oxygen. The amount of silica layer (SiO_2) on SiC particles depends on the particle size of SiC. Also, moisture in the air, additives, and impurities affect the oxidation of SiC [6, 7]. The diffusion of oxygen through the oxide layer controls the oxidation of SiC particles above 600°C [6, 7, 75]. The thickness of the oxide layer increases with temperature[6]. The transport of oxygen molecules dominate at low temperature, and the transport of ionic oxygen molecules dominate at a higher temperature (over 1300°C)[6, 75].

The oxygen content of non-oxide ceramics may increase during processing, even when in an inert environment. One example of this occurring is in the milling of fine TiB_2

powders, where experimental results showed that the oxygen content increased even when the milling was conducted in a nonpolar organic solvent and in an inert gas environment, resulting in grain coarsening [76].

Boron carbide may also have a B_2O_3 oxide layer during processing. This layer causes grain coarsening at low temperatures and prevents high density [8].

The most common ways to remove an oxide layer are adding additional carbon and etching using hydrofluoric acid. Hydrofluoric acid will reduce the oxygen content with an etching method. The carbon addition removes the SiO_2 layers on the SiC surfaces by reacting with SiO_2 to form SiC. This inhibits grain growth [77-79].

2.6. Sintering

2.6.1. Pressureless Sintering

Pressureless sintering is the way to densify materials without external pressure [80]. Since the pressureless sintering method allows the materil to be sintered into complex shapes, it is practicable in the industry [28]. The cost of processing is remarkably lower than any other sintering method [80]. Lankau et al. studied the pressureless sintering of SiC-B_4C composites. SiC-B_4C compositions were 100% SiC, 80%SiC-20%B_4C, 60% SiC-40%B_4C, and 40% SiC-60% B_4C. Powders were mixed in water with organic additives and uniaxially pressed (30MPa). The bars were pressed again with the isostatic press at 150 MPa. Samples were sintered under argon at 2150 °C for 75 min. Almost complete densification of composites with > 50 vol. % SiC was achieved. Higher boron carbide content led to lower density, being< 90% of the theoretical value [81]. Pressureless sintering can be categorized as solid state sintering and liquid phase sintering [80].

2.6.1.1. Solid State Sintering

The densification of a well dispersed compact under a constant rate of heating has a density increase of about 2% in the initial stage, significant densification in the intermediate stage, and rapidly decreasing rate of densification in the final stage of solid stage sintering. In a heterogeneous compact containing particles, agglomerates, and pores of different size and shape, the transitions between stage may occur at different rates in different regions. The driving force of sintering is in the reduction of the total free energy of the system. This includes the change in free energy associated with volume, boundaries, and surfaces of grains [82]. In the solid state sintering method, the sintering temperature should be 0.5-0.9% of T_{melt} so densification occurs without any liquid phase [83]. Solid state sintering is classified three stages: initial stage, intermediate stage, final stage [20]. Although these stages are discussed with separate features, there is no clear distinction when moving from one stage to another [84]. During the initial stage,the main form of mass transport occurrs in the surface transport between two particles in contact, which results in rapid neck growth. This occurs at low temperatures and over the short distance between particles. There is no change in density during this stage because surface transport does not result in shrinkage; the porosity remains continuous and the grain size of the particles does not change. The initial stage often results in a green density increase from approximately 50% to 70% of the theoretical density. In the intermediate stage, diffusion occurs from inside of the particle to the neck, which means long distance diffusion. Shrinkage and limited grain growth can occur due to the densification. The pores become isolated. Density changes 70% to 90% of theoretical density due to the decreased amount of porosity. In the final stage of solid state sintering, shrinkage slows and significant grain

growth can be observed. The isolated pores close off. At this stage, the density changes slightly [83-87]. In Figure 12, the three stage of solid state sintering is shown.

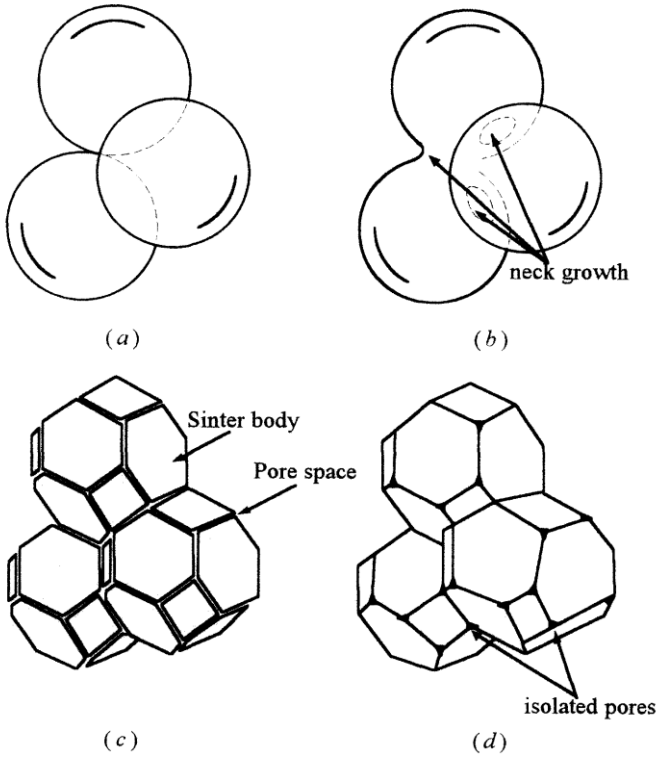

Figure 12. (a) Initial stage of sintering, (b) End of initial stage of sintering, (c) Intermediate stage of sintering and (d) Final stage of sintering [86]

Mechanisms for mass transport in sintering include: surface diffusion, evaporation condensation, boundary diffusion, lattice diffusion, viscous flow, and plastic flow. Mass transport mechanisms by diffusion can be seen in Figure 13. Surface diffusion can produce surface smoothing, particle joining, and pore rounding, but it cannot induce shrinkage. When the vapor pressure of a material is high, sublimation and vapor transport of the surface of lower vapor pressure produces the same effects as surface diffusion. Bulk viscous flow is effective when a wetting liquid is present, and plastic deformation is effective when an external pressure is applied [82, 85, 86].

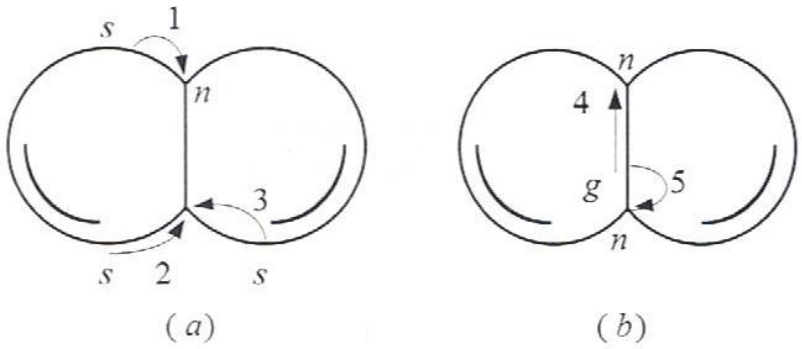

Figure 13. (1) Evaporation and condensation, (2) surface diffusion, (3) volume diffusion, (4) grain boundary diffusion, and (5) volume diffusion [86]

The concentration of vacancies beneath a concave surface is higher than beneath a flat or convex surface due to the difference in chemical potential. Lattice and boundary diffusion can transport vacancies from a concave surface with a concomitant flow of atoms in the opposite direction. Pore shrinkage occurs by the diffusion of vacancies to the grain boundaries, where they are destroyed. Microcreep at the grain boundary eliminates vacancies and bring the particles closer together, resulting in shrinkage.

In the intermediate stage, shrinkage is limited by grain growth and the change in pore shape. Sintering in this stage is dependent on size, shape, packing of the particles, and chemical dopants that increase the vacancy flux of the diffusing species. Particle aggregates cause packing heterogeneity and inhomogeneous sintering. The dispersion of aggregates results in better particle packing and an improvement in sintering behavior, leading to a higher final density and a more homogeneous compact.

In the intermediate and final stages, the densification behavior is dependent on the relationship between the pores with grain boundaries and the rate and mode of growth. The grain boundary may move due to grain boundary diffusion and the disordered region between grains. Heating causes large grains to grow at the expense of smaller grains. This

results in an increase in the mean grain size with a decrease in the total grain boundary area. Grains that have an isotropic interfacial tension will shrink if the grain has less than six sides and has convex boundaries, whereas the grain will grow if the grain has more than six sides and concave boundaries. The grain boundary will then move towards the center of curvature.

Pores and small solids may intersect a grain boundary. A bimodal grain size distribution is created when those inclusions disappear, and coarsening occurs. This form of grain coarsening is called exaggerated grain growth or discontinued grain growth. The inclusions decrease grain mobility by creating a drag force on the boundary. Ostwald ripening is a form of pore growth where pores gather on a boundary, or the diffusion of vacancies brings small pores to larger pores rather than to the grain boundaries.

In the final stage of sintering, when processing is not controlled, exaggerated grains appear separated from pores. Exaggerated grains tend to form when powder aggregates or when coarse particles are present, causing the pore distribution to be inhomogeneous. A high sintered density can be achieved when the material contains densely packed fine particles and when a grain growth inhibitor is dispersed and evenly distributed.

A rapid heating schedule may produce densification with smaller concomitant grain size. Surface diffusion can cause grain coarsening when it dominates at low temperatures. Grain coarsening can also occur when fast heating increases vacancy diffusion and when densification occurs at a faster rate than diffusion.

The atmosphere is important in sintering as well. When gas is trapped inside a pore, the pore will be unable to shrink unless the gas is soluble in the grain boundary and can diffuse out of the pore. The sintering atmosphere may influence the sublimation or

stoichiometry of the particles or dopant. The oxygen pressure must be controlled when sintering compounds because the vaporization rate is lower when the oxygen pressure is higher and in a closed container saturated with the vapor. The oxidation state of the transition metal ions and lattice vacancies depend on the atmosphere, and the partial pressure of oxygen is controlled to obtain a high density and proper magnetic phases. When sintering non-oxide ceramics such as silicon carbide doped with B_4C at a temperature above 2000^oC, a nitrogen atmosphere causes BN to form in the SiC lattice, which reduces the vaporization of boron. The reaction bonding may produce a significant increase in density.

The sintering of ceramics also depends on the distribution of pore sizes and the homogeneity of the porosity. Uniform interstices smaller than the grains will shrink quickly at a uniform rate as the compact has homogeneous particles. However, large pores in a compact shrink slowly. When pressed at high pressure, the pore size range will narrow, and a higher green density can be achieved.

Inhomogeneous sintering and shrinkage will occur in materials containing densely packed regions or regions of finer particles that are separated by porous regions with large pores. Regions with smaller pores will densify earlier, and coarser pores in the boundary remain. Chemical densification aids have a similar effect when distributed inhomogeneously in the material [82].

2.6.1.2. Liquid Phase Sintering

In liquid phase sintering, at least one component or more should melt in the system to densify materials. When the liquid phase wets the solid particles due to the surface tension, capillary forces are formed, helping the densification of materials because of its

power to keep grains together. General capillary pressure is explained with the following equation [15];

$$P = \frac{\gamma Lv}{\rho} \tag{18}$$

The capillary pressure is P, the liquid-vapor interfacial energy is γLV, and radius of the curve is ρ [15].

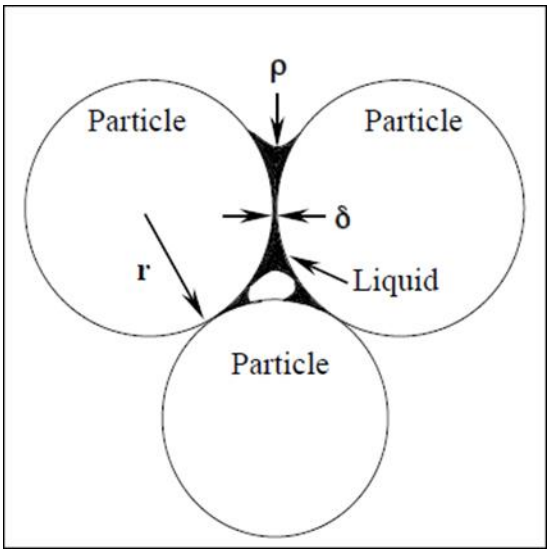

Figure 14. Under capillary force stage of particles[15]

Liquid phase sintering consists of three stage which are rearrangement, solution-reprecipitation, and solid state sintering [84]. The stages of liquid phase sintering are shown in Figure 15 [88].

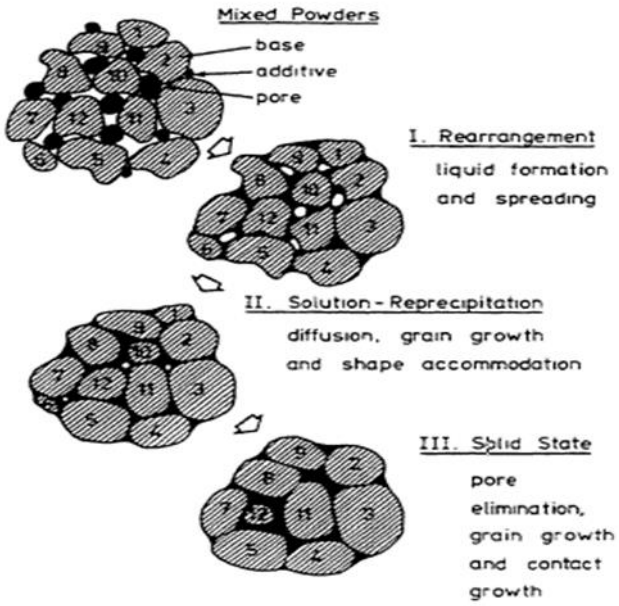

Figure 15. The stages of liquid phase sintering [88]

During this initial stage of liquid sintering, the densification is fast due to the capillary forces. Densification may change due to the amount of liquid phase, grain size, and solubility of solid particle in the liquid phase. Better rearrangement requires small particle size. Around 35% liquid phase is required to have a fully dense material in rearrangement stage [88]. In the second stage of the liquid phase, sintering is based on increasing grain size. The liquid phase fills the pores between solid particles. Since small solid particles desolve in the liquid phase and form bigger particles, grain coarsening occurs [15, 88]. The final stage of liquid phase sintering is controlled by solid state sintering. This stage is slower than the earlier stages because of the increase in solidity, however, grain growth still continues by diffusion [88]. A summary of the liquid phase sintering is shown in Figure 16 [51].

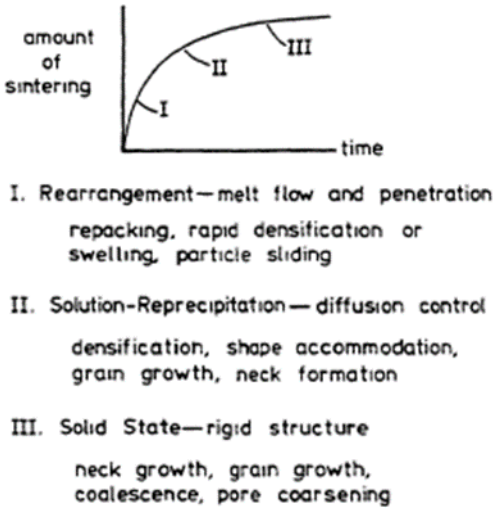

Figure 16. A summary of thee three stages of liquid phase sintering [88]

Sahani et al. sintered SiC-B_4C composites addition of 5-10-20 wt% Al by pressureless sintering and SPS method. Al causes liquid phase sintering. Due to the low melting temperature of Al, samples were sintered at 1950°C for 30 min under argon by pressureless sintering and sintered at 1300°C for 5 min under 50MPa pressure by SPS. Pressureless sintering time and temperature were not enough to reach a density above 90%. SPS sintering conditions were allowed to reach density 97%. 23.80 GPa hardness value with 10% Al addition was achieved. However, composites hardness values were quite low due to the presence of Al [89].

2.6.2. Reaction Bonding

The reaction bonding method is an alternative method to hot pressing or pressureless sintering to densify silicon carbide composites [90, 91]. The reaction bonded silicon carbide composites have a lower sintering temperature, shorter sintering time, high density, and low cost of the sintering process [92]. Many researchers have shown that it is possible to densify SiC-B_4C composites by reaction bonding. Zhou and his coworkers

showed that dense composites could be produced by reaction bonding with high elastic modulus and fracture toughness, however, hardness values were lower due to the excess Si [93]. Reaction bonding can be used to produce a net shape or complex shape product. In this process, a porous preformed silicon carbide-carbon or boron carbide-carbon is infiltrated with molten silicon, and this silicon reacts with carbon to form silicon carbide. The disadvantage of this process is that residual silicon left over after the process [92, 94-96].

2.6.3. Hot Pressing

Hot pressing is a high-pressure, high-temperature synthesis process with a low strain rate that is used to form a dense material out of powder. Densification is achieved by applying pressure along the vertical axis by graphite punches on a rigid, heated die containing the powder [97, 98]. This processing method is used to densify carbides, borides, nitrides, oxides, as well as ceramic/metal composites [28, 82, 85, 97, 98]. The basic components of a hot-press are a hydraulic ram, an induction furnace, and graphite die. The general hot press set-up is shown in Figure 17 [99].

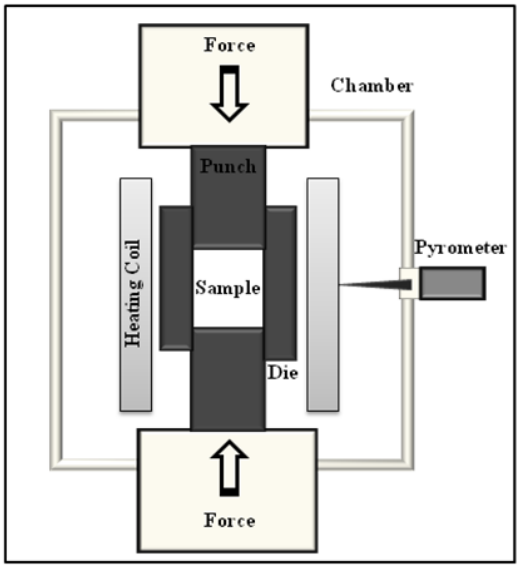

Figure 17. General hot press set-up [99]

The key to obtaining a high-quality sample is to control the two main factors of sintering: temperature and pressure [97]. The hydraulic ram applies uniaxial pressure as high as 80 MPa. Graphite is the most common die material used because it is cheap and has high creep resistance at high temperatures. Standard graphite is used for pressures below 40 MPa. Specialty graphite, ceramics, or refractory metals are used for higher pressures. Graphite must be used in an inert or reducing atmosphere when heated to temperatures above 1200^{o}C to avoid oxidation. Another issue with the use of graphite is its reactivity with other ceramics, causing deterioration or sticking to the sample. However, this can be prevented by coating the contact surfaces of the die with boron nitride at temperatures under 1350^{o}C or lining the die with graphite foil [85, 98]. The simplest method of hot pressing is applying the required pressure to the die and releasing the pressure before heating. The system is heated rapidly, and pressure is reapplied once the

sintering temperature is reached. The pressure is released once more when densification is complete, and the system begins cooling. Generally, 10-20 MPa pressure is applied to die and increases it to 40-50 MPa once sintering temperature is reached. In this case, the pressure is kept constant during the heating and cooling of the system. The densification can be observed by ram displacement. The sintering temperature is chosen to complete densification within 30 min- 2 hours and is often found through trial and error. Hot pressing causes significant axial strain on the sample, which can result in texture. Texture can also be developed by the rotation of elongated particles within the powder. Equiaxial particles may undergo shape change due to the applied stress, which also alters the texture [85]. Illustrating the microstructural texturing during hot pressing can be seen in Figure 18.

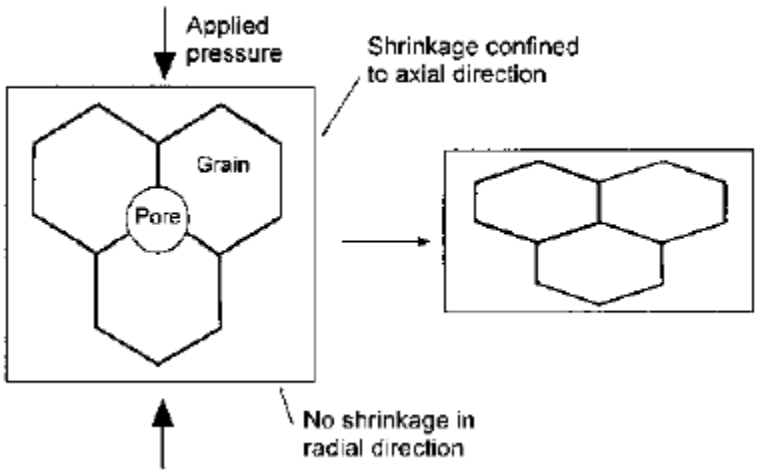

Figure 18. Microstructural texturing during hot pressing [85]

Due to the applied pressure, pores move through from the neck to the particles, so it helps to eliminate large pores and provide densification. However, grain coarsening is dependent on temperature; it is not related to applied pressure. Usually, powders densify by hot pressing between 2100-2250°C and up to 2400°C [27, 98, 99]. The main

disadvantages are the expense and low heating rate, and relatively long dwelling time [28, 82, 99].

Uehara et al. studied SiC-B_4C composites for synergistic enhancement of thermoelectric property. The powder was hot pressed with SiC-30wt. % B_4C and SiC-70wt. % B_4C using graphite mold for 0.5h at 1800-2100°C under the uniaxial pressure of 50 MPa in Ar atmosphere. The relative density reached up to 99% at 2000 °C for SiC–70wt. %B_4C. SiC–30wt.%B_4C was densified to 99% at a lower temperature of 1900°C [100].

2.6.4. Spark Plasma Sintering

One of the new developments in the sintering technique is called spark plasma sintering (SPS) [27]. The basic components of SPS are uniaxial pressurization, water-cooled special energizing mechanism, a water-cooled vacuum chamber, atmosphere controls,vacuum unit, sintering DCpulse generator and an SPS controller[101]. Spark plasma sintering equipment is shown in Figure 19 [101]. A high DC passes through conductive powder at 5000-20000A. Applied pressure can be range between 10-100MPa, and SPS has a heating rate up to 1000°C/min [25, 101].

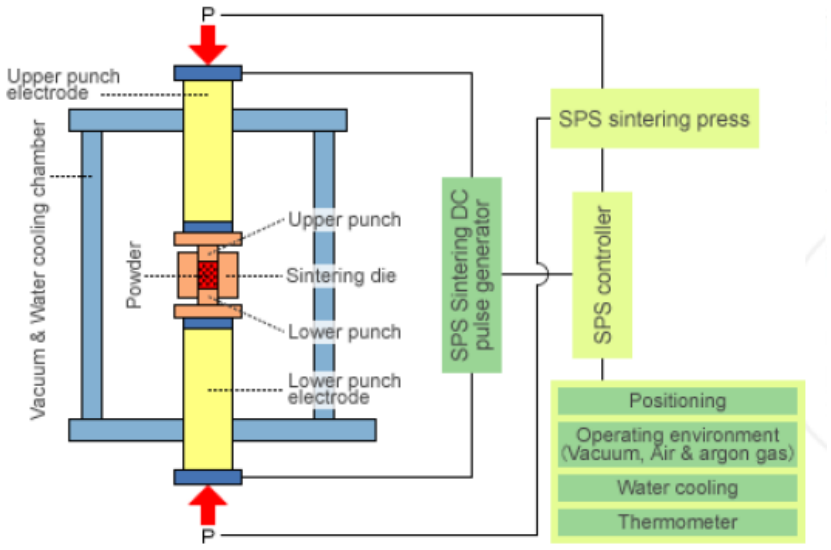

Figure 19. Spark plasma sintering equipment [101].

By spark plasma sintering, materials can achieve to high density in a shorter time to inhibit grain growth [27]. One of the more generally known theories is that, due to the high continuous current, intensely high temperatures occur between particles and establishes regional plasma. At that time this plasma releases, it goes throughout intergrain pathways and the consequent regional temperature reach thousands. This method allows lower temperature and faster sintering periods than other methods [102, 103]. DC path of the SPS is shown in Figure 20 [99].

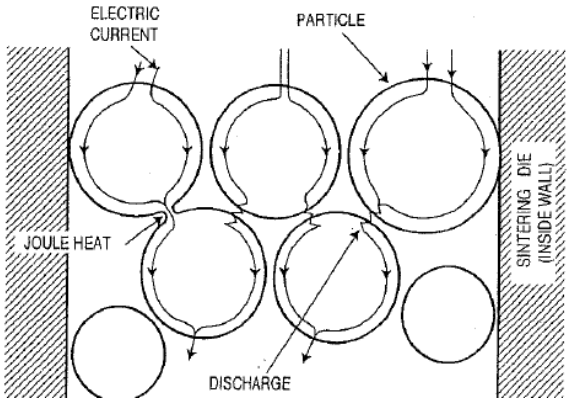

Figure 20. Current path through precompacted powder of the SPS [99]

Genckan also studied B_4C/SiC by SPS. 5%, 10%, 15%, and 20% SiC was added to B_4C and C. Si, B_4C, and C powders were mixed with alcohol. Powders were sintered at 1700°C (5 min) at 1750°C (5 min), and at 1670°C (15 min) under 40 MPa pressure. Maximum densities were obtained at 1670 °C. The final products were 5, 10, 15, and 20%SiC in B_4C. For each mixture, the highest relative densities respectively were 98.3%, 95.4%, 90.3% and 88.6% [104]

2.7. SiC-B_4C Composites

Whether composite materials are metal, organic, or inorganic, combining two or more materials produce higher mechanical and physical properties than their components. Components of composite materials are usually chemically different and do not desolve in each other [1, 2]. Some materials properties can be improved by producing composite materials, such as toughness, corrosion resistance, wear resistance, elastic properties, density, fatigue, temperature-dependent behavior, heat insulation, and thermal conductivity [1, 3]

Since boron and silicon are in the same group in periodic table, both SiC and B_4C have similar physical and chemical properties. For instance, high covalent bonding, a high melting point, very high hardness, high mechanical strength, a high Young's modulus, low thermal expansion, and excellent chemical stability [4, 5]

Table 4. Physical and Mechanical Properties of B_4C and SiC [20]

Property	**B_4C**	**SiC**
Crystal structure	rhombohedral	hexagonal
Density (g/cm^3)	2.52	3.2
Linear thermal expansion, α ($10^{-6}/K$)	4.5	5.68
Thermal conductivity (W/m.K)	27.63	15-155
Electrical resistivity (10^{-6} Ω.cm)	10^6	$>10^5$
Fracture toughness, K_{IC}($MPa.m^{1/2}$)	3-3.5	2.5-6
Elastic modulus (GPa)	450	480
Hardness (GPa)	37-47	20-35
Three-point flexural strength (MPa)	300	300-800
Enthalpy(kJ/m)	72	71.6
Oxidation resistance(°C)	1100	1400

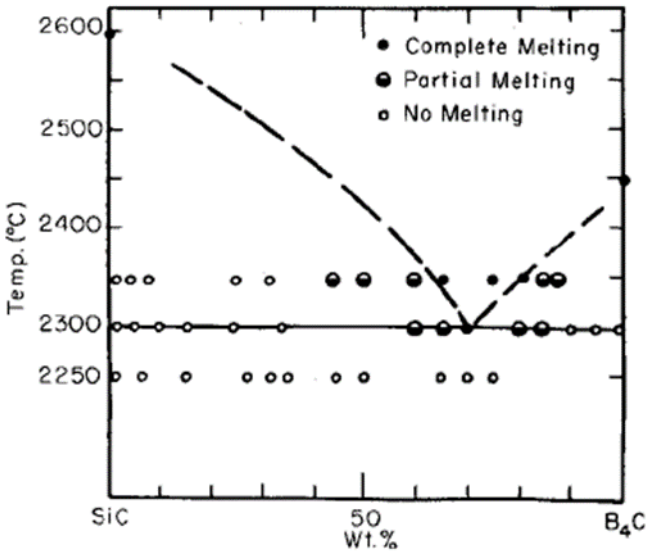

Figure 21. The system B_4C-SiC [105]

According to the phase diagram, eutectic points between B_4C and SiC are at 70±2 wt% B_4C and 30±2 wt% SiC at 2300± 20°C. These can also be seen from the binary phase diagram given in Figure 21 [105].

The presence of boron affects the properties of the composites. Increasing the amount of boron carbide decreases the density of composite and reduces the oxidation resistance. However, the composite will be lighter and will have higher fracture toughness. Such composites also exhibit high heat resistance and impact resistance [104, 106]. The presence of silicon carbide inhibits grain growth in SiC- B_4C composites [12].

SiC- B_4C composites are used as nozzles, turbine engines, heat conducting tube, and in the defense industry (armor plate) [104, 107, 108].

2.7.1. Previous studies on SiC- B_4C composites

In 1978, Prochazka et al. sintered SiC-10-30% B_4C with pressureless sintering at temperature ranging from 2080-2090°C. The relative density decreased from 92% to 85% when the B_4C content increased [109].

Thevenot studied pressureless sintering 10%-90%SiC-B_4C at 2100°C under argon. SiC and B_4C were mixed with 2.5% resin and 4% plasticizer. The relative densities were increased from 93 to 99% when the SiC content was increased from 10 to 90%. In low SiC content, samples had a bigger grain size, proving that SiC inhibited grain growth in SiC-B_4C composites [110].

Magnani at al. studied the pressureless sintering and properties of the αSiC-B_4C composite. 94% SiC-5%B_4C-1%C powders were mixed with ethanol. By using a graphite furnace, sintering was investigated in the temperature range of 1950-2200°C for 30 min. A density of 96% TD was reached at 2150°C [111].

Zhang at al. studied the preparation of B_4C-SiC composite ceramics by mechanical alloying. B_4C and SiC ratio was 1:1 and powders were mixed with ethanol. Composites were sintered at 1800-1950° C for 30 min by hot pressing. The relative density was 72%TD at 1800°C and 96%TD at 1950°C. The hardness value was 24GPa at 9.8N load. Their research showed that SiC-B4C composites fracture mode is transgranular [66].

Sahani and coworker densified 60%SiC- B_4C-2-5-10-20%Si composites by pressureless sintering at 1950°C for 30 min and spark plasma sintering at 1350°C for 5 min under 50MPa pressure. The highest relative density was achieved with 10%Si addition for

both sintering methods; pressureless sintering and SPS had density values of 92% and 98% respectively. The hardness values were 18.1GPa for pressureless sintering and 27.8GPa for SPS. SPS method provides higher density and hardness than pressureless sintering [112].

Moshtaghioun et al. used C as a sintering additive to B_4C-15%SiC. Also they made samples without 2% C additive and only B_4C to see the differences. Samples were sintered at 1650°C for 5 min and 1700°C for 3 min under 75 MPa pressure by spark plasma sintering. The results showed that 2% C additive helped achieve full densification at 1700°C. Since pure B_4C showed transgranular fracture mode, composites showed mix mode fracture [113].

Sahin et al. studied spark plasma sintering of B_4C-SiC composites from three different groups B_4C- SiO_2- C, B_4C- SiC, and B_4C- SiC-Y_2O_3. 5%Y_2O_3 was used as an additive. Powders were mixed B_4C 5, 10, and 15 vol. % SiC in ethanol. Samples were sintered at 1750°C for 5 minutes under 40MPa pressure. 5, 10, and 15 vol. % SiC- B_4C relative density results were 98.0%, 98.0%, and 97.8% respectively. 5, 10, and 15 vol. % SiC- B_4C- 5%Y_2O_3 relative density results were 98.3%,98.8%, and 98.2% respectively. Yttrium oxide increased densities values slightly due to the form of the glassy phase. The density decreased with increasing SiC content because of the oxidation of SiC to SiO phase [114].

3. Method of Attack

The goals of this thesis are producing high dense SiC-B_4C composites, optimizing mechanical properties of SiC-B_4C composites and understanding the role of excess oxygen content on sinterability. In meeting this goal, three primary objectives will be examined. First, two different silicon carbide powders were selected to be characterized. This included modifying the oxygen content of the powder by acid washing. Second, an understanding of the sinterability of SiC-B_4C composites as a function of carbon addition had to be examined. Third, the dense composite samples microstructure and mechanical properties were characterized through different techniques.

3.1. Objective 1: Understanding and Controlling Surface Oxygen in Micron sized SiC and B_4C powders

To evaluate the role of excess oxygen content on the sinterability, microstructure, and mechanical properties of dense composites, the starting powders had to be examined. This objective was derived into four tasks; powder choice, develop a safe and effective laboratory scale acid etching process to evaluate the powders oxygen content, powder cleaning to remove B_2O_3 layer, and powder characterization.

3.1.1. Powder Choice

A total of four different types of raw materials were used for this research including H.C. Starck- UF 25 silicon carbide, Saint Gobain silicon carbide, HC. Starck HD 20 boron carbide, and carbon-lamb black from Fisher Scientific. In the case of the Saint Gobain powder, it was obtained directly from the Saint Gobain, Niagara Falls, New York plant, and it was not commercially available. Previous researchers showed that these powders grade could be densified under suitable conditions [111, 113, 114].

3.1.2. Develop a Safe and Effective Laboratory Scale Acid Etching Process

According to Wilhelm, the high oxygen level of starting SiC powders affects the mechanical properties of the densified composites [79]. Silicon carbide of both starting powders were observed to have an elevated oxygen content. This oxygen level was too high for SiC to produce dense composites, so an etch protocol was developed. SiC was etched with different concentrations of hydrofluoric acid for 1- hour, 4 hours, and 24 hours.

3.1.3. Powder Cleaning to Remove B_2O_3 Layer

Since commercial B_4C was used to produce composites, the B_4C powder was washed with HCl to remove the excess B_2O_3 layer [115].

3.1.4. Powder Characterization

Powder characterization was performed before and after the acid washing process to document the change on SiC powders. XRD analysis was used to determine the polytype and purity of initial SiC and B_4C powders by using a Panalytical X'Pert X-Ray diffractometer. LECO TC600 oxygen/nitrogen analyzer was used to determine the oxygen content of silicon carbide and boron carbide powders. Particle size was determined using a Malvern Matersize 2000 and FESEM analysis

3.2. Objective 2: Densification of Silicon Carbide-Boron Carbide Composites

To investigate the role of excess oxygen on microstructural and mechanical properties of silicon carbide boron carbide composite, powders had to be densified. This objective was split into five tasks; densify SiC powder, find an optimal SPS cycle to densify composite, evaluate the role of homogeneity on the composite microstructure, evaluate powder mixing method, prepare mixture, and produce the dense sample.

3.2.1. Densification of Etched SiC

Etched silicon carbide was sintered with the addition of boron carbide and carbon to effect the acid ething process and oxygen content.

3.2.2. Optimal SPS Cycle

Sintering process plays a major role in grain growth and obtaining dense composites. For this reason, finding optimum sintering conditions to achieve full density is very important. 50%B_4C-1.5%C-48.5%SiC composition was sintered at different combinations of temperature and pressure to achieve optimal density. Different compositions might need variying combinations of different temperature and pressure to reach full density. However, compare samples, all samples were sintered under the same conditions to understand the effect of temperature and pressure.

3.2.3. Evaluate the role of homogeneity in the composite microstructure

To investigate the role of mixture method on microstructural and mechanical properties of the composites, two different methods were used. Dry mixing by Specktromill (Spex Inc. 8000M) and wet mixing by ball milling were used.

3.2.4. Mixture Preparation

All samples matrix were mixed with ethanol and SiC media by ball milling for 24 hours.

3.2.5. Production of Dense Samples

Spark plasma sintering method was used to sinter composite samples. Sintering temperature and applied pressure were determined after sintered study.

3.3. Objective 3: Characterization of dense Silicon Carbide- Boron Carbide Composites

To investigate the role of excess oxygen on microstructural and mechanical properties of silicon carbide boron carbide composite, dense composite samples had to be fully characterized. This objective was divided to three tasks: microstructure characterization, phase determination by X-Ray diffraction, and mechanical properties characterization.

3.3.1. Microstructure Characterization

Microstructural analysis was used to determine properties of sintered dense composite samples. The Zeiss Sigma field emission scanning electron microscope was used to define pores, inhomogeneities, grain size, and shape. The linear intercepts method was used to measure grain size using Lince 2.4.2. image analysis software.

3.3.2. Phase Determination by X-Ray Diffraction

XRD diffraction analysis using a Panalytical X'Pert X-Ray diffractometer was used to determine polytype of composition, and to establish whether any solid solubility had occurred. Rietveld analysis was done using Jade software to determine the phase of the composite.

3.3.3. Mechanical Properties Characterization

Silicon carbide and boron carbide have high hardness and high elastic properties. To understand the role of oxide layer on the mechanical properties of composites, Poisson's ratio, Young's modulus, shear modulus, and bulk modulus were measured by ultrasound analyses. Since densification of ceramics affects having good mechanical properties, the Archimedes method was used to determine the density of sintered composite samples. Polished samples were used for hardness testing using a Vickers diamond tipped (9.8 N load) LECO-M-400-G3 and Berkovich nano-hardness (100 mN-500 mN load).

3.3.4. Data Analysis

To understand the relationship between free carbon, the hardness and mechanical properties like the elastic modulus and fracture toughness. Microsoft Excel was used to analyze data and correlate a meaningful relationship.

4. Experimental Procedures

4.1. Powder Characterization

4.1.1. Particle Size Analysis

Particle size analysis of the silicon carbide and boron carbide powders were measured using Malvern Master Sizer 2000. Hydro 2000S was attached to the Malvern Master Sizer 2000 for wet measurement. This system uses light scattering to determine the particle size distribution. Particle sizes can be measured from 500nm to 2000µm with this method. 0.10-0.20 grams of silicon carbide and boron carbide powders were dispersed in 10-20 ml DI water individually and ultrasonicated for 5 minutes to eliminate agglomeration. This slurry was pumped into the instrument and analyzed. Each test was run five times.

4.1.2. Chemical Analysis

The total wt. % oxygen in silicon carbide and boron carbide powders was analyzed using a LECO TC 600 O/N analyzer. This analyzer uses a combustion method. Sample powders were heated to high temperature under helium. The oxygen in the sample powder was reacted with carbon to form CO_2, and then oxygen content can be measured with the Leco's infrared detector. Oxygen standard was LECO 502-399 for both silicon carbide and boron carbide powders. For each sample, three analyses were performed and both the mean and standard deviation were noted. For all steps of analysis, graphite crucible was prepared with 0.05g graphite powder and 0.45g Nibble nickel. Three blank analysis and three standard analysis were done before the run sample. For blank analysis, three blank nickel

capsules and three graphite crucibles were used. For standard analysis, 0.14g standard powder put into each nickel capsule. For sample analysis, 0.1g was sample put into each capsule.

4.1.3. X-Ray Diffraction

X-ray diffraction was performed to determine polytype and purity of initial silicon carbide and boron carbide powders. Each silicon carbide and boron carbide was placed on a zero background sample holder. A Panalytical X'Pert X-Ray diffraction unit with a Cu Kα x-ray source at 45kV and 40 mA was used for analysis. Scan range was from 10° to 90° 2θ. The virtual step size was 0.0131° and rotation was 16 rpm for each scan. All scans were recorded by Data collector, after using MDI Jade 9 software the pattern was determined. First, pattern background should be edited to find the best fit curve for each pattern using the background curve editing cursor. Search/match procedure was used to define all phases using standard powder diffraction files. Also, phase intensities should be adjusted to the scanned patterns. Rietveld refinement can be done using options/WPF refinement. For all samples, profile shape function was Pseudo-Voight. The refinement parameters were lattice constants (unit cell) (LC), overall intensity scale factor (SF), and individual peak broad and shape (f0, f1, f2). While all key was selected, all refined parameter should be unselected and run the test. Then, LC and SF parameters should be run for all phase. After that, all key should be unselected and run f0, f1, and an f2 parameter for each phase individually. Two patterns (scanned and standard patterns) should have a flat difference for a well- defined.

4.1.4. Scanning Electron Microscopy

The Zeiss Sigma field emission scanning electron microscope was used to define grain size, and shape of grains. An aluminum stub was covered with carbon tape, and a small amount of powder was placed on carbon tape. Compressed air was used to blow off excess powder. Powder images were taken at 25000 magnification with 3kV accelerating voltage using SE2 detector.

4.2. Powder Preparation

4.2.1. Acid Etching

For etching study, Saint Gobain and HC. Starck UF 25 silicon carbide powders were etched to reduce oxygen content.

To reduce the oxygen content of powder H.C. Starck- UF 25 Silicon carbide was etched with 20%, 40%, 50% HF, and HF&NHO_3 acid for 1, 4, and 24 hours. To neutralize acidic slurry ethanol and ammonium hydroxide were used.

Table 5. Acid etching conditions

Acid	Concentration (%)	Etching Time (Hour)	Neutralized with
HF	20	24	Ethanol
HF	40	1-4-24	Ammonium Hydroxide
HF	50	1-4-24	Ammonium Hydroxide
HF& HNO_3	40-65	1-4-24	Ammonium Hydroxide

60 g SiC powder was mixed with 200 ml different concentration of HF (Acros Organics) and magnetically stirred for 1, 4, or 24 hours in a Nalgene HDPE beaker. The acidic slurry was neutralized until it reached pH 7 and centrifuged to separate the silicon carbide powder from the liquid. After that, wet silicon carbide was washed with DI water three times and centrifuged to get silicon carbide. Silicon carbide powder was placed in a drying oven to dry powder for around 3 hours. Dry powder cake was ground to a fine powder with a mortar and pestle.

After these experiments, 1-hour etching with 50% HF and neutralized with ammonium hydroxide was chosen. Saint Gobain SiC powder was etched only with this method.

4.2.2. Powder Cleaning to Remove B_2O_3 Layer

To clean the surface oxide from the boron carbide particles, the powder was mixed with diluted hydrochloric acid (HCl, pH 3.5) in a beaker and ultrasonicated and heated for 30 minutes. After the powder settled, the HCl solution was decanted out and the container was filled with DI water. The powder was washed with DI water and excess DI water was decanted as needed until all acid was removed. Then, the wet powder was mixed with

ethanol. After the solution settled, the excess ethanol was decanted and placed in a drying oven at 100°C to evaporate the ethanol.

4.2.3. Powder Mixing

Two different methods were used to mix powders. One of them was dry mixing by Speckromill; the other was wet mixing by ball milling. H.C. Starck- UF 25 silicon carbide, HC. Starck HD 20 boron carbide, and carbon-lamp black from Fisher Scientific were used as starting materials.

Dry mixing series, B_4C, C, and SiC were weighed and put in a small bottle without media by Specktromill for 5 minutes.

Wet mixing series, B_4C, C, and SiC were weighed and put in a Nalgene bottle with SiC ball and ball milled for 24 hours in ethanol media. After milling, the mixture was sieved to separate media from the liquid mixture using a 1.4 mm mesh sieve. The liquid mixture was placed on a hot plate at 275°C and allow to dry. Then, powder chunks were ground to uniformity with mortar and pestle.

Table 6. 10 % Boron Carbide- Etched Silicon Carbide Series

Sample	**B_4C (g)**	**SiC (g)**	**C (g)**	**Mixing Method**
10B_4C-SiC-1.5C	0.50	0.07	4.43	Dry Mixing
10B_4C-SiC-0.5C	3.00	26.85	0.15	Ball Milling
10B_4C-SiC-1.0C	3.00	26.70	0.30	Ball Milling
10B_4C-SiC-1.5C	3.00	26.55	0.45	Ball Milling

Table 7. 20 % Boron Carbide- Etched Silicon Carbide Series

Sample	B_4C (g)	SiC (g)	C (g)	Mixing Method
$20B_4C$-SiC-1.5C	1.00	0.07	3.93	Dry Mixing
$20B_4C$-SiC-0.5C	6.00	23.85	0.15	Ball Milling
$20B_4C$-SiC-1.0C	6.00	23.70	0.30	Ball Milling
$20B_4C$-SiC-1.5C	6.00	23.55	0.45	Ball Milling

Table 8. 30 % Boron Carbide- Etched Silicon Carbide Series

Sample	B_4C (g)	SiC (g)	C (g)	Mixing Method
$30B_4C$-SiC-1.5C	1.50	0.07	3.43	Dry Mixing
$30B_4C$-SiC-0.5C	9.00	20.85	0.15	Ball Milling
$30B_4C$-SiC-1.0C	9.00	20.70	0.30	Ball Milling
$30B_4C$-SiC-1.5C	9.00	20.55	0.45	Ball Milling

Table 9. 40 % Boron Carbide- Etched Silicon Carbide Series

Sample	B_4C (g)	SiC (g)	C (g)	Mixing Method
$40B_4C$-SiC-1.5C	2.00	0.07	2.93	Dry Mixing
$40B_4C$-SiC-0.5C	12.00	17.85	0.15	Ball Milling
$40B_4C$-SiC-1.0C	12.00	17.70	0.30	Ball Milling
$40B_4C$-SiC-1.5C	12.00	17.55	0.45	Ball Milling

Table 10. 50 % Boron Carbide- Etched Silicon Carbide Series

Sample	B_4C (g)	SiC (g)	C (g)	Mixing Method
$50B_4C$-SiC-1.5C	2.50	0.07	2.43	Dry Mixing
$50B_4C$-SiC-0.5C	15.00	14.85	0.15	Ball Milling
$50B_4C$-SiC-1.0C	15.00	14.70	0.30	Ball Milling
$50B_4C$-SiC-1.5C	15.00	14.55	0.45	Ball Milling

Table 11. 10% Boron Carbide Series- Unetched Silicon Carbide

Sample	B_4C (g)	SiC (g)	C (g)
10B_4C-SiC-0.5C	3.00	26.85	0.15
10B_4C-SiC-1.0C	3.00	26.70	0.30
10B_4C-SiC-1.5C	3.00	26.55	0.45
10B_4C-SiC-2.0C	3.00	26.40	0.60
10B_4C-SiC-2.5C	3.00	26.25	0.75

Table 12. 20% Boron Carbide Series- Unetched Silicon Carbide

Sample	B_4C (g)	SiC (g)	C (g)
20B_4C-SiC-0.5C	6.00	23.85	0.15
20B_4C-SiC-1.0C	6.00	23.70	0.30
20B_4C-SiC-1.5C	6.00	23.55	0.45
20B_4C-SiC-2.0C	6.00	23.40	0.60
20B_4C-SiC-2.5C	6.00	23.25	0.75

Table 13. 30% Boron Carbide Series- Unetched Silicon Carbide

Sample	B_4C (g)	SiC (g)	C (g)
30B_4C-SiC-0.5C	9.00	20.85	0.15
30B_4C-SiC-1.0C	9.00	20.70	0.30
30B_4C-SiC-1.5C	9.00	20.55	0.45
30B_4C-SiC-2.0C	9.00	20.40	0.60
30B_4C-SiC-2.5C	9.00	20.25	0.75

Table 14. 40% Boron Carbide Series- Unetched Silicon Carbide

Sample	B_4C (g)	SiC (g)	C (g)
40B_4C-SiC-0.5C	12.00	17.85	0.15
40B_4C-SiC-1.0C	12.00	17.70	0.30
40B_4C-SiC-1.5C	12.00	17.55	0.45
40B_4C-SiC-2.0C	12.00	17.40	0.60
40B_4C-SiC-2.5C	12.00	17.25	0.75

Table 15. 50% Boron Carbide Series- Unetched Silicon Carbide

Sample	B_4C (g)	SiC (g)	C (g)
50B_4C-SiC-0.5C	15.00	14.85	0.15
50B_4C-SiC-1.0C	15.00	14.70	0.30
50B_4C-SiC-1.5C	15.00	14.55	0.45
50B_4C-SiC-2.0C	15.00	14.40	0.60
50B_4C-SiC-2.5C	15.00	14.25	0.75

Table 16. 60% Boron Carbide Series- Unetched Silicon Carbide

Sample	B_4C (g)	SiC (g)	C (g)
60B_4C-SiC-0.5C	18.00	11.85	0.15
60B_4C-SiC-1.0C	18.00	11.70	0.30
60B_4C-SiC-1.5C	18.00	11.55	0.45
60B_4C-SiC-2.0C	18.00	11.40	0.60
60B_4C-SiC-2.5C	18.00	11.25	0.75

Table 17. 70% Boron Carbide Series- Unetched Silicon Carbide

Sample	B_4C (g)	SiC (g)	C (g)
70B_4C-SiC-0.5C	21.00	8.85	0.15
70B_4C-SiC-1.0C	21.00	8.70	0.30
70B_4C-SiC-1.5C	21.00	8.55	0.45
70B_4C-SiC-2.0C	21.00	8.40	0.60
70B_4C-SiC-2.5C	21.00	8.25	0.75

Table 18. 80% Boron Carbide Series- Unetched Silicon Carbide

Sample	B_4C (g)	SiC (g)	C (g)
80B_4C-SiC-0.5C	24.00	5.85	0.15
80B_4C-SiC-1.0C	24.00	5.70	0.30
80B_4C-SiC-1.5C	24.00	5.55	0.45
80B_4C-SiC-2.0C	24.00	5.40	0.60
80B_4C-SiC-2.5C	24.00	5.25	0.75

Table 19. 90% Boron Carbide Series- Unetched Silicon Carbide

Sample	B_4C (g)	SiC (g)	C (g)
90B_4C-SiC-0.5C	27.00	2.85	0.15
90B_4C-SiC-1.0C	27.00	2.70	0.30
90B_4C-SiC-1.5C	27.00	2.55	0.45
90B_4C-SiC-2.0C	27.00	2.40	0.60
90B_4C-SiC-2.5C	27.00	2.25	0.75

4.3. Sintering of Composites

Spark plasma sintering (Thermal Technology) technique was used to sinter samples. 5 grams of each powder mixture was loaded into a 20 mm inner diameter graphite die with graphite punches. The inside of graphite die was lined with graphite foil. The

graphite die had a small hole on it; this hole was used to detect the actual temperature of the sample by optical pyrometer during the heating cycle. Die was loaded into SPS unit with 5 MPa applied pressure. Sintering cycle started and heated to 600°C and wait 1 minute. Optical pyrometer started temperature after 600°C. Basic die diagram can be seen in Figure 22.

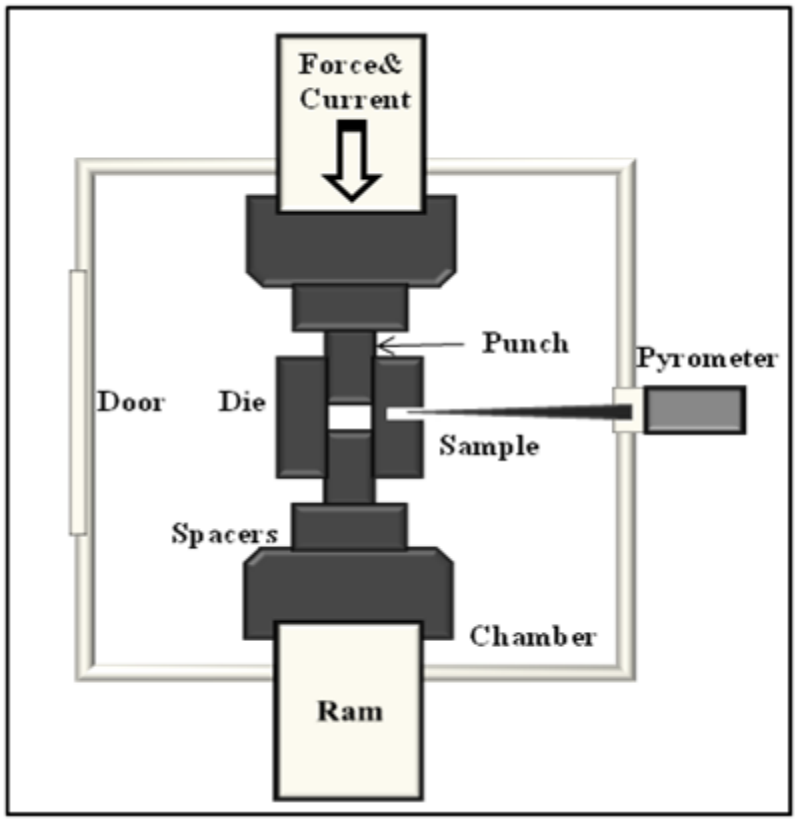

Figure 22. Basic die diagram [99]

To find the best sintering temperature 50%B_4C-1.5%C-48.5%SiC composition was sintered under four different temperatures of 1800°C, 1850°C, 1900°C, 1950°C. Two stage sintering was used to sinter samples. The dry powder was SPSed by heating to 1400°C with a 200°C/min heating rate under vacuum with an applied pressure of 50MPa

and dwell time of 1 minute. After 1-minute holding time, the samples were heated to sintering temperature at 200°C/ min under 50MPa applied pressure and held for 5 min.

To find the best applied pressure 50%B_4C-1.5%C-48.5%SiC composition was sintered at 1950°C with four different applied pressures (20, 30, 40 and 50MPa). Two stage sintering was used to sinter samples. The dry powder was SPSed by heating to 1400°C with a 200°C /min heating rate under vacuum with an applied pressure of 20, 30, 40 and 50MPa and holding for 1 minute. After 1-minute holding time, the samples were heated to 1950°C at 200°C/ min, under 20, 30, 40, and 50MPa applied pressure and held for 5 min.

All samples were sintered using SPS by heating to 1400°C with a 200°C /min heating rate under vacuum with an applied pressure of 50MPa and holding for 1 minute. After 1-minute holding time, the samples were heated to 1950°C at 200°C/min, under 50MPa applied pressure and held for 5 min. Afterward, the SPS was shut down and the samples were allowed to cool.

4.4. Post Sintering Processing of Dense Samples

After sintering processing, the dense samples needed sandblasting to remove excess graph foil from the surface. Surface grinding was necessary after sand blasting to produce a smooth and flat surface for ultrasound analysis and X-ray diffraction since samples had remaining carbon from graph foil and imperfection from sandblasting. Samples were cut close to the center of the sample using a LECO Vari/Cut 50 diamond saw. Two small pieces were chosen and mounted with epoxy using a Buehler SimpliMet 1000 mounting press. Samples were then polished to 0.25 µm finish using Buehler- Ecomet 250-Grinder-Polisher. The polishing procedure can be seen in Table 5. Between each step, the samples

and sample holder were cleaned under water and ultrasonicated to remove any residual diamond left to avoid contamination of the pads.

Table 20. Polishing method for SiC-B_4C composites

Step	Diamond Size (µm)	Pad	Fluids	RPM	Pressure (lb)	Time	Rotation Direction
1.	125	Diamond Embedded	Water	180	5	30s	Counter
2.	70	Diamond Embedded	Water	180	5	30s	Counter
3.	45	Diamond Embedded	Water	180	5	30s	Counter
4.	15	Diamond Embedded	Water	180	5	30s	Counter
5.	9	Cloth	9 µm diamond suspension	150	5	10m	Counter
6.	6	Cloth	6 µm diamond suspension	150	5	10m	Same
7.	1	Cloth	1 µm diamond suspension	150	5	10m	Same
8.	0.25	Cloth	0.25 µm diamond suspension	150	5	10m	Same

One piece of the two polished samples was etched first by a modified Murakami method (20g KOH and 20g $K_3Fe(CN)_6$ in 60 ml DI water) for 4.5 min to highlight SiC grain boundaries, then etched B_4C grains with 100g water, 1g potassium hydroxide, voltage 5V for 30 s. Etched samples were washed with acetone and ethanol to remove residual salt.

Another small piece was cut, and cross section milled for 5 hours with 6kV acceleration voltage using a Hitachi IM4000 Plus ion milling system. After cross section,

samples were flat milled for 5 min at 80 °tilt angle with 3kV acceleration voltage to remove imperfections from sample surfaces.

4.5. Characterization of Dense Composites

4.5.1. Density Measurements

The density was measured using the Archimedes method. The density was measured after surface grinding. All samples were cleaned using acetone and dried for 1 hour in a drying oven. Each sample was weighed five times dry with Adam PGW analytical balance with 0.001 g accuracy. Then the samples were suspended five times in water as shown in Figure 23.

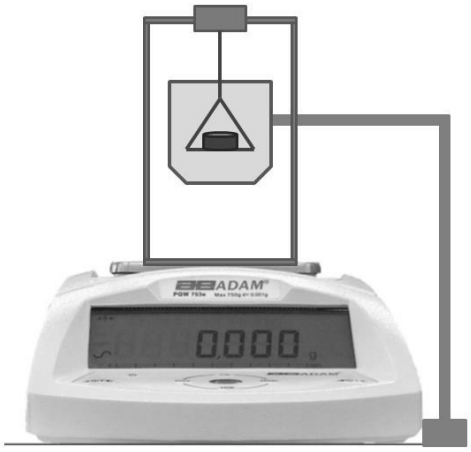

Figure 23. Archimedes density measurement set-up

An average of five measurements were used in the equation to calculate density. The following equation was used to calculate the density:

$$\rho = \frac{\text{dry weight}}{\text{dry weight} - \text{suspended weight}} \tag{20}$$

In Equation (20), “dry weight- suspended weight” means the displacement gram of water. Since water has a density of 1g/cm^3 , the volume of the object will be equal the difference between dry and suspended samples weight. So the density’s unit is g/cm^3.

The % theoretical density was measured using the following equation;

$$\%\ \text{theoretical density} = \frac{\rho}{\rho t} * 100 \qquad (21)$$

4.5.2. X-Ray Diffraction

X-ray diffraction was performed on dense samples to determine polytype of composition and to establish whether any solid solubility had occurred. A Panalytical X’Pert X-Ray diffraction unit with a Cu Kα x-ray source at 45kV and 40 mA was used for analysis. Scan range was from 10° to 90° 2θ. The virtual step size was 0.0131° and rotation was 16 rpm for each scan. All scans were recorded by Data collector, after that Rietveld analysis was done using Jade software to determine the phase of the composite. Especially the free carbon peak present at 26.6° 2θ was important to understand if the addition of carbon was reacted during sintering processing or not.

4.5.3. Ultrasound Measurements

Ultrasound analysis method was used to calculate dense sample’s elastic properties. For each sample, elastic properties were measured 5 times, and both the mean and standard deviation were noted. For this analysis, one transducer was used which could emit and receive the ultrasound energy. The longitudinal (LTOF) wave was measured using Olympus V316 20 MHz transducer, and shear (STOF) wave was measured using Olympus V222-BA-RM. Using these measurements, longitudinal (c_L) and shear (c_S) sound speeds were calculated by the following equations:

$$c_L = \frac{2\mathrm{d}}{\mathrm{LTOF}} \tag{22}$$

$$c_S = \frac{2d}{\mathrm{STOF}} \tag{23}$$

d is the thickness of the sample. Poisson's ration, Young's modulus (E), bulk modulus (K), and shear modulus (G) were calculated by the following equations:

Poisson's Ratio:

$$v = \frac{1 - 2\left(\frac{c_S}{c_L}\right)^2}{2 - 2\left(\frac{c_S}{c_L}\right)^2} \tag{24}$$

Young's Modulus:

$$E = \frac{(1-2v)(1+v)\rho {c_L}^2}{\frac{1-v}{1000000}} \tag{25}$$

Bulk Modulus:

$$K = \frac{\mathrm{E}}{3(1-2v)} \tag{26}$$

Shear Modulus:

$$G = \frac{\mathrm{E}}{2(1+v)} \tag{27}$$

4.5.4. Scanning Electron Microscopy

Pores, inhomogeneity, grain size, and shape of grains were examined by the Zeiss Sigma field emission scanning electron microscope. Ion milled samples' images were taken at 1000, 2500, 5000, 15000 magnifications using SE2 and in-lens detectors with a 5kV accelerating voltage to check microstructure of dense samples. To examine fracture surface morphology, one piece of each sample was fractured and analyzed. Polished and etched samples' images were taken at 15000 magnification using SE2 detector with 5° tilted specimen holder with a 10 kV accelerating voltage to use measure grain size of each sample. Grain size was measured by linear intercepts method using Lince 2.4.2. image analysis software.

4.5.5. Vickers Hardness and Indentation Fracture Toughness

Hardness test was completed using LECO M-400-G3 microhardness tester with a Vickers diamond indenter. 9.8 N load was applied for 10 seconds on polished sample surfaces. At least ten acceptable indentations were made. Indent sizes were measured using a Keyence VHX 5000 digital microscope.

By the following equation, Vickers hardness value was calculated to refer to ASTM C1327-15:

$$H_v\ (\text{GPa}) = 1.8544\frac{\text{P}}{d^2} \tag{28}$$

Where P (kgf) is a force, and d (mm) is the average length of the two diagonals of the indentation. Each hardness value presents the mean of the 10 calculated hardness.

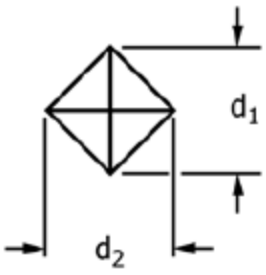

Figure 24. Vickers indenter

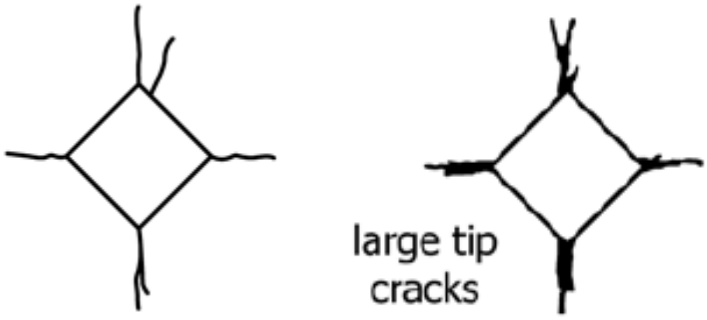

Figure 25. (a) A typically acceptable indentation, (b) a typically unacceptable indentation

The indentation fracture can be calculated by measuring Vickers indenter crack length. The indentation fracture toughness is affected by load of indentation, crack length, elastic modulus, and hardness of the materials [116]. Each indentation fracture toughness value presents the mean of 10 calculated fracture toughness. Indentation fracture toughness was calculated by the following equation:

$$K_c = 0.018(E/H_v)^{0.5}\,(P/c^{1.5}) \tag{29}$$

4.5.6. Berkovich Nano-Hardness

Nanoindentation test was performed using MicroMaterials NanoTest Vantage tester with Berkovich indenter. For this test 100Mn, 300mN, and 500mN loads were applied to polished sample surfaces. 20 indents were made for each load, and both the mean

and standard deviation were noted. The MicroMaterials software was used to calculate the hardness value of samples.

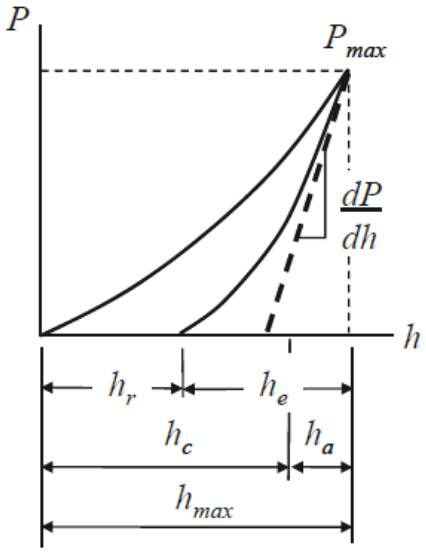

Figure 26. A typical load and unload curves with maximum load P_{max} [117].

Indenter load and depth of penetration are used to determine materials elastic modulus and hardness values. When the load is applied to indenter, material changes shape; when the load is removed the material wants to return to original shape, but it cannot return to original shape because of plastic deformation. This gives an approximation of the elastic modulus [117]. From the figure, the final contact depth and the stiffness are determined. Stiffness and contact depth can be determined by the following equations[118]:

$$S = \frac{dP}{dh} \tag{30}$$

$$h_c = h_{max} - \epsilon\left(\frac{P_{max}}{S}\right) \tag{31}$$

For Berkovich indenter, ϵ value is 0.75. Where ϵ is constant, P_{max} is the maximum indentation load during unloading, S is the unloading stiffness, and h_{max} is maximum depth [119]. Contact area and hardness are measured by the following equations[117]:

$$A = 24.5{h_c}^2 \tag{32}$$

$$\mathrm{H} = \frac{P_{max}}{24.5{h_c}^2} = \frac{P_{max}}{A} \tag{33}$$

Young modulus can be calculated by Sneddon equation[119]:

$$\mathrm{E}^* = \frac{\sqrt{\pi}}{2\beta}\frac{\mathrm{S}}{\sqrt{\mathrm{A}}} \tag{34}$$

Here E^* is composite elastic modulus, S is stiffness, β is a correction coefficient which is 1.034 for Berkovich indent. Material elastic modulus is calculated based on composite properties (E^*) and indenter properties (E_i).

$$\frac{1}{E^*} = \frac{1-v^2}{E} + \frac{1+{v_i}^2}{E_i} \tag{35}$$

5. Results and Discussion

5.1. Understanding and Controlling Surface Oxygen in Micron Sized SiC and B_4C Powders

5.1.1. Powder Choice

For this thesis H.C. Starck- UF 25 silicon carbide, Saint Gobain silicon carbide, HC. Starck HD 20 boron carbide and carbon-lamp black from Fischer Scientific were used as they have been demonstrated in the prior literature.

5.1.2. Develop a Safe and Effective Laboratory Scale Acid Etching Process

SiC powders were etched with acid as described in section 4.2.1. The oxygen content was measured for both SiC powders using a LECO TC 600 oxygen/nitrogen analyzer. Each oxygen content result represents the mean of three analyses. H.C. Starck SiC had 1.69±0.04 wt% oxygen before the acid etching process. The acid etching conditions and oxygen content of H.C. Starck SiC after etching process can be seen in Table 21. Increasing concentration of hydrofluoric acid, the efficiency of acid etching also increased to remove the oxide layer. The oxygen content of SiC powder for 20% HF, 40%HF,and 50% HF for 24-hours etching was 1.09±0.04 wt%, 0.75±0.03 wt%, and 0.48±0.03 wt% respectively. The oxygen content of the etched powder slightly decreased when increased the etching time. However increasing the etching time did not reduce oxygen as expected it might be due to the agglomerates. The oxygen content of powder for 40% HF and 50% HF for 1 hour, 4 hours, and 24 hours was 0.82±0.01 wt%, 0.81±0.01 wt%, 0.75±0.03 wt%, 0.60±0.02 wt%, 0.56±0.02 wt%, and 0.48±0.03 wt%, respectively.

Since 1-hour etching process was more effective in the time frame. The SiC powder etched for 1 hour with 50% HF was chosen despite the lower oxygen content in 50% HF for 4 and 24-hour etching. Etching SiC powder with 75% HF& 25%HNO_3 did not reduce oxygen content; on the contrary, it increased the oxygen content of powder since HNO_3 was a strong oxidizing agent. The oxygen content of powder for 1 hour, 4 hours and 24 hours was 1.45±0.02 wt%, 5.07 ±0.06 wt%, and 5.92±0.04 wt%, respectively. While the etching procedure removes the oxide layer, it has opened up a new surface on the powder which tends to oxidize. The oxide layer forms on the surface of freshly etched powders as soon as it exposed to the air. Therefore, the oxygen content of powder cannot be lowered to 0%.

Table 21. Acid etching conditions and oxygen content of SiC powder

Acid	**Concentration (%)**	**Etching Time (Hour)**	**Neutralized with**	**Oxygen Content (wt.%)**
HF	20	24	Ethanol	1.09±0.04
HF	40	1	Ammonium	0.82 ±0.01
		4	Hydroxide	0.81 ±0.01
		24		0.75±0.03
HF	50	1	Ammonium	0.60±0.02
		4	Hydroxide	0.56±0.02
		24		0.48±0.03
HF&	75% HF- 25%	1	Ammonium	1.45±0.02
HNO_3	HNO_3	4	Hydroxide	5.07±0.06
	40-65	24		5.92±0.04

After acid etching, H.C. Starck powder's oxygen content dramatically decreased to 0.60±0.02 wt% from 1.69±0.04 wt%. Acid etched dry powder was allowed to age at ambient conditions to determine the lifetime of the powder. The oxygen growth curve of acid etched SiC may be seen in Figure 27. The HF treated SiC's oxygen content was

measured at different times, and after 15 days oxygen content slowly increased to 0.77±0.01 wt%.

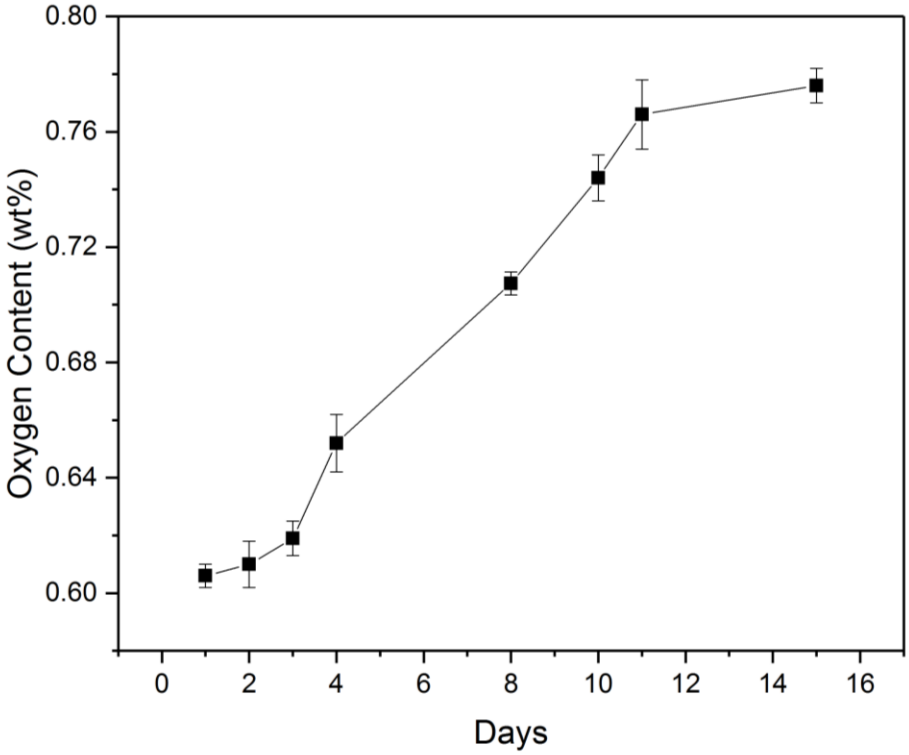

Figure 27. Oxygen growth curve for H.C. Starck SiC

Saint Gobain SiC had 0.38±0.01 wt% oxygen content. The powder was etched with 50% HF for 1-hour, and measured oxygen content was 0.20±0.01 wt%. Acid etched dry powder was allowed to age at ambient conditions to determine the lifetime of the powder. The oxygen growth curve of acid etched SiC may be seen in Figure 28. HF treated SiC's oxygen content was measured at different times, and after 14 days oxygen content increased to 0.31±0.01 wt%.

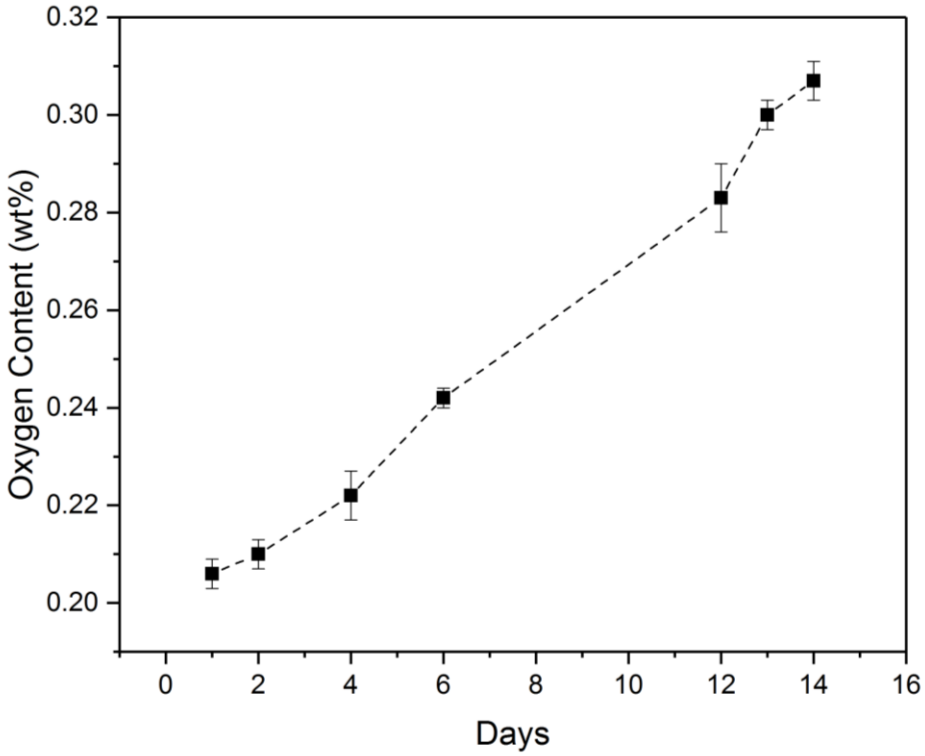

Figure 28. Oxygen growth curve for Saint Gobain SiC

5.1.3. Powder Cleaning to Remove B_2O_3 Layer

The B_4C powder was washed with HCl as described in section 4.2.2. The oxygen content of B_4C powder was measured using a LECO TC 600 oxygen/nitrogen analyzer. B_4C has 2.90±0.02 wt% oxygen content as received. After HCl washing, the oxygen content decreased to 1.70±0.01 wt%.

5.1.4. Powder Characterization

5.1.4.1. X-Ray Diffraction

The phase identification of H.C. Starck SiC, Saint Gobain, and B_4C powders was done using X-ray diffraction as described in section 4.1.3. Rietveld refinement analysis was done to calculate the percentage of initial polytype of starting powders. Figure 29

shows the phase identification of the XRD patterns of silicon carbide powder produced by H.C. Starck.

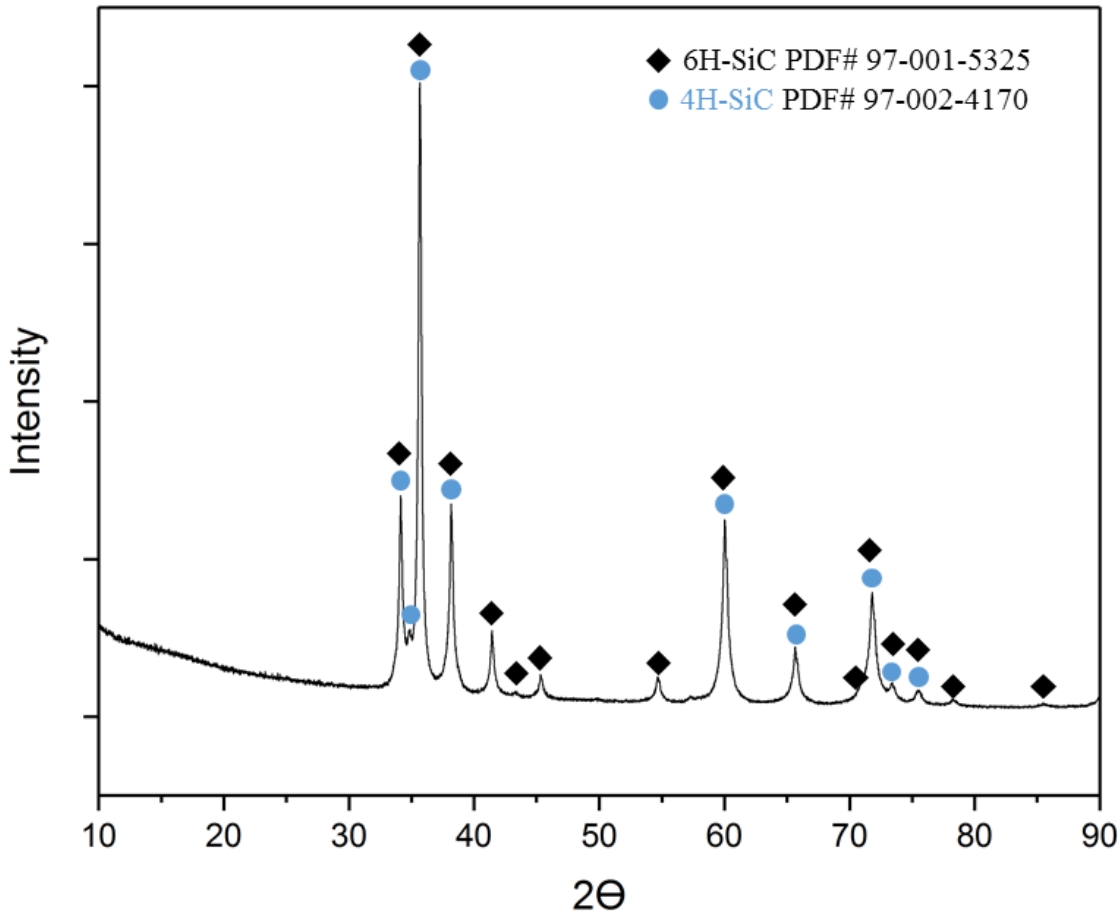

Figure 29. H.C. Starck SiC Powder XRD

The XRD pattern for the SiC powder was matched with patterns of 6H and 4H polytypes. Excluding two types of SiC polytypes, the XRD pattern did not show any other types of contaminates. The Rietveld refinement analysis result showed that SiC has two polytypes which are 72.3±0.10 (wt%) 6H and 27.7±0.10 (wt%) 4H.

Figure 30 shows the phase identification of the XRD patterns of silicon carbide powder produced by Saint Gobain.

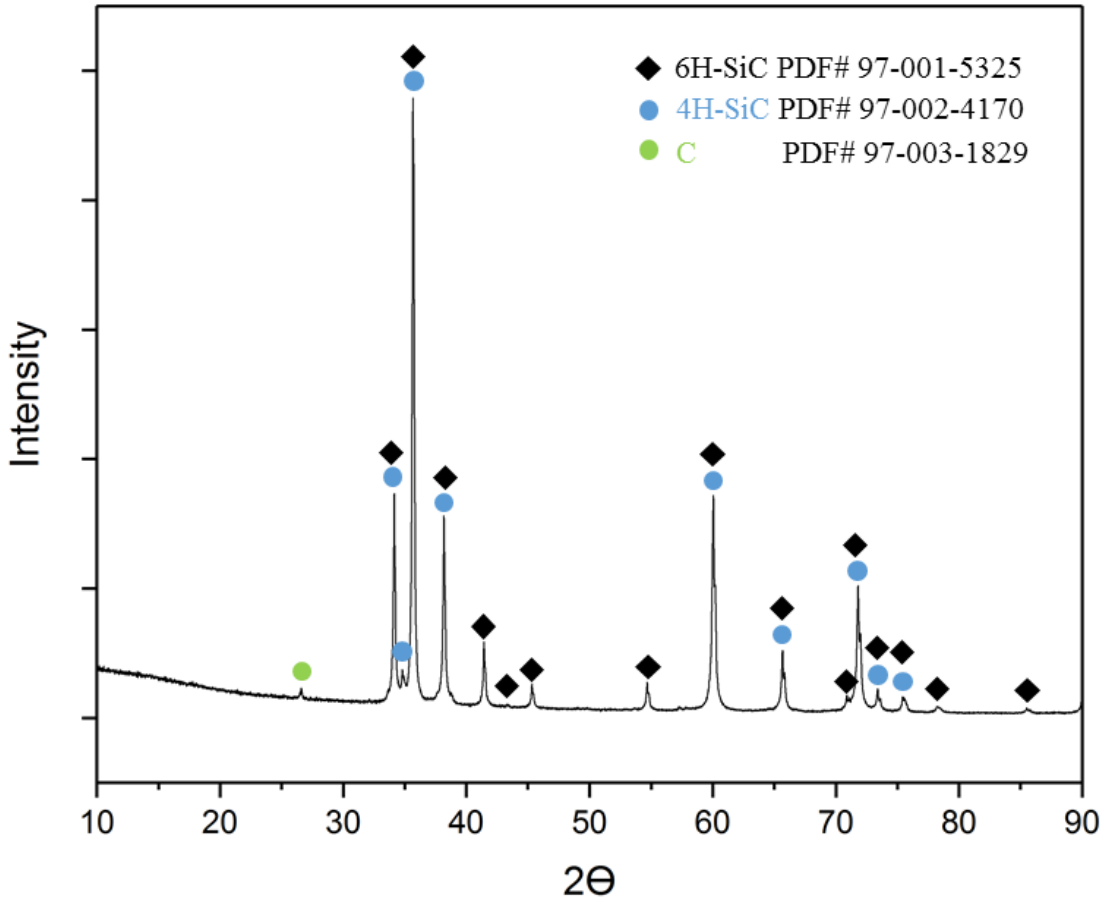

Figure 30. Saint Gobain Starck Powder XRD

The XRD pattern for the Saint Gobain SiC powder was matched with pattern of 6H and 4H polytypes. SiC powder had a small amount of free carbon as contamination. The Rietveld refinement analysis result showed that SiC has two polytypes which are 83.6±0.50 (wt%) 6H, 15.4±0.40 (wt%) 4H, and 1.0±0.20 (wt%) free carbon.

Figure 31 shows the phase identification of the XRD patterns of boron carbide powder produced by H.C. Starck. All peaks were matched with B_4C patterns, and only a low intensity broad peak was matched with carbon. Commercial boron carbide usually has a small amount of free carbon due to the synthesis process. This free carbon peak is located

at ~ 26.6° 2θ. The Rietveld refinement analysis result shows that B_4C has 0.96±0.04 (wt%) free carbon.

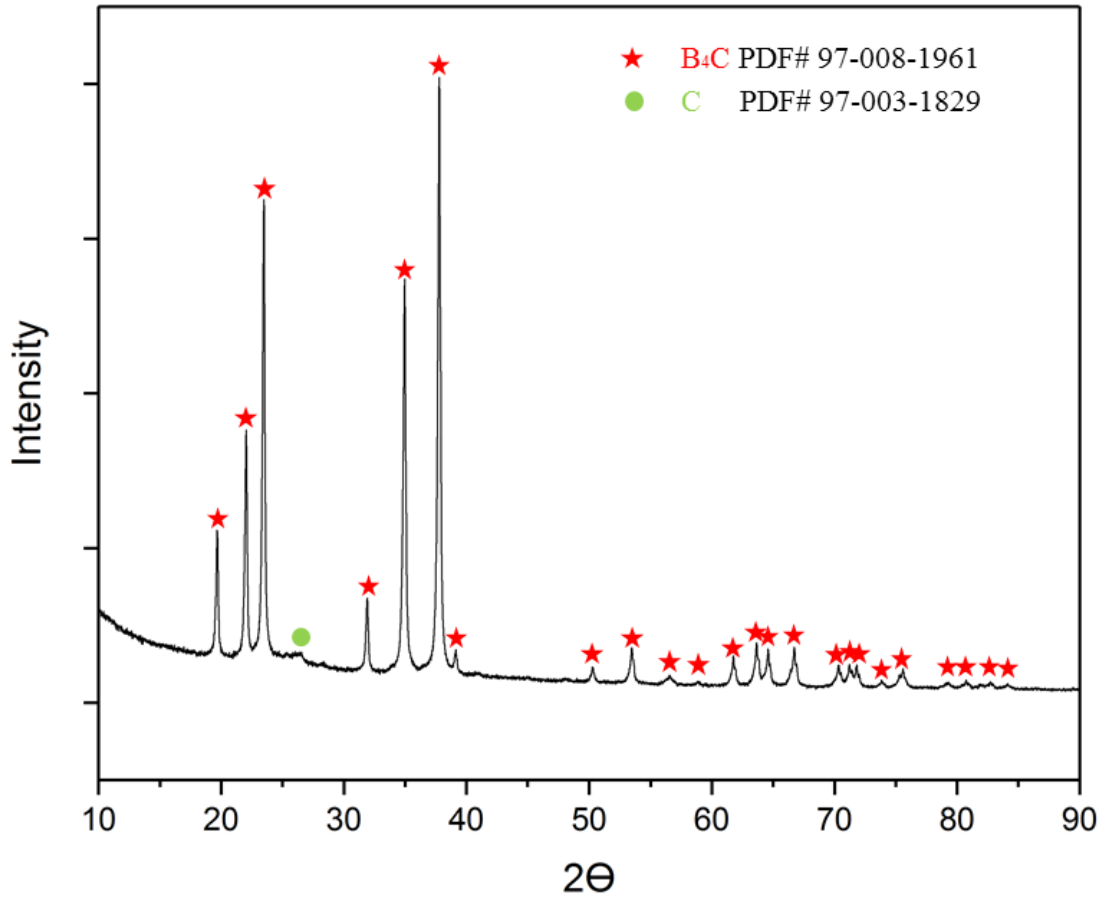

Figure 31. B_4C Powder XRD

5.1.4.2. Particle Size Analysis

The particle size of the silicon carbide and boron carbide powders was measured by dynamic light scattering using a Malvern Mastersizer 2000 with Hydro 2000S cell. Particle size distribution of starting powders can be seen in Table 22. The distribution of particle sizes of the H.C. Starck silicon carbide powder may be seen in Figure 32. Starck SiC has mainly particle size 0.65 microns, and overall particles are submicron.

Table 22. Particle size distribution of starting powder

	d_{10} (µm)	d_{50} (µm)	d_{90} (µm)
H.C. Starck SiC	0.35	0.65	1.00
Saint Gobain SiC	1.00	2.00	10.00
B_4C	0.30	0.60	1.50

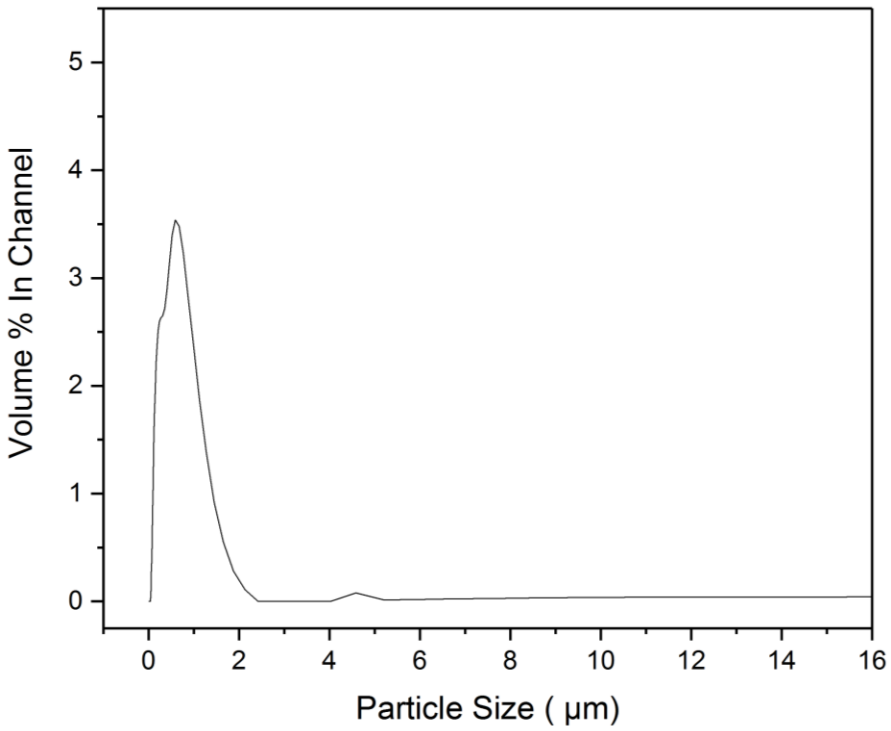

Figure 32. H.C. Starck SiC Powder Particle Size

The distribution of particle sizes for the Saint Gobain silicon carbide powder may be seen in Figure 33. It mainly has a particle size of 2.00 microns which means it has a larger particle size than Starck SiC.

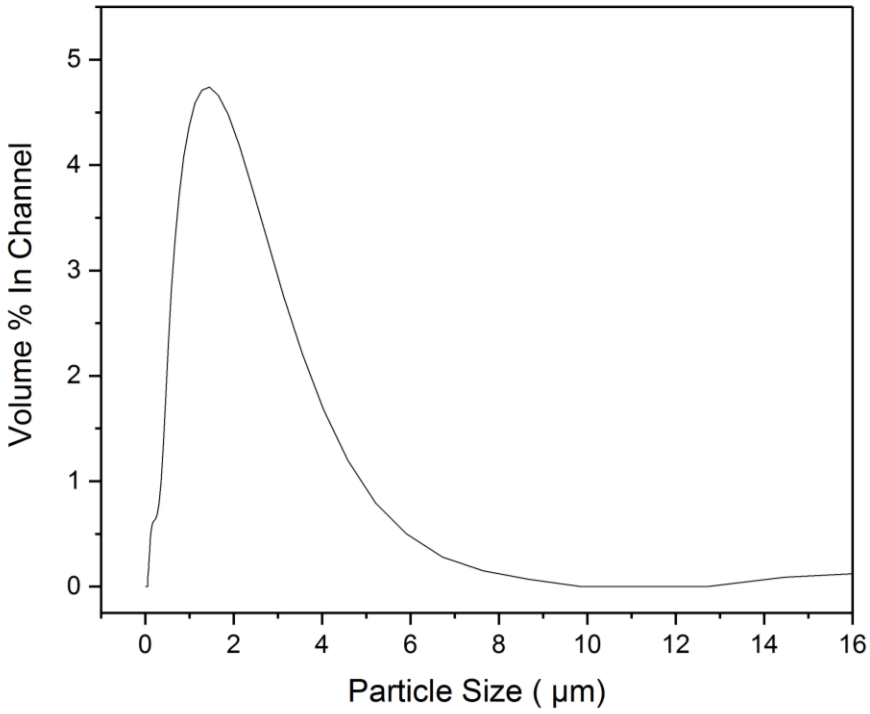

Figure 33. Saint Gobain SiC Powder Particle Size

The distribution of the particle size for the boron carbide powder may be seen in Figure 34. H.C. Starck B_4C mainly has submicron particle size of approximately 0.60 microns.

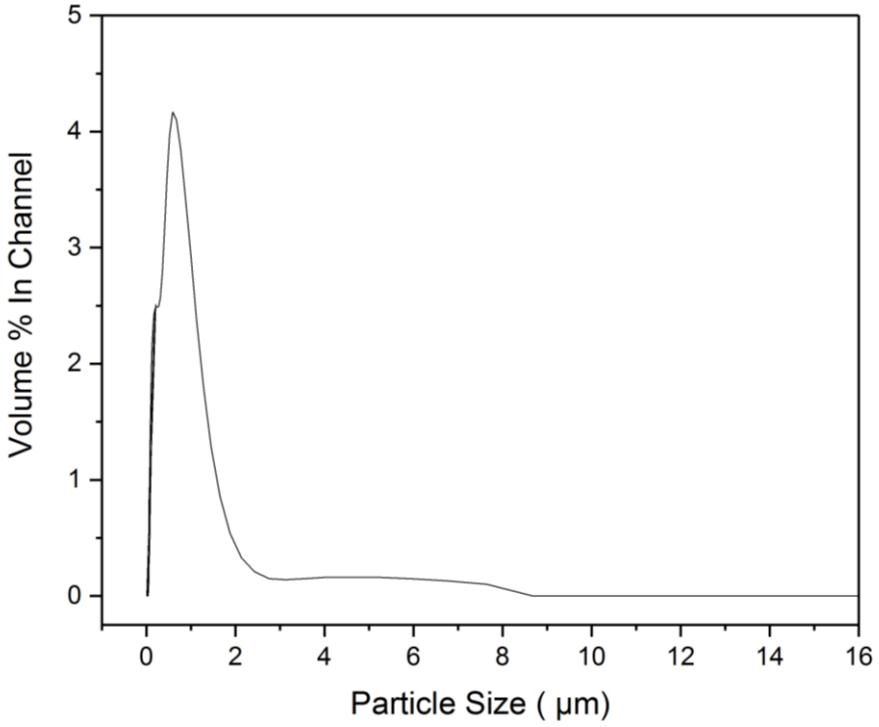

Figure 34. B_4C Powder Particle Size

5.1.4.3. FESEM Image Analysis

Scanning electron microscopy imaging was performed on the SiC and B_4C powders to verify the measured particle sizes and observe the morphology of the powders. The images for H.C. Starck SiC, Saint Gobain SiC, and B_4C powders may be seen in Figure 35, Figure 36, and Figure 37 respectively. FESEM images confirmed that Saint Gobain SiC had higher particle sizes than H.C. Starck SiC. The images also confirmed that the morphology of the powder particles appeared to be evenly distributed and have sub-micron size particles for H.C. Starck SiC and HD 20 B_4C, and 1.50-2.00 microns particle sizes for Saint Gobain SiC. Since large particles cannot be seen in FESEM images, larger measured particles in the results obtained from dynamic light scattering particle size analysis can be called agglomerates.

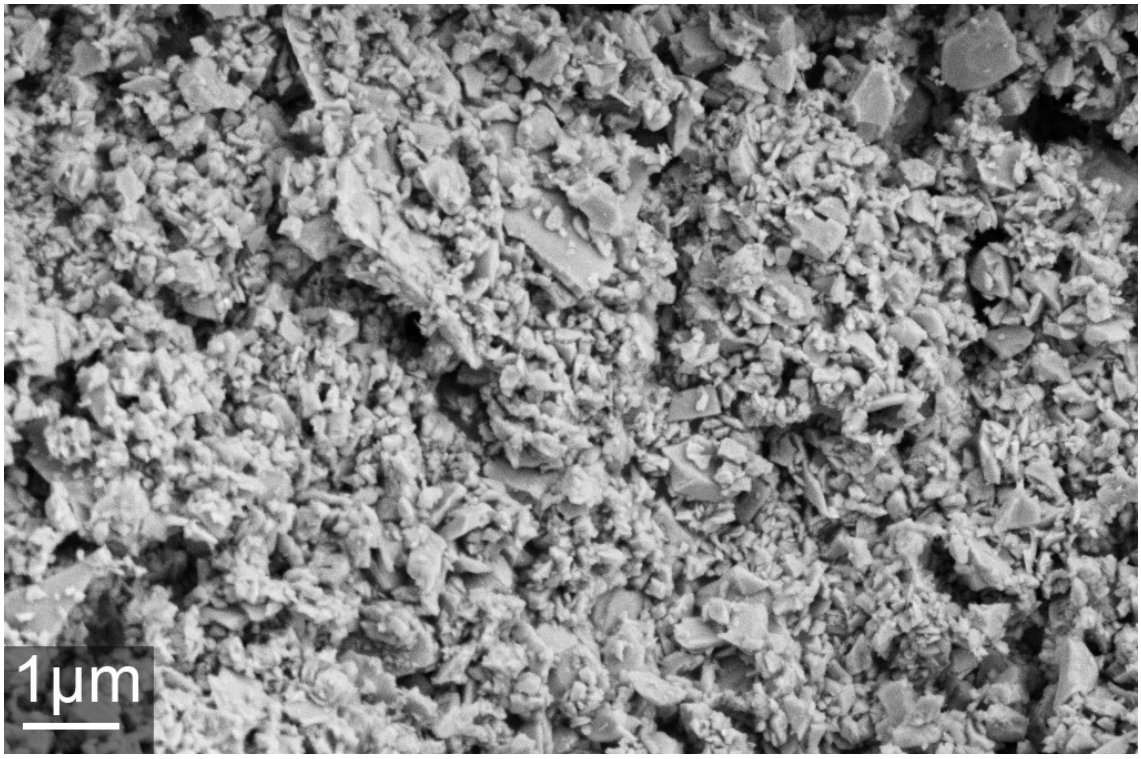

Figure 35. H.C. Starck SiC Powder

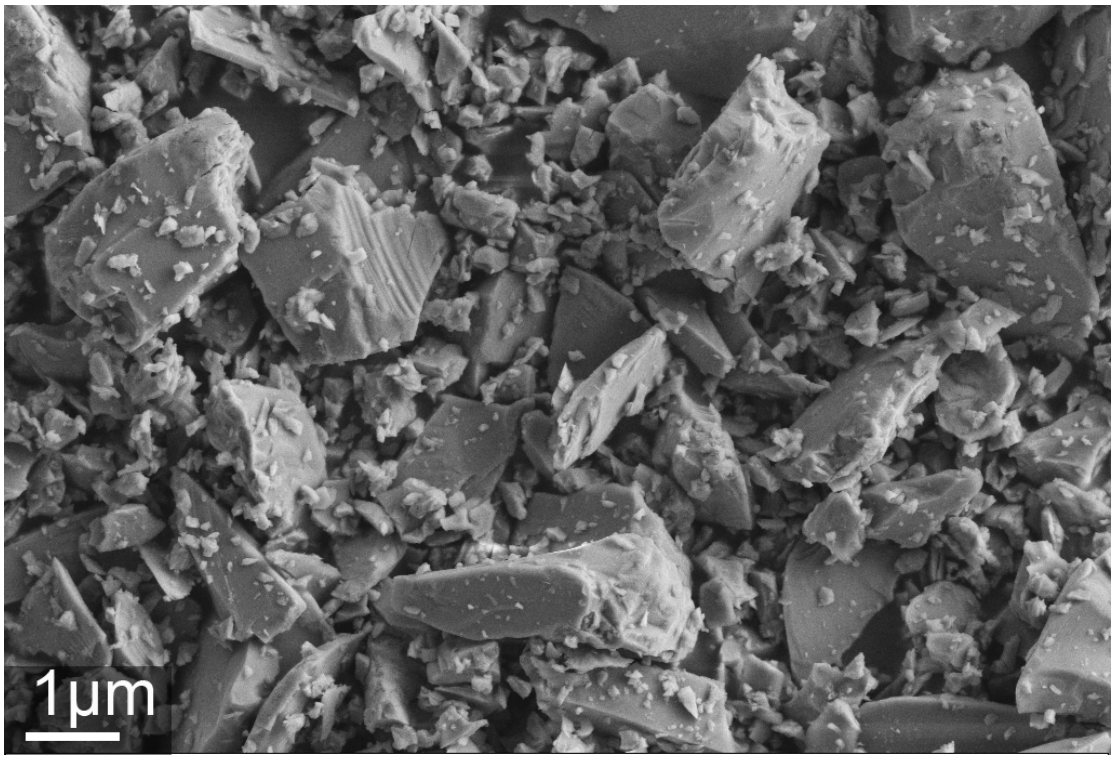

Figure 36. Saint Gobain SiC Powder

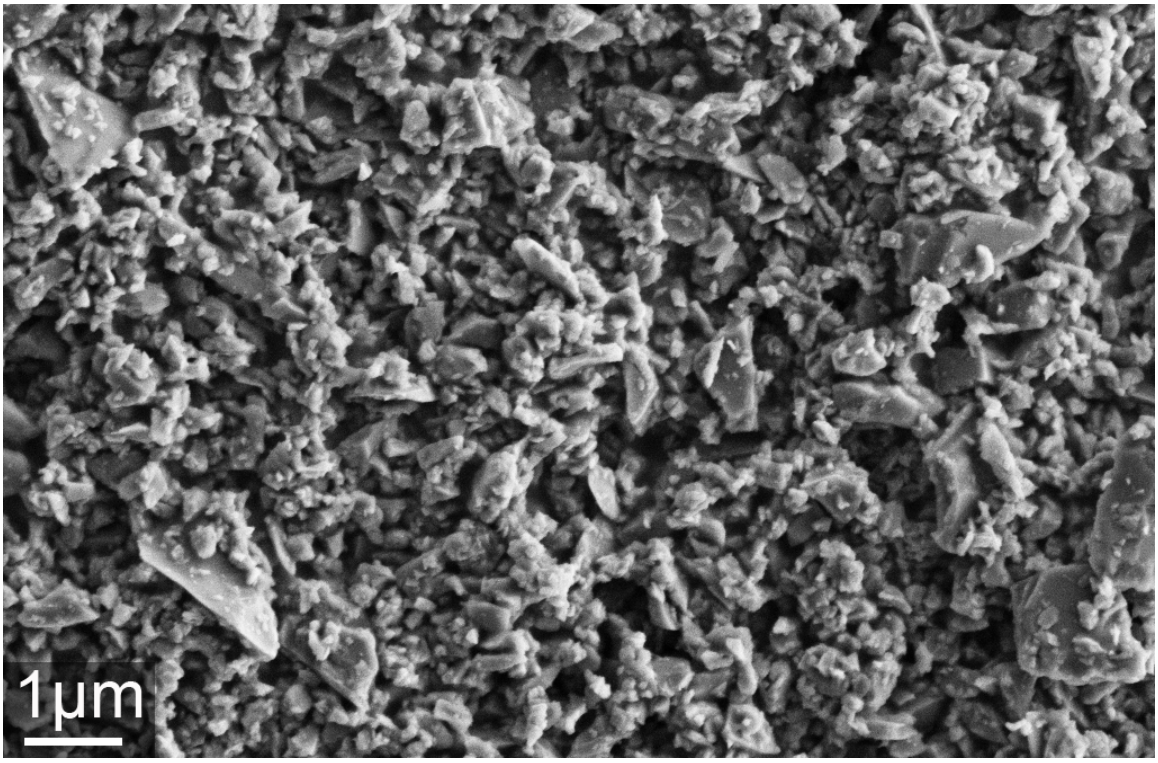

Figure 37. H.C. Starck B_4C Powder

5.2. Densification of Silicon Carbide- Boron Carbide Composites

5.2.1. Densification of Etched SiC

5.2.1.1. H.C. Starck SiC

H.C. Starck UF25 Silicon Carbide was etched with different concentrations of acid and different times as described in section 4.2.1. Etched silicon carbide was mixed with 1.5wt.% Carbon Lamp black and 0.5wt.% H.C. Starck HD20 Boron Carbide and pressure densified using spark plasma sintering. All samples were sintered at 1950°C for 5 minutes with an intermediate dwelling for 1 minute at 1400°C. Figure 38 shows microstructure images of 40% HF, 50%HF, and HF and HNO_3 etched silicon carbide. Table 23 shows the average grain size of SiC with standard deviations. Overall H.C. Starck SiC mainly had elongated grains. When the etching time is increased, the grains tend to get smaller. For

40%HF etched samples, the grain size changed from 3.57µm to 2.80µm as the etching time increased. The 1-hour (3.57µm) and 4-hour (3.02µm) 40% HF etched samples showed some exaggerated grain growth with several micron grains, while the 24-hour (2.80µm) 40% HF etched sample shows smaller grains. The 40%HF etched samples had bigger grain sizes than the 50% HF etched samples because the oxygen content of the starting powder was higher. The 50% HF etched samples showed a slight decrease in grain size with decreased oxygen content. The 1-hour, 4-hour, and 24 hours samples had a 2.89µm, 2.71µm, and 2.63µm grain size respectively. The HF and HNO_3 etched samples showed different morphologies since their oxygen content was higher than the other etched samples. While the 1-hour HF and HNO_3 etched sample had mostly elongated grains, the 4-hour and 24-hour HF and HNO_3 etched samples had small grains. 1-hour, 4-hour and 24-hour HF and HNO_3 etched samples have 6.68µm, 1.75µm, and 1.57µm average grain size respectively. To be consistent, 1.5 wt. % carbon was added to all the samples' matrix. The 4-hour and 24-hour HF and HNO_3 etched SiC powders have 5.07 wt.% and 5.92 wt.% oxygen content respectively. Since these two powders have a high oxygen content, the amount of additional carbon was insufficient to remove residual oxygen; consequently, the samples could not have high density.

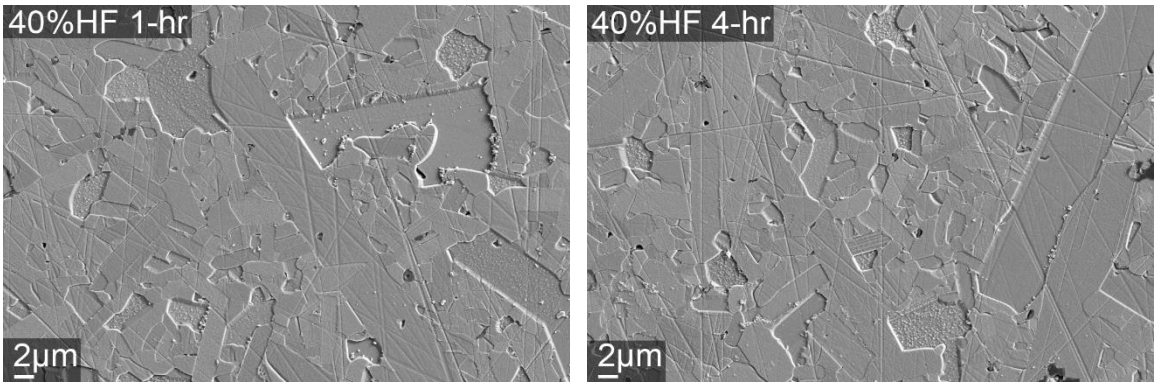

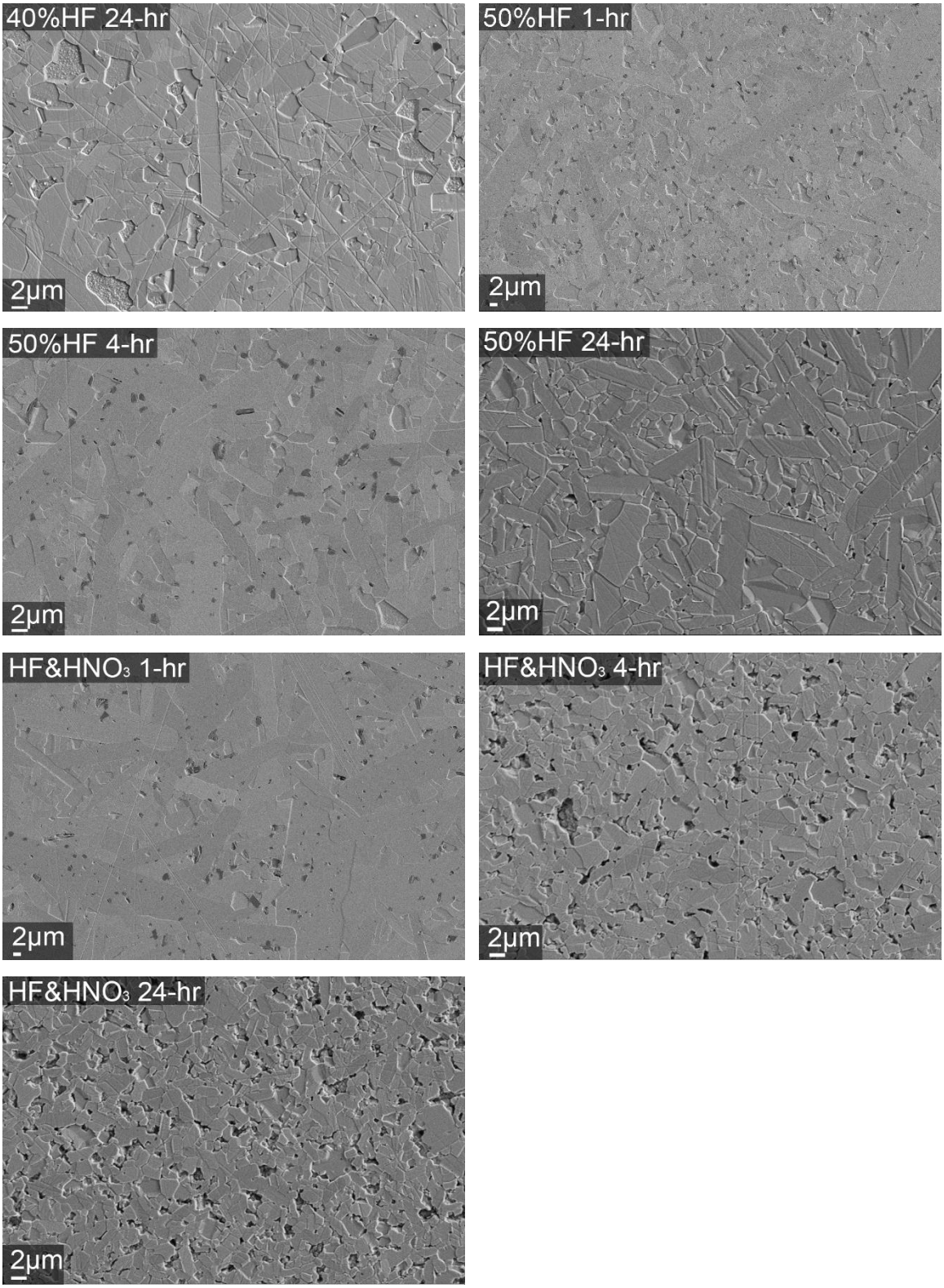

Figure 38. Microstructure images for different etched SiC

Table 23. Grain size of H.C. Starck SiC

Sample	Average Grain Size (µm) (Std. Dev)
40%HF-1-hr	3.57±1.30
40%HF-4-hr	3.02±0.61
40%HF-24-hr	2.80±0.89
50%HF-1-hr	2.89±0.99
50%HF-4-hr	2.71±0.82
50%HF-24-hr	2.63±0.79
HF&HNO_3- 1-hr	6.68±1.39
HF&HNO_3- 4-hr	1.75±0.26
HF&HNO_3- 24-hr	1.57±0.44

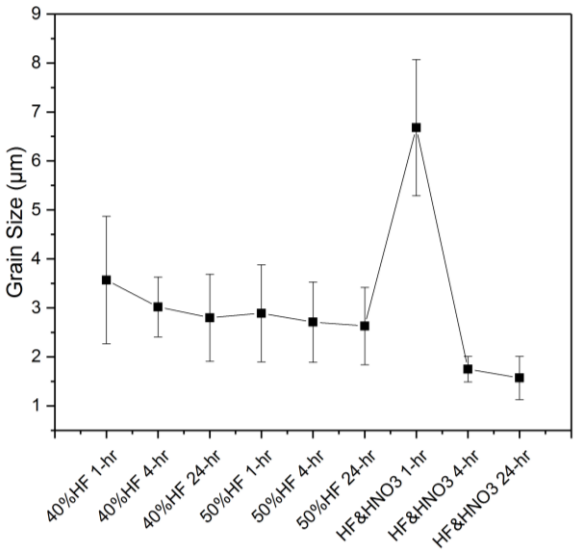

The density of the samples was measured using the Archimedes method as described in section 4.5.1., and the elastic properties were measured using the ultrasound analysis method. c_L (longitudial sound speed), c_S (shear sound speed), Poisson's ratio, Young's modulus (E), shear modulus (G), and bulk modulus (K) values were calculated from equations 22, 23, 24, 25, 26, and 27 respectively as described in section 4.5.3. The results can be seen in Table 24 and Figures 39 through 43. Each value represents the mean of five analyses. 1-hour, 4-hour and 24 hour 40% HF etched samples' Poisson's ratio, density, Young's modulus, shear modulus and bulk modulus values are 0.177, 3.18g/cm^3, 416- 417 GPa, 177 GPa, and 215 GPa respectively. The density and elastic properties are almost the same since their etched starting powder's oxygen content was similar. The 1-hour and the 4-hour 50% HF etched samples' density values are 3.21 g/cm^3, while the 24-

hour 50% HF etched sample's density value is 3.20 g/cm^3. The samples have reached full density. 1-hour, 4-hour, and 24 hour 50% HF etched samples' Poisson's ratio, Young's modulus, shear modulus and bulk modulus values are 0.178, 0.179, 0.179; 423, 424, 417 GPa;180, 180, 177 GPa; and 219, 220, 216 GPa respectively. Since the HF and HNO_3 etched samples' starting powders had a high oxygen content, the samples could not reach high density. The Poisson's ratio value slightly changed from 0.177 to 0.174, the density of the sample dropped from 3.17 g/cm^3 to 3.09 g/cm^3, the Young's modulus decreased from 418 GPa to 407 GPa, the shear modulus changed from 178 GPa to 173 GPa, and the bulk modulus dropped from 216 GPa to 208 GPa while increasing the etching time. It is clear that an increasing oxygen content has a negative effect on density and elastic properties of samples. Increasing the oxygen content decreases the density, and consequently, the samples that have a lower density will have greater porosity as shown in literature [30]. Having porosity in samples reduce the elastic properties of samples. Wilhelm et al. also mention that oxygen content of silicon carbide was one of the reasons to affect mechanical properties [120].

Table 24. Elastic properties of dense SiC

Sample	**c_L (m/s)**	**c_S (m/s)**	**Poisson's Ratio**	**Density (g/cm^3)**	**E (GPa)**	**G (GPa)**	**K (GPa)**
40%HF-1-hr	11906	7456	0.177±0.004	3.180±0.002	416±8	177±4	215±4
40%HF-4-hr	11917	7468	0.177±0.004	3.180±0.002	417±8	177±4	215±4
40%HF-24-hr	11916	7466	0.177±0.004	3.180±0.001	417±8	177±4	215±4
50%HF-1-hr	11950	7481	0.178±0.004	3.210±0.001	423±9	180±4	219±4
50%HF-4-hr	11971	7482	0.179±0.004	3.210±0.001	424±9	180±4	220±4
50%HF-24-hr	11883	7430	0.179±0.004	3.200±0.001	417±8	177±4	216±4
HF&HNO_3-1-hr	11950	7488	0.177±0.004	3.170±0.001	418±8	178±4	216±4
HF&HNO_3-4-hr	11919	7468	0.177±0.004	3.140±0.002	412±8	175±4	213±4
HF&HNO_3-24-hr	11914	7487	0.174±0.003	3.090±0.002	407±8	173±4	208±4

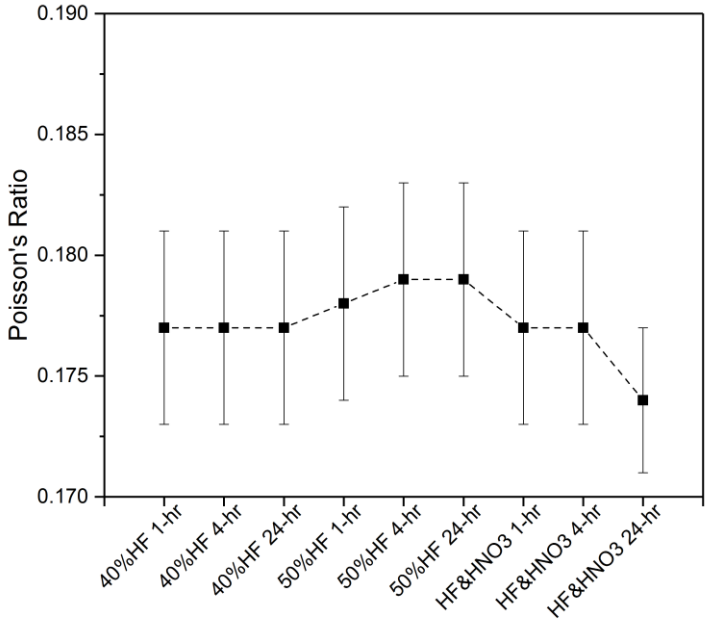

Figure 39. Effect of etching time and acid concentration on the Poisson's ratio of Starck SiC

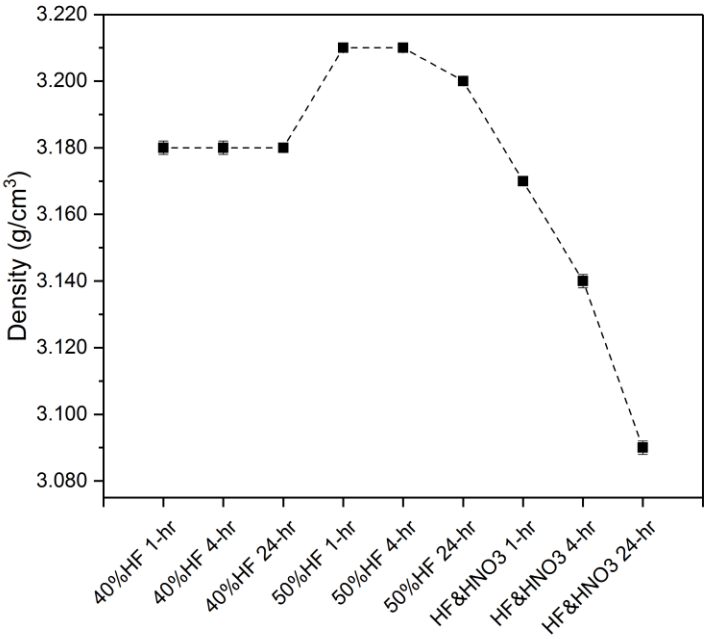

Figure 40. Effect of etching time and acid concentration on the density of Starck SiC

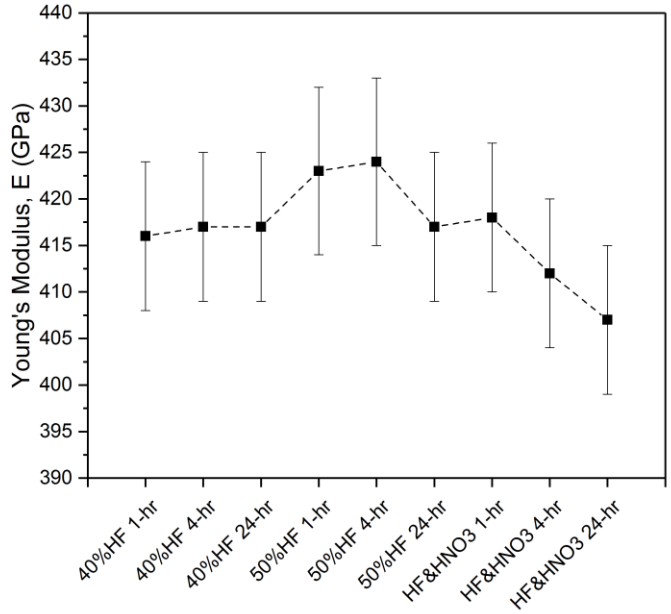

Figure 41. Effect of etching time and acid concentration on the Young's modulus of Starck SiC

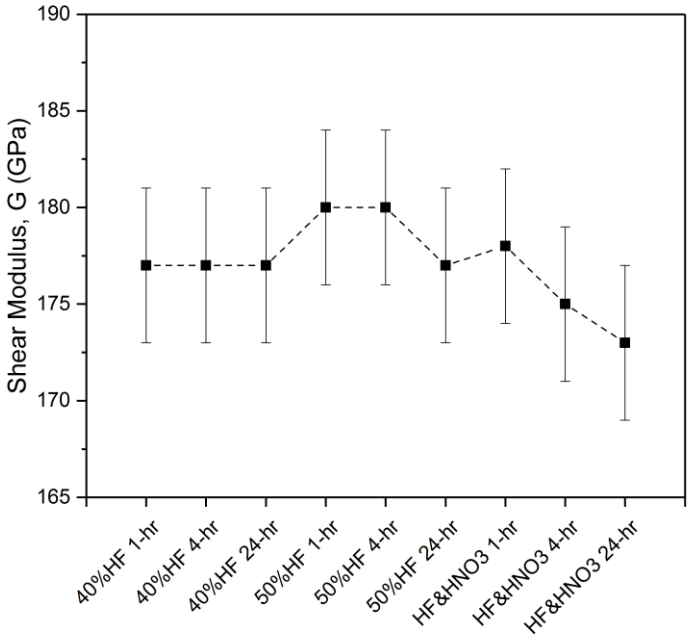

Figure 42. Effect of etching time and acid concentration on the shear modulus of Starck SiC

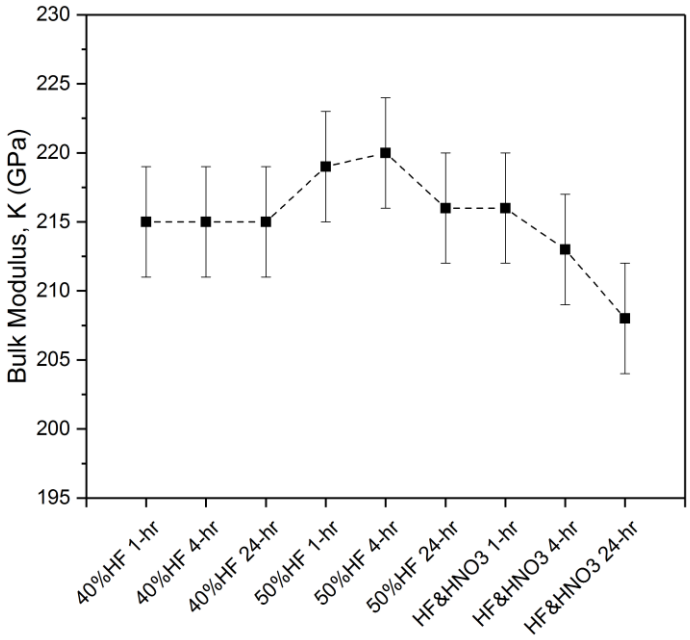

Figure 43. Effect of etching time and acid concentration on the bulk modulus of Starck SiC

5.2.1.2. Saint Gobain SiC

Saint Gobain Silicon Carbide was etched with 50% HF for 1 hour as described in section 4.2.1. Acid etched dry silicon carbide was allowed to age at ambient conditions to determine the lifetime of the powder. Powders were sintered at different times to see the effect of oxygen content of powder. Etched silicon carbide was mixed with 1.5wt.% Carbon Lamp black and 0.5wt.% H.C. Strack HD20 Boron Carbide and densified using spark plasma sintering. All samples were sintered at 1950°C for 5 minutes with an intermediate dwelling time of 1 minute at 1400°C. Saint Gobain SiC samples microstructural images can be seen in Figure 44. The grain morphology seemed to be similar between samples, but showed little difference in grain size. Average grain size of samples increased with increased oxygen content. Sample made with fresh etched powder (day 0) displayed equiaxed and 1.68μm average grain sizes while higher oxygen content

sample (day 9) showed equiaxed and 3.34μm average grain sizes. It showed that the oxygen content of the starting powder affects the grain size of the materials. This result was also supported with the literature, when Vassen et. al. mentioned that oxygen content of silicon carbide caused grain growth and inhibited the density [121].

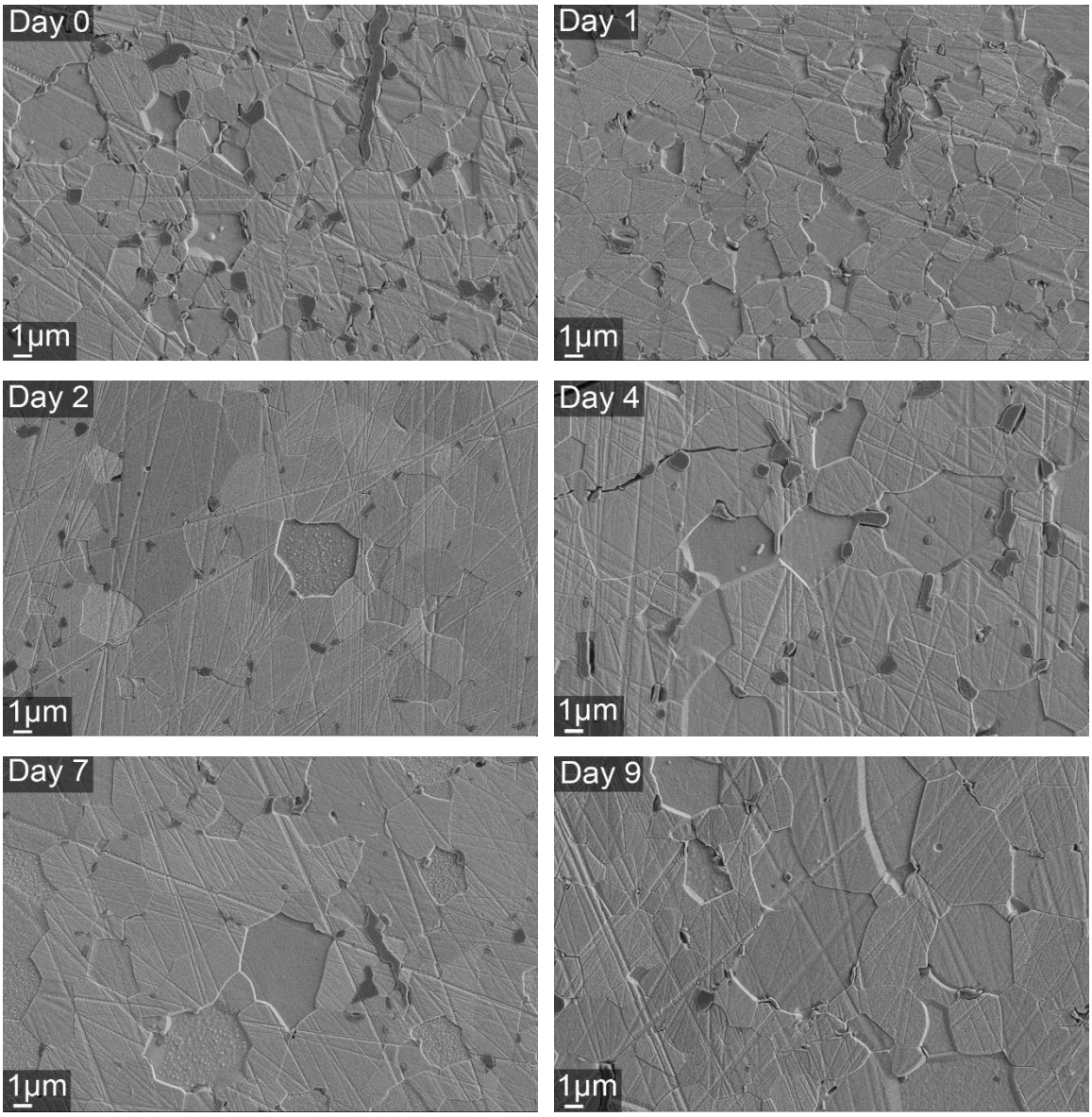

Figure 44. Microstructure images of aged SiC for different days

Table 25. Grain size of Saint Gobain SiC

Sample	Average Grain Size (µm) (Std. Dev)
Day 0	1.68±0.46
Day 1	1.85±0.33
Day 2	2.69±0.41
Day 4	2.73±0.81
Day 7	3.07±1.16
Day 9	3.34±0.93

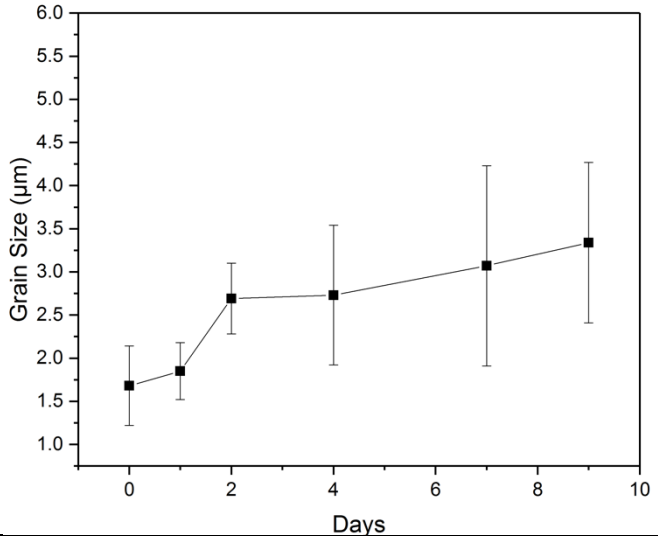

The density of the samples was measured using the Archimedes method as described in section 4.5.1. and the elastic properties were measured using the ultrasound analysis method. c_L (longitudial sound speed), c_S (shear sound speed), Poisson's ratio, Young's modulus (E), shear modulus (G), and bulk modulus (K) values were calculated from equations 22, 23, 24, 25, 26, and 27 respectively as described in section 4.5.3. The results can be seen in Table 26 and Figures 45 through 49. Each value represents the mean of five analyses. The Poisson's ratio value slightly changed from 0.179 to 0.178, the density of the sample dropped from 3.17 g/cm^3 to 3.14 g/cm^3, the Young's modulus decreased from 417 GPa to 407 GPa, the shear modulus changed from 177 GPa to 173 GPa, and the bulk modulus dropped from 217 GPa to 210 GPa while aging the powder. It was clear that increasing the oxygen content had a negative effect on the density and elastic properties of samples. Increasing the oxygen content decreased the density and elastic properties values.

Table 26. Elastic properties of aged SiC for different days

Sample	c_L (m/s)	c_S (m/s)	Poisson's Ratio	Density (g/cm^3)	E (GPa)	G (GPa)	K (GPa)
Day 0	11950	7469	0.179±0.004	3.170±0.001	417±8	177±4	217±4
Day 1	11929	7466	0.178±0.004	3.160±0.002	415±8	176±4	215±4
Day 2	11896	7447	0.178±0.004	3.160±0.001	413±8	175±4	214±4
Day 4	11890	7444	0.178±0.004	3.160±0.002	412±8	175±4	213±4
Day 7	11874	7425	0.179±0.004	3.160±0.003	411±8	174±4	213±4
Day 9	11851	7421	0.178±0.004	3.140±0.002	407±8	173±4	210±4

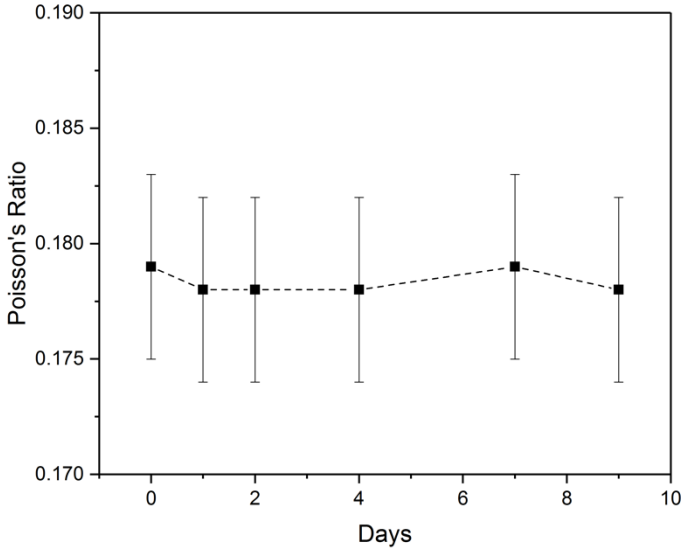

Figure 45. Effect of oxygen content on the Poisson's ratio of Saint Gobain SiC

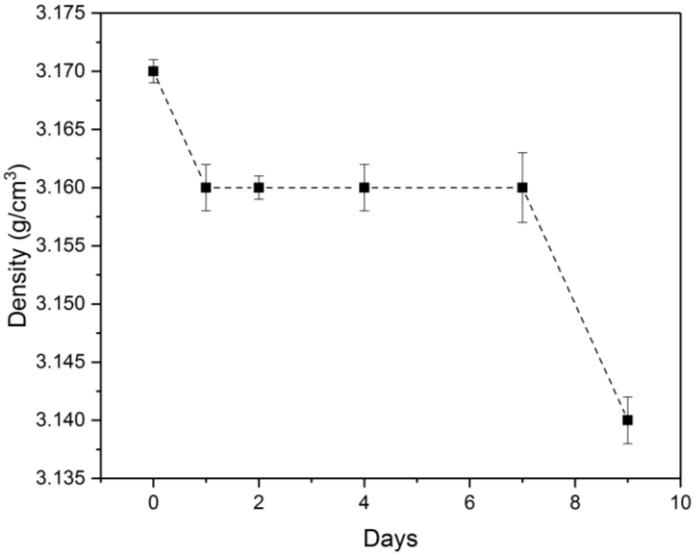

Figure 46. Effect of oxygen content on the density of Saint Gobain SiC

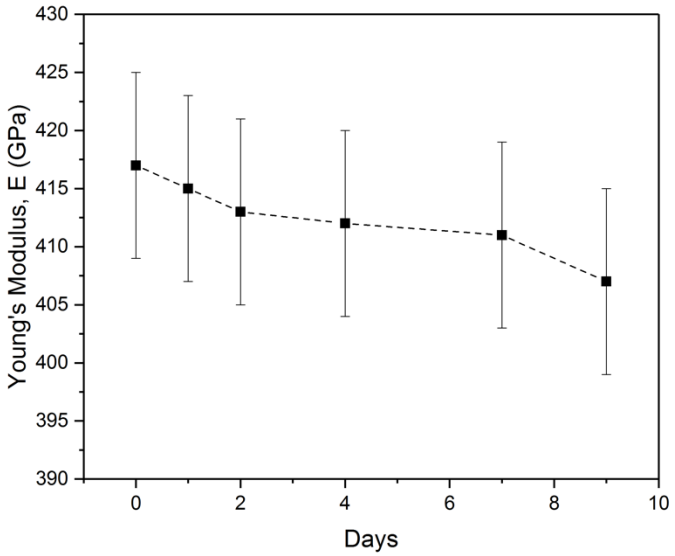

Figure 47. Effect of oxygen content on the Young's modulus of Saint Gobain SiC

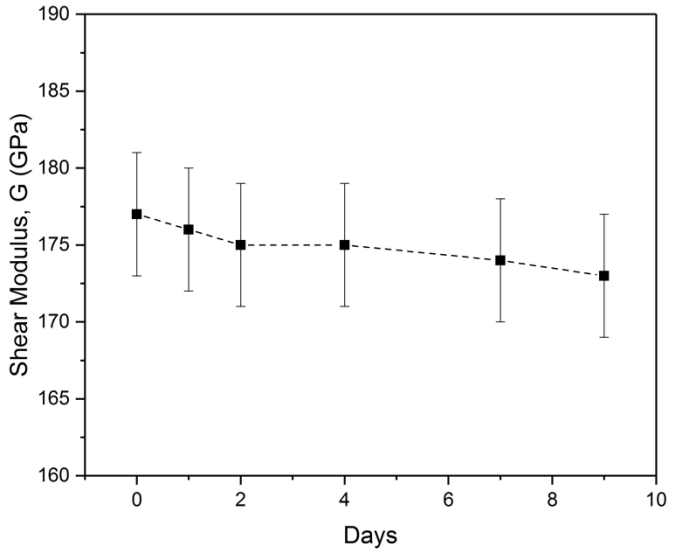

Figure 48. Effect of oxygen content on the Shear modulus of Saint Gobain SiC

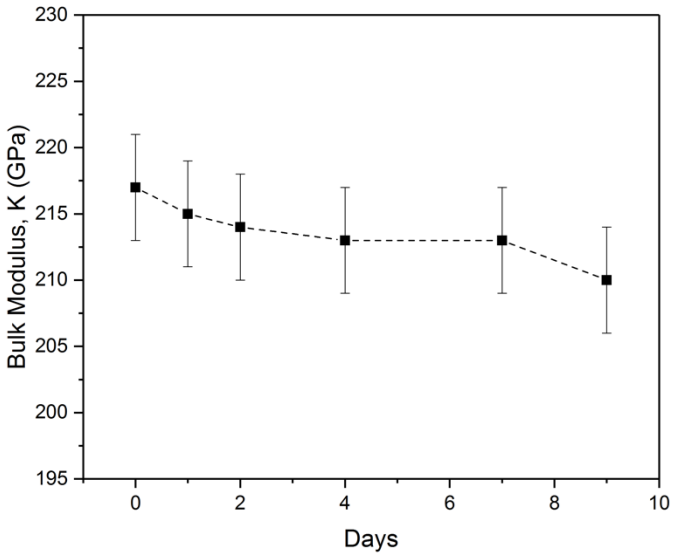

Figure 49. Effect of oxygen content on the bulk modulus of Saint Gobain SiC

5.2.1. Optimal SPS Cycle

5.2.1.1. Effect of Sintering Temperature

To find the optimal sintering temperature, 50%B_4C-1.5%C-48.5%SiC composition was sintered under four different temperatures: 1800°C, 1850°C, 1900°C, 1950°C. Two stage sintering was used to sinter the samples. The dry powder was Spark Plasma Sintered by being heated to 1400°C with a 200°C/min heating rate under vacuum, an applied pressure of 50MPa, and a dwelling time of 1 minute. After the 1 minute holding time, the samples were heated to a sintering temperature of 200°C/min under 50MPa applied pressure and held for 5 min.

The density values of the SPS samples were determined using the Archimedes method, as described in section 4.5.1. Table 27 shows the sintering conditions and relative density of the samples. It may be seen that the sample sintered at 1950°C with 50 MPa applied pressure is almost fully dense. It can also be seen that there was a significant increase in relative density from 93.59% to 99.64%. While the relative density of the sample sintered at 1800°C was 93.59%, for the sample sintered at 1950°C the relative density was 99.64 %.

Table 27. SPS sintering conditions for the effect of sintering temperature

Sample	Sintering Temperature (°C)	Applied Pressure (MPa)	Dwelling Time (min)	Density (g/cm^3)	Theoretical Density (g/cm^3)	Average Percent Density (%)
1400-1-1800-5-50	1800	50	5	2.630±0.002	2.81	93.59
1400-1-1850-5-50	1850	50	5	2.730±0.002	2.81	97.15
1400-1-1900-5-50	1900	50	5	2.770±0.001	2.81	98.57
1400-1-1950-5-50	1950	50	5	2.800±0.002	2.81	99.64

Figure 50 shows the effect of the sintering temperature on the density. Each density value represents the mean of five analyses. The results showed that the density of the material increases with increasing sintering temperature. Increasing the sintering temperature had increased the diffusion between particles so that the material's density had increased. This increase in density was also shown in literature, they found that increasing the sintering temperature increased the relative denisty of silicon carbide- boron carbide composites with spark plasma sintering and hot pressing. However even at same sintering temperature, spark plasma sintering promoted higher density than hot pressing [66, 122, 123].

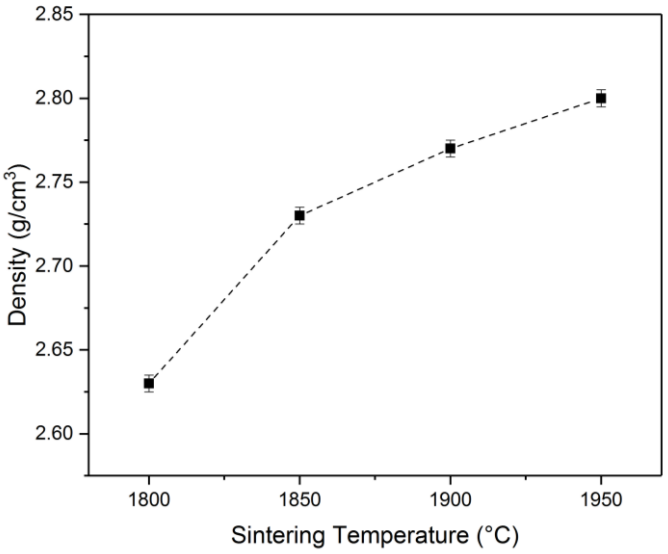

Figure 50. Effect of the sintering temperature on the density

The microstructure images for different sintering temperature can be seen in Figure 51. The light area was SiC, and the dark area was B_4C. Also, the images supported the Archimedes density results since they showed irregular pores at the low sintering temperature and a fully dense microstructure at 1950°C.

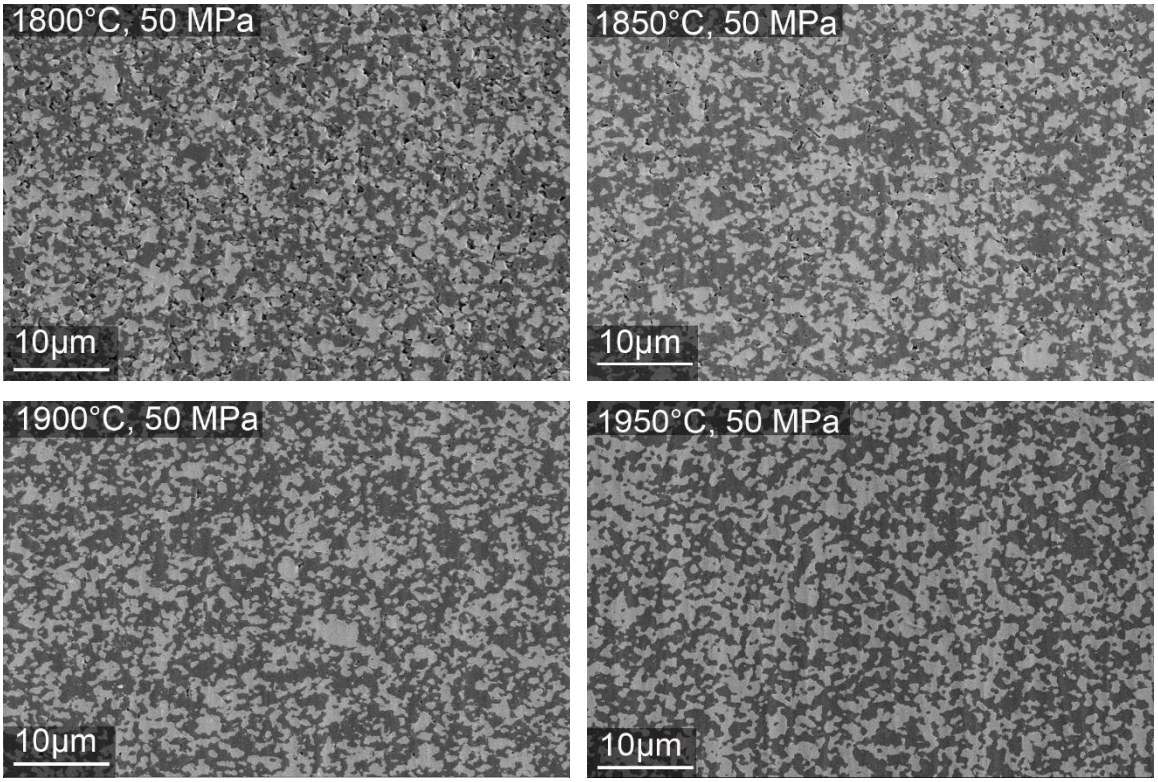

Figure 51. Microstructure images for sintering temperature 1800°C, 1850°C, 1900, °C 1950°C

Table 28 and Figures 52 and 53 show average grains size of boron carbide and silicon carbide with standard deviations. Even at the same combination, by increasing the sintering temperature, boron carbide grains reduced from 0.46μm to 0.44μm. On the other hand, silicon carbide grains tended to coarsen from 0.31μm to 0.44μm with increasing sintering temperature. Smaller grain sizes were found in this research than in literature: they found 2 μm boron carbide grains, and 1 μm silicon carbide grains [122].

Table 28. Average grain sizes for different sintering temperature

Sample	Average Grain Size of B_4C (µm) (Std. Dev)	Average Grain Size of SiC (µm) (Std. Dev)
1400-1-1800-5-50	0.46±0.05	0.31±0.03
1400-1-1850-5-50	0.44±0.04	0.34±0.03
1400-1-1900-5-50	0.43±0.04	0.41±0.04
1400-1-1950-5-50	0.44±0.04	0.44±0.04

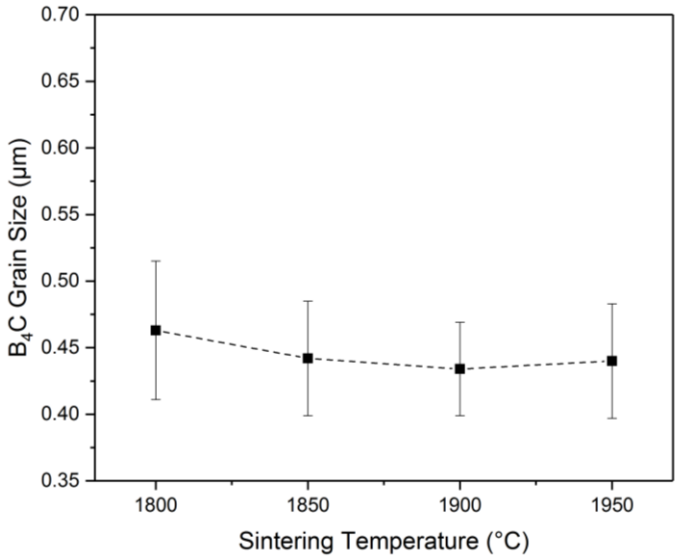

Figure 52. Effect of the sintering temperature on the B_4C grains

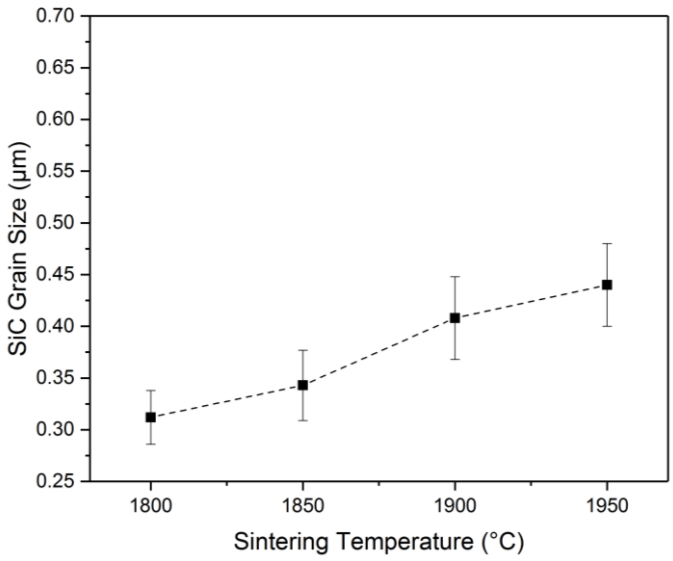

Figure 53. Effect of the sintering temperature on the SiC grains

X-ray diffraction patterns of the samples can be seen in Figure 54. All samples showed the same patterns. The XRD data samples had silicon carbide, boron carbide and a small amount of carbon as expected. Compared with raw starting materials, no unexpected phase occurred. Since the composites were not made from in-situ processing, the sintering temperature did not affect the peak intensity.

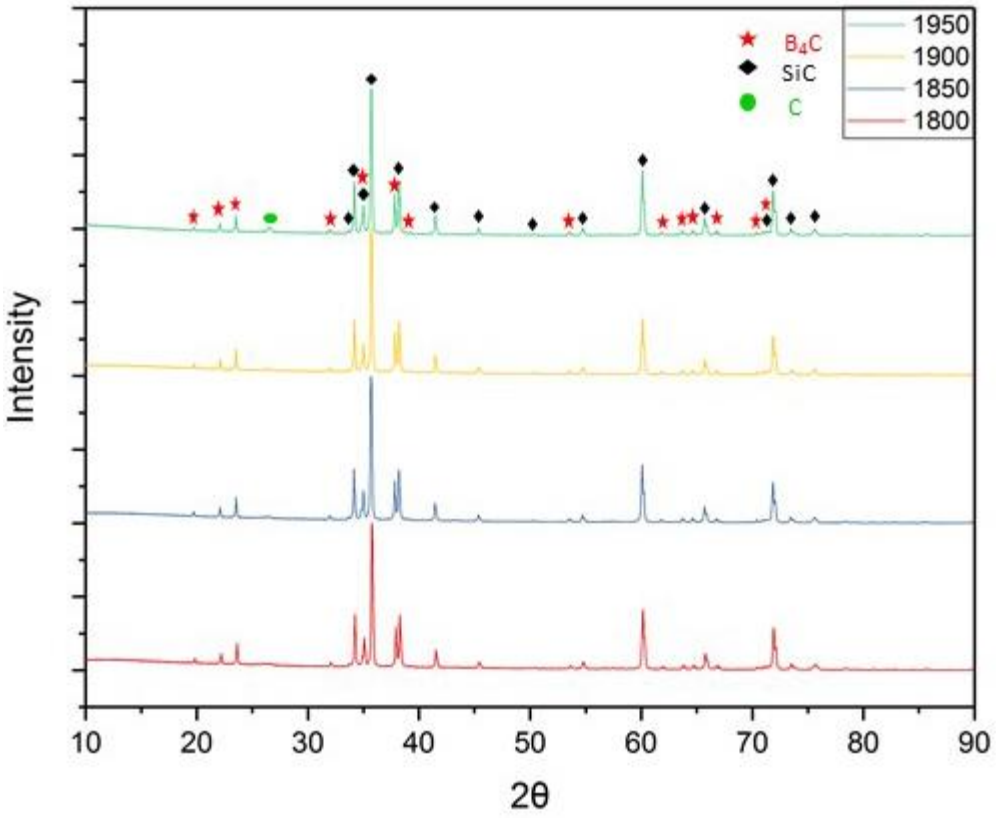

Figure 54. X-ray diffraction patterns of samples sintered at different temperature

The samples' elastic properties were measured using ultrasound analysis. c_L (longitudial sound speed), c_S (shear sound speed), Poisson's ratio, Young's modulus (E), shear modulus (G), and bulk modulus (K) values were calculated from equations 22, 23, 24, 25, 26, and 27 respectively as described in section 4.5.3. The results can be seen in Table 29 and Figures 55 through 58. Each value represents the mean of five analyses. Since elastic properties had a direct relation to density, the elastic modulus, bulk modulus, and shear modulus increased with increasing sintering temperature. The Poisson's ratio value increased from 0.160 to 0.165. Young's modulus showed a significant increase from 333 GPa to 409 GPa. The shear modulus changed from 144 GPa to 176 GPa, and the bulk modulus increased from 163 GPa to 203 GPa.

Table 29. Elastic properties for different sintering temperatures

Sample	c_L (m/s)	c_S(m/s)	Poisson's Ratio	E (GPa)	G (GPa)	K (GPa)
1400-1-1800-5-50	11611	7387	0.160±0.003	333±7	144±3	163±3
1400-1-1850-5-50	12525	7944	0.163±0.003	401±8	172±3	199±4
1400-1-1900-5-50	12523	7928	0.166±0.003	405±8	174±4	202±4
1400-1-1950-5-50	12506	7921	0.165±0.003	409±8	176±4	203±4

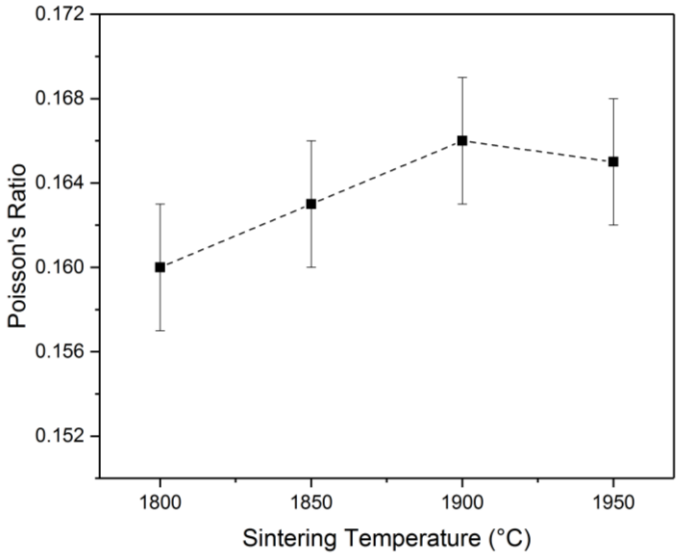

Figure 55. Effect of the sintering temperature on the Poisson's ratio

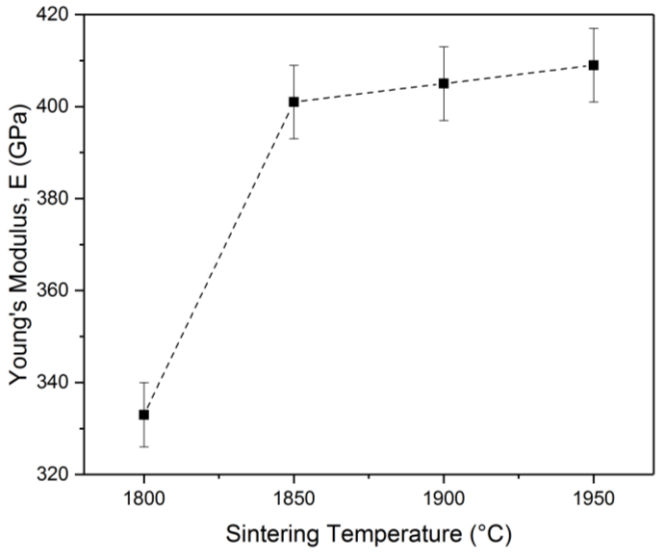

Figure 56. Effect of the sintering temperature on the Young's modulus

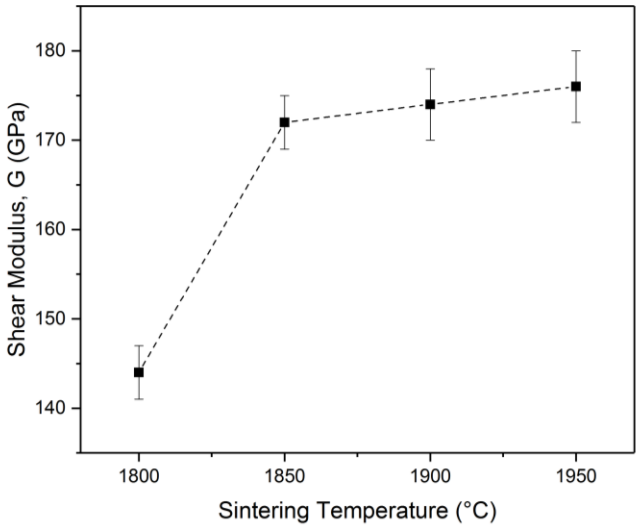

Figure 57. Effect of the sintering temperature on the shear modulus

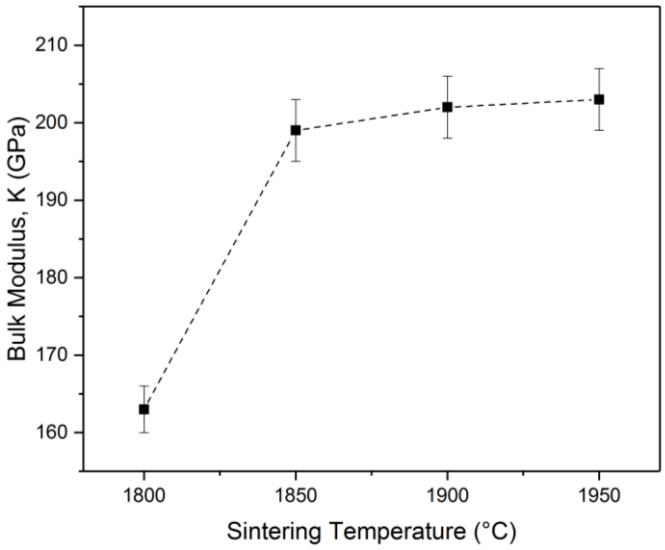

Figure 58. Effect of the sintering temperature on the bulk modulus

SEM imaging was used to determine the mode of fracture. Figure 59 shows the fracture surface of samples sintered with different temperature and Figure 60 shows indentation crack in polish surface. Images showed that the composites show transgranular fracture. The sintering temperature did not affect the fracture mode of the composite. Zhang et. El also found transgranular fracture in silicon carbide boron carbide samples with different sintering temperatures [66].

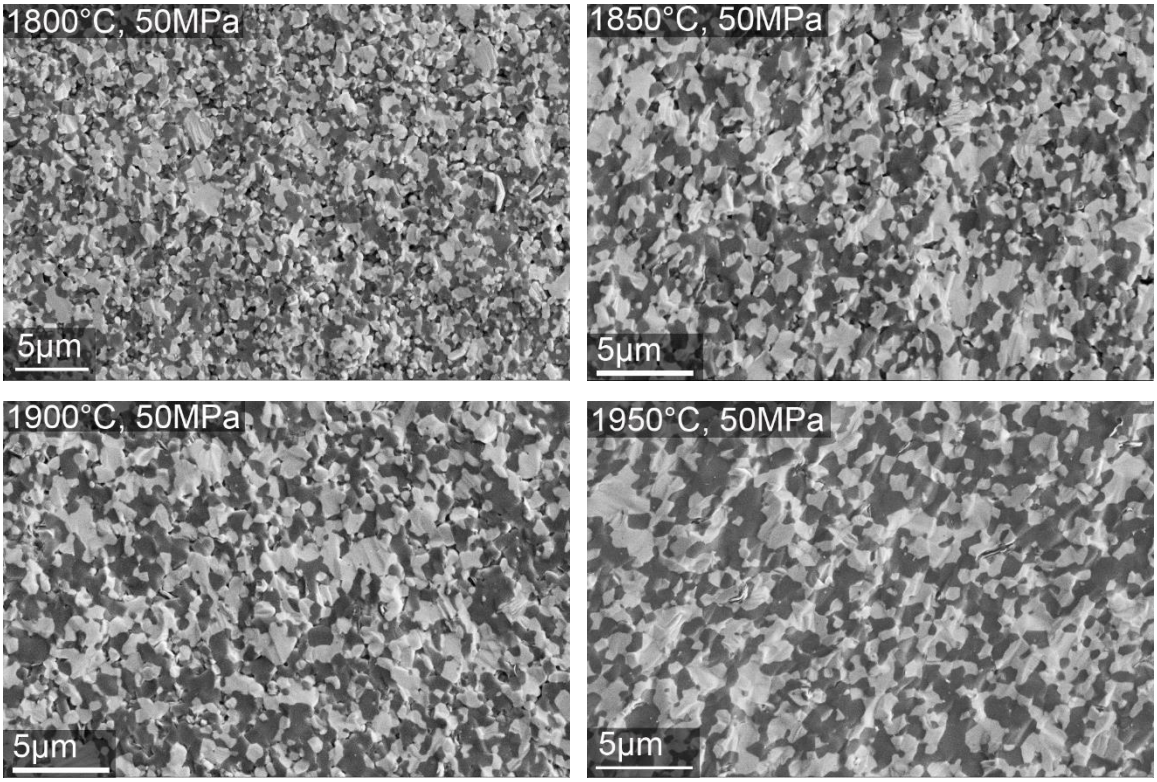

Figure 59. Fracture surface for sintering temperature 1800°C, 1850°C, 1900, °C 1950°C

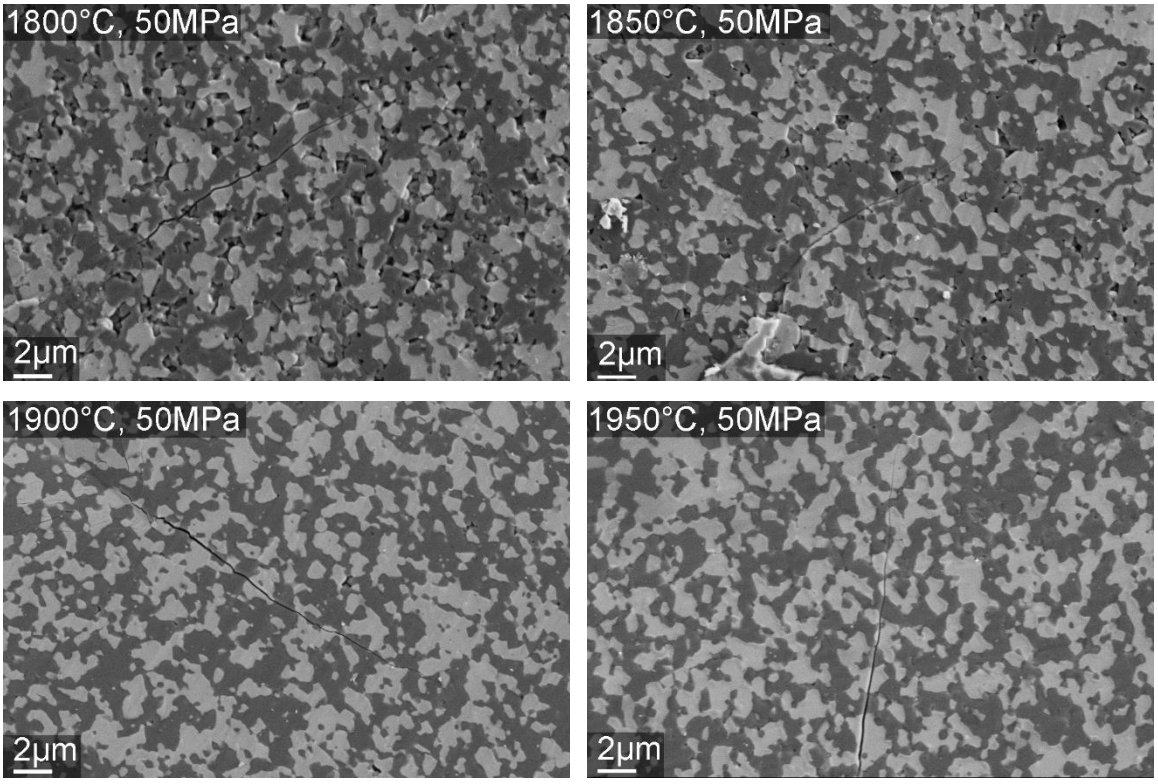

Figure 60. Indentation crack in polish surface for sintering temperature 1800°C, 1850°C, 1900, °C 1950°C

The samples hardness values were measured using Vickers diamond intentation, and the fracture toughness values were calculated by measuring Vickers indenter crack length, as described in section 4.5.5. using equations 28 and 29. Hardness and fracture toughness results are shown in Table 30 and Figures 61, and 62. Each value represents the mean of ten calculated hardness and indentation fracture toughness. Hardness values were 17.55 GPa at 1800°C, 28.63 GPa at 1850°C, 28.91 GPa at 1900°C, and 30.78 GPa at 1950°C. The measured hardness results showed that, with increasing sintering temperature, the composites hardness had increased. Since the porosity decreased with increasing sintering temperature, increasing the sintering temperature showed positive effect on

materials hardness. This relationship was also mentioned in literature; Zhang et. al. found inceased hardness values with increasing the sintering temperature in silicon carbide- boron carbide samples [123].

Since the sample that was sintered at 1800°C had pores on the surface, the crack size could not be measured and this sample did not have a fracture toughness value. Fracture toughness values were 2.49 at 1850 °C, 2.60 at 1900°C, and 2.63 at 1950°C. The fracture toughness results showed that increasing the sintering temperature increased the fracture toughness.

Table 30. Effect of sintering temperature on hardness and indentation fracture toughness

Sample	**Hardness (GPa)**	**Fracture Toughness ($MPa.m^{1/2}$)**
1400-1-1800-5-50	17.55±0.78	-
1400-1-1850-5-50	28.63±1.11	2.50±0.05
1400-1-1900-5-50	28.91±0.68	2.60±0.14
1400-1-1950-5-50	30.78±1.79	2.64±0.24

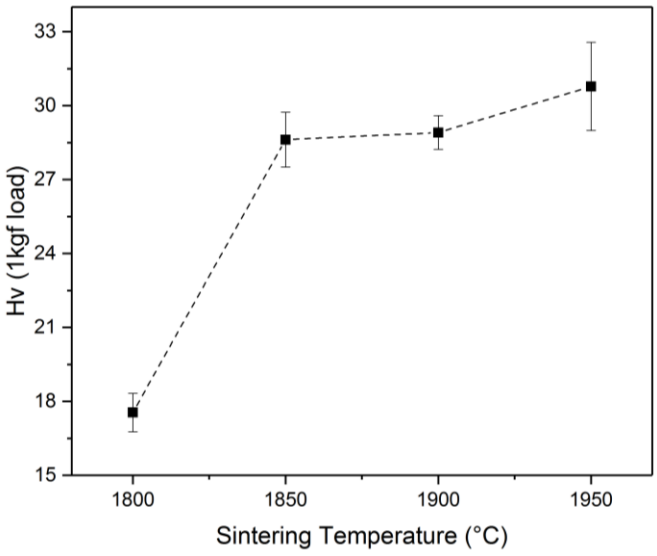

Figure 61. Effect of the sintering temperature on the measured hardness

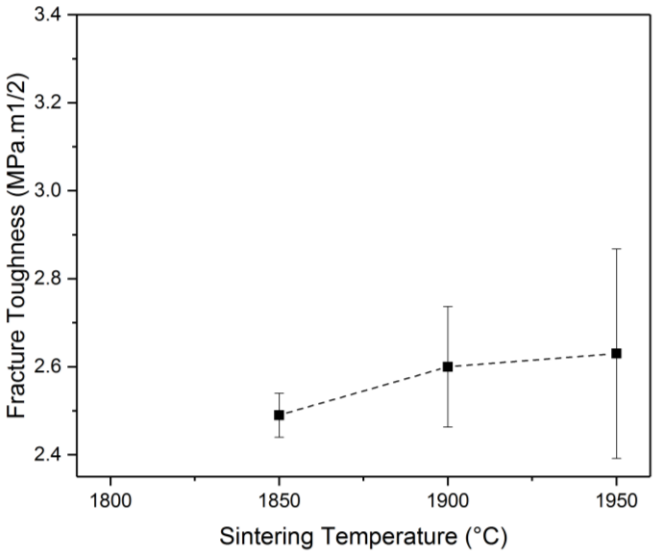

Figure 62. Effect of the sintering temperature on the indentation fracture toughness

5.2.1.2. Effect of Applied Pressure

To find the optimal applied pressure, 50%B_4C-1.5%C-48.5%SiC composition was sintered at 1950°C with four different applied pressures (20, 30, 40 and 50MPa). Two stage sintering was used to sinter samples. The dry powder was Spark Plasma Sintered and

heated to 1400°C with a 200°C/min heating rate under vacuum, an applied pressure of 20, 30, 40 and 50MPa, and a dwelling time of 1 minute. After the 1 minute holding time, the samples were heated to 1950°C at 200°C/min, under 20, 30, 40, and 50MPa applied pressure, and held for 5 min.

The density values of the SPS samples were determined using the Archimedes method as described in section 4.5.1. Table 31 shows the sintering conditions and relative density of the samples. It may be seen that sample sintered at 1950°C with 50 MPa applied pressure is almost fully dense. The relative density changed from 98.57% to 99.64%. While the relative density of the sample sintered at 1950°C with 20 MPa applied pressure was 98.57%, the sample sintered at 1950°C with applied pressure 50 MPa was 99.64 %.

Table 31. SPS conditions for the effect of applied pressure

Sample	**Sintering Temperature (°C)**	**Applied Pressure (MPa)**	**Dwelling Time (min)**	**Density (g/cm^3)**	**Theoretical Density (g/cm^3)**	**Average Percent Density (%)**
1400-1-1950-5-20	1950	20	5	2.770±0.004	2.81	98.57
1400-1-1950-5-30	1950	30	5	2.780±0.002	2.81	98.93
1400-1-1950-5-40	1950	40	5	2.790±0.006	2.81	99.28
1400-1-1950-5-50	1950	50	5	2.800±0.002	2.81	99.64

Figure 63 shows the effect of applied pressure on the density. The results showed that the density of the material increases with increasing applied pressure even at the same sintering temperature. Increasing the applied pressure had increased the diffusion between particles so that the material's density had increased.

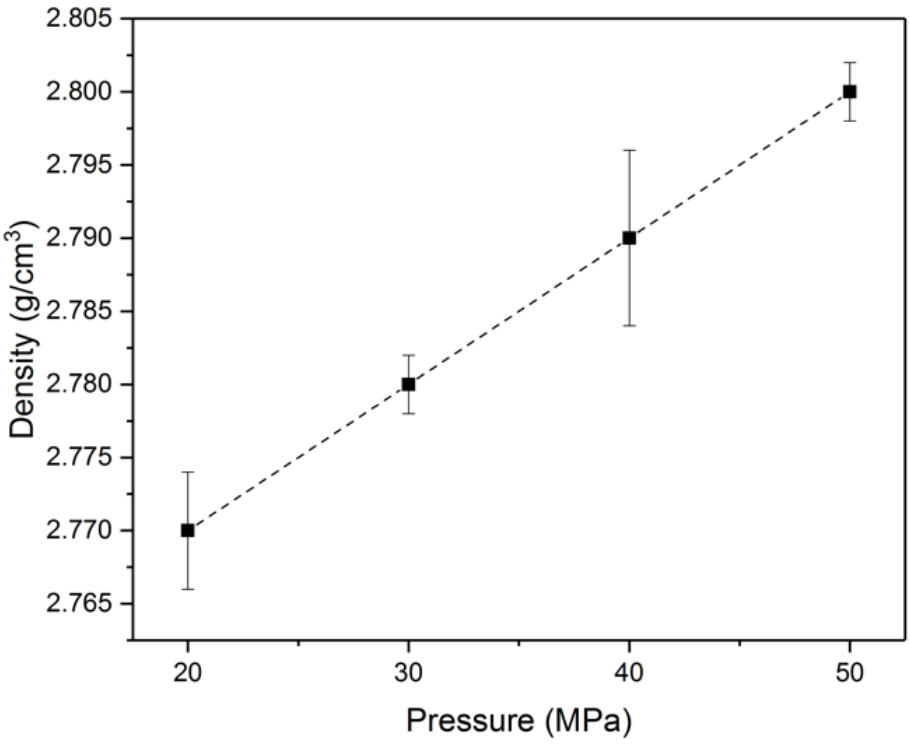

Figure 63. Effect of the applied pressure on the density

The microstructure images for different sintering temperatures can be seen in Figure 64. The light area was SiC, and the dark area was B_4C. Also, the images supported the Archimedes density results since almost all samples are fully dense. Even at low applied pressure, pores cannot be seen.

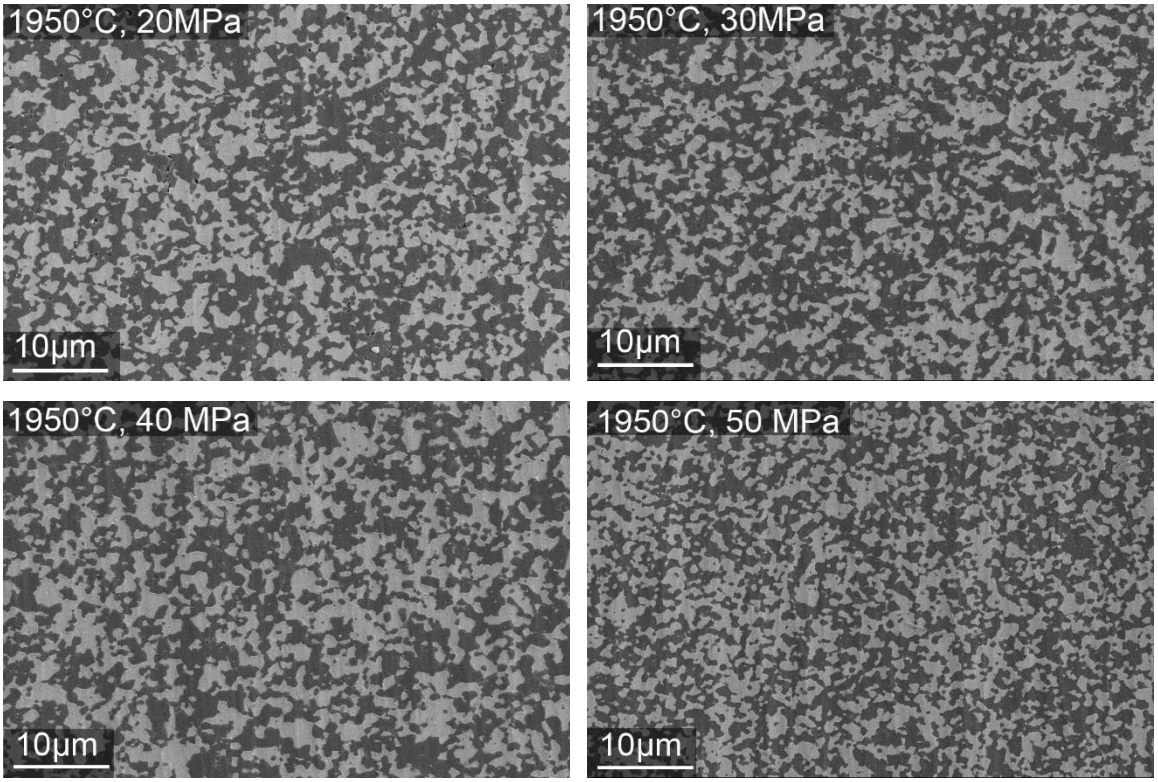

Figure 64. Microstructure images for different applied pressure 20MPa, 30MPa, 40MPa, and 50MPa

Table 32 and Figures 65 and 66 show average grain sizes of boron carbide and silicon carbide grains with standard deviations for different applied pressure. At the same combination, by increasing the applied pressure at the same sintering temperature, boron carbide grains reduced from 0.63µm to 0.44µm and silicon carbide grains reduced from 0.53µm to 0.44µm.

Table 32. Average grain sizes for different applied pressure

Sample	Average Grain Size of B_4C (µm) (Std. Dev)	Average Grain Size of SiC (µm) (Std. Dev)
1400-1-1950-5-20	0.63±0.05	0.53±0.05
1400-1-1950-5-30	0.51±0.04	0.51±0.05
1400-1-1950-5-40	0.50±0.07	0.43±0.07
1400-1-1950-5-50	0.44±0.04	0.44±0.04

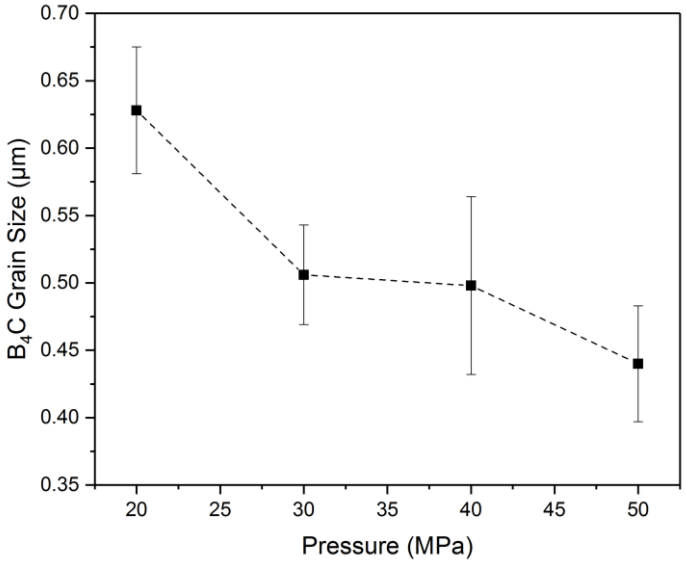

Figure 65. Effect of the applied pressure on the B_4C grain size

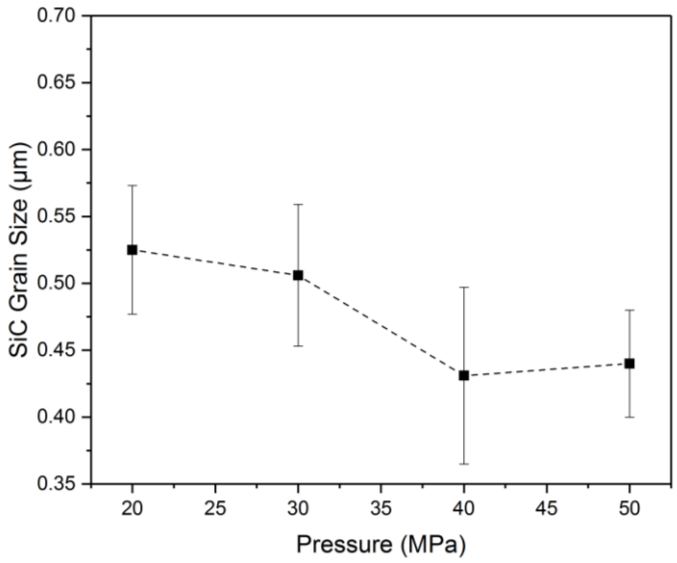

Figure 66. Effect of the applied pressure on the SiC grain size

X-ray diffraction patterns of the samples can be seen in Figure 67. All samples showed the same patterns. Through XRD data, the samples were shown to have silicon carbide, boron carbide and a small amount of carbon as expected. Compared with raw starting materials, no unexpected phase occurred. Since the composites were not made from in-situ processing, sintering temperature did not affect the peak intensity.

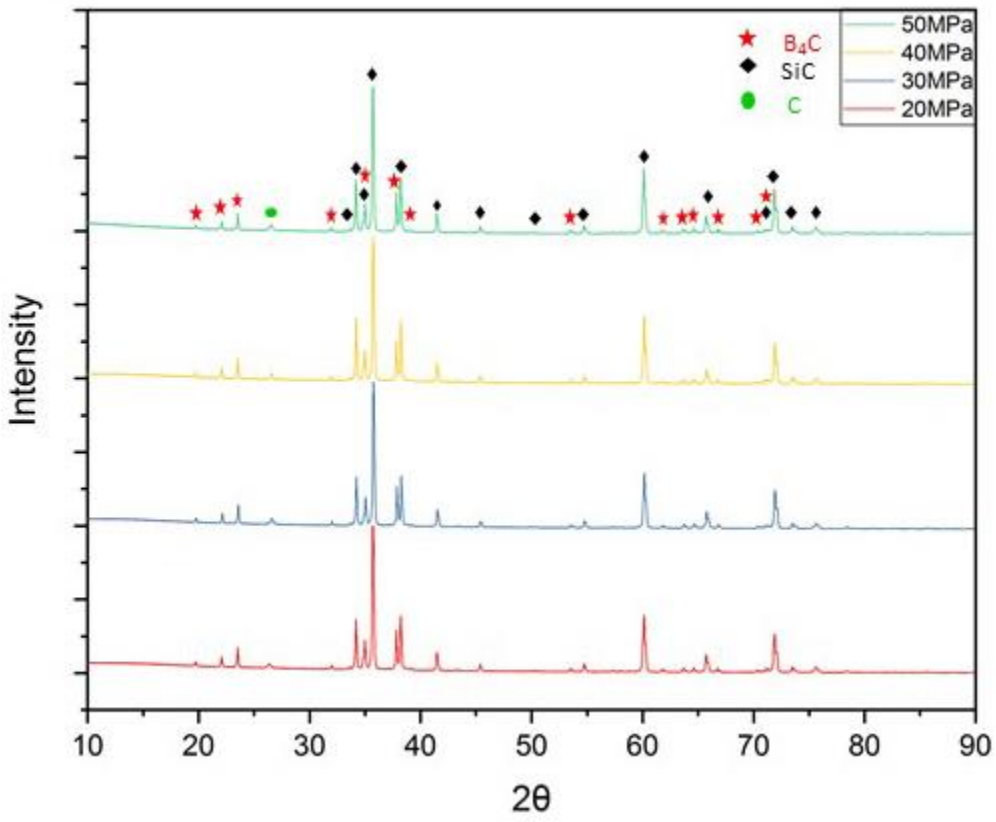

Figure 67. X-ray diffraction patterns of samples sintered at different applied pressure

The samples elastic properties were measured using ultrasound analysis. c_L (longitudial sound speed), c_S (shear sound speed), Poisson's ratio, Young's modulus (E), shear modulus (G), and bulk modulus (K) values were calculated from equations 22, 23, 24, 25, 26, and 27 respectively as described in section 4.5.3. The results can be seen in Table 33 and Figures 68 through 71. Each value represents the mean of five analyses. Since elastic properties had a direct relation to density, the elastic modulus, bulk modulus, and shear modulus increased with increasing sintering applied pressure. The Poisson's ratio value increased from 0.160 to 0.165, the Young's modulus increased from 390 GPa to 409 GPa, the shear modulus changed from 168 GPa to 176 GPa, and the bulk modulus increased from 192 GPa to 203 GPa.

Table 33. Elastic properties of different applied pressure

Sample	c_L (m/s)	c_S (m/s)	Poisson's Ratio	E (GPa)	G (GPa)	K (GPa)
1400-1-1950-5-20	12254	7794	0.160±0.003	390±8	168±3	192±4
1400-1-1950-5-30	12398	7852	0.165±0.003	400±8	172±3	199±4
1400-1-1950-5-40	12457	7891	0.165±0.003	406±8	174±4	202±4
1400-1-1950-5-50	12506	7921	0.165±0.003	409±8	176±4	203±4

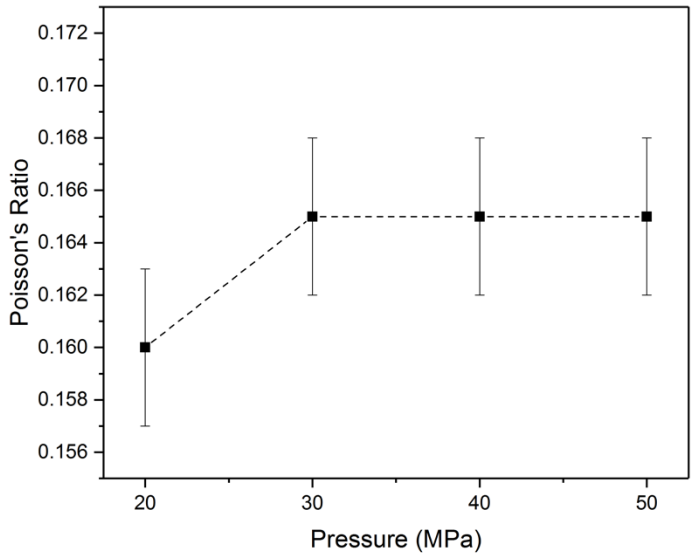

Figure 68. Effect of the applied pressure on the Poisson's ratio

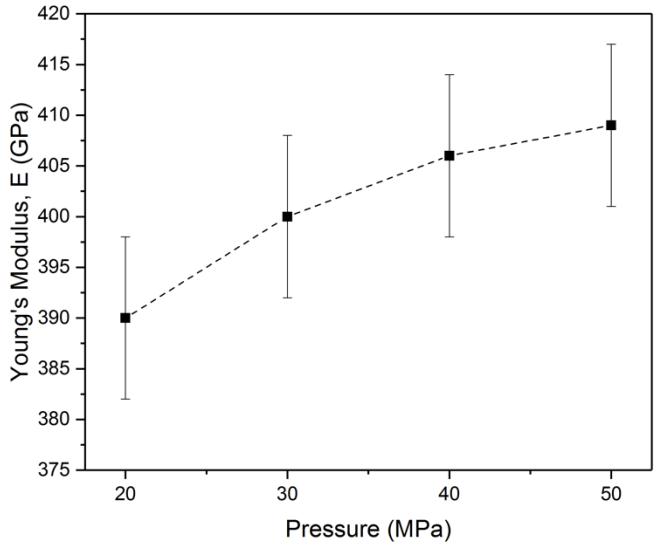

Figure 69. Effect of the applied pressure on the Young's modulus

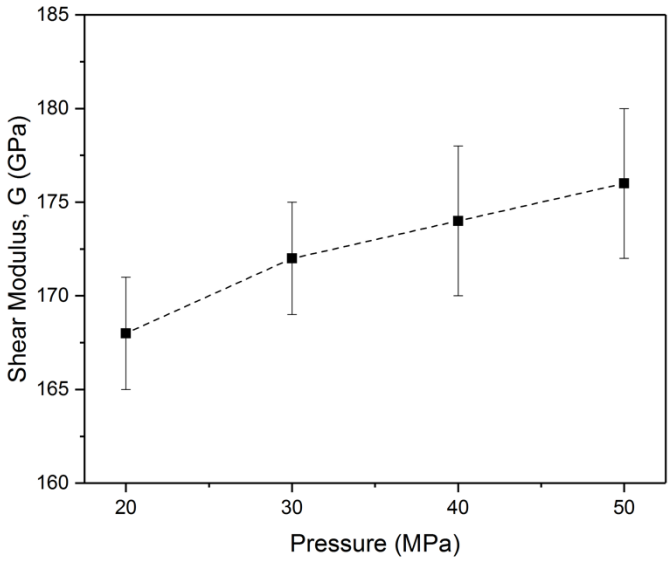

Figure 70. Effect of the applied pressure on the shear modulus

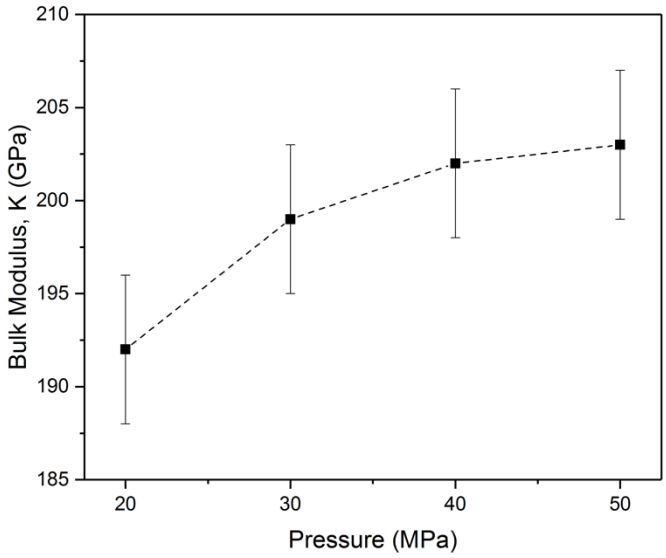

Figure 71. Effect of the applied pressure on the bulk modulus

SEM imaging was used to determine the mode of fracture. Figure 72 shows the fracture surface of samples sintered at 1950°C with different applied pressures. Images showed that composites showed transgranular fracture mode. Applied pressure did not affect the fracture mode of the composite.

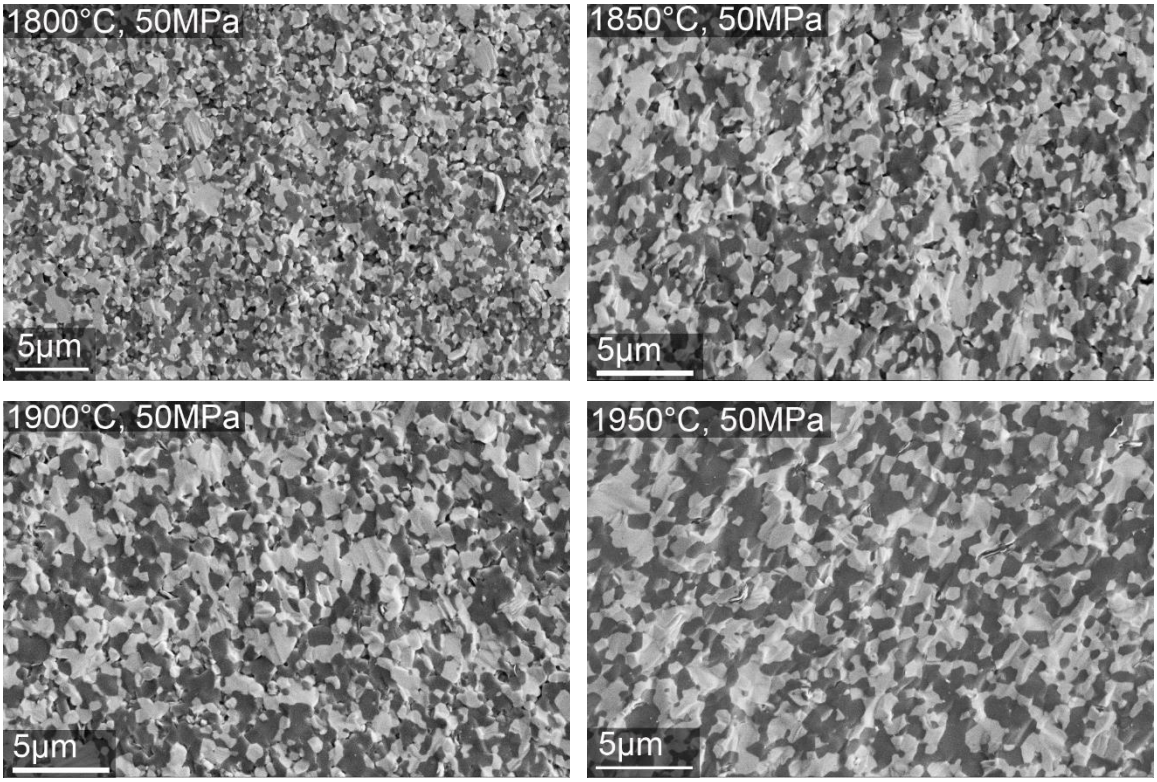

Figure 72. Fracture surface for different applied pressure 20MPa, 30MPa, 40MPa, and 50MPa

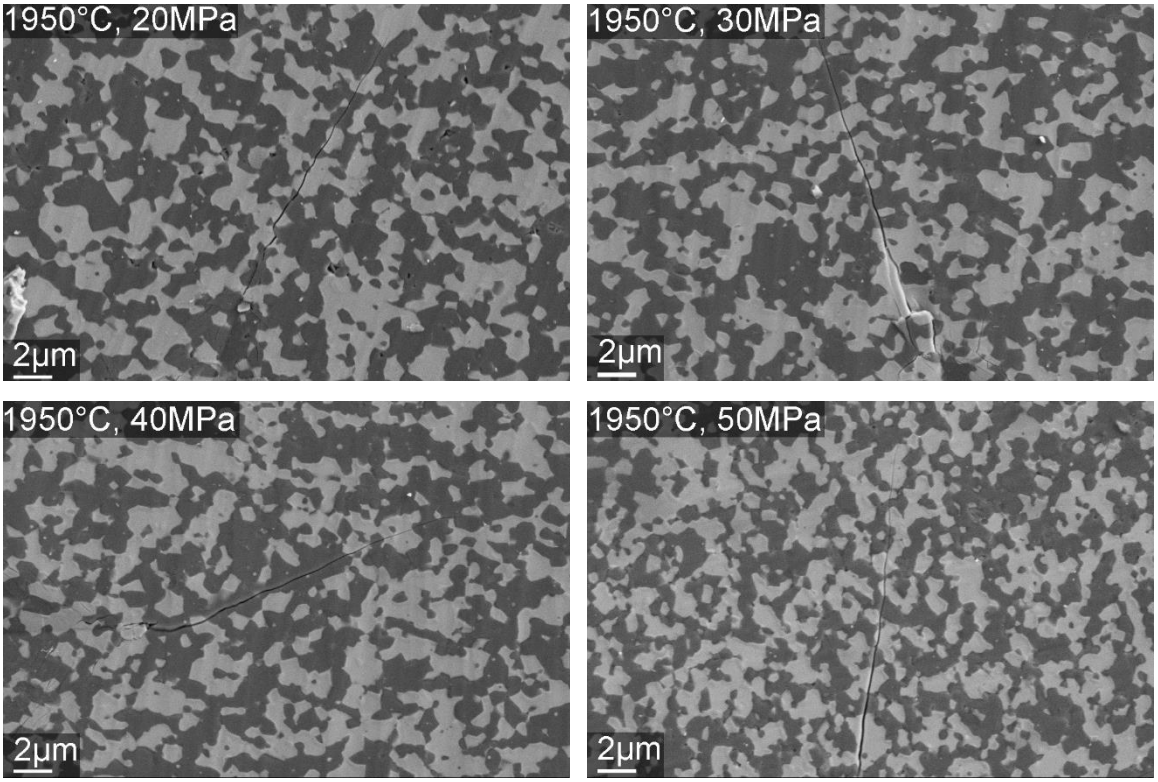

Figure 73. Intentation crack in polish surface for different applied pressure 20MPa, 30MPa, 40MPa, and 50MPa

The samples hardness values were measured using Vickers diamond intentation, and the fracture toughness values were calculated by measuring Vickers indenter crack lengths, as described in section 4.5.5. using equations 28 and 29. Table 34 and Figure 74,75 showed hardness and indentation fracture toughness of samples. Each value represents the mean of ten calculated hardness and indentation fracture toughness values. Hardness values were 28.72 GPa with 20 MPa, 28.76 GPa with 30 MPa, 29.21 GPa with 40 MPa, and 30.78 GPa with 50 MPa applied pressure. The measured hardness results showed that, when increasing the applied pressure at the same sintering temperature, the composites hardness had increased. It was again related with the amount of porosity in the

samples; if porosity decreases with increasing pressure, then the materials' hardness increases.

Fracture toughness values were 2.65 with 20 MPa, 2.69 with 30 MPa, 2.71 with 40 MPa, and 2.63 with 50 MPa applied pressure. The fracture toughness results showed that increasing the applied pressure increases the fracture toughness. However, the fracture toughness value decreased at 50 MPa.

Table 34. Effect of applied pressure on hardness and indentation fracture toughness

Sample	**Hardness (GPa)**	**Fracture Toughness ($MPa.m^{1/2}$)**
1400-1-1950-5-20	28.72±0.72	2.65±0.06
1400-1-1950-5-30	28.76±1.01	2.69±0.07
1400-1-1950-5-40	29.21±0.48	2.72±0.19
1400-1-1950-5-50	30.78±1.79	2.64±0.24

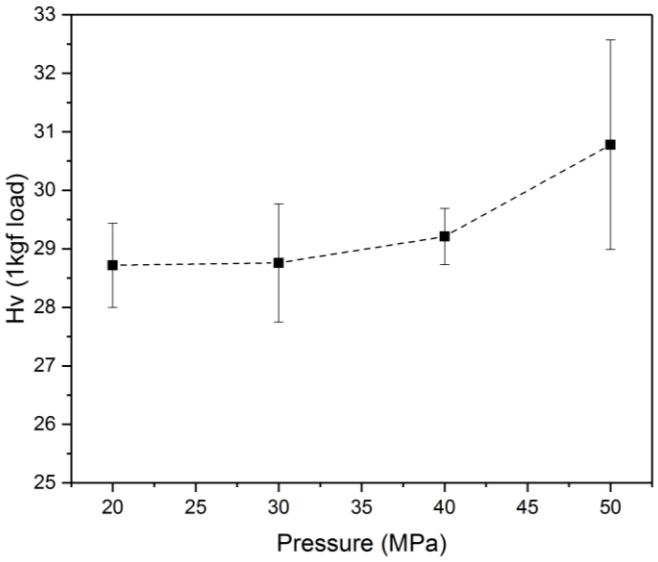

Figure 74. Effect of the applied pressure on the measured hardness

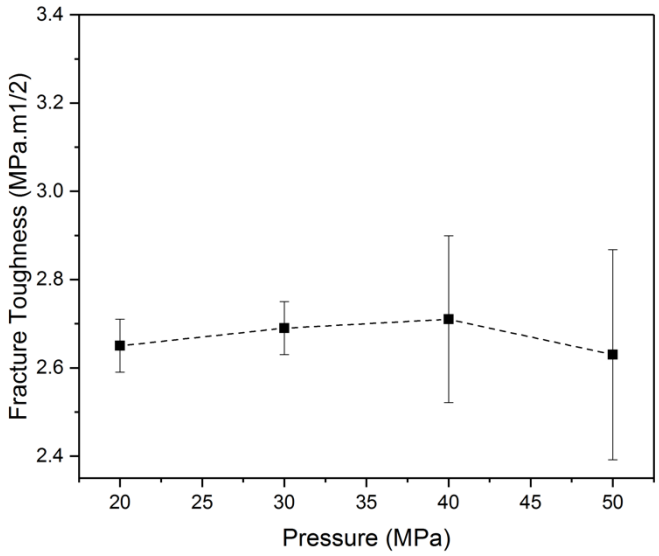

Figure 75. Effect of the applied pressure on the indentation fracture toughness

5.2.3. Evaluate the Role of Homogeneity in the Composite Microstructure

The density values of the SPS samples were determined using the Archimedes method as described in section 4.5.1. Table 35 shows the mixing method and relative density of the samples. It can be seen in Figure 76 that ball milling provided higher density values than dry mixing. Significant pores were not observed in either sample set. For both mixing methods, the density decreased with increasing B_4C content in the composites. Dry mixing samples' relative density changed from 98.60% to 97.50%, while the ball milling samples' relative density changed 99.60% to 98.9% with increasing B_4C content.

Table 35. Density of dry mixing and ball milling samples

Sample	Density (g/cm^3)		Theoretical Density (g/cm^3	Average Percent Density (%)	
	Dry Mixing	Ball Milling		Dry Mixing	Ball Milling
10B_4C-SiC-1.5C	3.070±0.002	3.100±0.002	3.11	98.60	99.60
20B_4C-SiC-1.5C	2.990±0.001	3.000±0.002	3.03	98.70	99.20
30B_4C-SiC-1.5C	2.900±0.003	2.910±0.001	2.95	98.50	98.80
40B_4C-SiC-1.5C	2.820±0.002	2.850±0.002	2.88	97.80	98.80
50B_4C-SiC-1.5C	2.740±0.001	2.780±0.003	2.81	97.50	98.90

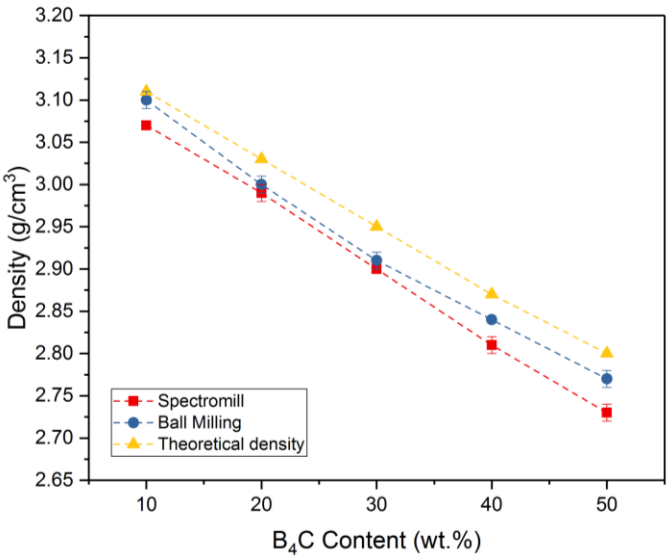

Figure 76. Density values of dry mixing and ball milling samples

Microstructure images in Figure 77 showed that dry mixing did not provide uniform mixing. Large pockets of individual components were clearly observed. Increasing the B_4C

amount caused bigger B_4C islands. Images also supported the density values showing that there was no significant porosity. On the other hand, ball milling provided uniform mixing. There were no pockets of individual components. Ball milled samples achieved high density since there were no visible pores.

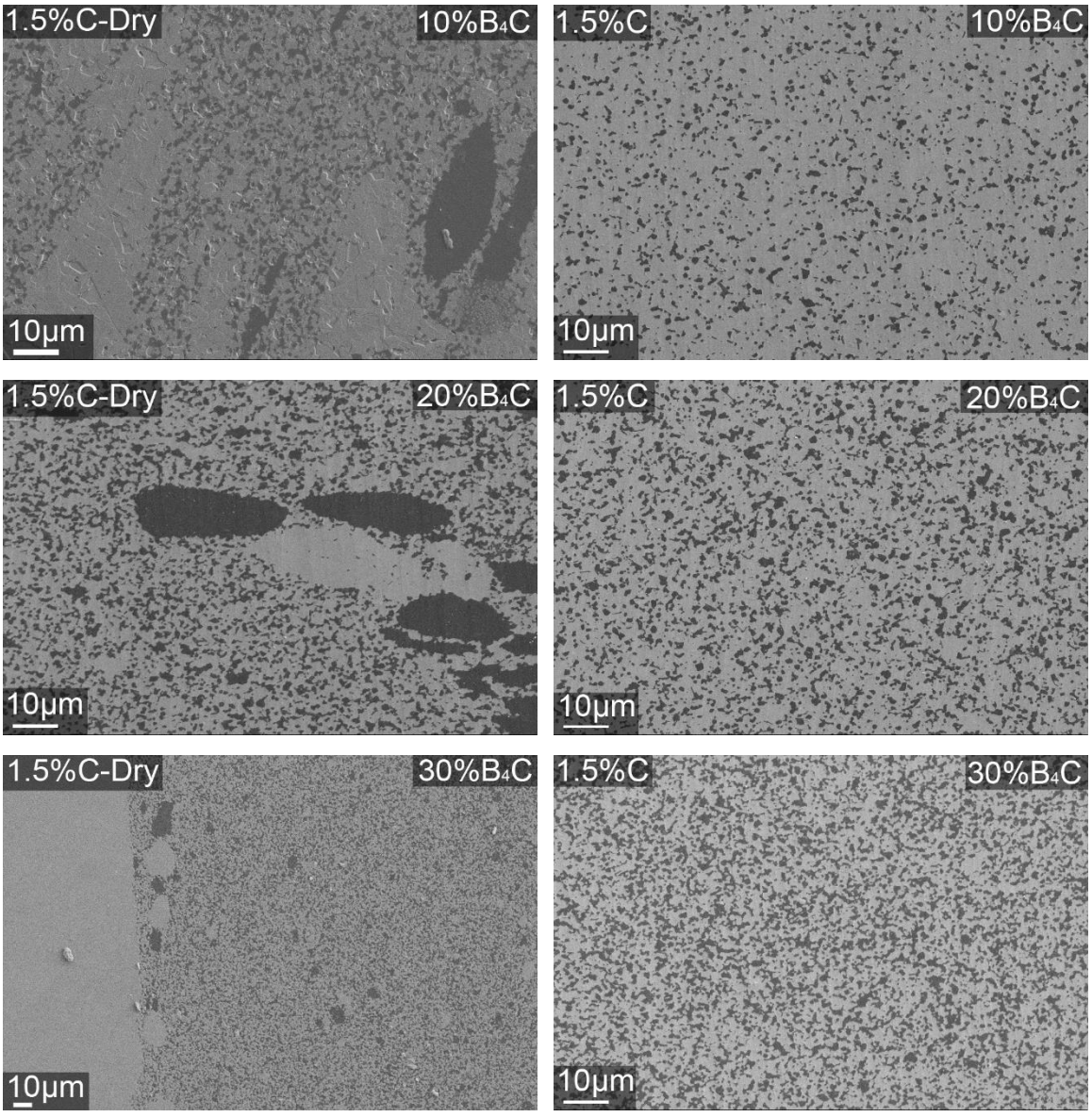

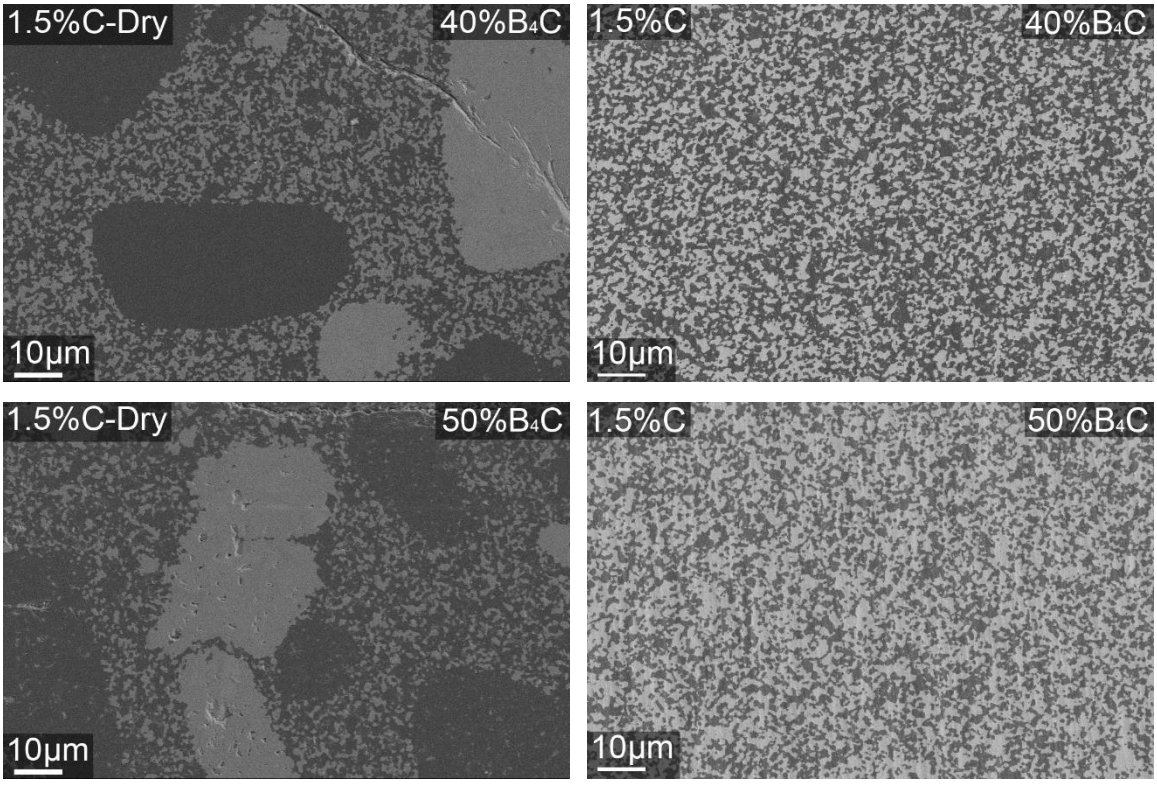

Figure 77. Microstructure of dry mixing and ball milling samples

The samples elastic properties were measured using ultrasound analysis. c_L (longitudial sound speed), c_S (shear sound speed), Poisson's ratio, Young's modulus (E), shear modulus (G), and bulk modulus (K) values were calculated from equations 22, 23, 24, 25, 26, and 27 respectively as described in section 4.5.3. The results can be seen in Table 36 and Figures 78 through 81. Each value represents the mean of five analyses. The dry mixing samples elastic properties values did not have any trend. The results were inconsistent and showed that the dry mixing did not provide efficient mixing. The ball milled samples' Poisson's ratio changed from 0.169 to 0.162, Young's modulus dropped from 415 GPa to 388 GPa, shear modulus reduced from 177 GPa to 167 GPa, and bulk modulus decreased from 209 GPa to 192 GPa while the B_4C content increased from 10% to 50% .

Table 36. Elastic properties of dry mixing and ball milling samples

Sample	Mixing Method	Poisson's Ratio	E (GPa)	G (GPa)	K (GPa)
10B_4C-SiC-1.5C		0.183±0.004	402±8	170±3	211±4
10B_4C-SiC-1.5C	Ball Milling	0.169±0.003	415±8	177±4	209±4
20B_4C-SiC-1.5C	Dry Mixing	0.213±0.004	379±8	156±3	220±4
20B_4C-SiC-1.5C	Ball Milling	0.168±0.003	409±8	175±4	205±4
30B_4C-SiC-1.5C	Dry Mixing	0.214±0.004	413±8	170±3	241±5
30B_4C-SiC-1.5C	Ball Milling	0.162±0.003	402±8	173±4	198±4
40B_4C-SiC-1.5C	Dry Mixing	0.195±0.004	396±8	166±3	216±4
40B_4C-SiC-1.5C	Ball Milling	0.163±0.003	392±8	169±3	194±4
50B_4C-SiC-1.5C	Dry Mixing	0.136±0.003	408±8	179±4	187±4
50B_4C-SiC-1.5C	Ball Milling	0.162±0.003	388±8	167±3	192±4

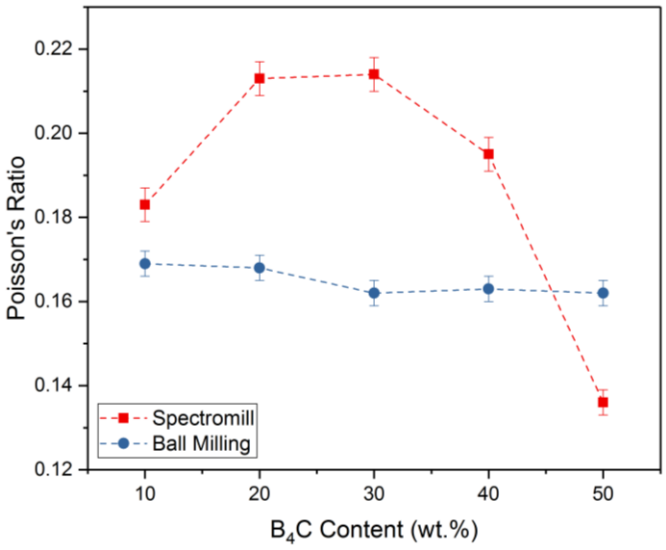

Figure 78. Effect of mixing method on the Poisson's ratio

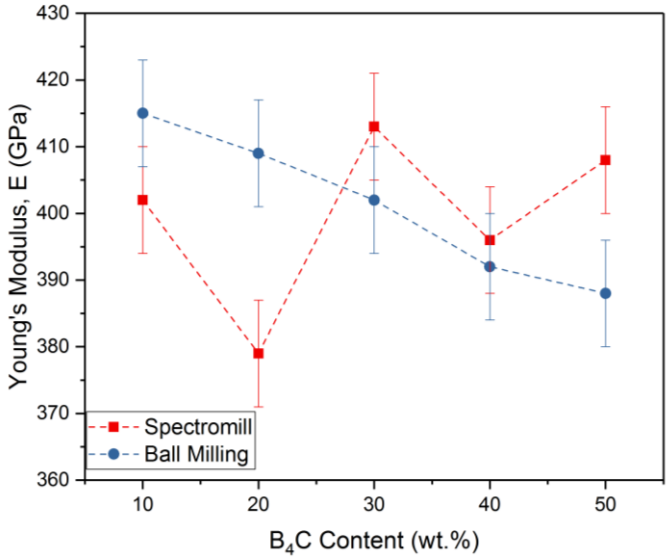

Figure 79. Effect of mixing method on the Young's modulus

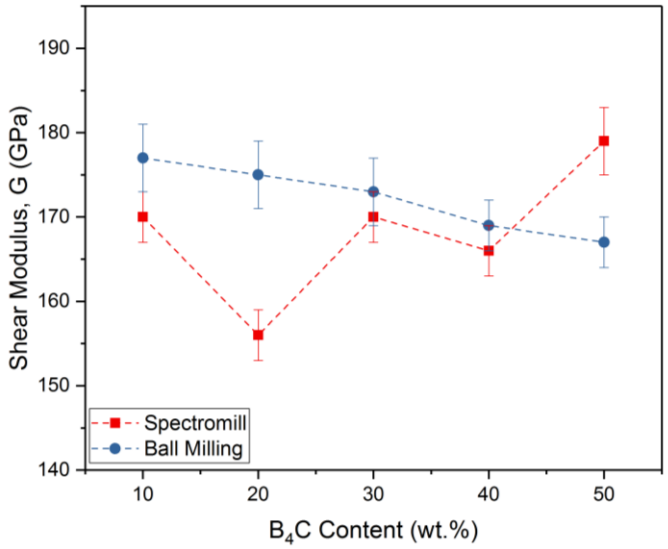

Figure 80. Effect of mixing method on the shear modulus

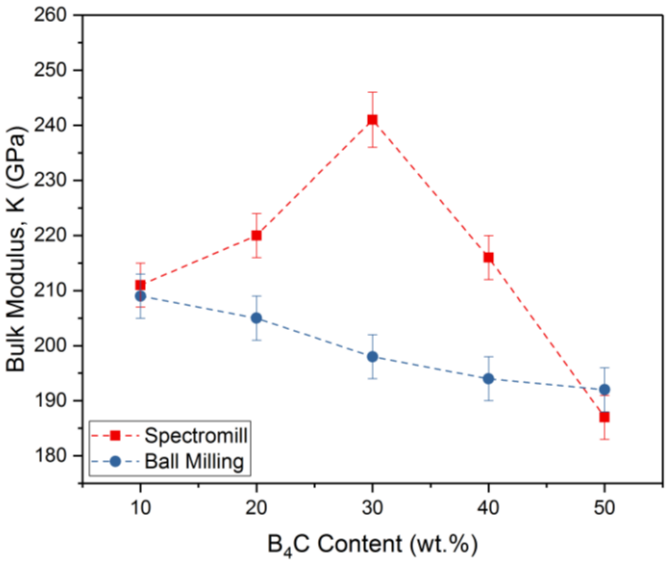

Figure 81. Effect of mixing method on the bulk modulus

As seen in the microstructure images below Figure 82, it was clear that larger pockets of individual components in the fracture surface of dry mixing samples were present, while ball milling samples had uniform mixing. Both series had transgranular fracture mode.

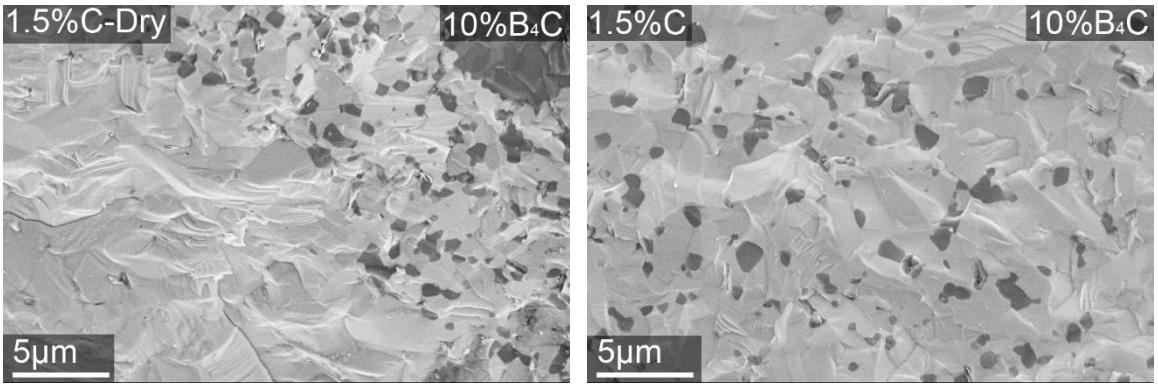

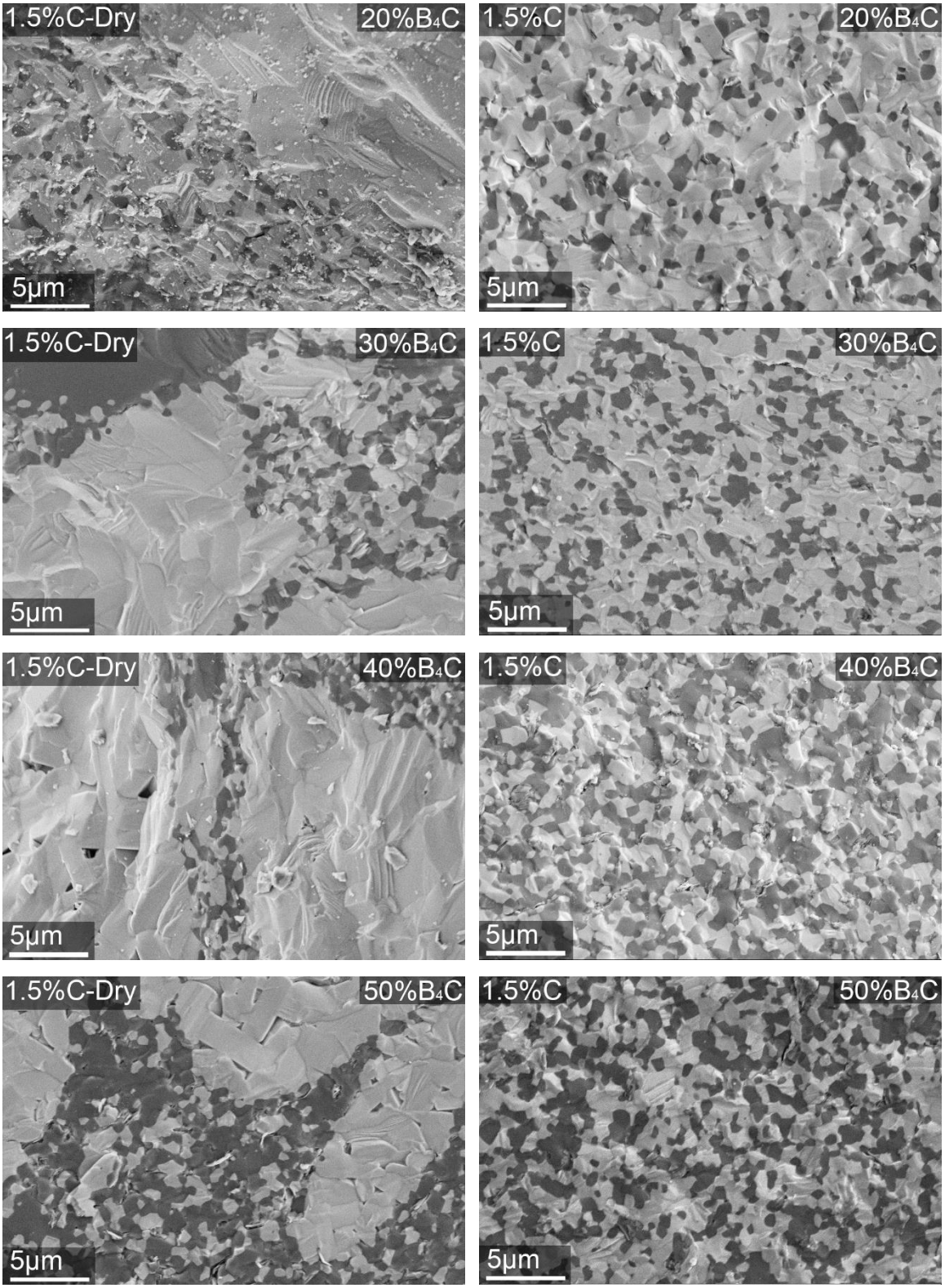

Figure 82. Fracture surface of dry mixing and ball milling samples

The samples hardness values were measured using Vickers diamond intentation, and fracture toughness values were calculated by measuring Vickers indenter crack length as described in section 4.5.5. using equations 28 and 29. Table 37 and Figures 83 and 84 showed hardness and indentation fracture toughness of samples. Each value represents the mean of ten calculated hardness and indentation fracture toughness values. Once again due to the nonuniform mixing, dry mixing samples had inconsistent hardness and indentation fracture toughness values. On the other hand, ball milling samples had a trend. The hardness values increased with increasing B_4C content. Since B_4C had higher hardness than SiC, the fracture toughness values decreased with increasing B_4C content.

Table 37. Effect of mixing method on hardness and indentation fracture toughness

	Hardness (GPa)		**Fracture Toughness (MPa.m$^{1/2}$)**	
Sample	**Dry Mixing**	**Ball Milling**	**Dry Mixing**	**Ball Milling**
10B_4C-SiC-1.5C	27.66±1.34	26.14±0.96	2.53±0.15	2.89±0.39
20B_4C-SiC-1.5C	26.57±1.76	28.79±0.81	2.71±0.53	2.79±0.15
30B_4C-SiC-1.5C	30.42±2.17	29.51±0.62	2.59±0.68	2.74±0.22
40B_4C-SiC-1.5C	29.09±1.13	29.99±1.67	2.60±0.76	2.66±0.10
50B_4C-SiC-1.5C	24.15±0.23	30.34±0/93	2.77±1.14	2.64±0.16

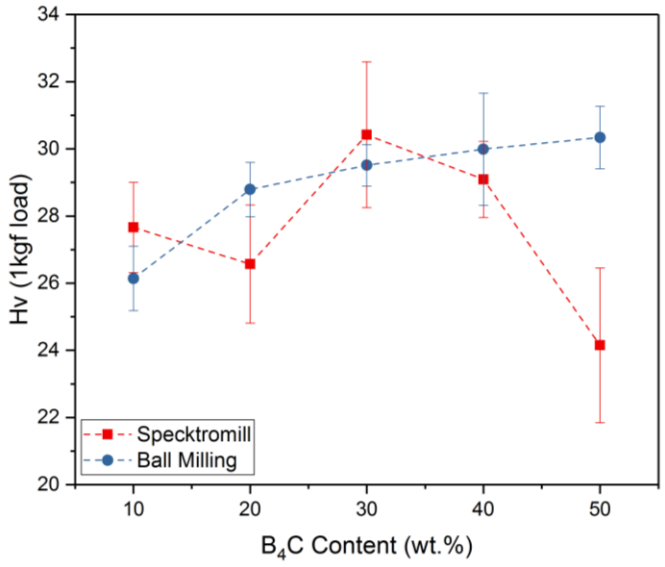

Figure 83. Effect of mixing method on hardness

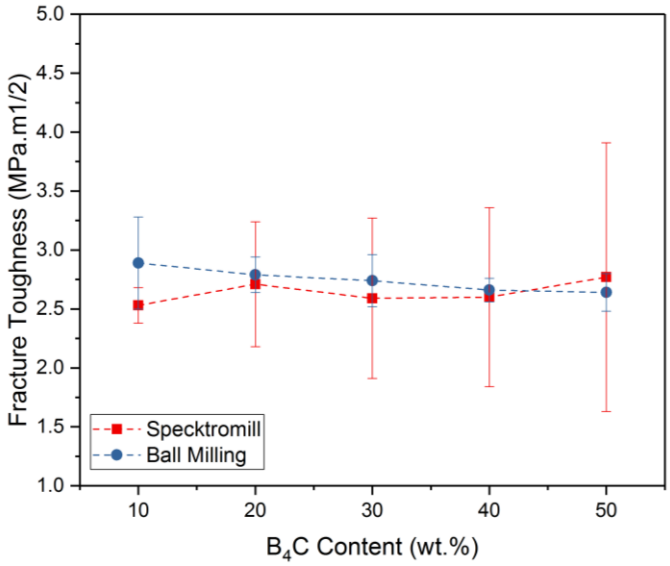

Figure 84. Effect of mixing method on intentation fracture toughness

5.2.4. Mixture Preparation

In this work, all mixtures were prepared by weight percentage. A 30 g batch of powder was prepared. B_4C, C, and SiC were weighed and put in a 250 ml Nalgene bottle. Around 150 g SiC media was added to the bottle, then ethanol was added to the dry powders and ball milled for 24 hours. The mixture was sieved to separate the media from the liquid mixture using a 1.4 mm mesh sieve. The liquid mixture was placed on a hot plate at 275°C and allow to dry. Then, powders chunks were ground to uniformity with a mortar and pestle.

5.2.5. Produce of Dense Samples

The spark plasma sintering (Thermal Technology) technique was used to sinter samples. 5 grams of each powder mixture was loaded into a 20 mm inner diameter graphite die with graphite punches. The inside of graphite die was lined with graphite foil. The graphite die had a small hole on it; this hole was used to detect the actual temperature of the sample by optical pyrometer during the sintering. The die was loaded into SPS unit with 5 MPa applied pressure. The sintering cycle started, was heated to 600°C, and held 1 minute. The optical pyrometer started measuring temperature after 600°C. The SPS was heated to 1400°C with a 200°C/min heating rate under vacuum, an applied pressure of 50MPa, and dwelling time of 1 minute. After the 1 minute holding time, the samples were heated to 1950°C at 200°C/min under 50MPa applied pressure and held for 5 min. Afterward, the SPS was shut down and the samples were allowed to cool.

5.3. Characterization of Dense Silicon Carbide- Boron Carbide Composites

5.3.1. Etched SiC-B_4C Series

5.3.1.1. Microstructure Characterization

To optimize the mechanical properties of ceramic composites, it is important to produce porosity free samples and obtain an even distribution of components in the material. As mentioned in the previous section (5.2.1), the existence of the oxide layer prevents the achievement of full density because of grain coarsening. The oxide layer reacts with silicon carbide and produces volatile SiO that causes surface grain growth without pore elimination. To avoid these problems, acid etched SiC powder was used as the starting material, and carbon was added to help remove any residual oxygen after the etching process. The residual oxide layer can be removed from silicon carbide according to equation 1, and from boron carbide according to equation 7. Moshtaghioun et. al. also mentioned that carbon helps to remove SiO_2 from SiC, and B_2O_3 from B_4C particles [113].

The SiC-B_4C composite samples were processed by SPS at 1950°C for 5min. The samples were cross-sectioned with ion milling to prepare the microstructure for examination as described in section 4.4. Microstructure images were taken as described in section 4.5.4.

The composite sample series of etched SiC powder with 10 to 50% B_4C and different several amounts of carbon can be seen in Figures 83 through 87. The light area in the photomicrographs are SiC regions, while the dark area is B_4C. The microstructure images, from the absence of pores, confirmed the spark plasma sintering method was successful in

producing fully dense SiC-B_4C composites. Surplus carbon was not evident, indicating that almost all of the carbon was reacted with the surface oxygen and removed as CO and/or reacted to form additional carbide.

Unlike the microstructure of Williams [124] and Hallam [125] silicon carbide boron carbide composites, in this research, the microstructure images showed that the samples had a homogeneous distribution of components.

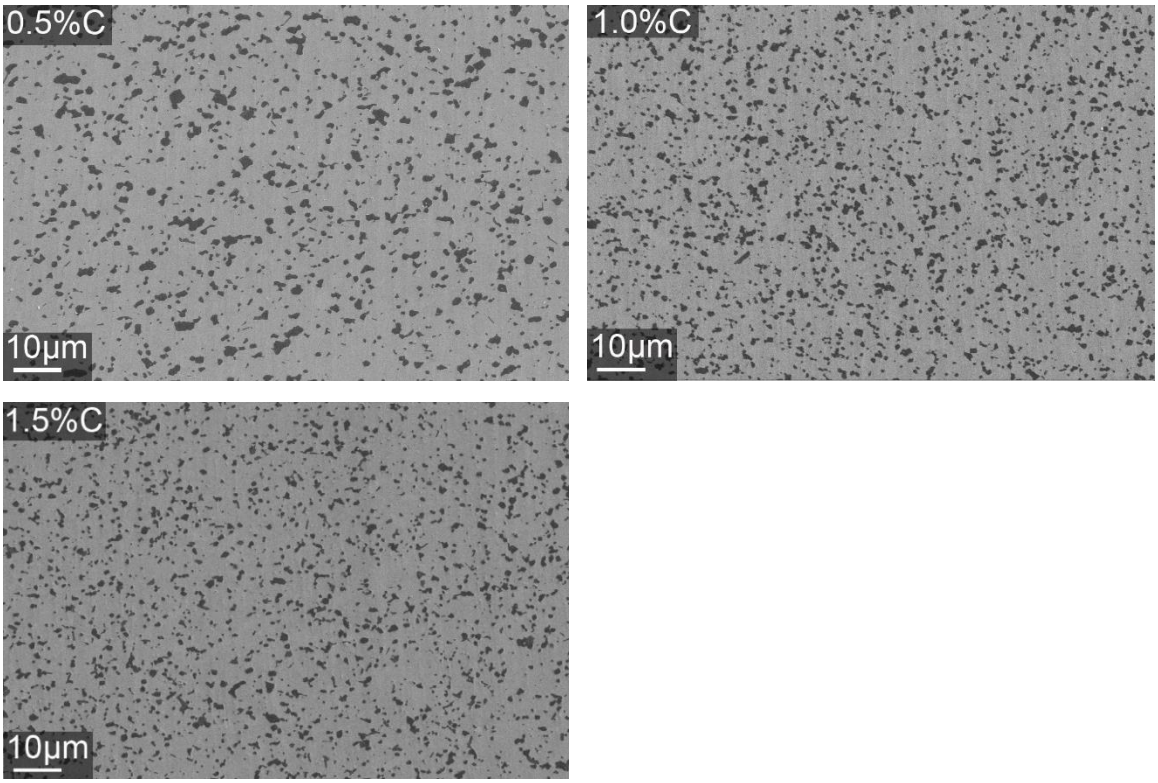

Figure 85. The microstructure of 10% B_4C- etched SiC with 0.5%C, 1.0%C, 1.5%C

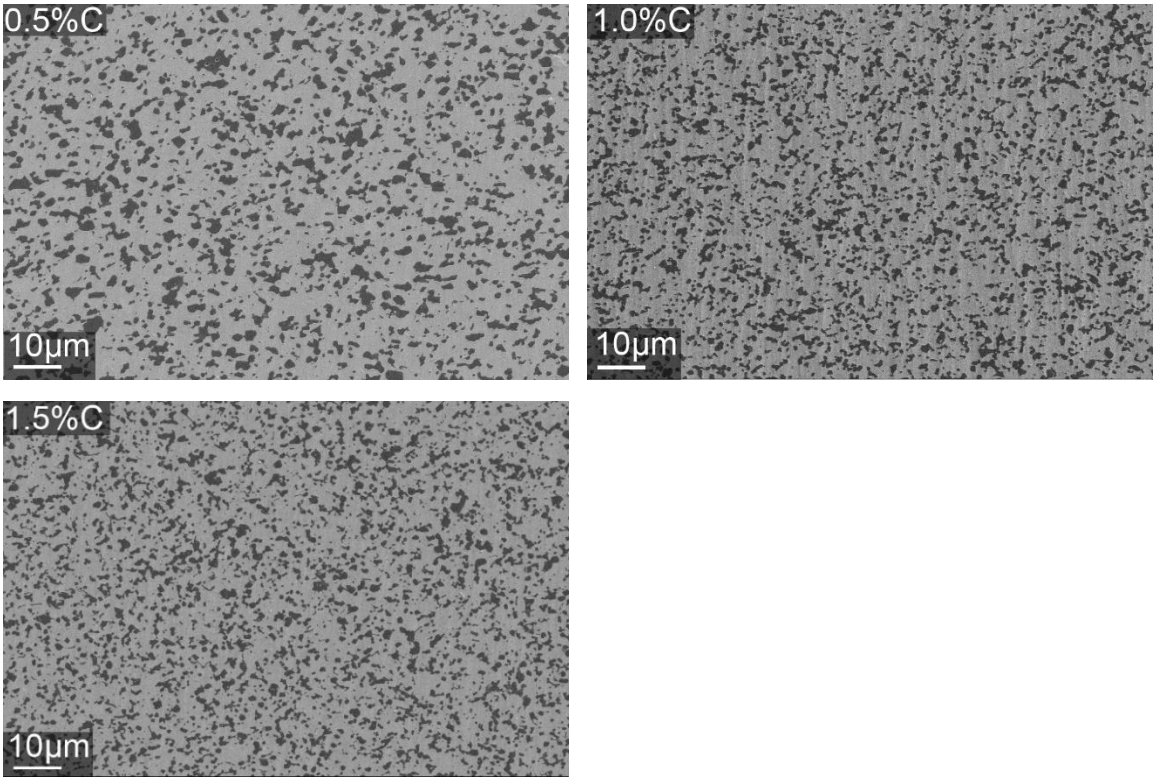

Figure 86. The microstructure of 20% B_4C- etched SiC with 0.5%C, 1.0%C, 1.5%C

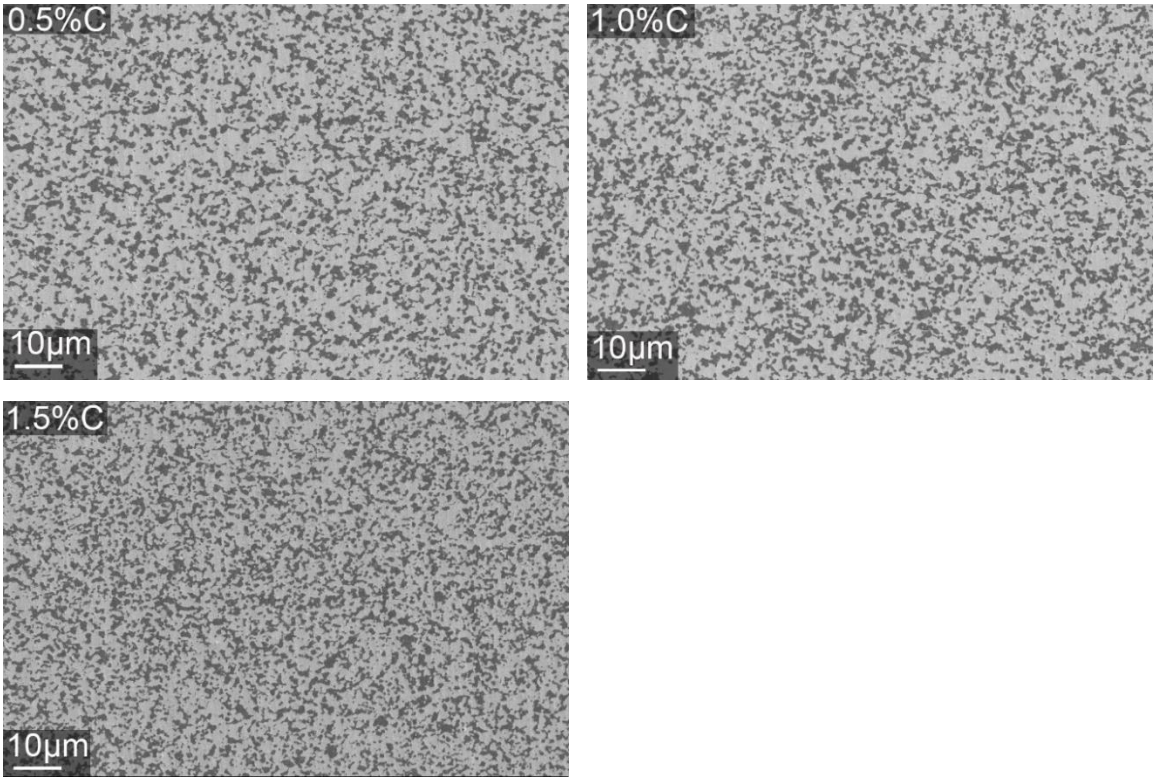

Figure 87. The microstructure of 30% B_4C- etched SiC with 0.5%C, 1.0%C, 1.5%C

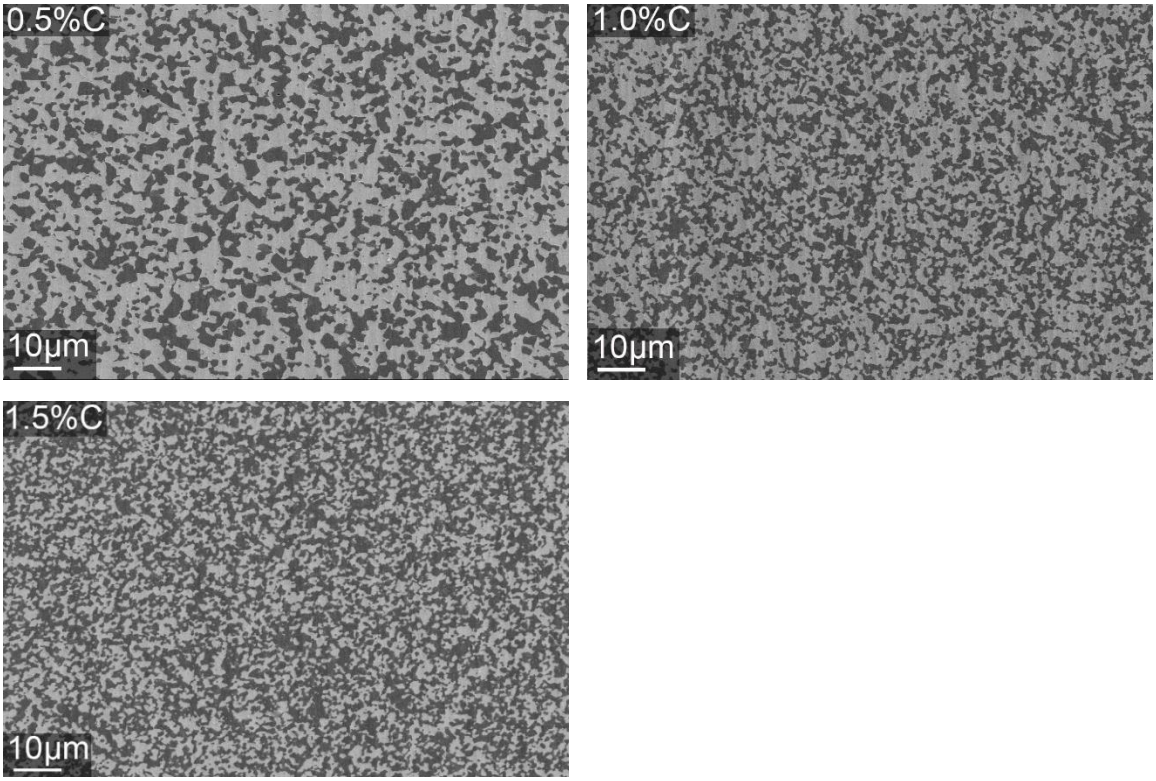

Figure 88. The microstructure of 40% B_4C- etched SiC with 0.5%C, 1.0%C, 1.5%C

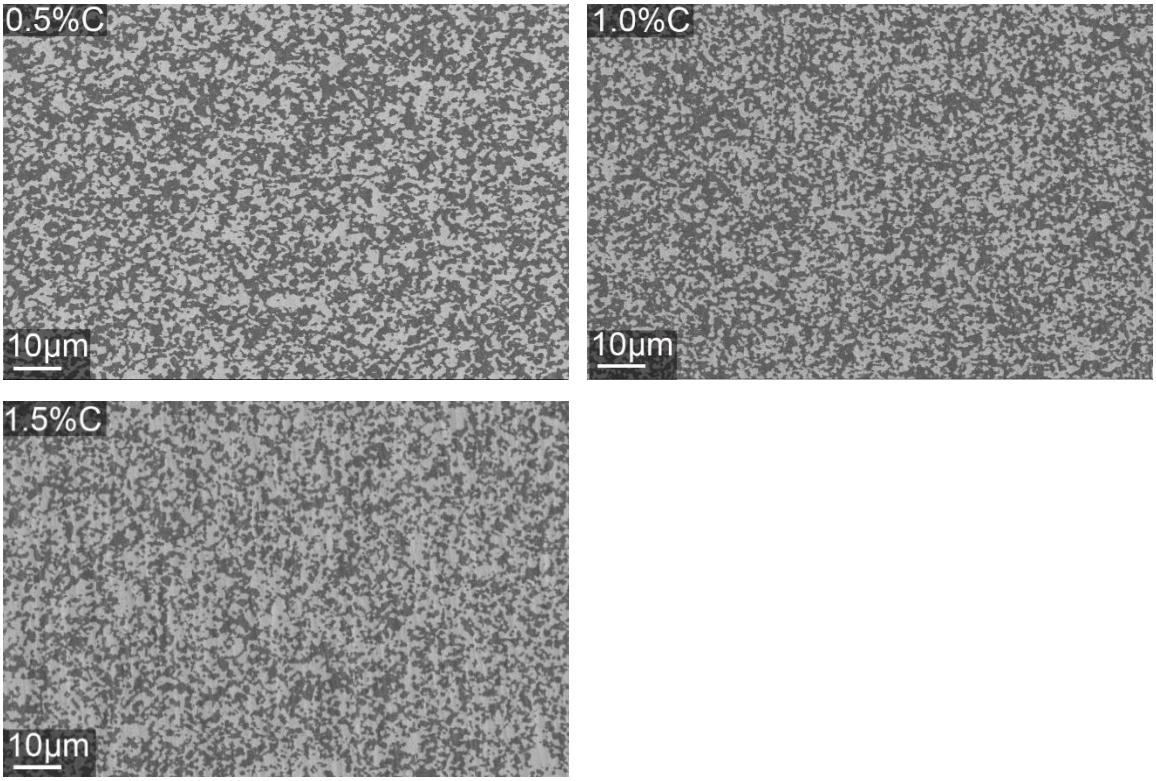

Figure 89. The microstructure of 50% B_4C- etched SiC with 0.5%C, 1.0%C, 1.5%C

Average grain sizes were determined by the linear intercepts method as described in section 4.5.4. Increasing the boron carbide content in the composites slightly increased the average boron carbide grain size, while decreasing the average grain size for silicon carbide. Grain sizes were largely submicron and close to the starting materials mean particle sizes. Since all the samples were sintered only for 5 min at 1950°C, significant grain growth was not observed. Increasing the amount of carbon decreased the grain size for both silicon carbide and boron carbide. It was clear that carbon is a grain growth preventor as mentioned in the literature [78]. Also, it was suggested that, in the presence of silicon carbide, the grain growth of boron carbide was prevented [123].

Table 38 shows average grains size of boron carbide and silicon carbide with standard deviations. After modifying the oxygen content by adding carbon, the boron carbide grains reduced from 0.31µm to 0.21µm, and silicon carbide grains reduced from 1.55µm to 1.12µm.

Table 38. Average grain sizes of 10% B_4C- etched SiC with 0.5%C, 1.0%C, 1.5%C

Sample	**Average Grain Size of B_4C (µm) (Std. Dev)**	**Average Grain Size of SiC (µm) (Std. Dev)**
10B_4C-SiC-0.5C	0.31±0.10	1.55±0.20
10B_4C-SiC-1.0C	0.29±0.06	1.37±0.18
10B_4C-SiC-1.5C	0.21±0.05	1.12±0.22

Table 39 shows the average grains size of boron carbide and silicon carbide with standard deviations. After modifying the oxygen content by adding carbon, the boron carbide grains reduced from 0.40µm to 0.29µm, and silicon carbide grains reduced from 1.09µm to 0.80µm.

Table 39. Average grain sizes of 20% B_4C- etched SiC with 0.5%C, 1.0%C, 1.5%C

Sample	**Average Grain Size of B_4C (µm) (Std. Dev)**	**Average Grain Size of SiC (µm) (Std. Dev)**
20B_4C-SiC-0.5C	0.40±0.08	1.09±0.16
20B_4C-SiC-1.0C	0.31±0.05	1.06±0.09
20B_4C-SiC-1.5C	0.29±0.05	0.80±0.10

Table 40 shows the average grains size of boron carbide and silicon carbide with standard deviations. After modifying the oxygen content by adding carbon, the boron carbide grains reduced from 0.38µm to 0.34µm, and silicon carbide grains reduced from 0.72µm to 0.66µm.

Table 40. Average grain sizes of 30% B_4C- etched SiC with 0.5%C, 1.0%C, 1.5%C

Sample	Average Grain Size of B_4C (µm) (Std. Dev)	Average Grain Size of SiC (µm) (Std. Dev)
30B_4C-SiC-0.5C	0.38±0.06	0.72±0.11
30B_4C-SiC-1.0C	0.41±0.07	0.74±0.07
30B_4C-SiC-1.5C	0.34±0.12	0.66±0.07

Table 41 shows the average grains size of boron carbide and silicon carbide with standard deviations. After modifying oxygen content by adding carbon, the boron carbide grains reduced from 0.55µm to 0.45µm, and silicon carbide grains reduced from 0.56µm to 0.41µm.

Table 41. Average grain sizes of 40% B_4C- etched SiC with 0.5%C, 1.0%C, 1.5%C

Sample	Average Grain Size of B_4C (µm) (Std. Dev)	Average Grain Size of SiC (µm) (Std. Dev)
40B_4C-SiC-0.5C	0.55±0.06	0.56±0.10
40B_4C-SiC-1.0C	0.47±0.06	0.49±0.06
40B_4C-SiC-1.5C	0.45±0.05	0.41±0.06

Table 42 shows the average grains size of boron carbide and silicon carbide with standard deviations. After modifying the oxygen content by adding carbon, the boron carbide grains reduced from 0.59µm to 0.47µm, and silicon carbide grains reduced from 0.48µm to 0.43µm.

Table 42. Average grain sizes of 50% B_4C- etched SiC with 0.5%C, 1.0%C, 1.5%C

Sample	**Average Grain Size of B_4C (μm) (Std. Dev)**	**Average Grain Size of SiC (μm) (Std. Dev)**
50B_4C-SiC-0.5C	0.59±0.04	0.48±0.06
50B_4C-SiC-1.0C	0.53±0.05	0.45±0.03
50B_4C-SiC-1.5C	0.47±0.04	0.43±0.08

The scanning electron microscopy (SEM) images of the fracture surfaces, found in Figures 90 through 94, show the fracture surface of samples for different carbon additions. The figures were used to determine the mode of fracture. Even if the samples fracture surfaces were not perfectly smooth, the composites showed a transgranular fracture. Since the silicon carbide and boron carbide thermal expansion coefficients are close in value [126] ($5.68\pm0.11x10^{-6}$ and $6.02\pm0.51x10^{-6}$ respectively), the expected residual stress is small around the particles and not sufficient to cause crack deflection or to introduce intergranular fracture.

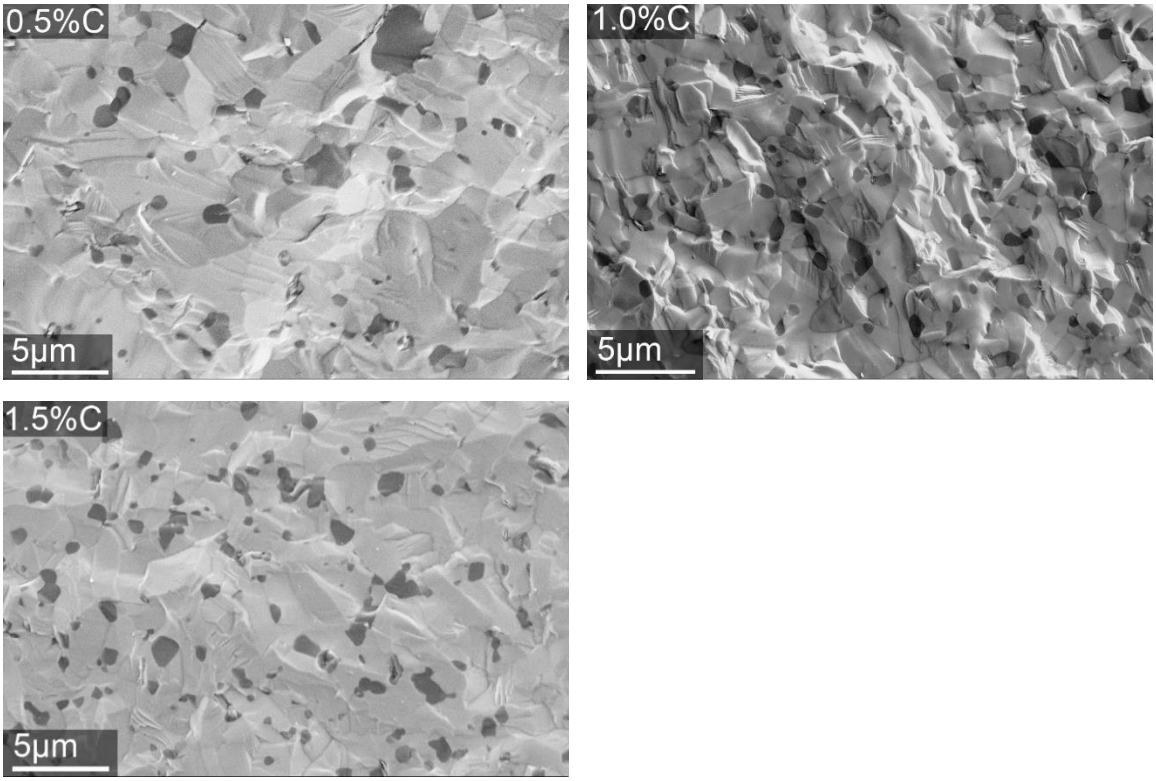

Figure 90. Fracture Surface of 10%B_4C-etched SiC composites

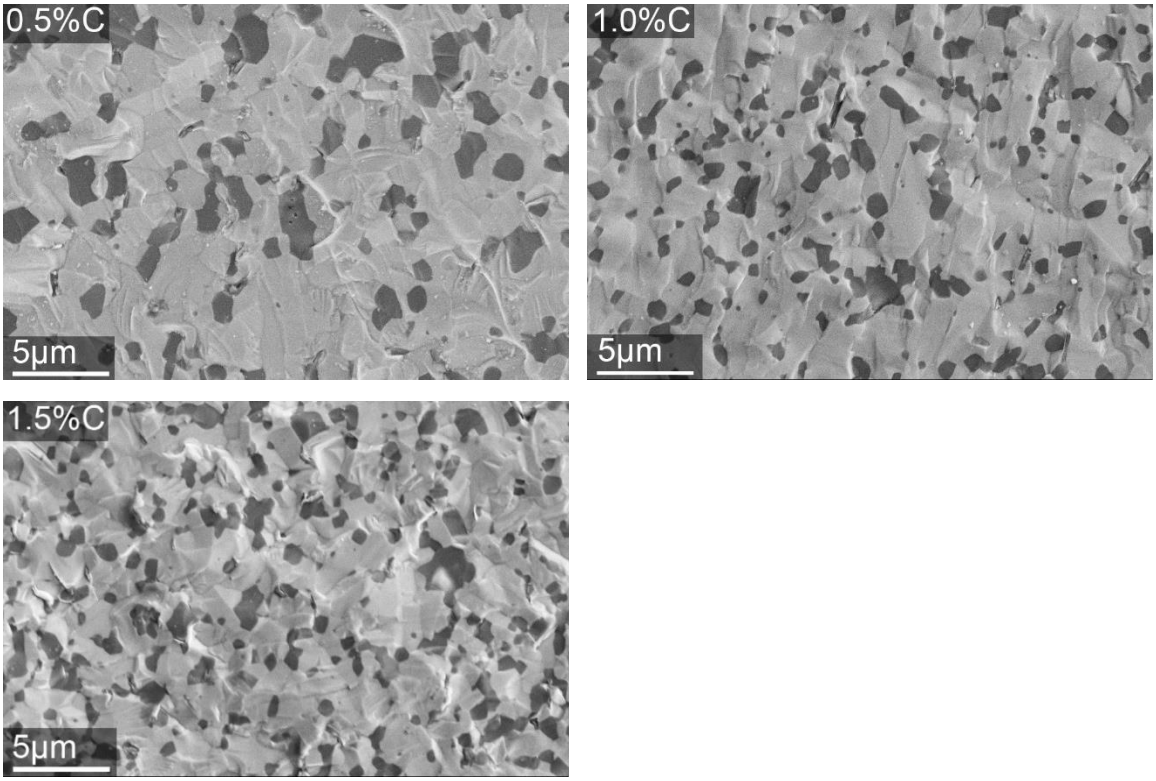

Figure 91. Fracture Surface of 20%B_4C-etched SiC composites

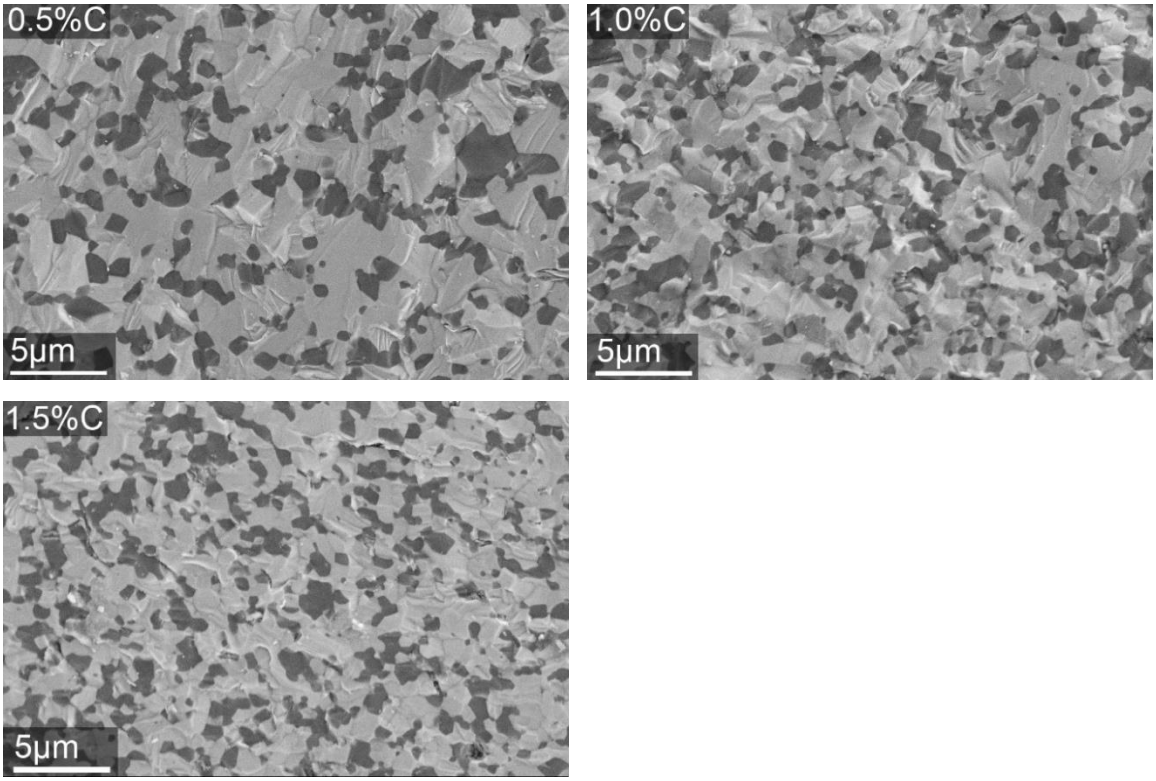

Figure 92. Fracture Surface of 30%B_4C-etched SiC composites

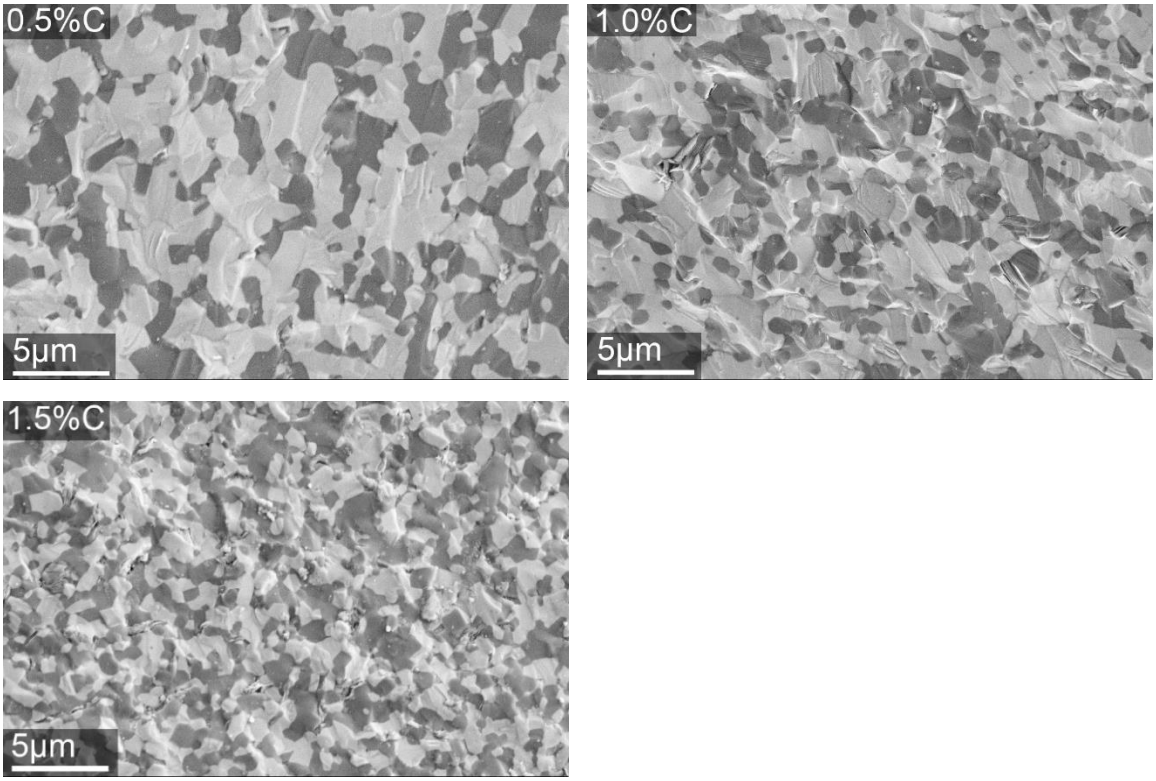

Figure 93. Fracture Surface of 40%B_4C-etched SiC composites

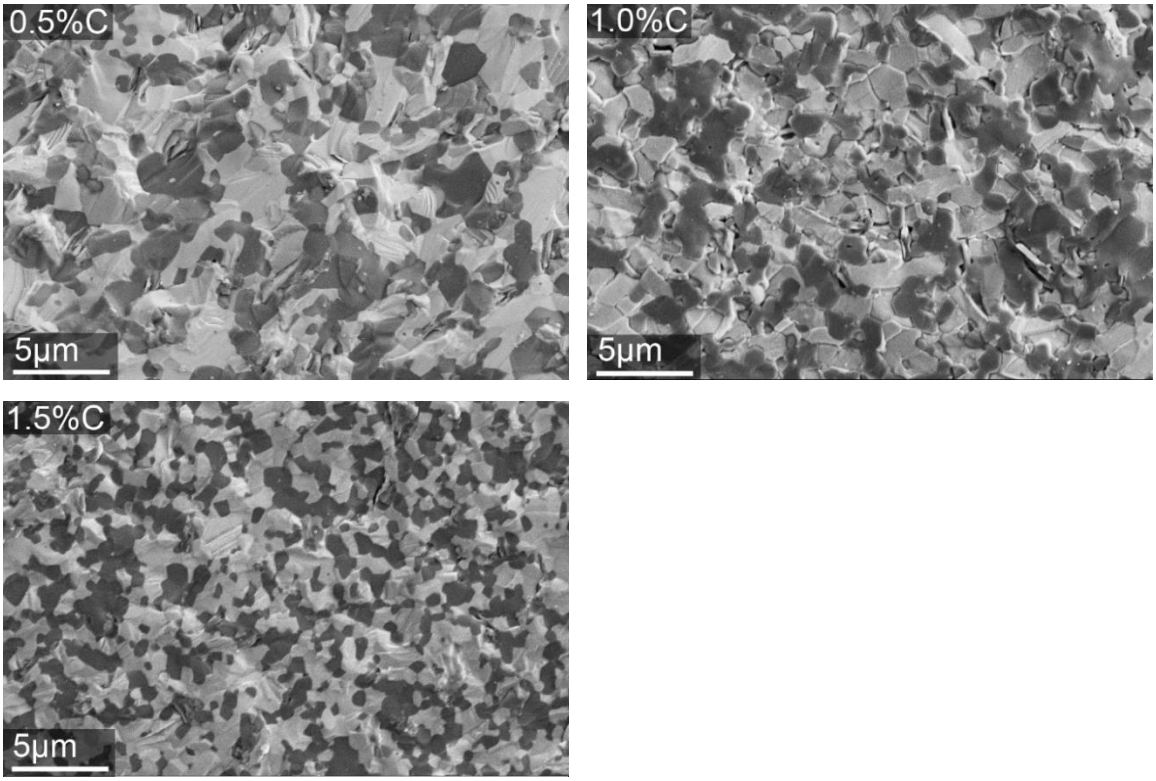

Figure 94. Fracture Surface of 50%B_4C-etched SiC composites

5.3.1.2. Phase Determination by X-Ray Diffraction

Phase identification of the fully sintered composite samples was done using X-ray diffraction analysis as described in section 4.5.2. X-ray diffraction patterns of the samples can be seen in Figure 95-99. Rietveld refinement of the XRD patterns of the samples may be seen in Table 43-47. Silicon carbide, boron carbide and a small amount of carbon were detected as expected in the XRD data. Boron carbide and silicon carbide have many diffraction peaks. Boron carbide's highest intensity peaks were located at ~35.0° 2θ and ~37.8° 2θ. Silicon carbide's highest intensity peaks were located at ~36.0° 2θ and ~60.0° 2θ. When compared with raw starting materials, no unexpected phase occurred during the sintering process. Since all peaks matched with silicon carbide and boron carbide standart

diffraction patterns, it was verified that no solid solubility occurred within the diffractometer measurement error. Also, it showed that impurities were not introduced to the powder during the mixing process. Increasing boron carbide from 10% to 50% increased the boron carbide intensity and decreased the silicon carbide intensity since the percentage of silicon carbide decreased in the composite. In the same composition, increasing the carbon addition from 0.5% to 1.5% did not change the silicon carbide and boron carbide intensities. All samples showed a residual carbon peak but, when the additional carbon was increased, the residual carbon peak located at ~ 26.6° 2θ also increased. For the etched silicon carbide series, silicon carbide powder was etched with hydrofluoric acid before the sintering process. The quantity of carbon needed to remove the oxide layer on powder surface was decreased as the oxygen decreased after etching,thus resulting in increased residual carbon.

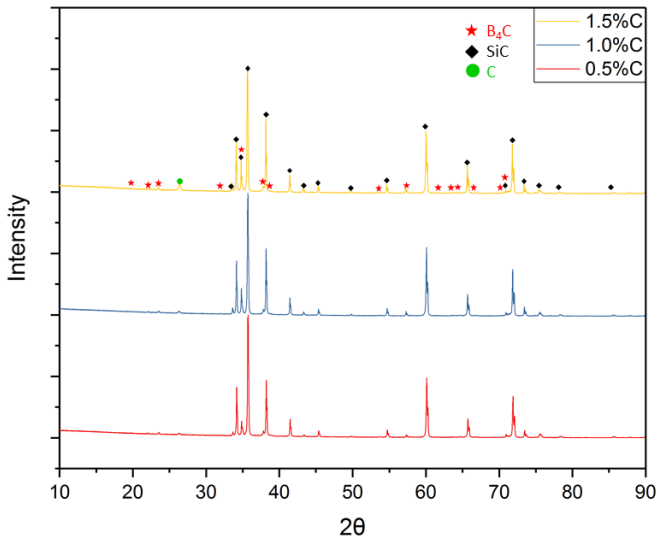

Figure 95. X-ray diffraction patterns of 10% B_4C-etched SiC with 0.5%C, 1.0%C, and 1.5%C

Table 43. Rietveld refinement analyses of 10%B_4C- etched SiC 0.5%C, 1.0%C, and 1.5%C

Nominal (wt. %)			Rietveld Refinement of the XRD Patterns		
B_4C	**SiC**	**C**	**B_4C**	**SiC**	**C**
10	89.5	0.5	10.6±0.1	89.2±0.4	0.2±0.1
10	89.0	1.0	10.4±0.4	89.2±0.3	0.4±0.1
10	88.5	1.5	10.8±1.0	88.3±0.4	0.9±0.2

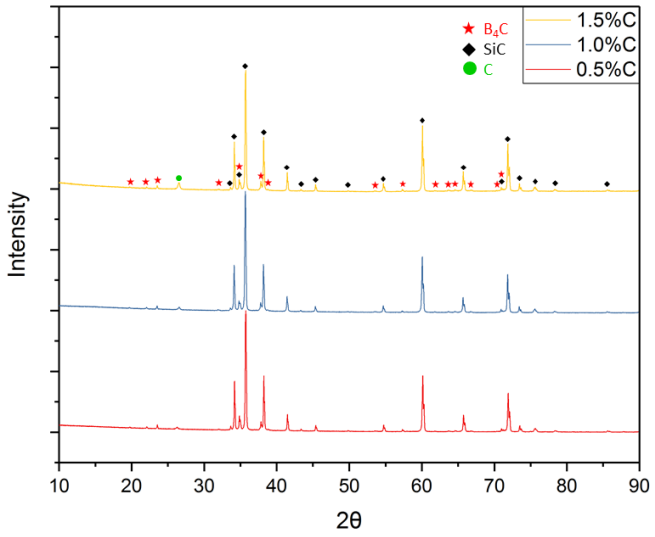

Figure 96. X-ray diffraction patterns of 20% B4C-etched SiC with 0.5%C, 1.0%C, and 1.5%C

Table 44. Rietveld refinement analyses of 20%B_4C- etched SiC 0.5%C, 1.0%C, and 1.5%C

Nominal (wt. %)			Rietveld Refinement of the XRD Patterns		
B_4C	**SiC**	**C**	**B_4C**	**SiC**	**C**
20	79.5	0.5	20.3±0.4	79.3±0.3	0.4±0.1
20	79.0	1.0	20.2±0.4	79.2±0.4	0.6±0.1
20	78.5	1.5	20.4±0.4	78.4±0.4	1.2±0.2

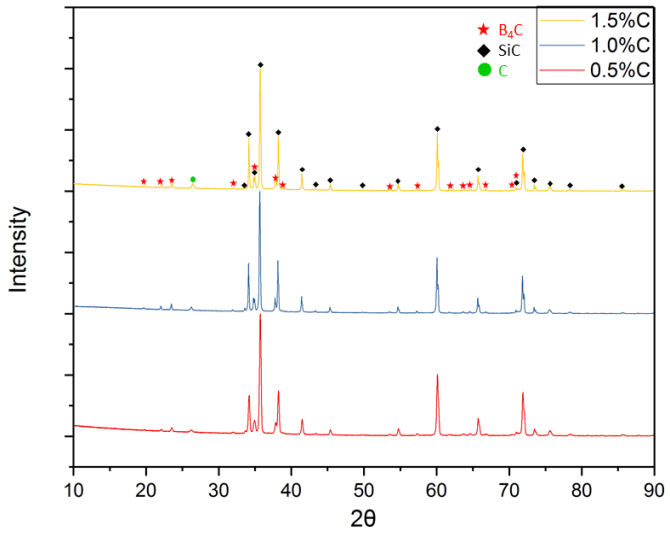

Figure 97. X-ray diffraction patterns of 30% B_4C-etched SiC with 0.5%C, 1.0%C, and 1.5%C

Table 45. Rietveld refinement analyses of 30%B_4C- etched SiC 0.5%C, 1.0%C, and 1.5%C

Nominal (wt. %)			**Rietveld Refinement of the XRD Patterns**		
B_4C	**SiC**	**C**	**B_4C**	**SiC**	**C**
30	69.5	0.5	30.6±0.4	68.9±0.3	0.5±0.1
30	69.0	1.0	30.9±0.4	68.3±0.3	0.8±0.1
30	68.5	1.5	30.5±0.3	68.2±0.2	1.3±0.1

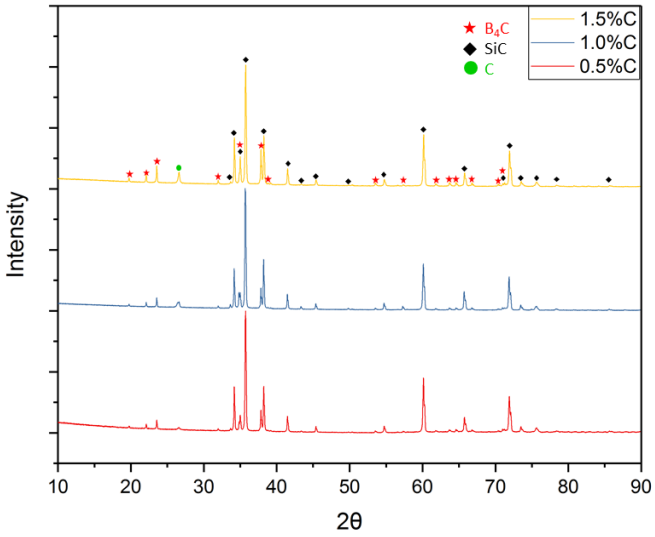

Figure 98. X-ray diffraction patterns of 40% B_4C-etched SiC with 0.5%C, 1.0%C, and 1.5%C

Table 46. Rietveld refinement analyses of 40%B_4C- etched SiC 0.5%C, 1.0%C, and 1.5%C

Nominal (wt. %)			**Rietveld Refinement of the XRD Patterns**		
B_4C	**SiC**	**C**	**B_4C**	**SiC**	**C**
40	59.5	0.5	40.5±0.4	59.0±0.4	0.5±0.1
40	59.0	1.0	40.4±0.5	58.6±0.3	1.0±0.1
40	58.5	1.5	40.7±0.3	57.8±0.3	1.5±0.1

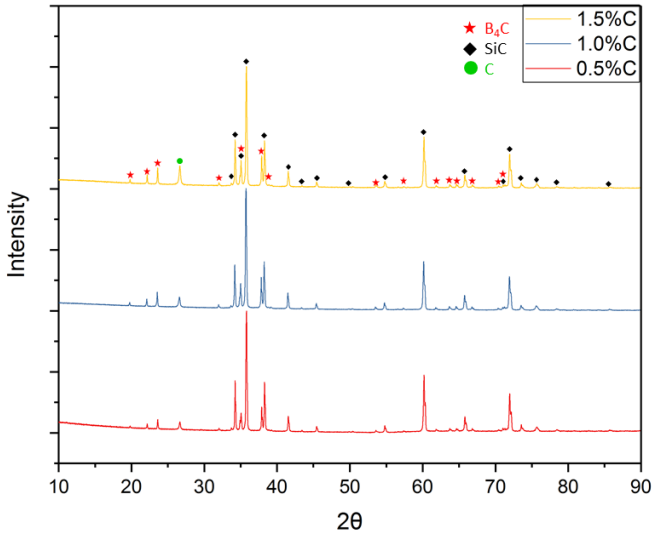

Figure 99. X-ray diffraction patterns of 50% B_4C-etched SiC with 0.5%C, 1.0%C, and 1.5%C

Table 47. Rietveld refinement analyses of 50%B_4C- etched SiC 0.5%C, 1.0%C, and 1.5%C

Nominal (wt. %)			**Rietveld Refinement of the XRD Patterns**		
B_4C	**SiC**	**C**	**B_4C**	**SiC**	**C**
50	49.5	0.5	50.6±0.4	48.7±0.2	0.7±0.1
50	49.0	1.0	50.7±0.3	48.0±0.2	1.3±0.2
50	48.5	1.5	50.6±0.4	47.6±0.2	1.8±0.1

5.3.1.3. Mechanical Properties

5.3.1.3.1. Ultrasound Analysis

The samples' elastic properties were measured using ultrasound analysis. c_L (longitudinal sound speed), c_S (shear sound speed), Poisson's ratio, Young's modulus (E), shear modulus (G), and bulk modulus (K) values were calculated from equations 22, 23, 24, 25, 26, and 27 respectively as described in section 4.5.3. The density values of the SPS

samples were determined using the Archimedes method as described in section 4.5.1. The theoretical density of samples was determined from the rule of mixtures using the concentra

The oxygen was managed with two methods, acid etching and carbon addition. However, carbon also played a role as well as the oxygen since the oxygen content was modified by adding varying amounts of carbon resulted in surplus carbon. Residual carbon could affect mechanical properties like porosity and decrease the mechanical properties of composites.

Looking at the density and elastic properties of all the samples, 0.5% added carbon was enough to remove oxygen since the silicon carbide was acid etched and thus less carbon was needed to remove oxygen. When the addition of carbon was more than 0.5% carbon, it remained in the structure as residual carbon. Since carbon density and elastic properties are lower than silicon carbide and boron carbide, surplus carbon affected those properties and reduced the lastic properties values.

The results of 10% B_4C- etched SiC composites can be seen in Table 48 and Figure 100. Each value represents the mean of five analyses. The relative density was 99.99% samples with 0.5%, 1.0%, and 1.5% carbon. The Poisson's ratio values for 0.5%C, 1.0%C, and 1.5%C were 0.169, 0.168, and 0.169 respectively. The Young's modulus decreased from 429 GPa to 415 GPa. The shear modulus changed from 184 GPa to 177 GPa, and the bulk modulus was reduced from 216 GPa to 209 GPa.

Table 48. Elastic properties of 10%B_4C- etched SiC composites

Sample	**c_L (m/s)**	**c_S (m/s)**	**Poisson's Ratio**	**Bulk Density (g/cm^3)**	**Porosity (%)**	**E (GPa)**	**G (GPa)**	**K (GPa)**
$10B_4C$-SiC-0.5C	12165	7676	0.169±0.003	3.110±0.001	<0.01	429±9	184±4	216±4
$10B_4C$-SiC-1.0C	12091	7636	0.168±0.003	3.110±0.001	<0.01	426±9	182±4	214±4
$10B_4C$-SiC-1.5C	11946	7536	0.169±0.003	3.100±0.002	<0.01	415±8	177±4	209±4

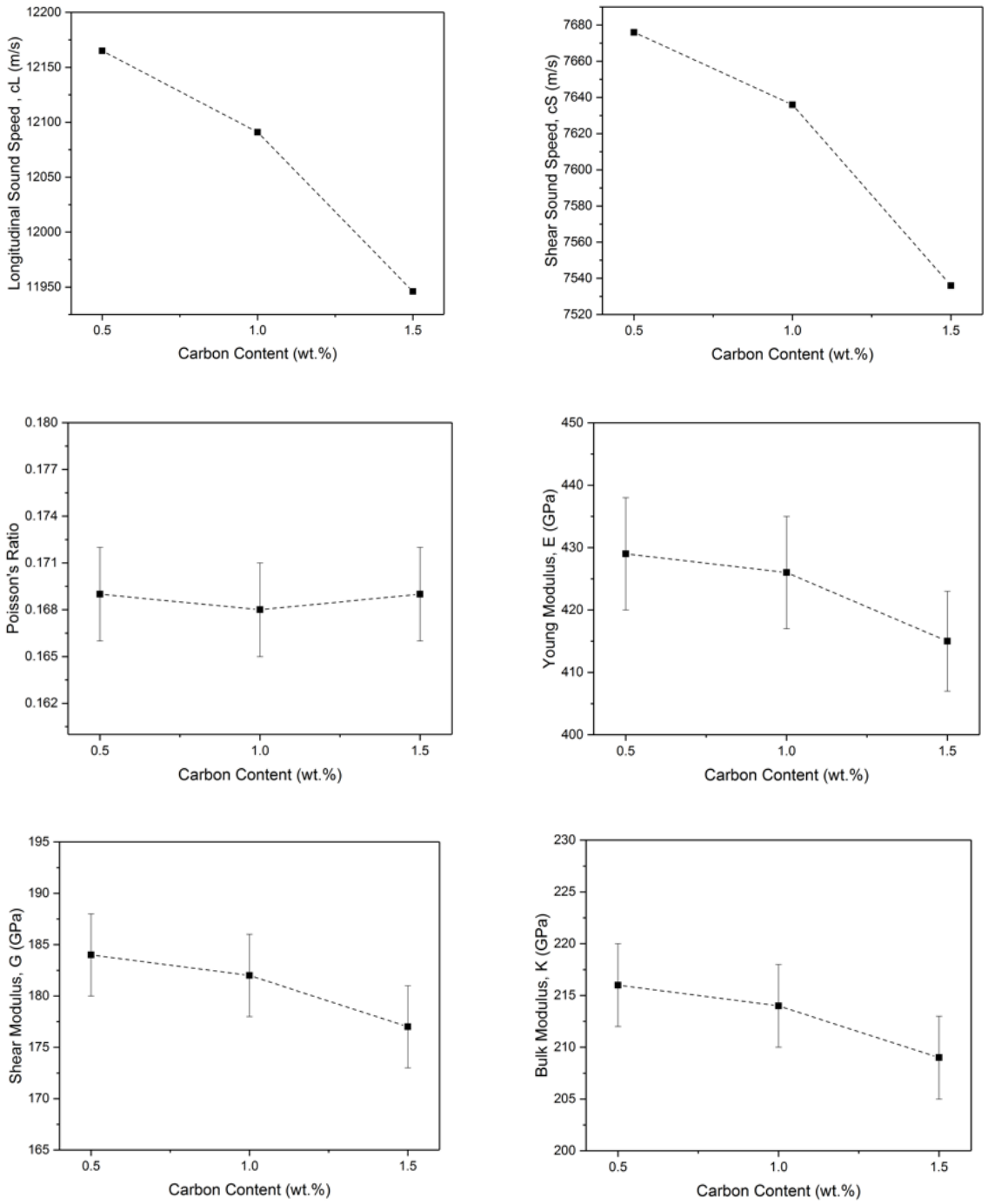

Figure 100. Effect of carbon content on elastic properties of 10%B_4C- etched SiC composites

The results of 20% B_4C- etched SiC composites can be seen in Table 49 and Figure 101. Each value represents the mean of five analyses. The relative density decreased from ≥99.99% to 99.67% while the relative density of the samples with 0.5% carbon was ≥99.99. For the sample with 1.5% carbon, the relative density was 99.67%. The Poisson's ratio values for 0.5%C, 1.0%C, and 1.5%C were 0.169, 0.168, and 0.168 respectively. The Young's modulus decreased from 424 GPa to 409 GPa. The shear modulus changed from 181 GPa to 175 GPa, and the bulk modulus was reduced from 213 GPa to 205 GPa.

Table 49. Elastic properties of 20%B_4C- etched SiC composites

Sample	**c_L (m/s)**	**c_S (m/s)**	**Poisson's Ratio**	**Bulk Density (g/cm^3)**	**Porosity (%)**	**E (GPa)**	**G (GPa)**	**K (GPa)**
20B_4C-SiC-0.5C	12189	7690	0.169±0.003	3.030±0.001	<0.01	424±9	181±4	213±4
20B_4C-SiC-1.0C	12166	7688	0.168±0.003	3.030±0.001	<0.01	421±8	180±4	211±4
20B_4C-SiC-1.5C	12016	7594	0.168±0.003	3.000±0.002	0.33	409±8	175±4	205±4

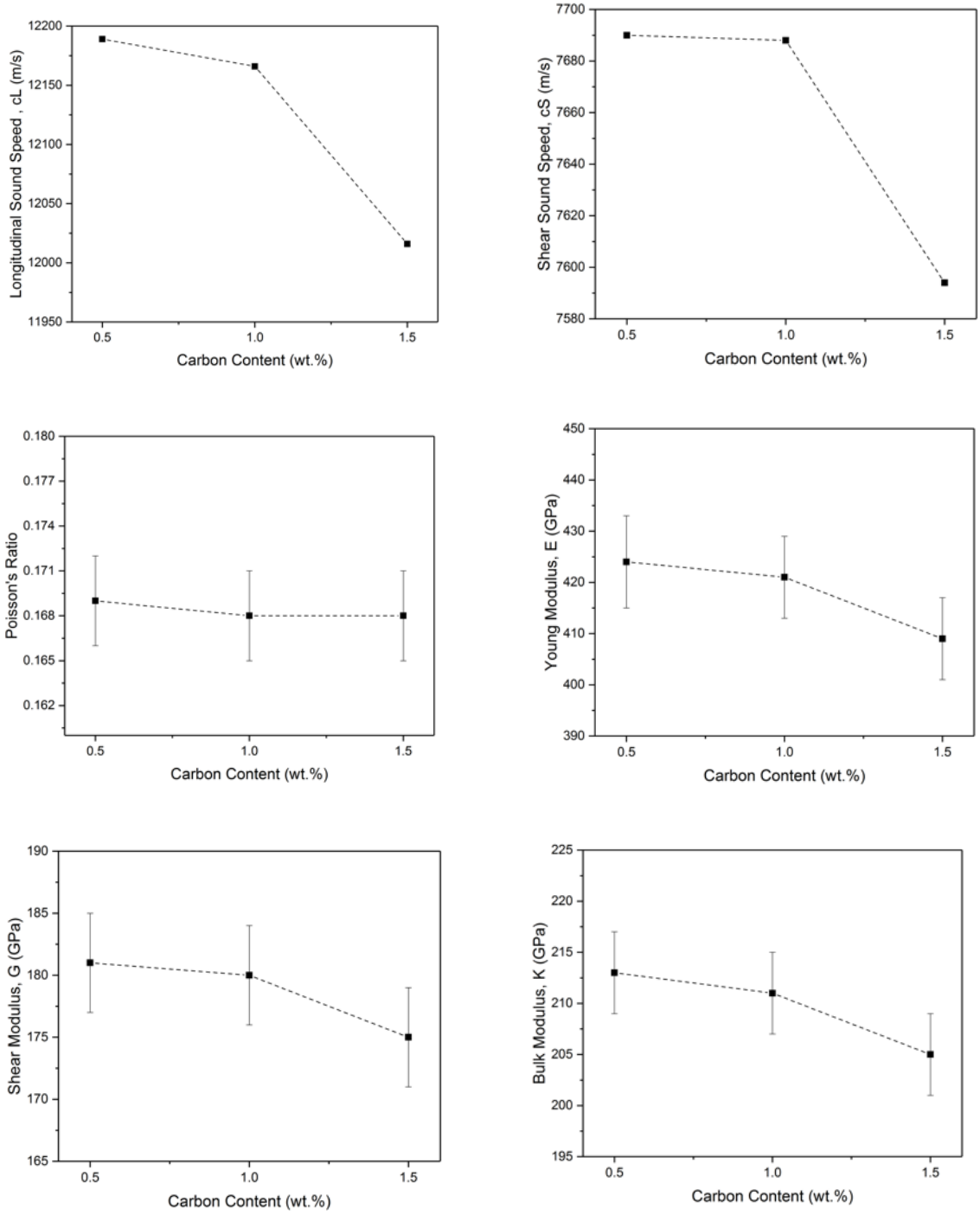

Figure 101. Effect of carbon content on elastic properties of 20%B_4C- etched SiC composites

The results of 30% B_4C- etched SiC composites can be seen in Table 50 and Figure 102. Each value represents the mean of five analyses. The relative density decreased from ≥99.99% to 98.98% while the relative density of the samples with 0.5% carbon was ≥99.99. For the sample with 1.5% carbon, the relative density was 98.98%. The Poisson's ratio values for 0.5%C, 1.0%C, and 1.5%C were 0.168, 0.163, and 0.162 respectively. The Young's modulus decreased from 408 GPa to 402 GPa. The shear modulus changed from 175 GPa to 173 GPa, and the bulk modulus was reduced from 205 GPa to 198 GPa.

Table 50. Elastic properties of 30%B_4C- etched SiC composites

Sample	**c_L (m/s)**	**c_S (m/s)**	**Poisson's Ratio**	**Bulk Density (g/cm^3)**	**Porosity (%)**	**E (GPa)**	**G (GPa)**	**K (GPa)**
30B_4C-SiC-0.5C	12167	7684	0.168±0.003	2.950±0.001	<0.01	408±8	175±4	205±4
30B_4C-SiC-1.0C	12092	7670	0.163±0.003	2.940±0.001	<0.01	410±8	176±4	203±4
30B_4C-SiC-1.5C	12050	7651	0.162±0.003	2.910±0.001	1.02	402±8	173±4	198±4

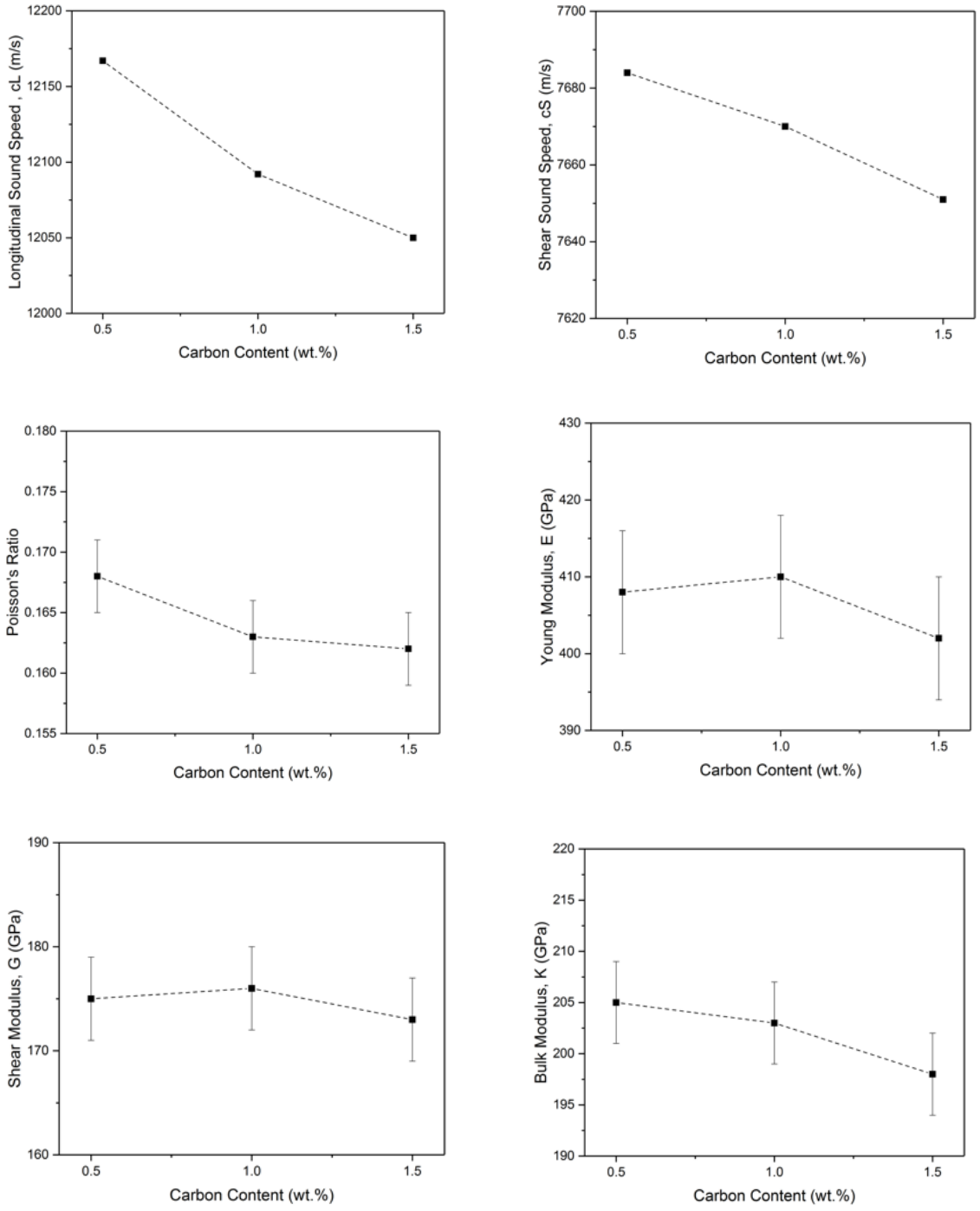

Figure 102. Effect of carbon content on elastic properties of 30%B_4C- etched SiC composites

The results of 40% B_4C- etched SiC composites can be seen in Table 51 and Figure 103. Each value represents the mean of five analyses. The relative density decreased from ≥99.99% to 98.65%, while the relative density of the samples with 0.5% carbon was ≥99.99. For the sample with 1.5% carbon, the relative density was 98.65%. The Poisson's ratio values for 0.5%C, 1.0%C, and 1.5%C were 0.167, 0.164, and 0.163 respectively. The Young's modulus decreased from 396 GPa to 392 GPa. The shear modulus changed from 170 GPa to 169 GPa, and the bulk modulus was reduced from 198 GPa to 194 GPa.

Table 51. Elastic properties of 40%B_4C- etched SiC composites

Sample	**c_L (m/s)**	**c_S (m/s)**	**Poisson's Ratio**	**Bulk Density (g/cm^3)**	**Porosity (%)**	**E (GPa)**	**G (GPa)**	**K (GPa)**
40B_4C-SiC-0.5C	12124	7667	0.167±0.003	2.880±0.001	<0.01	396±8	170±3	198±4
40B_4C-SiC-1.0C	12033	7631	0.164±0.003	2.870±0.001	<0.01	395±8	170±3	196±4
40B_4C-SiC-1.5C	12051	7649	0.163±0.003	2.850±0.002	0.35	392±8	169±3	194±4

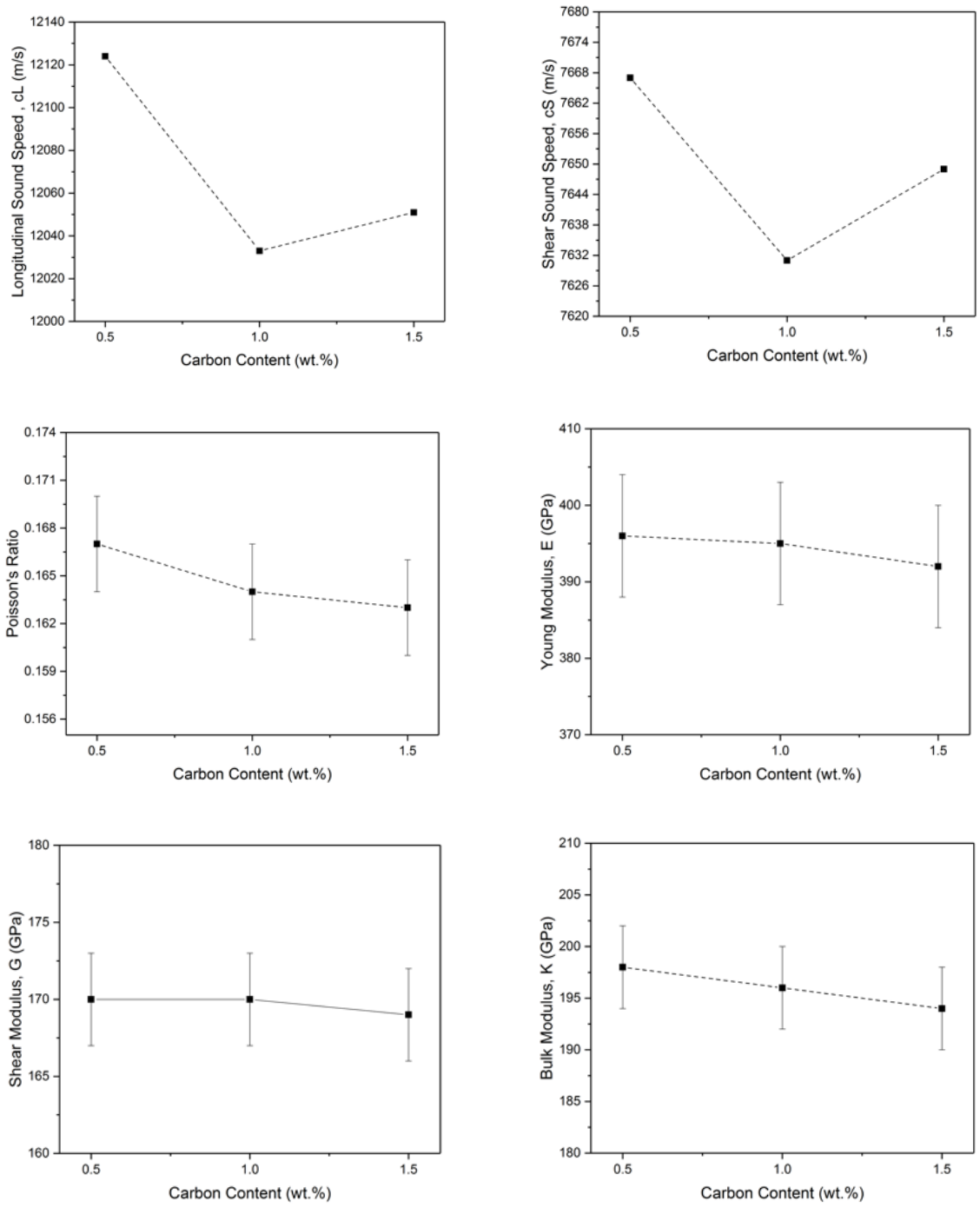

Figure 103. Effect of carbon content on elastic properties of 40%B_4C- etched SiC composites

The results of 50% B_4C- etched SiC composites can be seen in Table 52 and Figure 104. Each value represents the mean of five analyses. The relative density was ≥99.99% samples with the 0.5%, 1.0%, and 1.5% carbon. The Poisson's ratio values for 0.5%C, 1.0%C, and 1.5%C were 0.164, 0.162, and 0.162 respectively. The Young's modulus decreased from 390 GPa to 388 GPa. The shear modulus changed from 168 GPa to 167 GPa, and the bulk modulus was reduced from 194 GPa to 192 GPa.

Table 52. Elastic properties of 50%B_4C- etched SiC composites

Sample	**c_L (m/s)**	**c_S (m/s)**	**Poisson's Ratio**	**Bulk Density (g/cm^3)**	**Porosity (%)**	**E (GPa)**	**G (GPa)**	**K (GPa)**
50B_4C-SiC-0.5C	12195	7732	0.164±0.003	2.800±0.002	<0.01	390±8	168±3	194±4
50B_4C-SiC-1.0C	12156	7719	0.162±0.003	2.800±0.001	<0.01	392±8	168±3	193±4
50B_4C-SiC-1.5C	12125	7698	0.162±0.003	2.780±0.003	<0.01	388±8	167±3	192±4

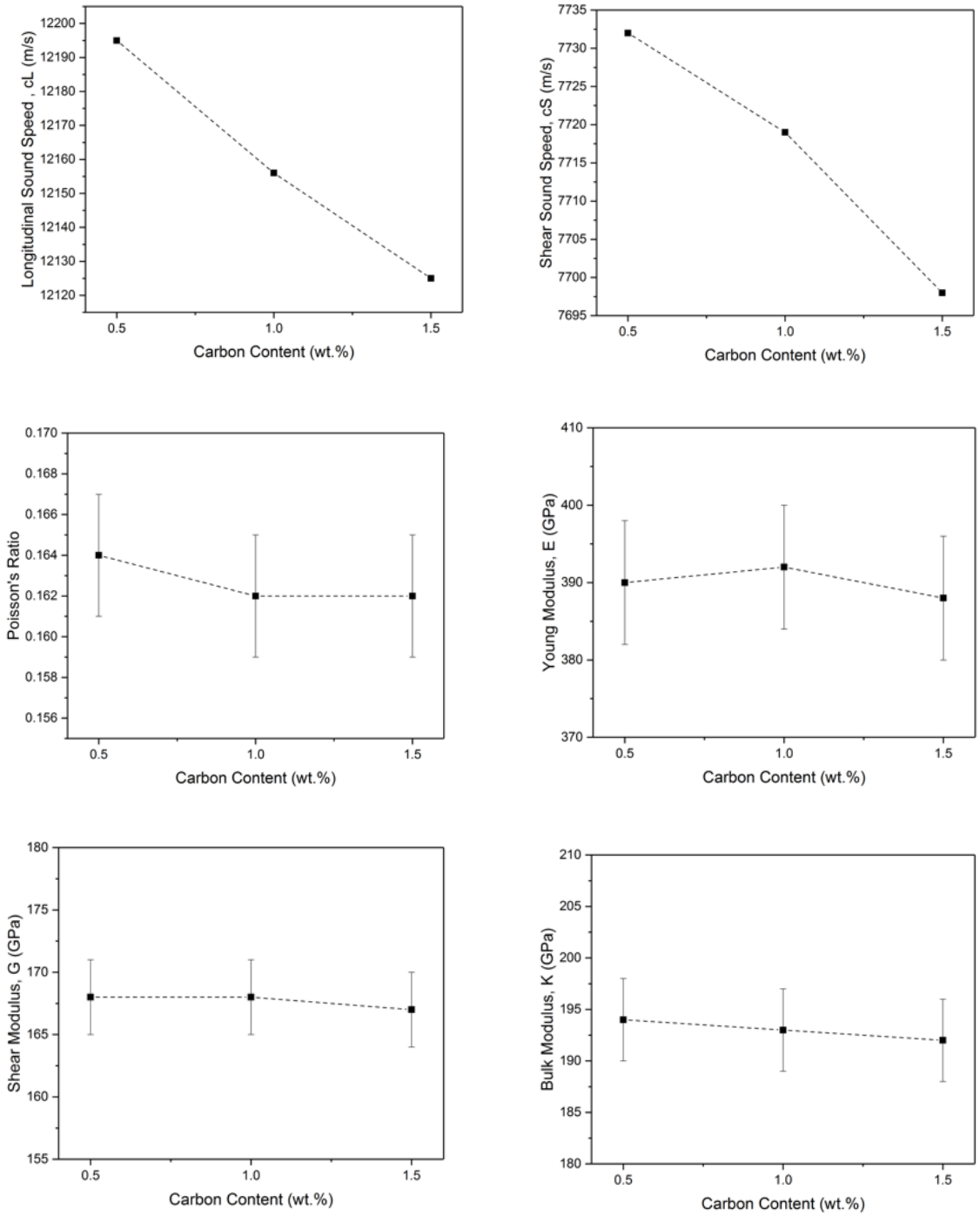

Figure 104. Effect of carbon content on elastic properties of 50%B_4C- etched SiC composites

5.3.1.3.2. Vickers Microhardness and Indentation Fracture Toughness

The samples' hardness values were measured using Vickers diamond intentation at 1 kgf for a 10 s dwell time, and the fracture toughness values were calculated by measuring Vickers indenter crack length, as described in section 4.5.5. using equations 28 and 29.

For all boron carbide content, the 0.5% carbon addition series obtained higher hardness values than the 1.0% and 1.5% carbon series. The 0.5% carbon addition was enough to remove excess oxygen in the powders, so the 1.0% and 1.5% carbon had surplus carbon in the samples, and the excess carbon cause decreased the density. Since density affects the hardness, decreasing the density decreased the hardness [123]. In addition to this, the presence of carbon is similar to porosity being present and will lead to similar affects on hardness and elastic properties. Boron carbide has a higher hardness than silicon carbide, meaning that increasing the boron carbide content in the matrix of the composite increased the hardness of samples. The highest hardness value was 30.55 GPa reached at a composition of 50%B_4C-0.5%C-SiC.

Commercially available widely used PAD-B_4C hardness was found ~25.82 GPa for 1kgf load [68]. For the composites, even the 10%B_4C-SiC sample reached 28.50 GPa hardness. By making composites, the hardness values can be enhanced.

Fracture toughness has an inverse relation to hardness. Even though both silicon carbide and boron carbide are hard ceramics and have a low fracture toughness, since boron carbide is harder than silicon carbide, the boron carbide fracture toughness values are lower than silicon carbide. So increasing the boron carbide content in the composites decreased

the fracture toughness of samples.The best indentation fracture toughness value was 2.89 MPa.$m^{1/2}$ and gained at a composition of 10%B_4C-1.5%C-SiC. The 1.5% C series had some pores or regions of carbon my contribute to obtain slightly higher fracture toughness values as mentioned in the literature [66]. Also, as mentioned above, the thermal expansion coefficients of silicon carbide and boron carbide are similar, so this difference cannot affect the fracture mode, but it can influence fracture toughness value.

The Vickers hardness and indentation fracture toughness results can be seen in Fifures 105 through 109, and Tables 53 through 57.

Table 53. Hardness and fracture toughness of 10%B_4C-etched SiC composites

Sample	**Hardness (GPa)**	**Fracture Toughness (MPa.$m^{1/2}$)**
10B_4C-SiC-0.5C	28.50±1.39	2.85±0.20
10B_4C-SiC-1.0C	27.87±1.14	2.86±0.17
10B_4C-SiC-1.5C	26.14±0.96	2.89±0.39

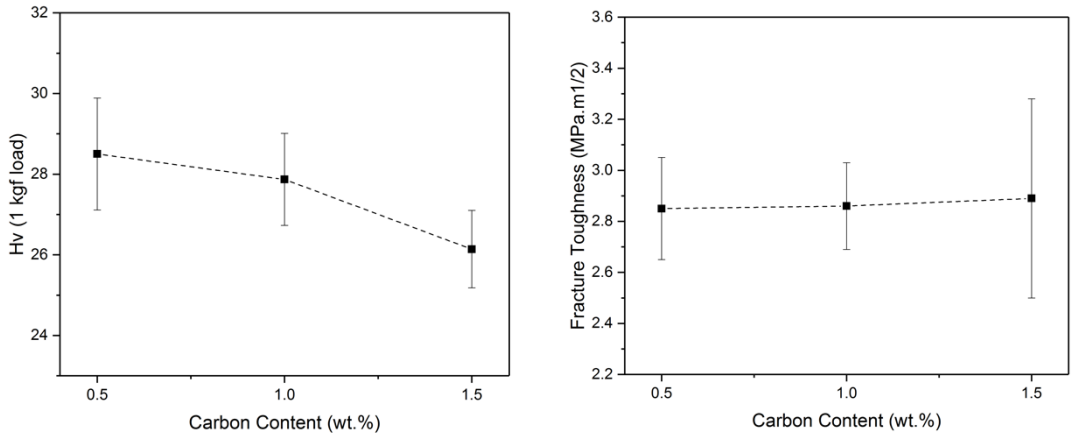

Figure 105. Effect of carbon content on hardness and fracture toughness of 10%B_4C-etched SiC composites

Table 54. Hardness and fracture toughness of 20%B_4C-etched SiC composites

Sample	Hardness (GPa)	Fracture Toughness ($MPa.m^{1/2}$)
20B_4C-SiC-0.5C	28.79±1.38	2.79±0.24
20B_4C-SiC-1.0C	28.08±1.40	2.79±0.25
20B_4C-SiC-1.5C	28.79±0.81	2.79±0.15

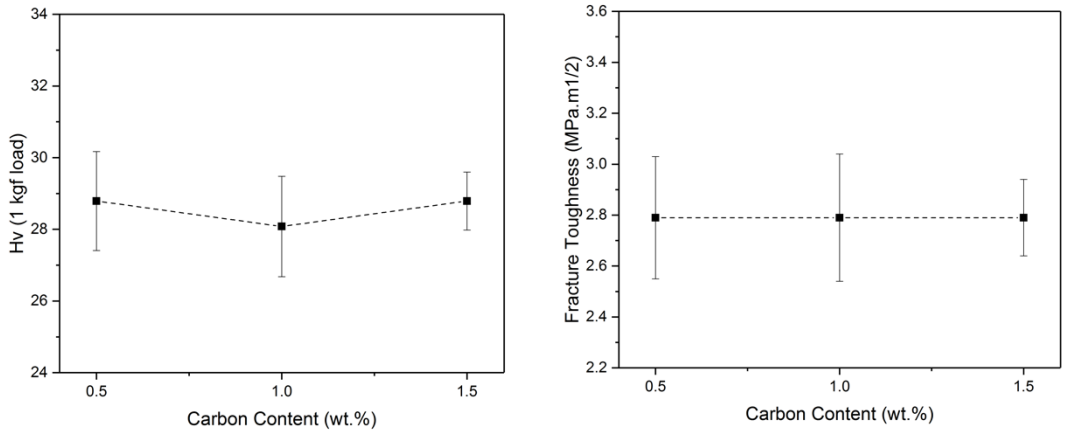

Figure 106. Effect of carbon content on hardness and fracture toughness of 20%B_4C-etched SiC composites

Table 55. Hardness and fracture toughness of 30%B_4C-etched SiC composites

Sample	Hardness (GPa)	Fracture Toughness ($MPa.m^{1/2}$)
30B_4C-SiC-0.5C	28.58±1.51	2.74±0.18
30B_4C-SiC-1.0C	29.95±0.64	2.72±0.19
30B_4C-SiC-1.5C	29.51±0.62	2.74±0.22

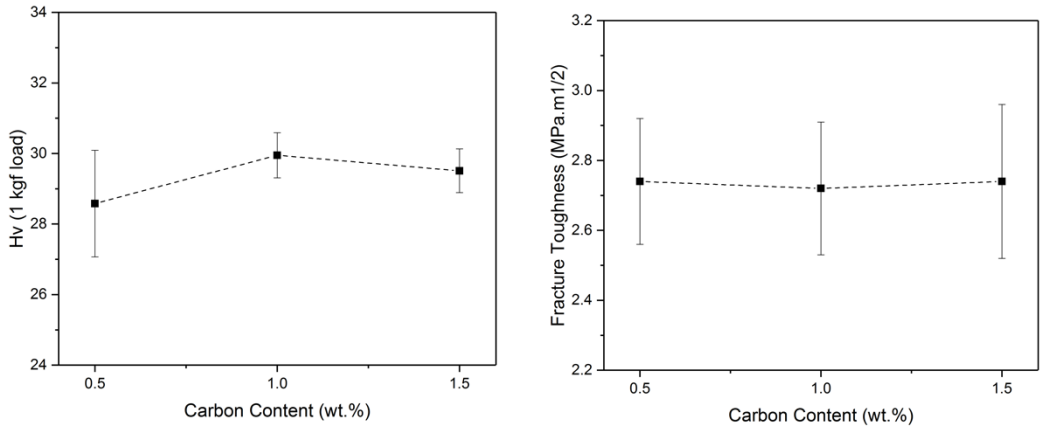

Figure 107. Effect of carbon content on hardness and fracture toughness of 30%B_4C-etched SiC composites

Table 56. Hardness and fracture toughness of 40%B_4C-etched SiC composites

Sample	Hardness (GPa)	Fracture Toughness ($MPa.m^{1/2}$)
40B_4C-SiC-0.5C	29.98±1.18	2.64±0.09
40B_4C-SiC-1.0C	29.98±1.20	2.64±0.13
40B_4C-SiC-1.5C	29.99±1.67	2.65±0.10

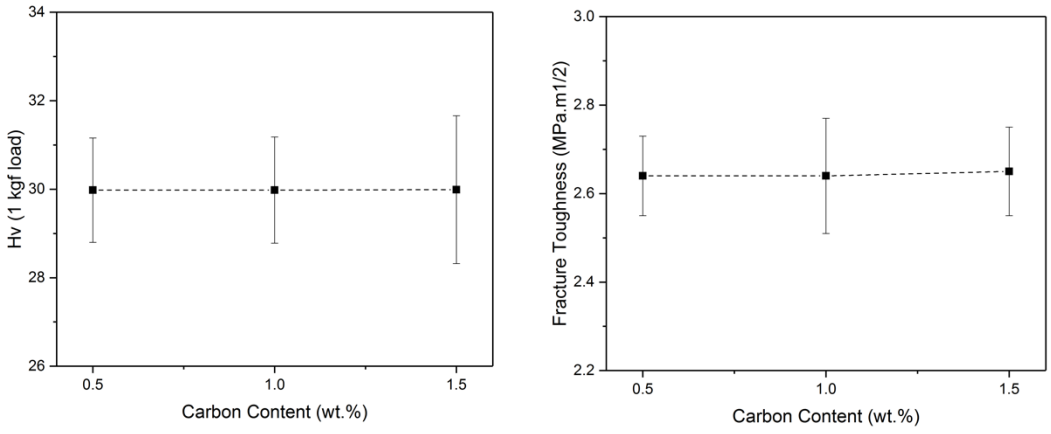

Figure 108. Effect of carbon content on hardness and fracture toughness of 40%B_4C-etched SiC composites

Table 57. Hardness and fracture toughness of 50%B_4C-etched SiC composites

Sample	Hardness (GPa)	Fracture Toughness ($MPa.m^{1/2}$)
50B_4C-SiC-0.5C	30.55±1.06	2.63±0.14
50B_4C-SiC-1.0C	30.46±0.66	2.63±0.13
50B_4C-SiC-1.5C	30.34±0.93	2.63±0.16

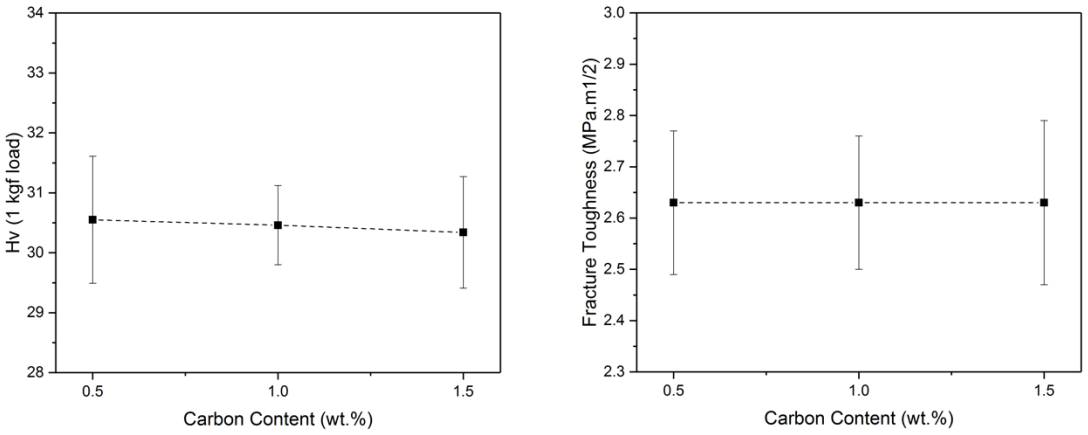

Figure 109. Effect of carbon content on hardness and fracture toughness of 50%B_4C-etched SiC composites

5.3.1.3.3. Berkovich Hardness and Reduced Modulus

The Berkovich hardness and reduced modulus were measured as described in section 4.5.6. Unlike microhardness, nanoindentation had the advantage of smaller indents to be analyzed since it had low load ability. These smaller indents could determine the effect of homogeneity in the material from the calculated nanoindentation hardness and reduced modulus.

For this test, twenty indents were made for each load at 100mN, 300mN, and 500mN to polished sample surfaces. The MicroMaterials software was used to calculate the hardness value of samples using the indenter load and the depth of penetration. Each

result represented the average of twenty indents (abnormal shaped indents were not included in the analysis), and these results are shown in Tables 58 through 62. Load versus hardness and reduced modulus curves can be seen in Figures 110 through 114. The plots showed that both hardness and reduced modulus values decreased with increasing applied load. Even if the values were close to each other, a slight decrease can still be seen. For each series, 0.5% carbon showed higher results for each series because the 1.0% and 1.5% carbon series had residual carbon included. Since the etched SiC series samples' starting powder had a lower oxygen content, the requirement of additional carbon content decreased. So, the addition of carbon was more than enough to remove oxide layer and cause excess carbon.

Table 58. Berkovich hardness and reduced modulus of 10%B_4C-etched SiC composites

100mN (10g)	**H (GPa)**	**Std. Dev.**	**Reduced Modulus (GPa)**	**Std. Dev.**
10B_4C-SiC-0.5C	32.46	1.82	318.78	08.18
10B_4C-SiC-1.0C	31.61	1.57	311.22	10.49
10B_4C-SiC-1.5C	32.71	1.61	308.46	11.29
300mN (30g)	**H (GPa)**	**Std. Dev.**	**Reduced Modulus (GPa)**	**Std. Dev.**
10B_4C-SiC-0.5C	31.87	0.94	318.87	10.54
10B_4C-SiC-1.0C	30.36	0.51	311.58	08.39
10B_4C-SiC-1.5C	30.39	1.64	297.51	08.39
500mN (50g)	**H (GPa)**	**Std. Dev.**	**Reduced Modulus (GPa)**	**Std. Dev.**
10B_4C-SiC-0.5C	31.32	0.86	308.22	06.19
10B_4C-SiC-1.0C	29.92	0.57	307.42	07.38
10B_4C-SiC-1.5C	29.19	0.48	292.70	10.49

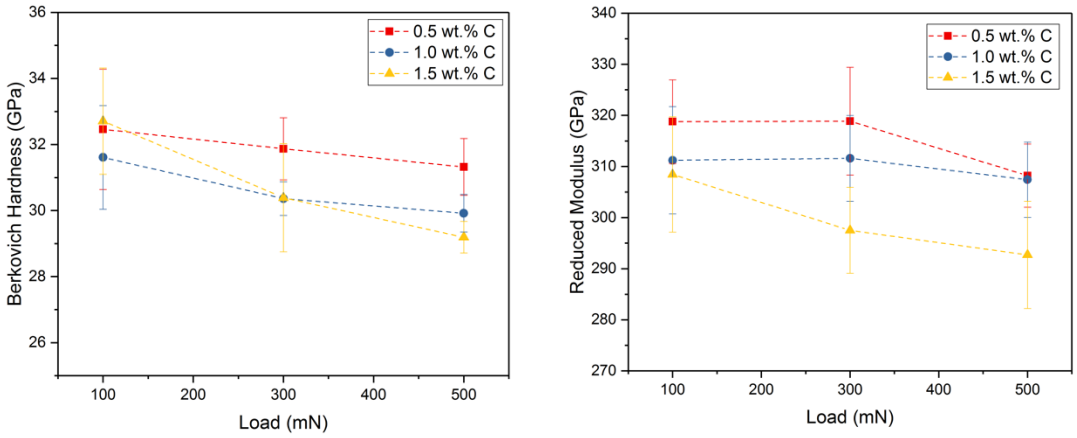

Figure 110. Load- hardness and load- reduced modulus curves for 10%B_4C-etched SiC composites

Table 59. Berkovich hardness and reduced modulus of 20%B_4C-etched SiC composites

100mN (10g)	**H (GPa)**	**Std. Dev.**	**Reduced Modulus (GPa)**	**Std. Dev.**
20B_4C-SiC-0.5C	34.77	0.97	338.99	10.05
20B_4C-SiC-1.0C	32.98	0.64	320.94	07.08
20B_4C-SiC-1.5C	34.48	0.97	305.29	10.15
300mN (30g)	**H (GPa)**	**Std. Dev.**	**Reduced Modulus (GPa)**	**Std. Dev.**
20B_4C-SiC-0.5C	34.41	0.50	336.03	08.08
20B_4C-SiC-1.0C	33.60	0.20	319.75	06.28
20B_4C-SiC-1.5C	34.38	0.88	292.92	08.58
500mN (50g)	**H (GPa)**	**Std. Dev.**	**Reduced Modulus (GPa)**	**Std. Dev.**
20B_4C-SiC-0.5C	32.98	0.97	328.91	09.69
20B_4C-SiC-1.0C	32.90	1.16	310.95	10.43
20B_4C-SiC-1.5C	32.61	0.84	276.31	09.65

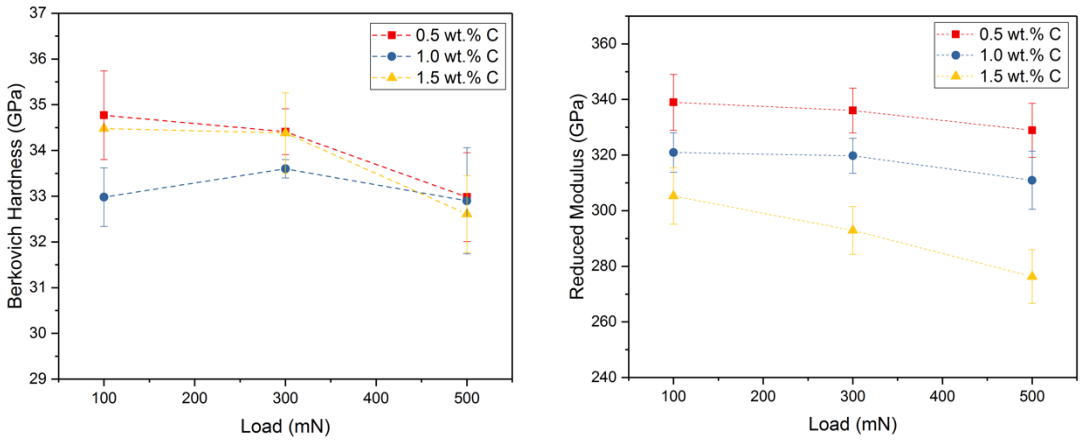

Figure 111. Load- hardness and load- reduced modulus curves for 20%B_4C-etched SiC composites

Table 60. Berkovich hardness and reduced modulus of 30%B_4C-etched SiC composites

100mN (10g)	**H (GPa)**	**Std. Dev.**	**Reduced Modulus (GPa)**	**Std. Dev.**
30B_4C-SiC-0.5C	36.81	1.93	324.06	10.60
30B_4C-SiC-1.0C	35.34	1.14	315.07	10.24
30B_4C-SiC-1.5C	34.79	1.21	313.74	10.29
300mN (30g)	**H (GPa)**	**Std. Dev.**	**Reduced Modulus (GPa)**	**Std. Dev.**
30B_4C-SiC-0.5C	35.64	0.82	323.38	10.94
30B_4C-SiC-1.0C	34.97	1.24	302.04	08.49
30B_4C-SiC-1.5C	33.96	1.95	300.77	10.20
500mN (50g)	**H (GPa)**	**Std. Dev.**	**Reduced Modulus (GPa)**	**Std. Dev.**
30B_4C-SiC-0.5C	33.93	1.02	317.76	10.57
30B_4C-SiC-1.0C	33.92	0.83	291.55	09.25
30B_4C-SiC-1.5C	33.82	1.37	289.39	10.42

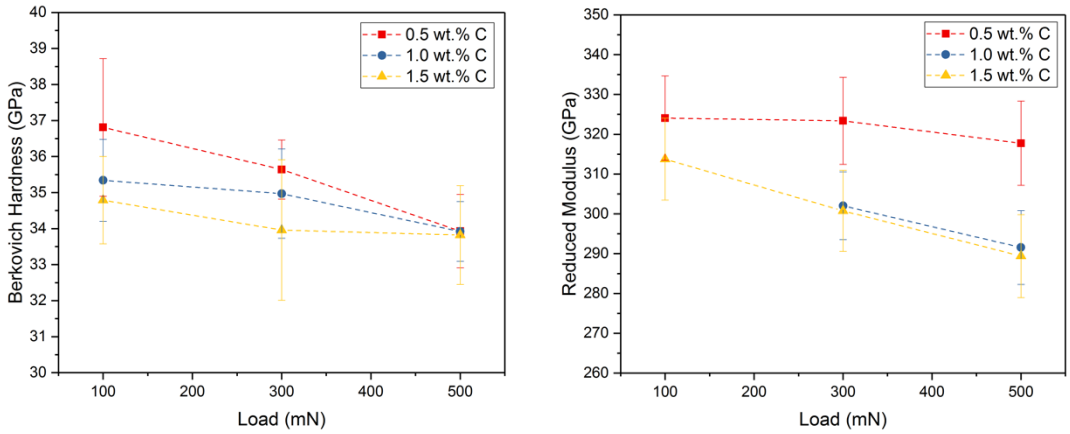

Figure 112. Load- hardness and load- reduced modulus curves for 30%B_4C-etched SiC composites

Table 61. Berkovich hardness and reduced modulus of 40%B_4C-etched SiC composites

100mN (10g)	**H (GPa)**	**Std. Dev.**	**Reduced Modulus (GPa)**	**Std. Dev.**
40B_4C-SiC-0.5C	35.48	1.96	337.90	10.79
40B_4C-SiC-1.0C	35.67	1.50	329.88	10.44
40B_4C-SiC-1.5C	32.87	1.23	330.61	10.83
300mN (30g)	**H (GPa)**	**Std. Dev.**	**Reduced Modulus (GPa)**	**Std. Dev.**
40B_4C-SiC-0.5C	35.71	1.42	336.18	10.37
40B_4C-SiC-1.0C	35.83	1.59	334.61	04.85
40B_4C-SiC-1.5C	34.78	1.00	317.82	10.88
500mN (50g)	**H (GPa)**	**Std. Dev.**	**Reduced Modulus (GPa)**	**Std. Dev.**
40B_4C-SiC-0.5C	34.84	0.89	335.53	08.28
40B_4C-SiC-1.0C	34.67	0.78	330.27	10.99
40B_4C-SiC-1.5C	34.65	1.33	312.30	09.39

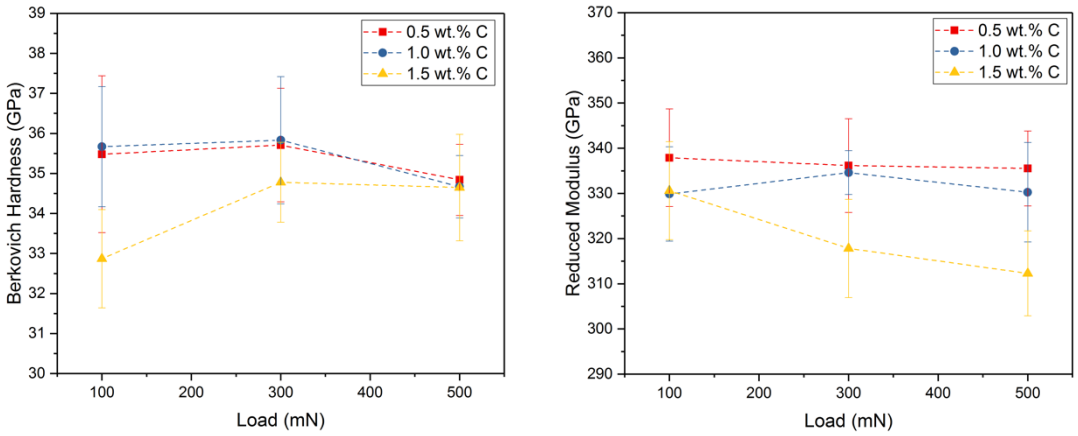

Figure 113. Load- hardness and load- reduced modulus curves for 40%B_4C-etched SiC composites

Table 62. Berkovich hardness and reduced modulus of 50%B_4C-etched SiC composites

100mN (10g)	**H (GPa)**	**Std. Dev.**	**Reduced Modulus (GPa)**	**Std. Dev.**
50B_4C-SiC-0.5C	36.95	1.08	343.17	06.60
50B_4C-SiC-1.0C	35.15	0.83	335.44	08.58
50B_4C-SiC-1.5C	34.70	1.38	334.74	10.55
300mN (30g)	**H (GPa)**	**Std. Dev.**	**Reduced Modulus (GPa)**	**Std. Dev.**
50B_4C-SiC-0.5C	36.50	1.66	348.89	10.41
50B_4C-SiC-1.0C	35.09	1.64	336.48	10.28
50B_4C-SiC-1.5C	35.16	1.49	326.10	10.73
500mN (50g)	**H (GPa)**	**Std. Dev.**	**Reduced Modulus (GPa)**	**Std. Dev.**
50B_4C-SiC-0.5C	35.13	1.83	345.52	09.77
50B_4C-SiC-1.0C	34.94	1.81	334.54	08.08
50B_4C-SiC-1.5C	34.97	1.50	321.15	08.34

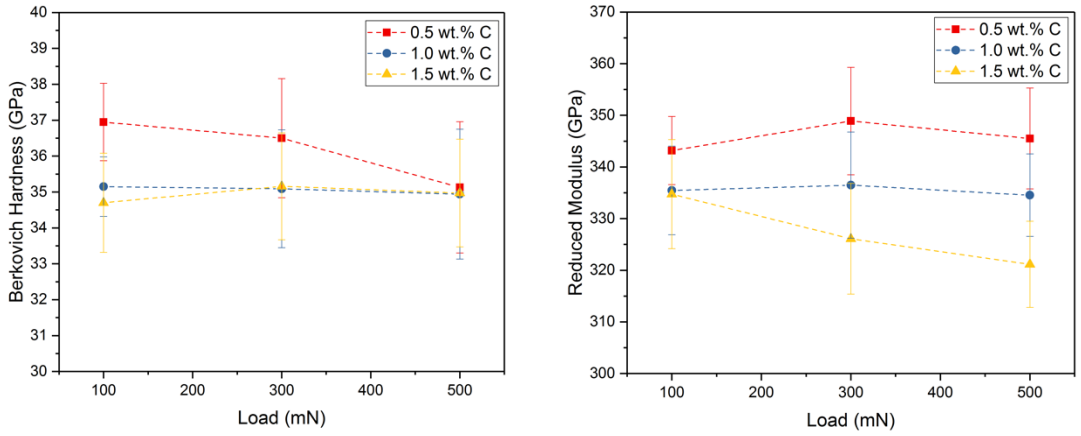

Figure 114. Load- hardness and load- reduced modulus curves for 50%B_4C-etched SiC composites

By using equation 35 in section 4.5.6., the reduced modulus can be converted to Young's modulus. In this equation, the measured Poisson's ratio from ultrasound analysis was used to measure Young's modulus. The Young's modulus from Berkovich and from ultrasound analysis followed the same trend, but they had some differences in values. The results can be seen in Tables 63 through 67. For both ultrasound and nanoindentation methods, with increasing the carbon content, the Young's modulus values decreased. However, the nanoindentation method provided higher Young's modulus values. Oliver et al. experimented one phase materials and ignored the reverse plasticity because they supposed that reverse plasticity was insignificant [118, 127]. On the other hand, Shuman's mentioned that using nanoindentation unload curves to measure elastic modulus can cause a higher calculated elastic modulus since reverse plasticity added to the elastic recovery. Reverse plasticity is brought by dislocations or grain boundary adjustment because of the indentation experiments. They have even found a 100 GPa difference between literature

and experimental elastic modulus values from unloading curves [128]. For this experiment, Shuman's assumption might be acceptable, since composite materials were analyzed.

Also, unlike the ultrasound measurement, the effect of excess carbon on Young's modulus was clearly seen with the Berkovich nanoindentation calculated Young's modulus values. 1% and 1.5% carbon samples showed drastically decreased Young's modulus values.

The Young's modulus decreased when increasing boron carbide content when measured with ultrasound analysis. This was expected since there was an increase in the boron carbide, residual carbon occurred and porosity increased. The Young's modulus for carbon is low compared to the two carbides, so it reduction in the Young's modulus of samples was expected. However, with the Berkovich indentation method, the Young's modulus increased with an increase in boron carbide content. This might be due to the size effect of the indenter tip. The indenter tip might hit mostly boron carbide grains and again reverse plasticity would come into play.

Table 63. Comparison of 10%B_4C-etched SiC of Young's modulus measured by ultrasound and nanoindentation

Sample	E (GPa)	500 mN Elastic Modulus	% Difference
10B_4C-SiC-0.5C	429	409	-05
10B_4C-SiC-1.0C	426	408	-04
10B_4C-SiC-1.5C	415	382	-07

Table 64. Comparison of 20%B_4C-etched SiC of Young's modulus measured by ultrasound and nanoindentation

Sample	E (GPa)	500 mN Elastic Modulus	% Difference
20B_4C-SiC-0.5C	424	448	05
20B_4C-SiC-1.0C	421	412	-02
20B_4C-SiC-1.5C	409	354	-13

Table 65. Comparison of 30%B_4C-etched SiC of Young's modulus measured by ultrasound and nanoindentation

Sample	E (GPa)	500 mN Elastic Modulus	% Difference
30B_4C-SiC-0.5C	408	427	04
30B_4C-SiC-1.0C	410	381	-20
30B_4C-SiC-1.5C	402	377	-06

Table 66. Comparison of 40%B_4C-etched SiC of Young's modulus measured by ultrasound and nanoindentation

Sample	E (GPa)	500 mN Elastic Modulus	% Difference
40B_4C-SiC-0.5C	396	461	16
40B_4C-SiC-1.0C	395	451	14
40B_4C-SiC-1.5C	392	417	06

Table 67. Comparison of 50%B_4C-etched SiC of Young's modulus measured by ultrasound and nanoindentation

Sample	E (GPa)	500 mN Elastic Modulus	% Difference
50B_4C-SiC-0.5C	390	481	23
50B_4C-SiC-1.0C	392	459	17
50B_4C-SiC-1.5C	388	433	12

5.3.2. Unetched SiC-B_4C Series

5.3.2.1. Microstructure Characterization

SiC-B_4C composite samples were processed by SPS at 1950°C for 5min. Samples were cross-sectioned with ion milling to prepare the microstructure to be examined as described in section 4.4. Both microstructure and fracture surface images were taken as described in section 4.5.4.

In this series, the boron carbide content ranged from 10 to 90% B_4C with the unetched SiC powders. The added carbon content was expanded from 0.5 to 2.5% for this series. The resulting microstructures can be seen in Figures 115 though 123. The light area is SiC, and the dark area is B_4C. The two components were homogeneously distributed throughout this extensive sample series. Porosity and any residual carbon were not evident in these images.

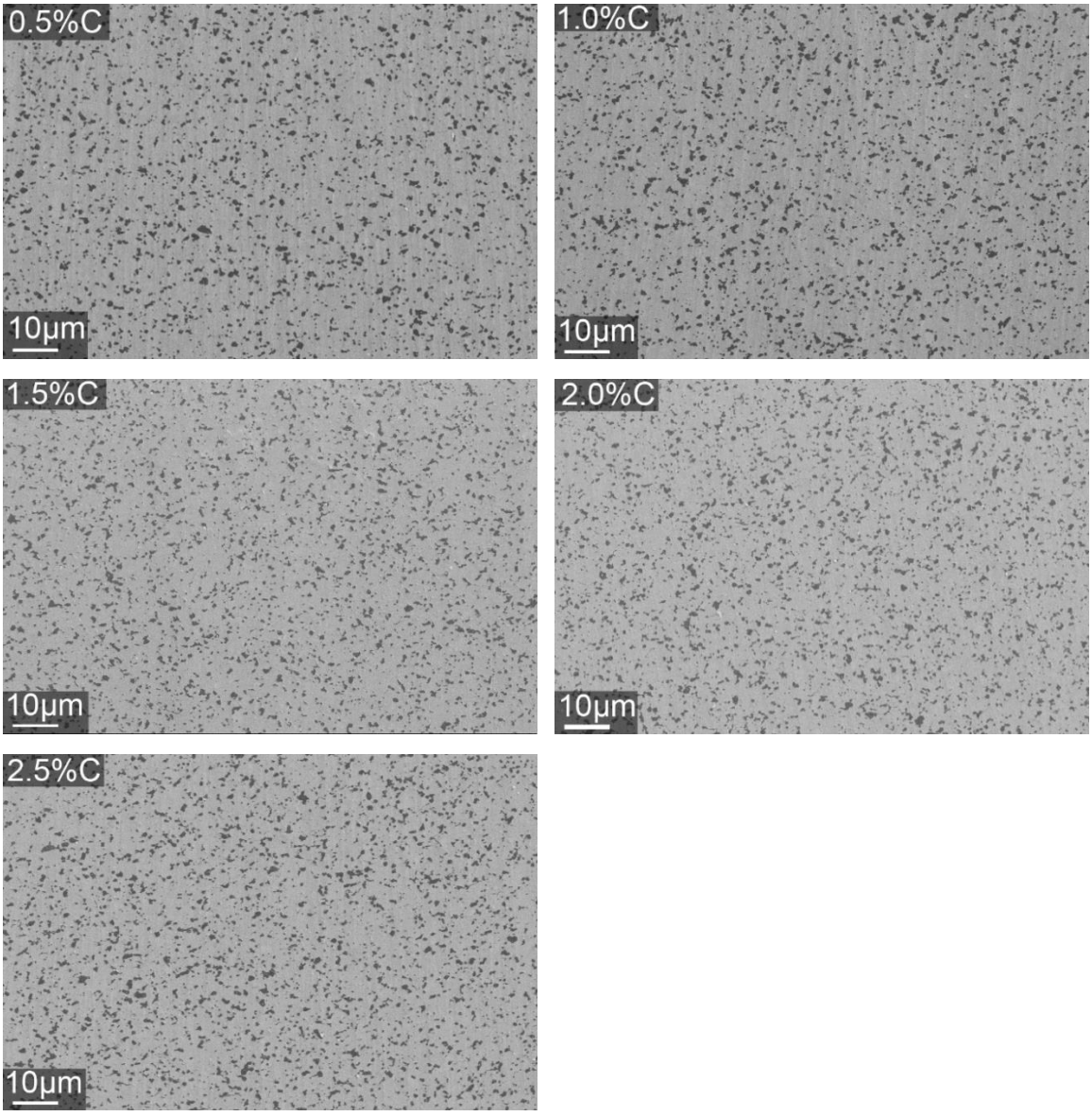

Figure 115. The microstructure of 10% B_4C- unetched SiC with 0.5%C, 1.0%C, 1.5%C, 2.0%C, and 2.5%C

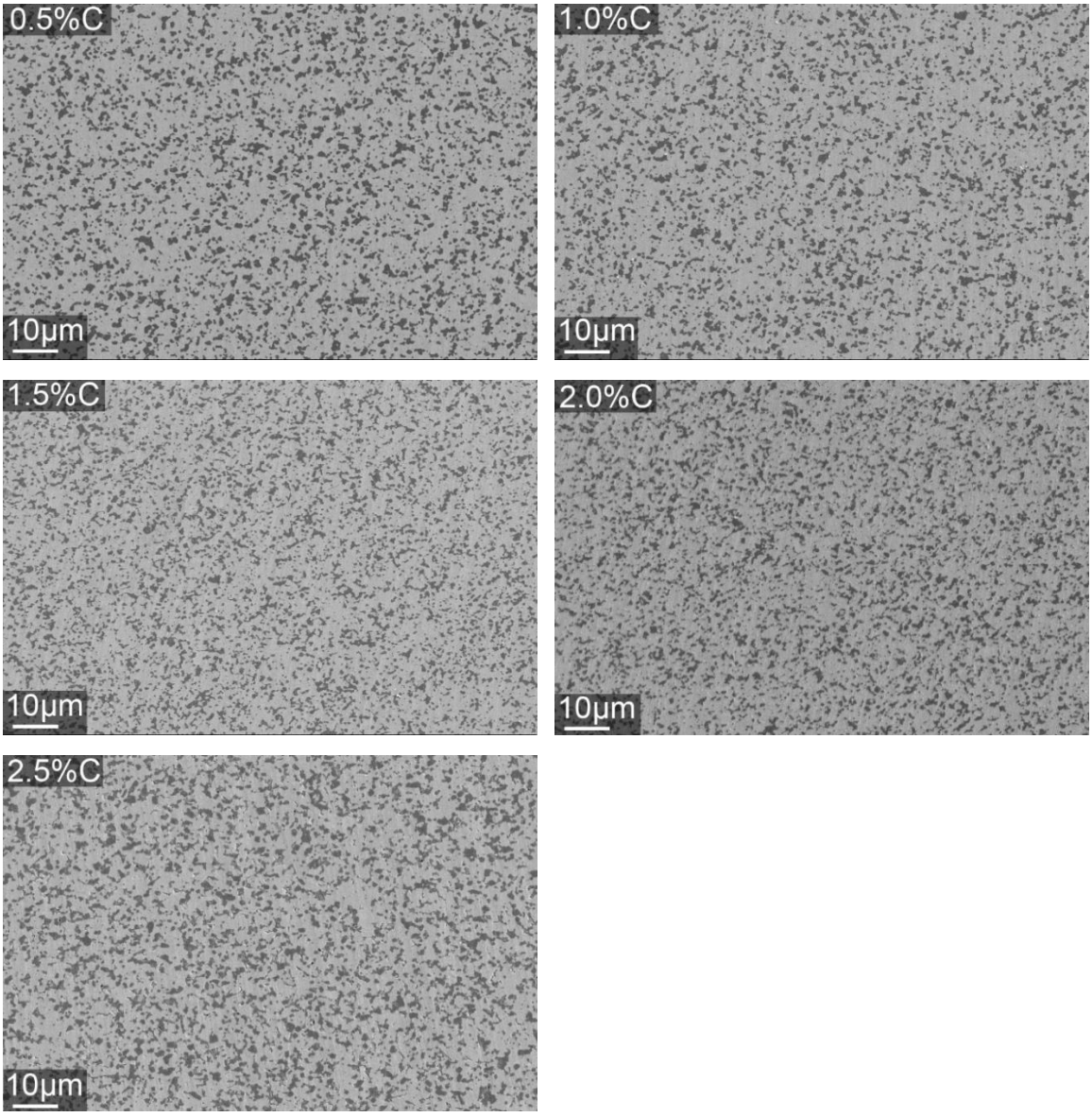

Figure 116. The microstructure of 20% B_4C- unetched SiC with 0.5%C, 1.0%C, 1.5%C, 2.0%C, and 2.5%C

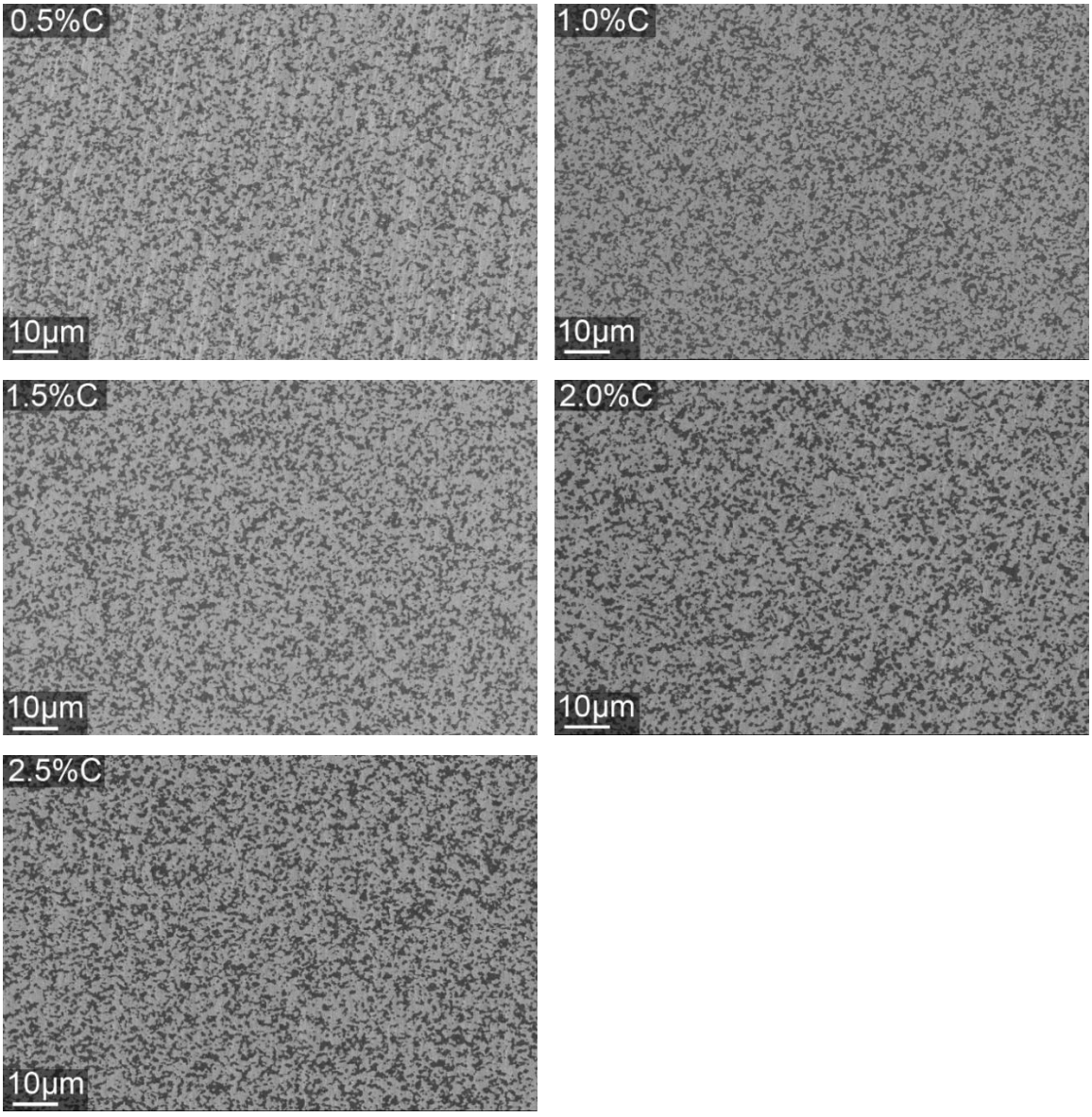

Figure 117. The microstructure of 30% B_4C- unetched SiC with 0.5%C, 1.0%C, 1.5%C, 2.0%C, and 2.5%C

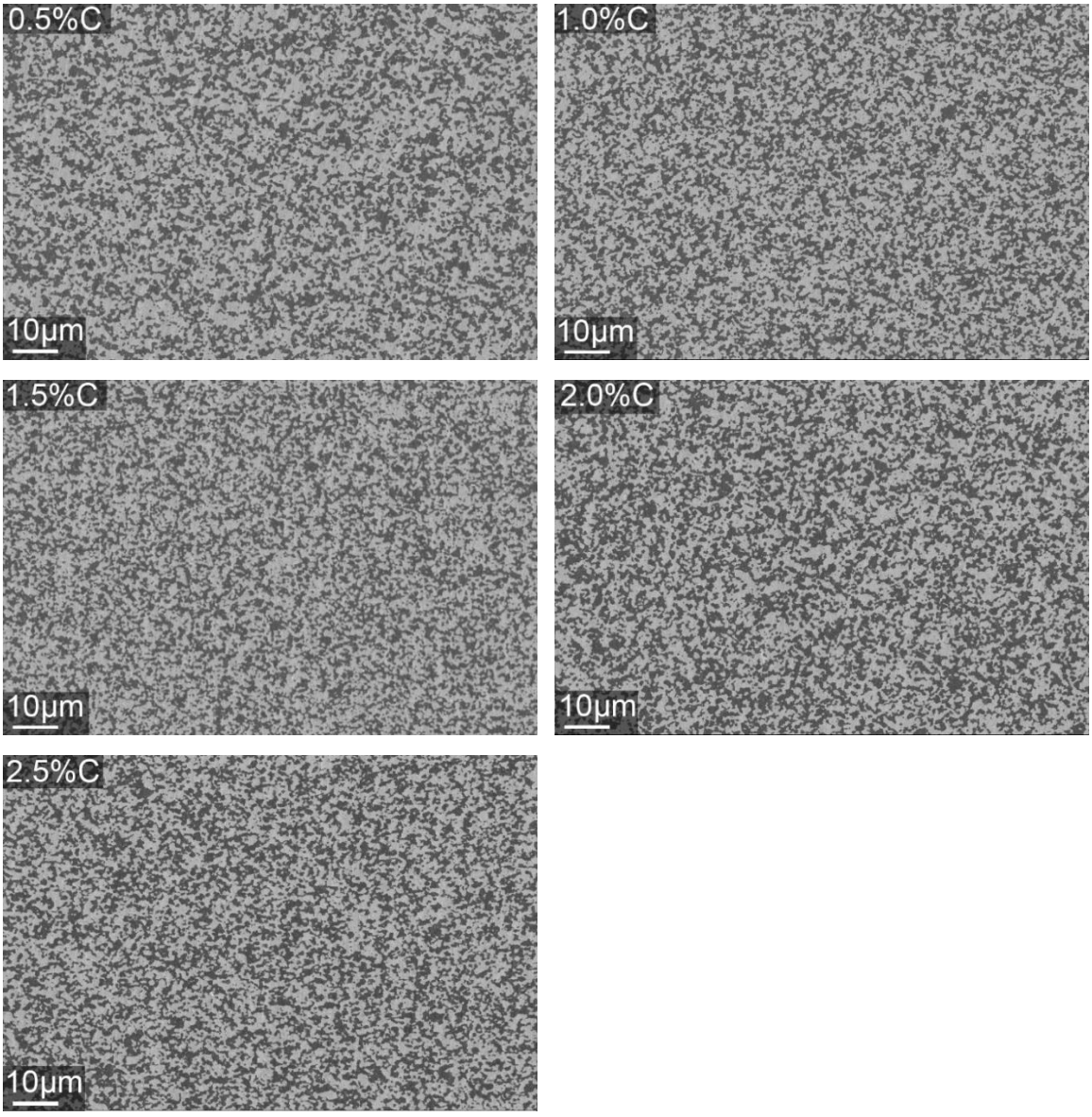

Figure 118. The microstructure of 40% B_4C- unetched SiC with 0.5%C, 1.0%C, 1.5%C, 2.0%C, and 2.5%C

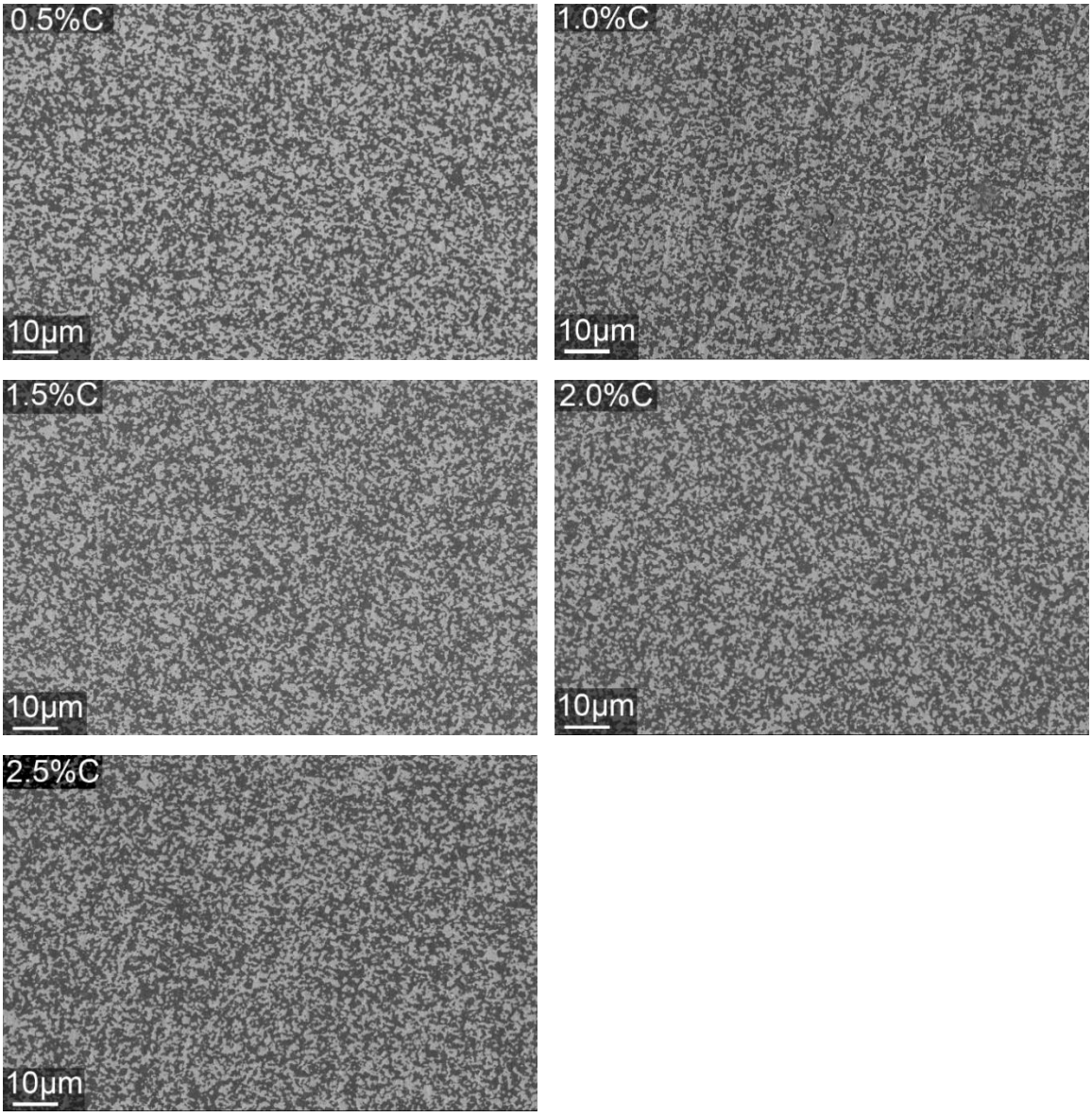

Figure 119. The microstructure of 50% B_4C- unetched SiC with 0.5%C, 1.0%C, 1.5%C, 2.0%C, and 2.5%C

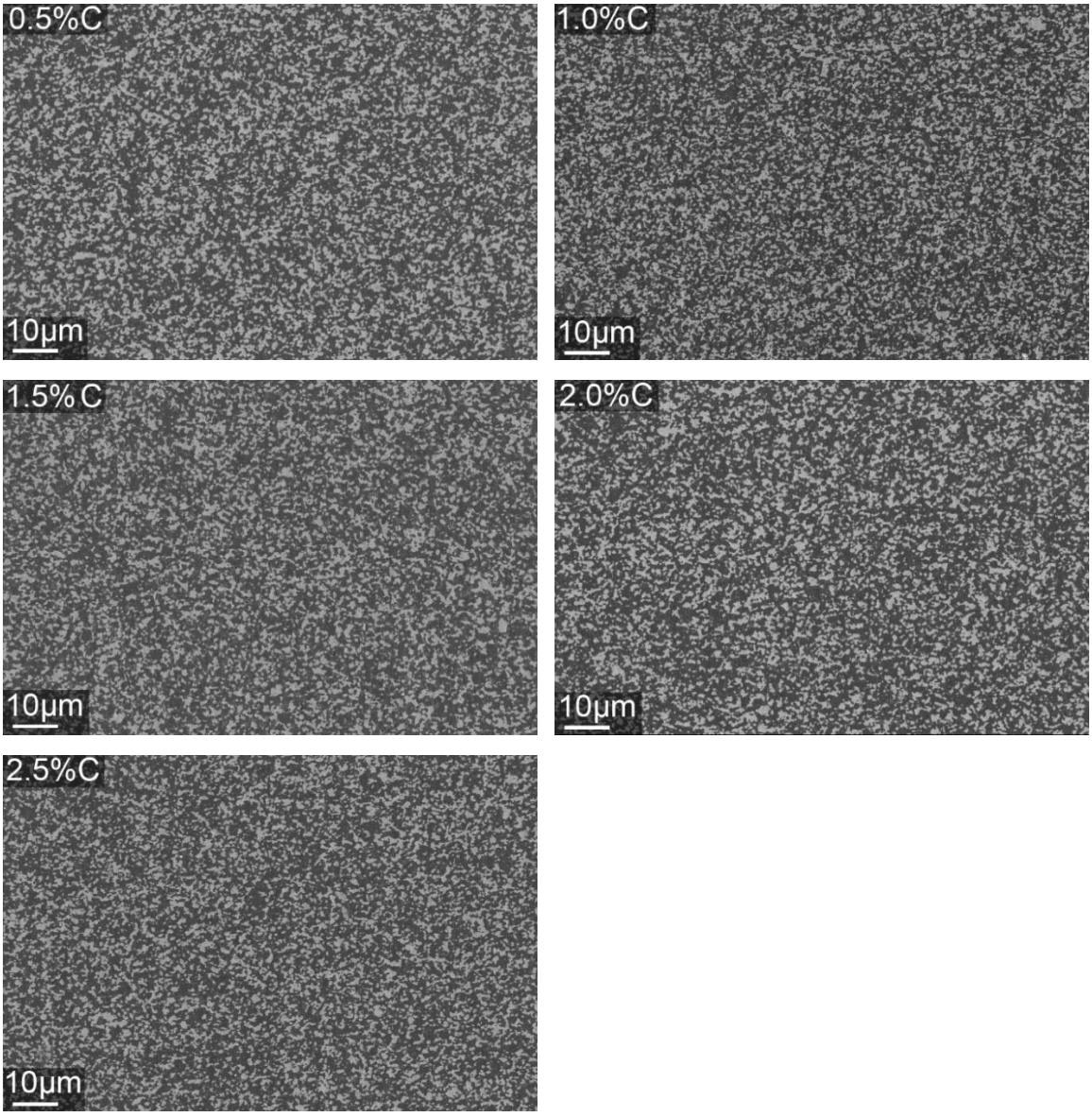

Figure 120. The microstructure of 60% B_4C- unetched SiC with 0.5%C, 1.0%C, 1.5%C, 2.0%C, and 2.5%C

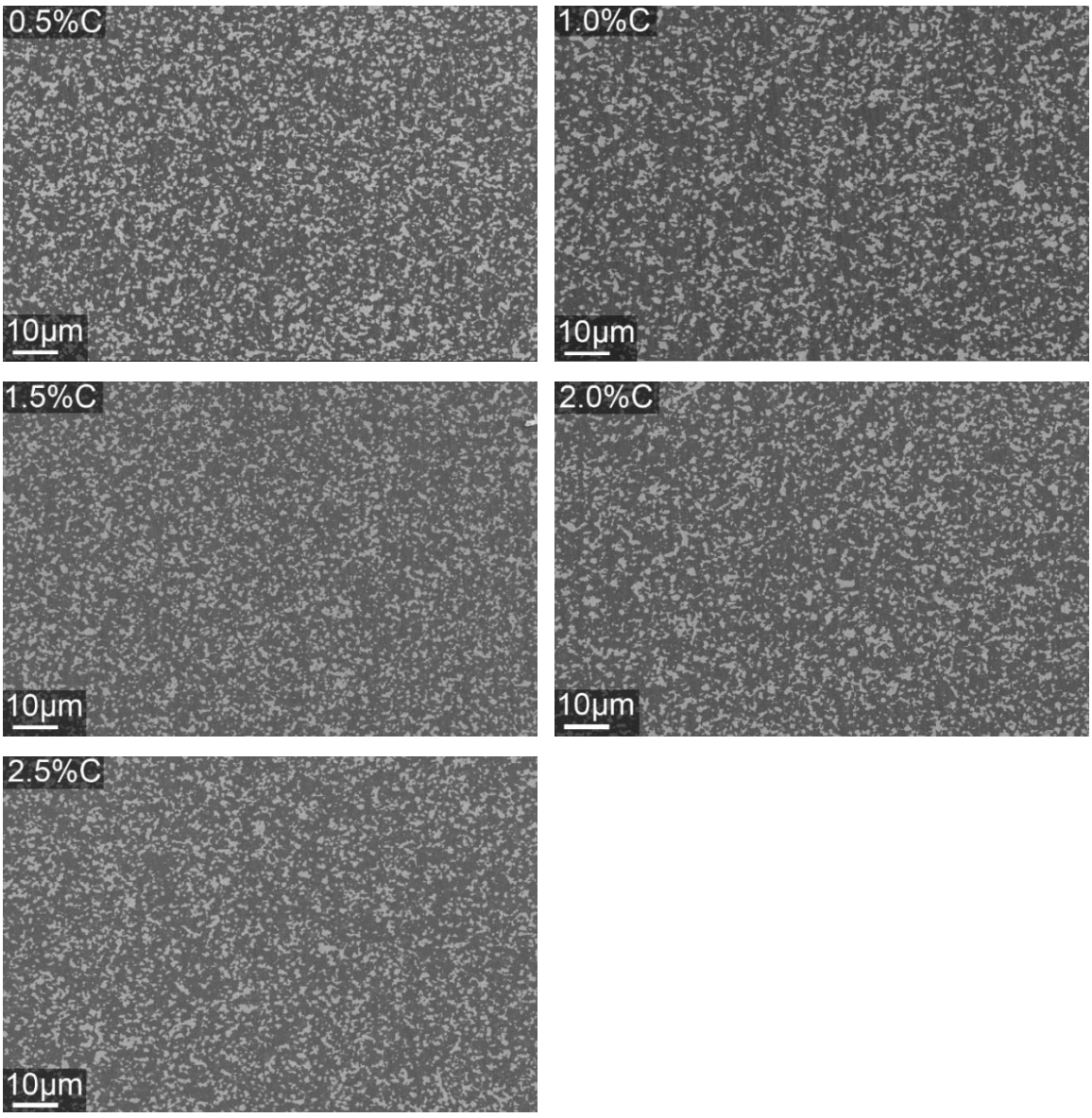

Figure 121. The microstructure of 70% B_4C- unetched SiC with 0.5%C, 1.0%C, 1.5%C, 2.0%C, and 2.5%C

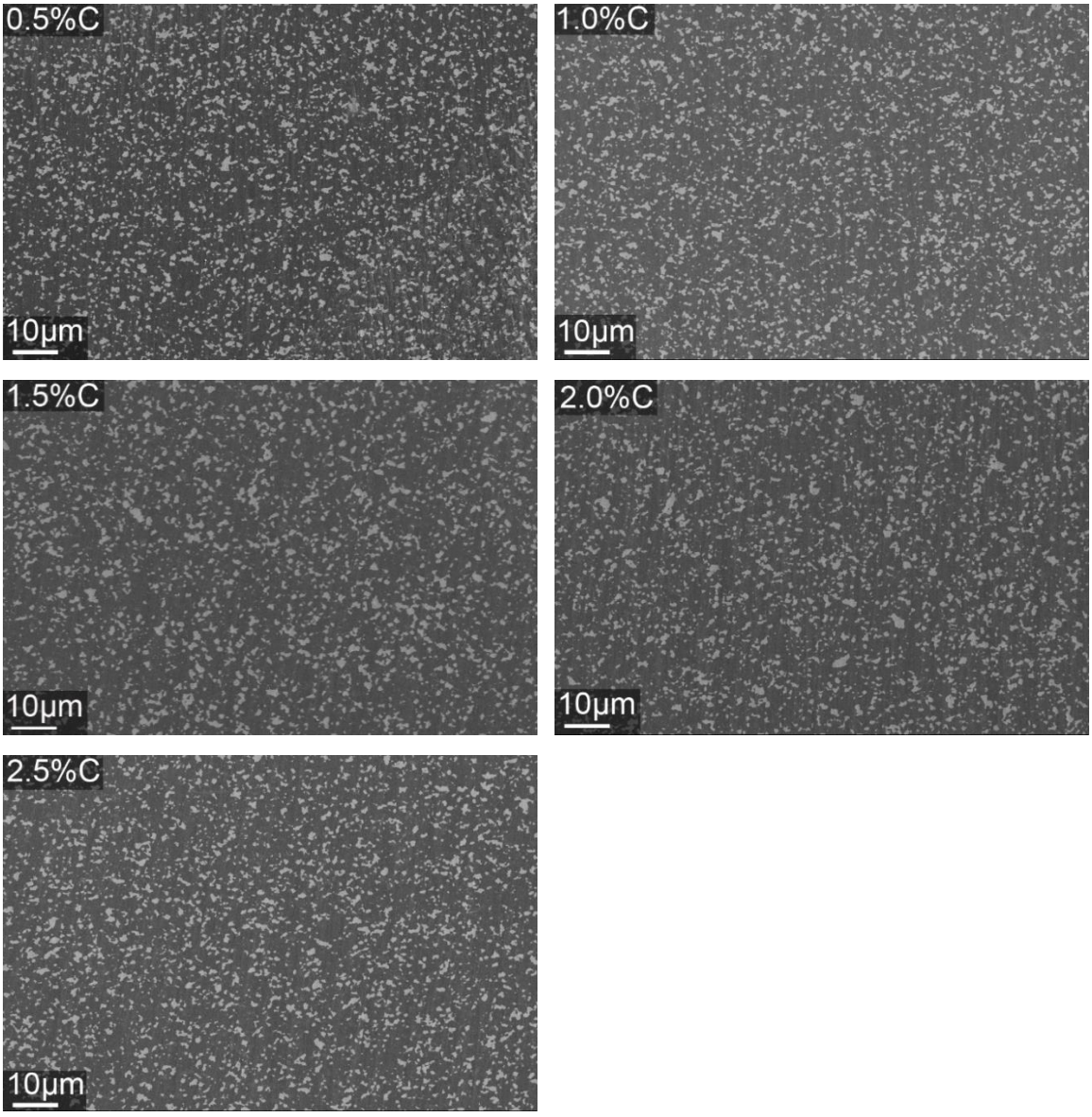

Figure 122. The microstructure of 80% B_4C- unetched SiC with 0.5%C, 1.0%C, 1.5%C, 2.0%C, and 2.5%C

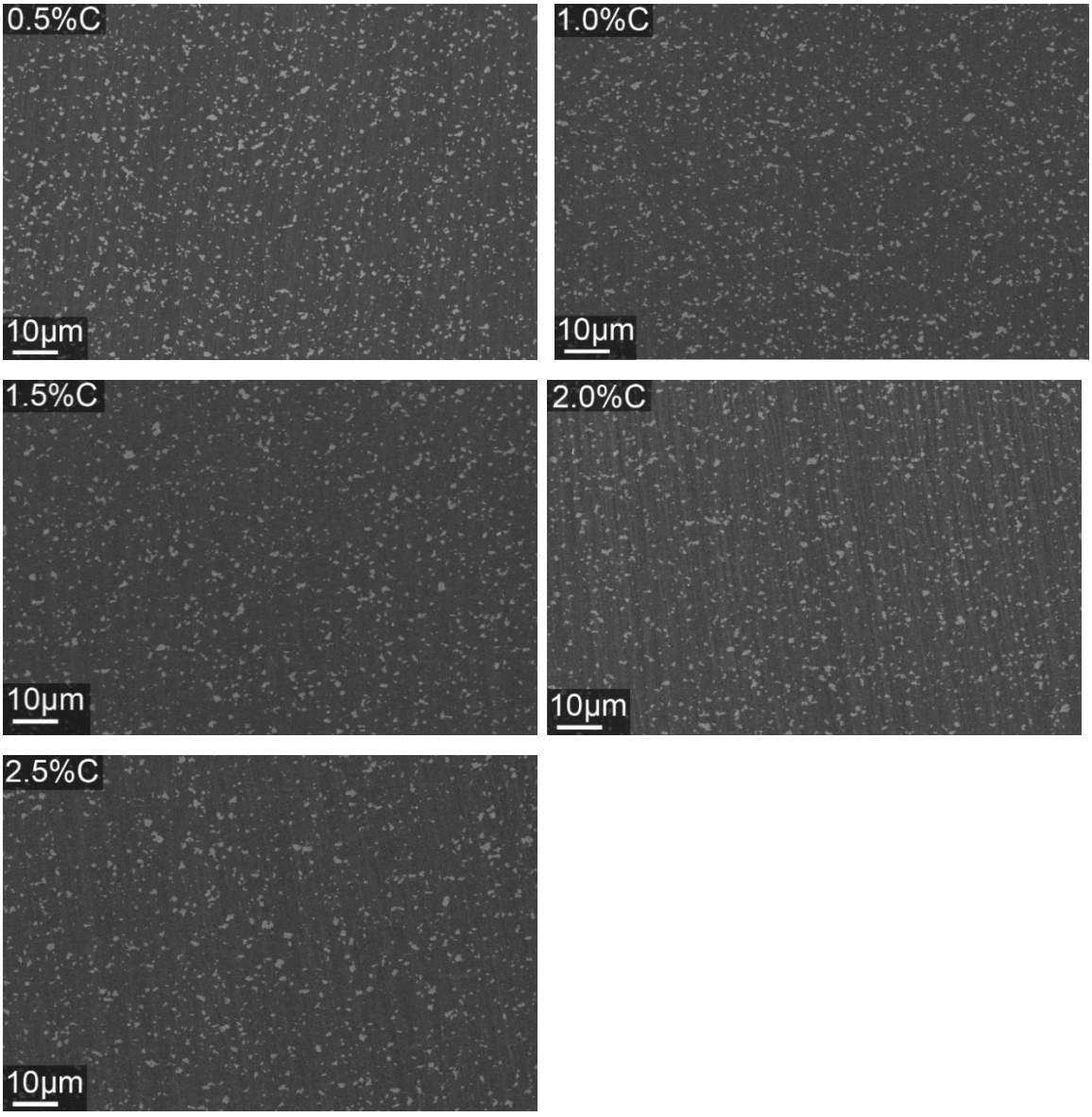

Figure 123. The microstructure of 90% B_4C- unetched SiC with 0.5%C, 1.0%C, 1.5%C, 2.0%C, and 2.5%C

As in the earlier series, increasing the boron carbide content in the composites increased the average grain size for boron carbide while decreasing of silicon carbide grain size. All the samples' grain sizes were submicron, which were close to the starting materials mean particle sizes. Increasing the amount of carbon decreased the grain size of

both silicon carbide and boron carbide. Sahani mentioned that SPS sintered SiC-B_4C particle sizes were usually less than 5 μm while pressureless sintered SiC-B_4C particle sizes were more than 5 μm [5]. It was clear that carbon is a grain growth inhibitor as mentioned in literature [78]. Also, it was suggested that in the presence of silicon carbide, the grain growth of boron carbide was also suppressed [123], and, in presence of boron carbide, the grain growth of silicon carbide was minimized [129].

Average grain sizes of boron carbide and silicon carbide with standard deviations can be seen in Tables 68 thought 76. After modifying the oxygen content by adding carbon, the boron carbide grains first coarsened when the carbon increased from 0.5% to 1.5%, then reduced when the carbon content increased from 1.5% to 2.5%.

Table 68. Average grain sizes of 10% B_4C- unetched SiC with 0.5%C, 1.0%C, 1.5%C, 2.0%C, and 2.5%C

Sample	**Average Grain Size of B_4C (μm) (Std. Dev)**	**Average Grain Size of SiC (μm) (Std. Dev)**
10B_4C-SiC-0.5C	0.19±0.03	1.09±0.08
10B_4C-SiC-1.0C	0.19±0.05	1.12±0.11
10B_4C-SiC-1.5C	0.26±0.07	1.12±0.12
10B_4C-SiC-2.0C	0.25±0.06	1.11±0.16
10B_4C-SiC-2.5C	0.24±0.06	1.11±0.11

Table 69. Average grain sizes of 20% B_4C- unetched SiC with 0.5%C, 1.0%C, 1.5%C, 2.0%C, and 2.5%C

Sample	Average Grain Size of B_4C (μm) (Std. Dev)	Average Grain Size of SiC (μm) (Std. Dev)
20B_4C-SiC-0.5C	0.30±0.06	0.79±0.12
20B_4C-SiC-1.0C	0.30±0.03	0.94±0.04
20B_4C-SiC-1.5C	0.33±0.02	0.98±0.08
20B_4C-SiC-2.0C	0.29±0.04	0.84±0.06
20B_4C-SiC-2.5C	0.29±0.05	0.83±0.06

Table 70. Average grain sizes of 30% B_4C- unetched SiC with 0.5%C, 1.0%C, 1.5%C, 2.0%C, and 2.5%C

Sample	Average Grain Size of B_4C (μm) (Std. Dev)	Average Grain Size of SiC (μm) (Std. Dev)
30B_4C-SiC-0.5C	0.37±0.06	0.64±0.07
30B_4C-SiC-1.0C	0.37±0.04	0.61±0.04
30B_4C-SiC-1.5C	0.38±0.06	0.75±0.07
30B_4C-SiC-2.0C	0.36±0.05	0.69±0.07
30B_4C-SiC-2.5C	0.36±0.02	0.58±0.04

Table 71. Average grain sizes of 40% B_4C- unetched SiC with 0.5%C, 1.0%C, 1.5%C, 2.0%C, and 2.5%C

Sample	Average Grain Size of B_4C (μm) (Std. Dev)	Average Grain Size of SiC (μm) (Std. Dev)
40B_4C-SiC-0.5C	0.40±0.04	0.48±0.05
40B_4C-SiC-1.0C	0.39±0.03	0.48±0.04
40B_4C-SiC-1.5C	0.42±0.06	0.73±0.08
40B_4C-SiC-2.0C	0.43±0.06	0.54±0.08
40B_4C-SiC-2.5C	0.43±0.05	0.51±0.07

Table 72. Average grain sizes of 50% B_4C- unetched SiC with 0.5%C, 1.0%C, 1.5%C, 2.0%C, and 2.5%C

Sample	Average Grain Size of B_4C (μm) (Std. Dev)	Average Grain Size of SiC (μm) (Std. Dev)
50B_4C-SiC-0.5C	0.42±0.03	0.40±0.06
50B_4C-SiC-1.0C	0.44±0.04	0.43±0.04
50B_4C-SiC-1.5C	0.44±0.04	0.44±0.04
50B_4C-SiC-2.0C	0.44±0.04	0.42±0.07
50B_4C-SiC-2.5C	0.43±0.04	0.42±0.05

Table 73. Average grain sizes of 60% B_4C- unetched SiC with 0.5%C, 1.0%C, 1.5%C, 2.0%C, and 2.5%C

Sample	Average Grain Size of B_4C (μm) (Std. Dev)	Average Grain Size of SiC (μm) (Std. Dev)
60B_4C-SiC-0.5C	0.57±0.04	0.35±0.06
60B_4C-SiC-1.0C	0.57±0.05	0.34±0.03
60B_4C-SiC-1.5C	0.60±0.06	0.42±0.03
60B_4C-SiC-2.0C	0.61±0.03	0.35±0.03
60B_4C-SiC-2.5C	0.60±0.05	0.35±0.03

Table 74. Average grain sizes of 70% B_4C- unetched SiC with 0.5%C, 1.0%C, 1.5%C, 2.0%C, and 2.5%C

Sample	Average Grain Size of B_4C (μm) (Std. Dev)	Average Grain Size of SiC (μm) (Std. Dev)
70B_4C-SiC-0.5C	0.68±0.05	0.20±0.04
70B_4C-SiC-1.0C	0.74±0.05	0.20±0.05
70B_4C-SiC-1.5C	0.74±0.05	0.31±0.03
70B_4C-SiC-2.0C	0.68±0.04	0.28±0.02
70B_4C-SiC-2.5C	0.66±0.04	0.27±0.04

Table 75. Average grain sizes of 80% B_4C- unetched SiC with 0.5%C, 1.0%C, 1.5%C, 2.0%C, and 2.5%C

Sample	Average Grain Size of B_4C (μm) (Std. Dev)	Average Grain Size of SiC (μm) (Std. Dev)
80B_4C-SiC-0.5C	0.73±0.04	0.16±0.02
80B_4C-SiC-1.0C	0.84±0.06	0.16±0.04
80B_4C-SiC-1.5C	0.86±0.07	0.18±0.06
80B_4C-SiC-2.0C	0.84±0.04	0.17±0.04
80B_4C-SiC-2.5C	0.78±0.07	0.16±0.03

Table 76. Average grain sizes of 90% B_4C- unetched SiC with 0.5%C, 1.0%C, 1.5%C, 2.0%C, and 2.5%C

Sample	Average Grain Size of B_4C (μm) (Std. Dev)	Average Grain Size of SiC (μm) (Std. Dev)
90B_4C-SiC-0.5C	0.77±0.08	0.12±0.02
90B_4C-SiC-1.0C	0.83±0.05	0.11±0.02
90B_4C-SiC-1.5C	0.98±0.06	0.17±0.03
90B_4C-SiC-2.0C	0.86±0.10	0.10±0.03
90B_4C-SiC-2.5C	0.85±0.07	0.10±0.02

The scanning electron microscopy (SEM) images of the fracture surfaces can be found in Figures 124 through 132. The images were used to determine the mode of fracture and show the fracture surface of samples for different carbon addition. Even if the samples fracture surfaces were not perfectly smooth, it can be concluded that the composites showed a transgranular fracture. Since the silicon carbide and boron carbide thermal expansion coefficients are close in value [126] ($5.68\pm0.11\times10^{-6}$ and $6.02\pm0.51\times10^{-6}$ respectively), there was a small residual stress around the particles. However, it was not enough to cause crack deflection or to introduce intergranular fracture.

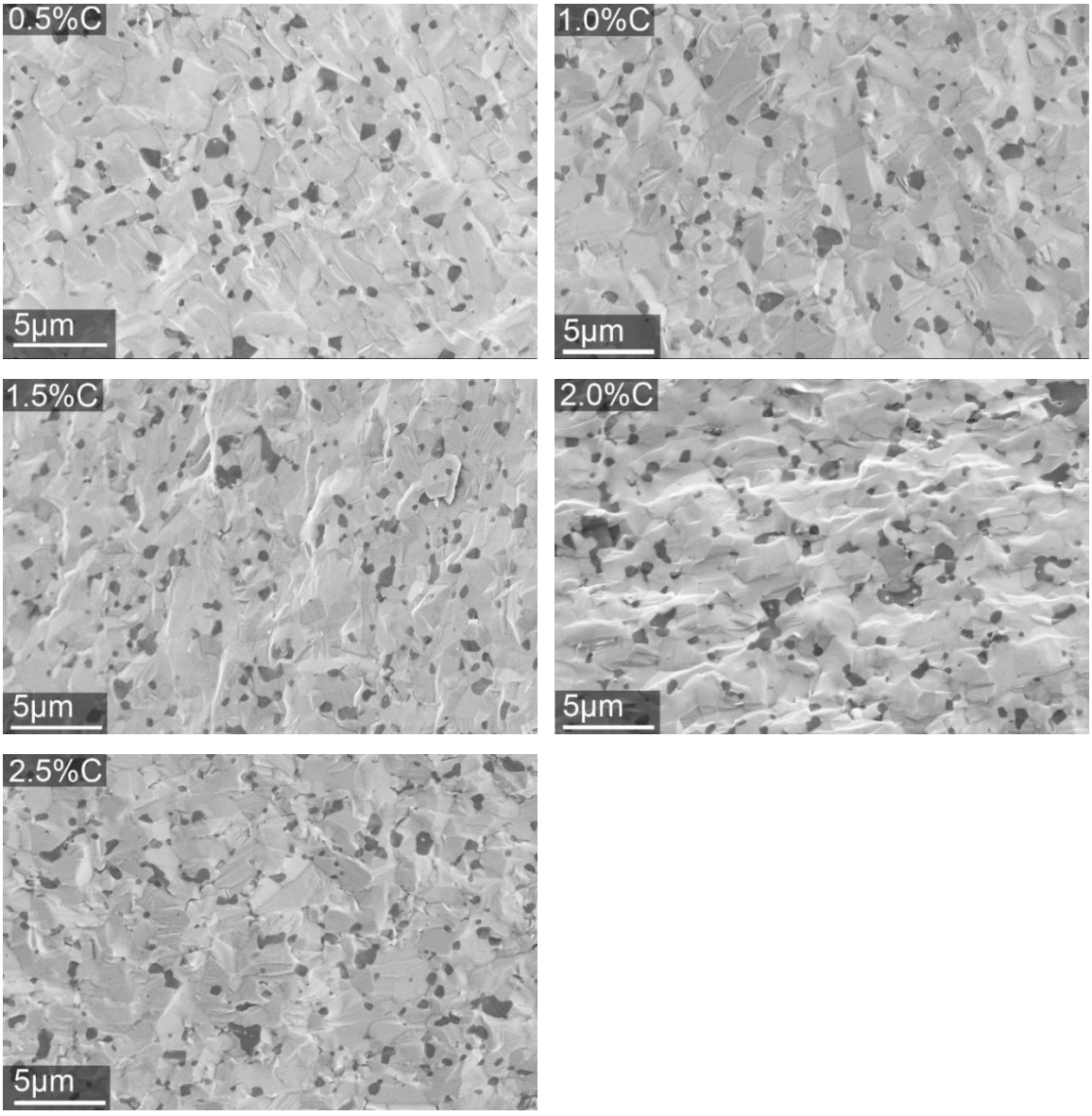

Figure 124. Fracture Surface of 10%B_4C-unetched SiC composites

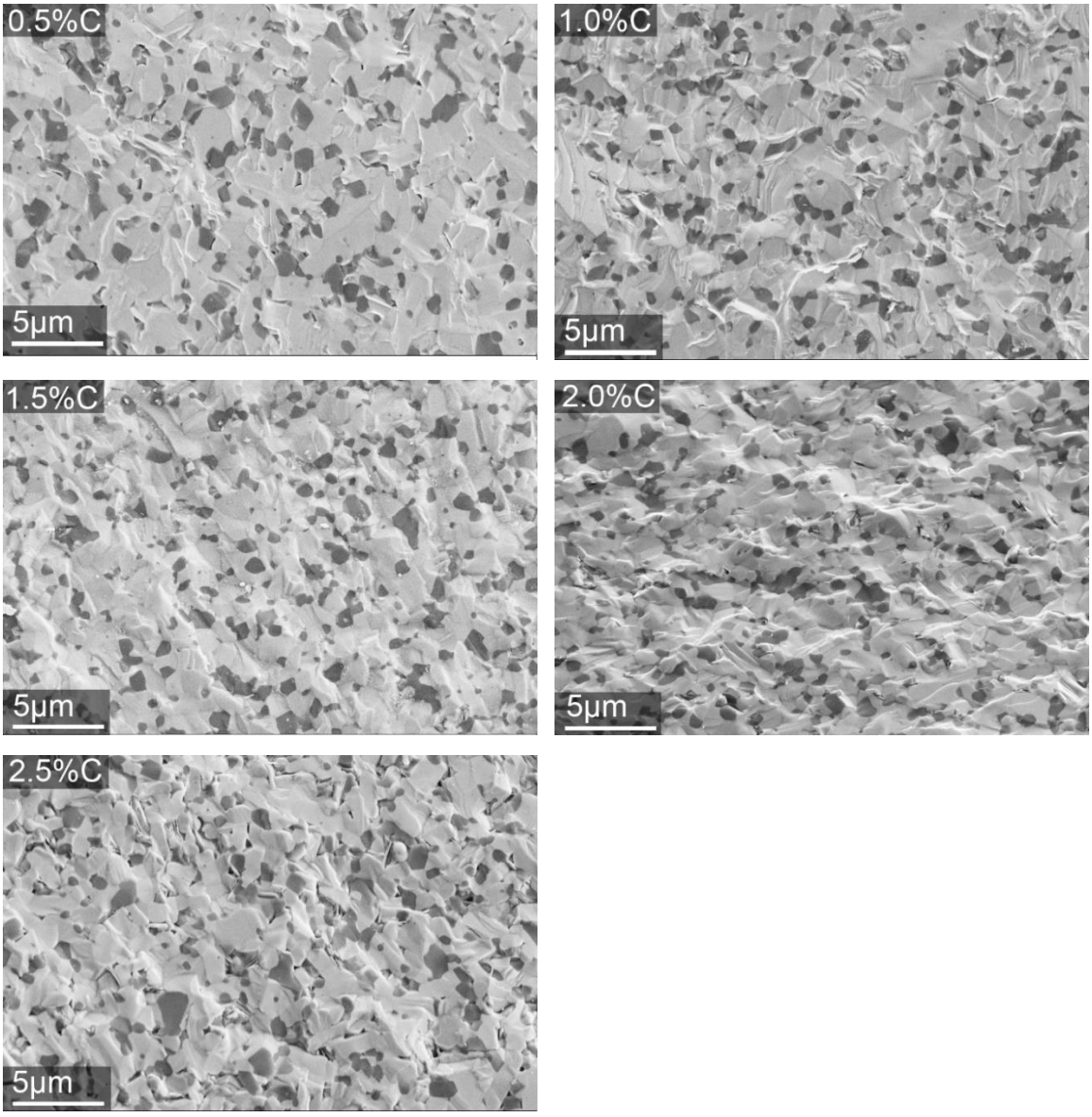

Figure 125. Fracture Surface of 20%B_4C-unetched SiC composites

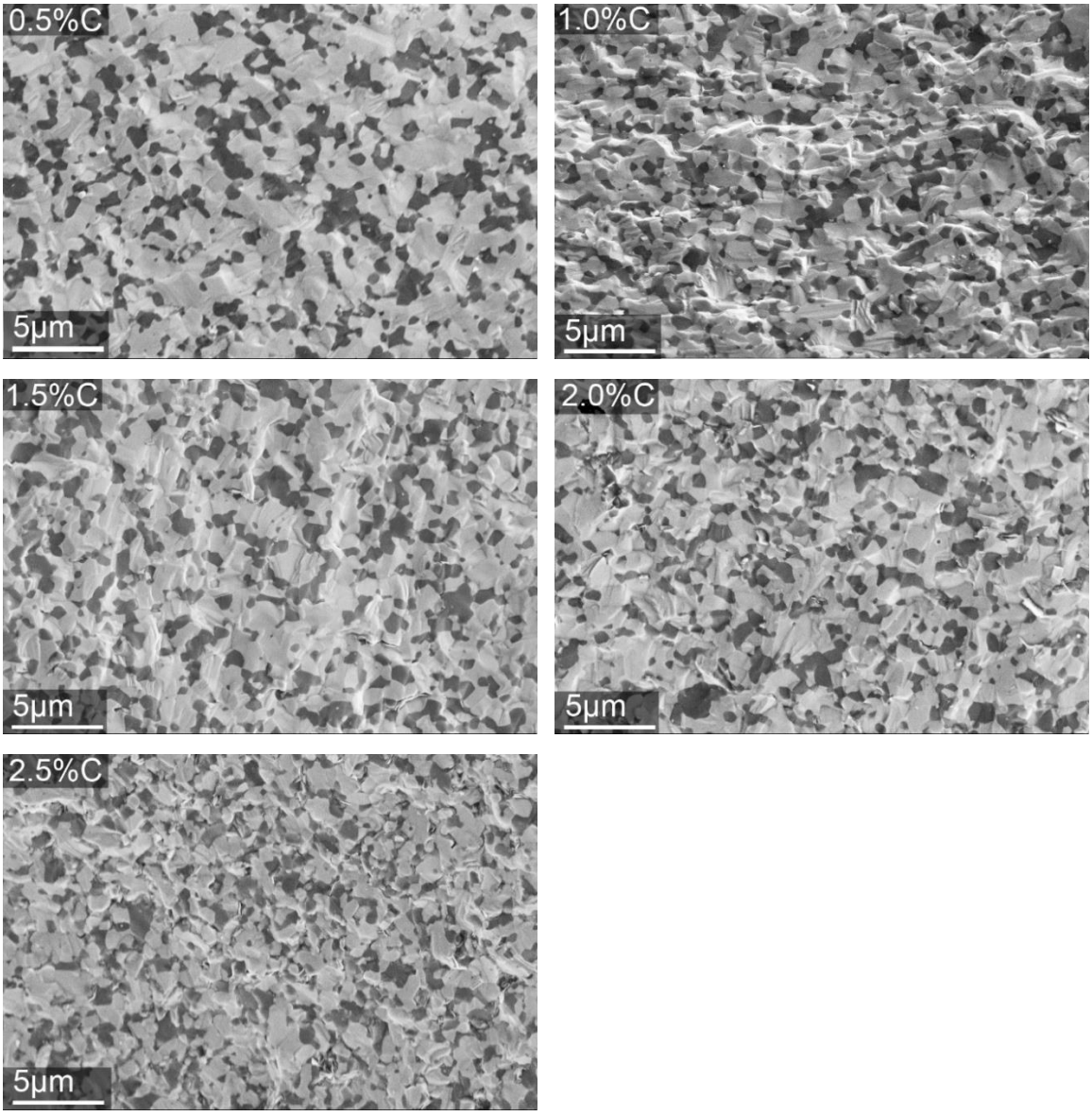

Figure 126. Fracture Surface of 30%B_4C-unetched SiC composites

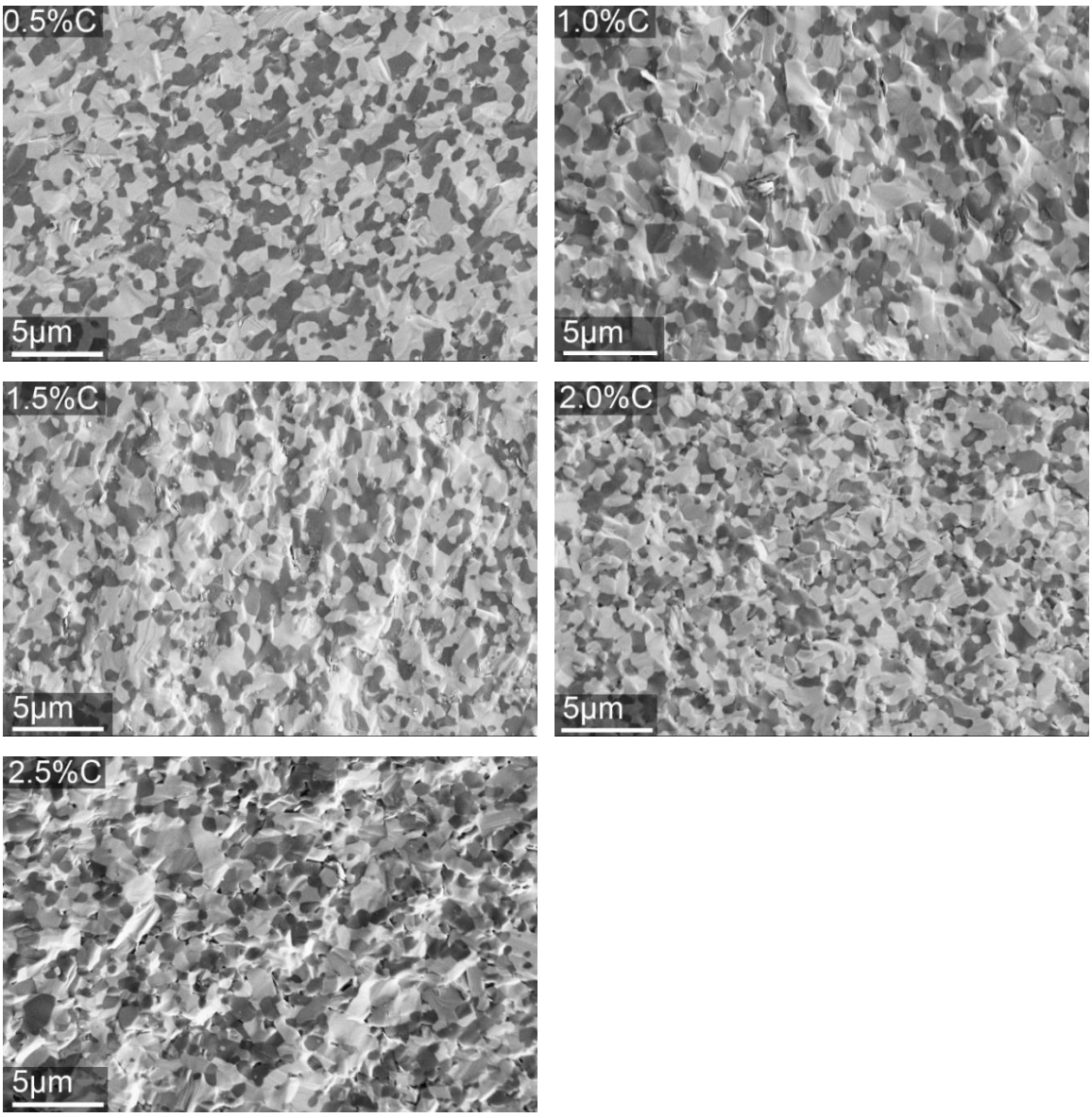

Figure 127. Fracture Surface of 40%B_4C-unetched SiC composites

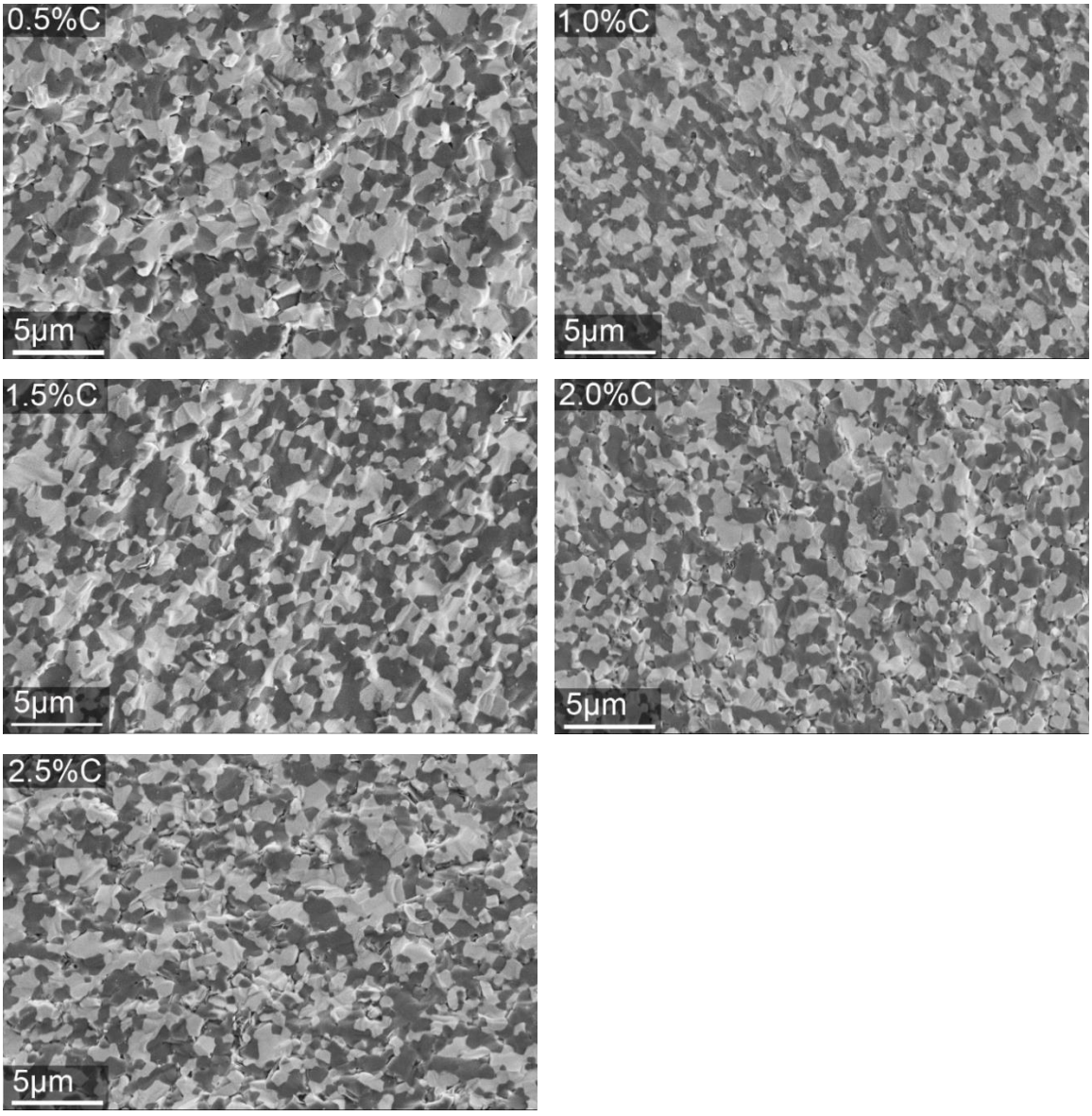

Figure 128. Fracture Surface of 50%B_4C-unetched SiC composites

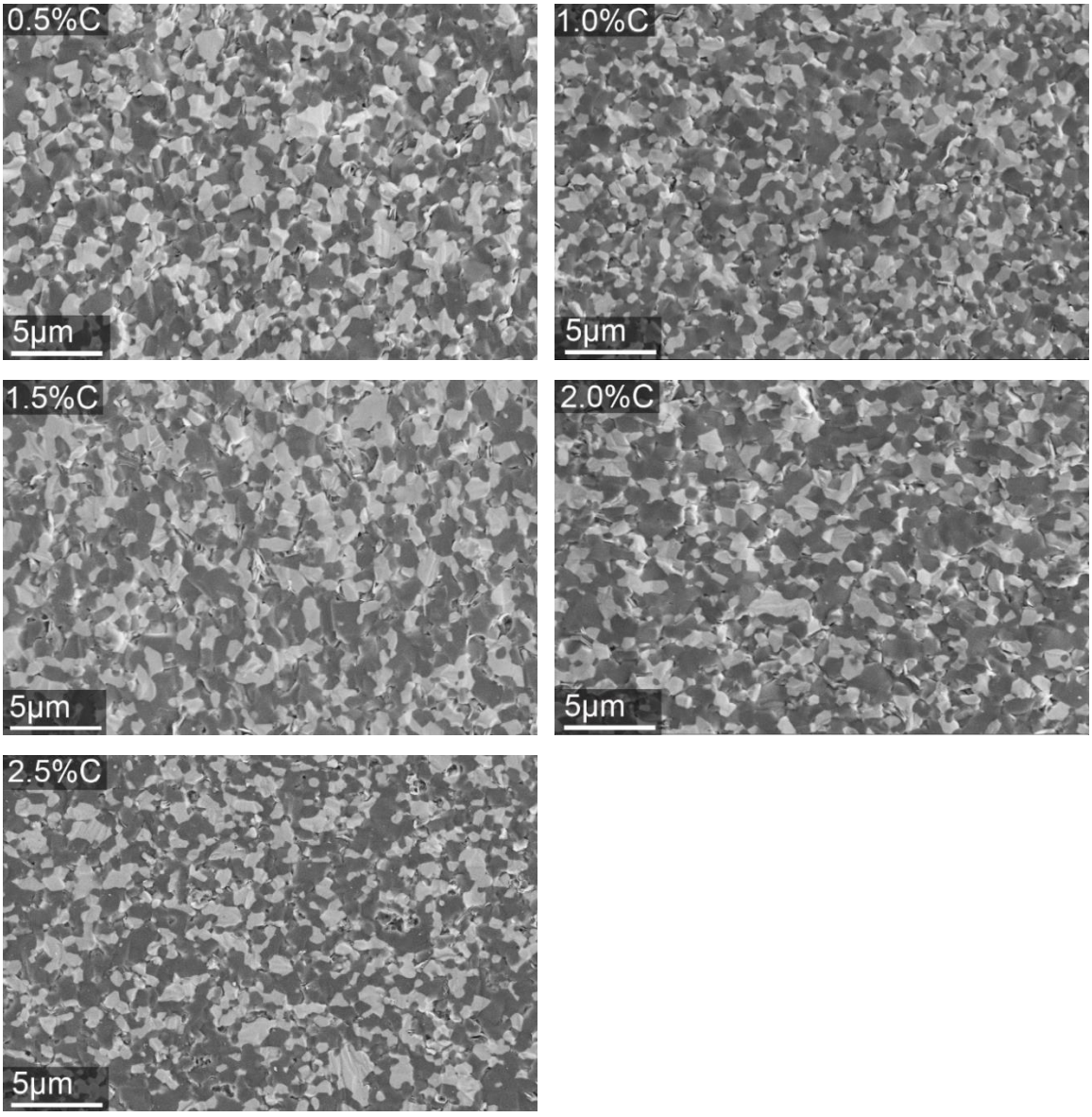

Figure 129. Fracture Surface of 60%B_4C-unetched SiC composites

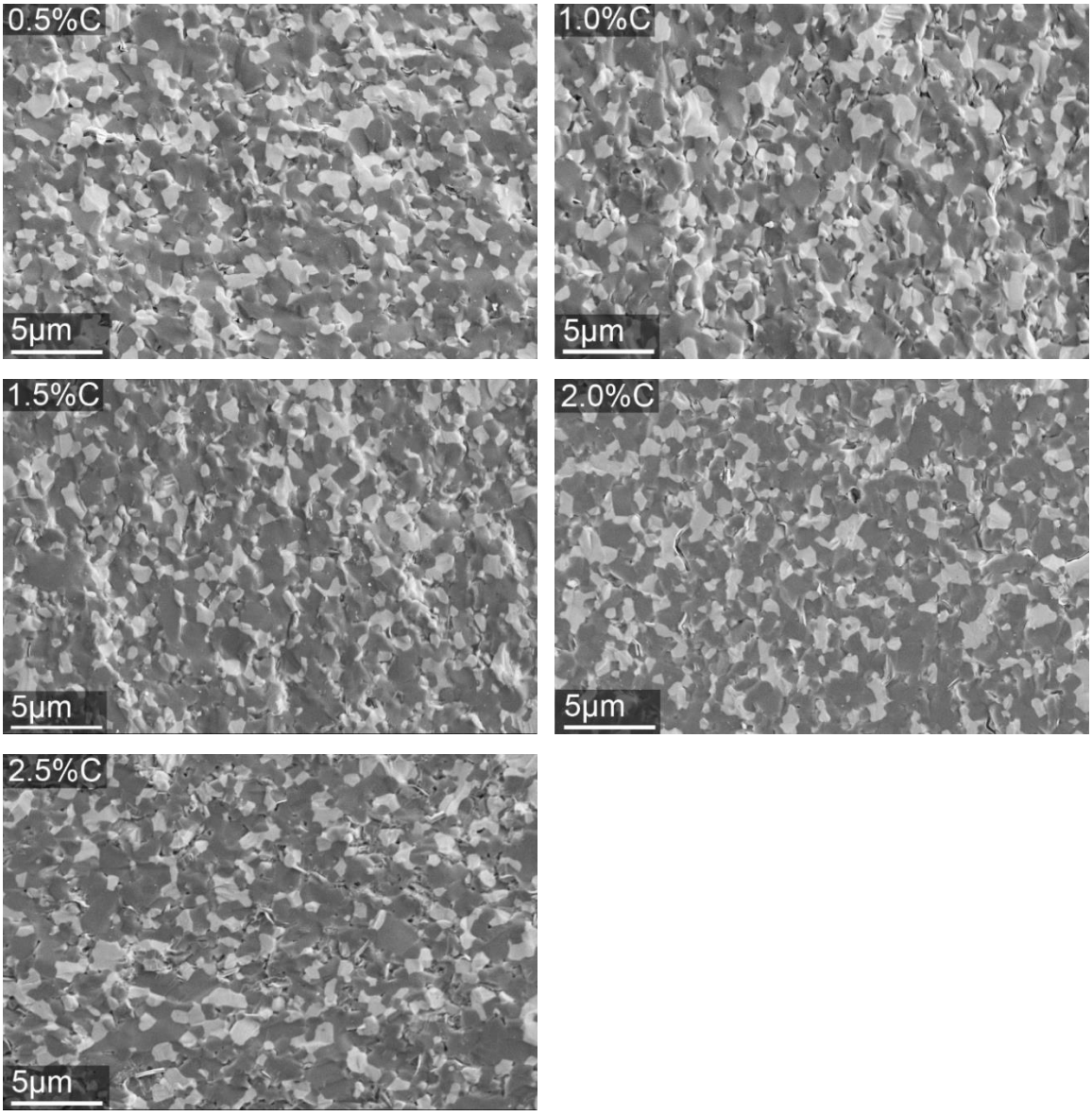

Figure 130. Fracture Surface of 70%B_4C-unetched SiC composites

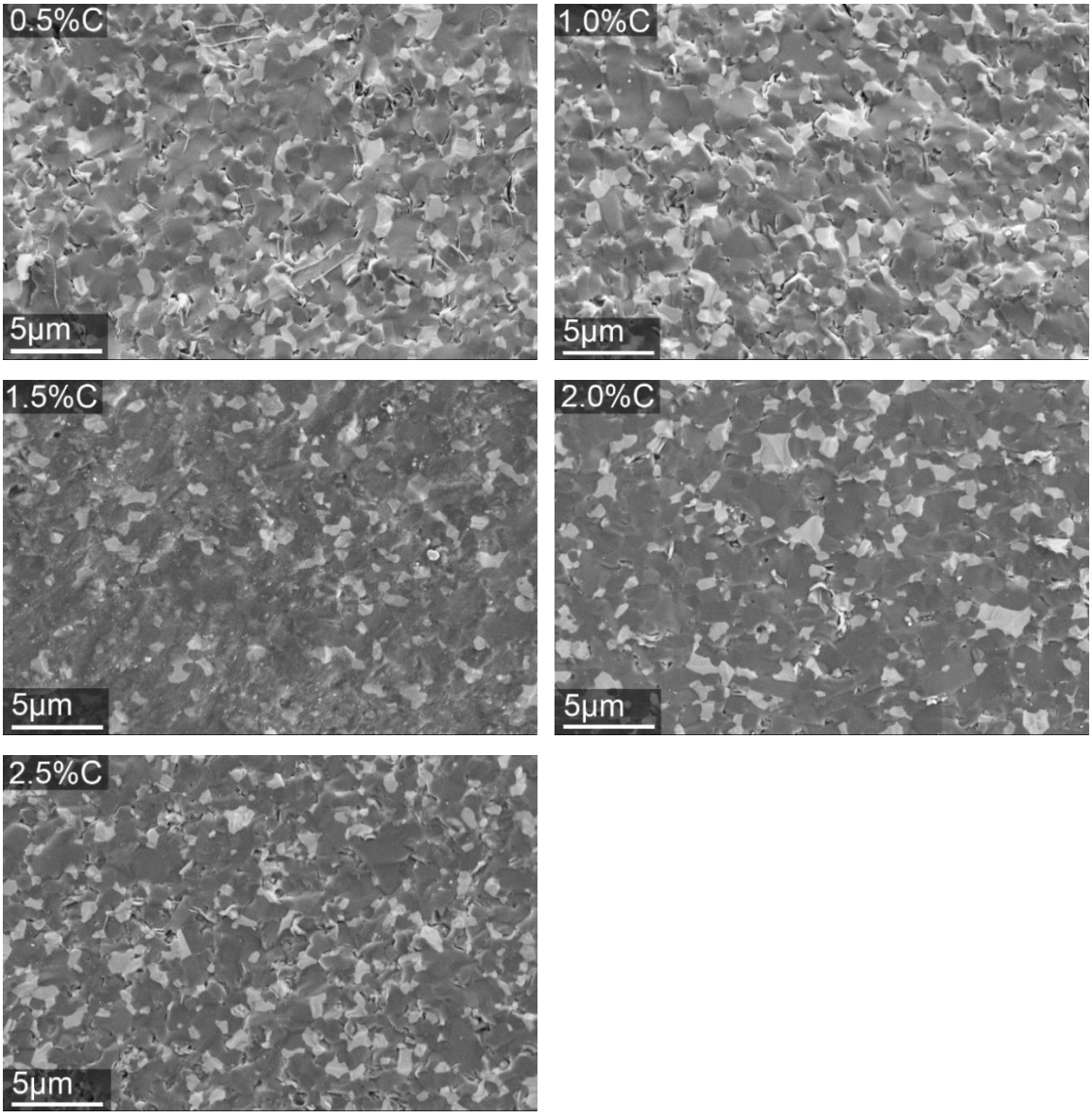

Figure 131. Fracture Surface of 80%B_4C-unetched SiC composites

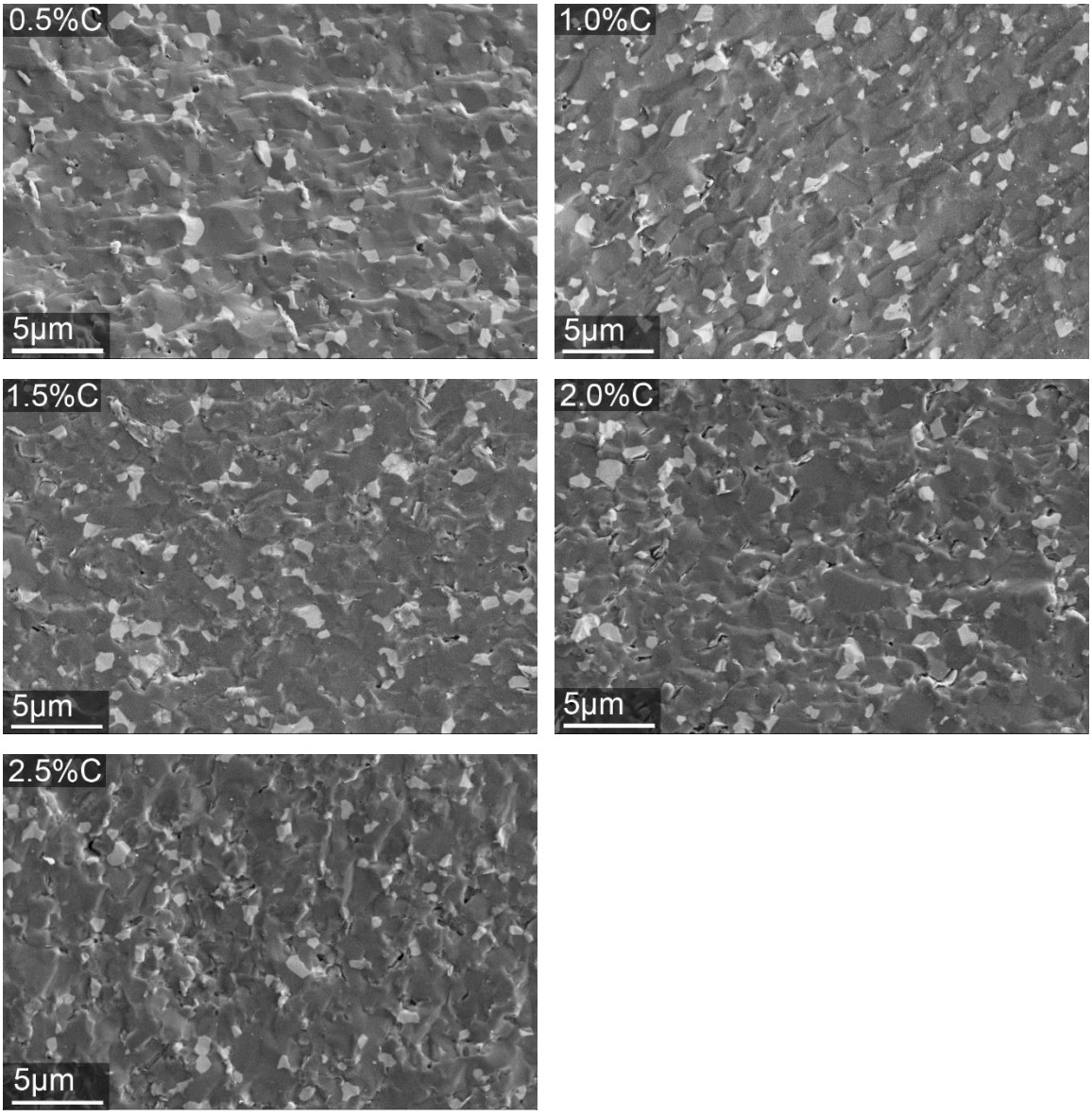

Figure 132. Fracture Surface of 90%B_4C-unetched SiC composites

5.3.2.2. Phase Determination by X-Ray Diffraction

Phase identification of the fully sintered composite samples was done using X-ray diffraction analysis as described in section 4.5.2. X-ray diffraction patterns of the samples can be seen in Figures 133-141. Rietveld refinement of the XRD patterns of the samples

may be seen in Tables 77-85. Silicon carbide, boron carbide and a small amount of carbon were detected as expected in the XRD data of samples. When compared with raw starting materials, no unexpected phase occurred during the sintering process. Since all peaks matched with standard silicon carbide and boron carbide no or undetectable solid solubility occurred. Also, it showed that impurities were not introduced to the powder during the mixing process. Increasing boron carbide from 10% to 90%, increased the boron carbide intensity and decreased the silicon carbide intensity since the percentage of silicon carbide decreased in the composite. In the same composition, increasing the carbon addition from 0.5% to 2.5% did not change the silicon carbide and boron carbide intensities. Some samples showed a residual carbon peak, which increased when the added carbon was increased. In Figures 147-148, the 10% and 20% B_4C series showed a carbon peak only with the addition of 2.5% C. For the 30% and 40% B_4C series (Figures 149-150), only the 2.0% and 2.5%C samples showed a residual carbon peak. In Figures 151-155, all of the remaining samples showed a residual carbon peak. It was clear that increasing the boron carbide percentage in the system, decreased the need for additional carbon. Uehara et al. mentioned that B_4C helped sinter SiC and it could be sintered by without additional carbon when that B_4C powder already had residual carbon [100].

Since the 10% and 20% B_4C samples with different carbon content did not have an excess carbon peak, it showed that the mixing method was effective the excess carbon was in boron carbide from the beginning.

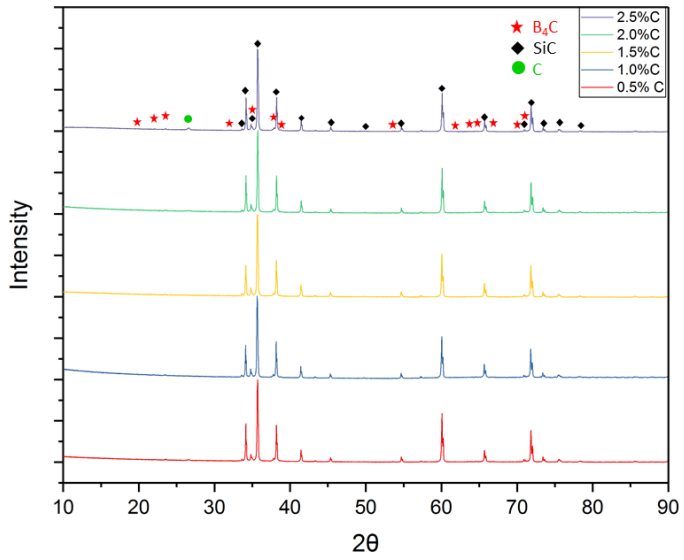

Figure 133. X-ray diffraction patterns of 10% B_4C-unetched SiC with 0.5%C, 1.0%C, 1.5%C, 2.0%C, and 2.5%C

Table 77. Rietveld refinement analyses of 10% B_4C-unetched SiC with 0.5%C, 1.0%C, 1.5%C, 2.0%C, and 2.5%C

Nominal (wt. %)			**Rietveld Refinement of the XRD Patterns**		
B_4C	**SiC**	**C**	**B_4C**	**SiC**	**C**
10	89.5	0.5	10.1±0.1	89.9±0.2	-
10	89.0	1.0	10.6±0.6	89.4±0.7	-
10	88.5	1.5	10.4±0.4	89.6±0.4	-
10	88.0	2.0	10.5±0.6	89.5±0.6	-
10	87.5	2.5	10.5±0.6	89.2±0.6	0.3±0.1

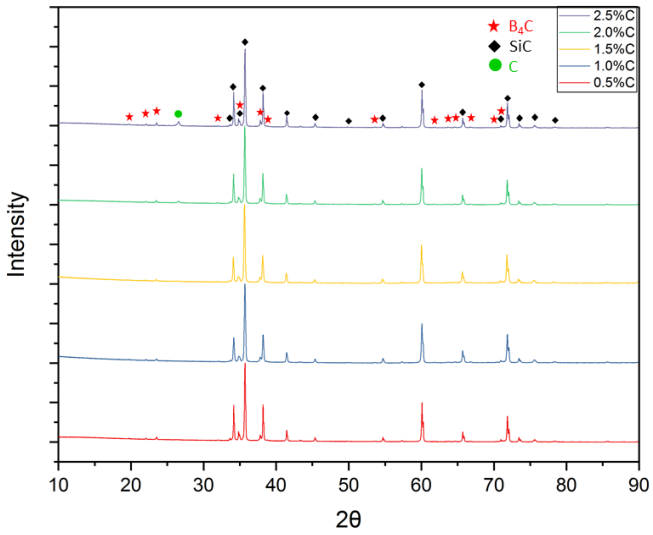

Figure 134. X-ray diffraction patterns of 20% B_4C-unetched SiC with 0.5%C, 1.0%C, 1.5%C, 2.0%C, and 2.5%C

Table 78. Rietveld refinement analyses of 20% B_4C-unetched SiC with 0.5%C, 1.0%C, 1.5%C, 2.0%C, and 2.5%C

Nominal (wt. %)			**Rietveld Refinement of the XRD Patterns**		
B_4C	**SiC**	**C**	**B_4C**	**SiC**	**C**
20	79.5	0.5	20.6±0.4	79.4±0.4	-
20	79.0	1.0	20.4±0.4	79.6±0.4	-
20	78.5	1.5	20.4±0.4	79.6±0.4	-
20	78.0	2.0	20.7±0.4	79.0±0.3	0.3±0.1
20	77.5	2.5	20.6±0.5	78.7±0.5	0.7±0.1

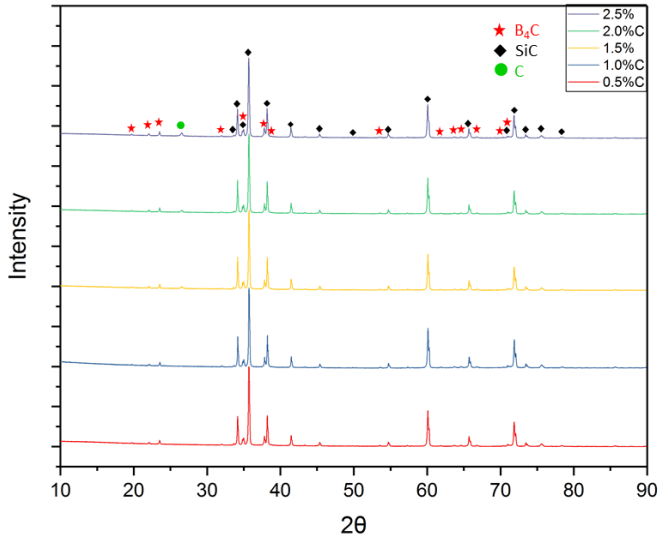

Figure 135. X-ray diffraction patterns of 30% B_4C-unetched SiC with 0.5%C, 1.0%C, 1.5%C, 2.0%C, and 2.5%C

Table 79. Rietveld refinement analyses of 30% B_4C-unetched SiC with 0.5%C, 1.0%C, 1.5%C, 2.0%C, and 2.5%C

Nominal (wt. %)			**Rietveld Refinement of the XRD Patterns**		
B_4C	**SiC**	**C**	**B_4C**	**SiC**	**C**
30	69.5	0.5	31.4±0.5	68.6±0.4	-
30	69.0	1.0	31.0±0.5	69.0±0.4	-
30	68.5	1.5	30.7±0.4	69.2±0.4	0.1±0.1
30	68.0	2.0	31.1±0.4	68.3±0.3	0.6±0.2
30	67.5	2.5	30.9±0.4	68.4±0.3	0.7±0.1

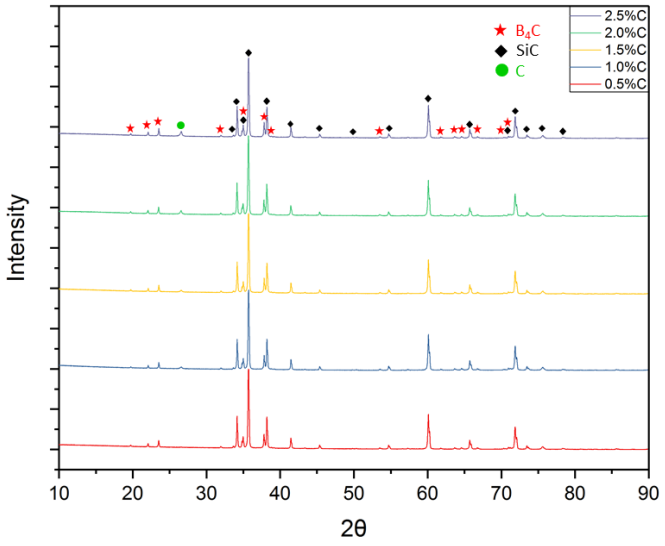

Figure 136. X-ray diffraction patterns of 40% B_4C-unetched SiC with 0.5%C, 1.0%C, 1.5%C, 2.0%C, and 2.5%C

Table 80. Rietveld refinement analyses of 40% B_4C-unetched SiC with 0.5%C, 1.0%C, 1.5%C, 2.0%C, and 2.5%C

Nominal (wt. %)			**Rietveld Refinement of the XRD Patterns**		
B_4C	**SiC**	**C**	**B_4C**	**SiC**	**C**
40	59.5	0.5	40.0±0.4	60.0±0.4	-
40	59.0	1.0	41.0±0.4	58.7±0.4	0.3±0.1
40	58.5	1.5	40.3±0.4	59.3±0.4	0.4±0.2
40	58.0	2.0	40.2±0.4	58.9±0.4	0.9±0.1
40	57.5	2.5	40.5±0.4	58.4±0.3	1.1±0.1

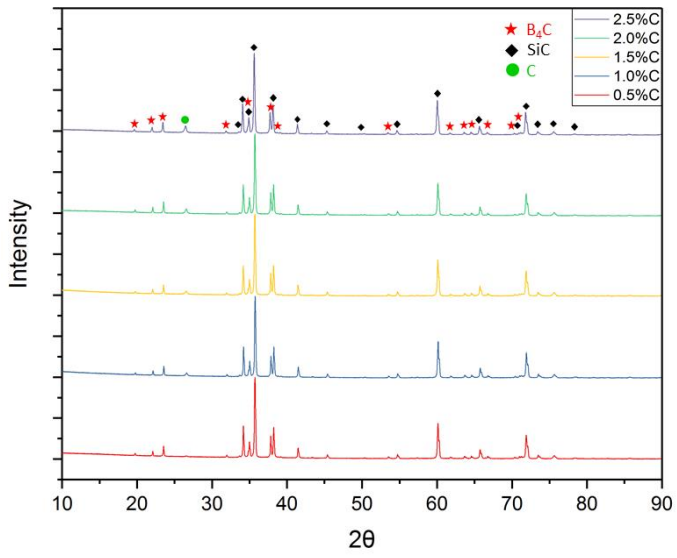

Figure 137. X-ray diffraction patterns of 50% B_4C-unetched SiC with 0.5%C, 1.0%C, 1.5%C, 2.0%C, and 2.5%C

Table 81. Rietveld refinement analyses of 50% B_4C-unetched SiC with 0.5%C, 1.0%C, 1.5%C, 2.0%C, and 2.5%C

Nominal (wt. %)			**Rietveld Refinement of the XRD Patterns**		
B_4C	**SiC**	**C**	**B_4C**	**SiC**	**C**
50	49.5	0.5	50.0±0.4	49.9±0.4	0.1±0.1
50	49.0	1.0	50.3±0.4	49.3±0.3	0.4±0.1
50	48.5	1.5	50.9±0.4	48.7±0.3	0.4±0.1
50	48.0	2.0	50.5±0.4	48.2±0.3	1.3±0.1
50	47.5	2.5	50.6±0.3	47.9±0.3	1.5±0.1

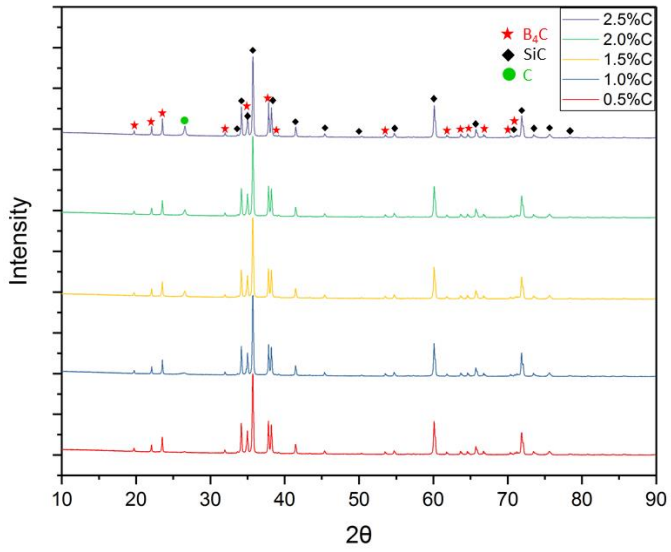

Figure 138. X-ray diffraction patterns of 60% B_4C-unetched SiC with 0.5%C, 1.0%C, 1.5%C, 2.0%C, and 2.5%C

Table 82. Rietveld refinement analyses of 60% B_4C-unetched SiC with 0.5%C, 1.0%C, 1.5%C, 2.0%C, and 2.5%C

Nominal (wt. %)			**Rietveld Refinement of the XRD Patterns**		
B_4C	**SiC**	**C**	**B_4C**	**SiC**	**C**
60	39.5	0.5	61.1±0.3	38.6±0.3	0.3±0.1
60	39.0	1.0	60.7±0.4	38.9±0.3	0.4±0.1
60	38.5	1.5	60.5±0.4	38.8±0.3	0.7±0.1
60	38.0	2.0	60.7±0.4	37.7±0.2	1.6±0.1
60	37.5	2.5	60.6±0.4	37.6±0.3	1.8±0.1

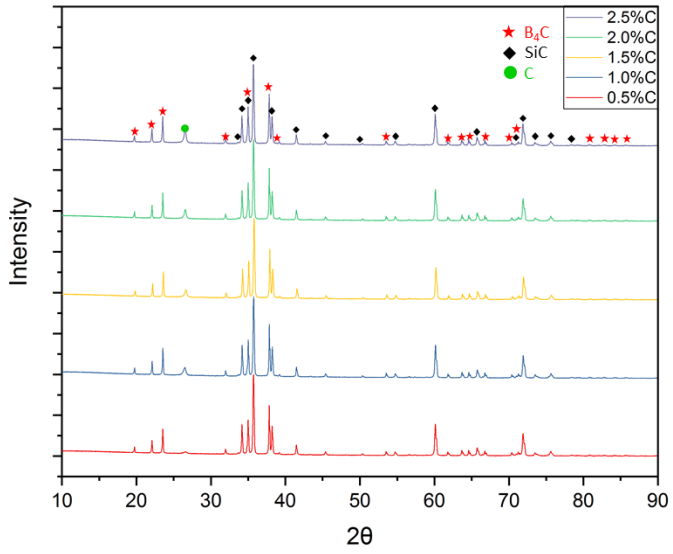

Figure 139. X-ray diffraction patterns of 70% B_4C-unetched SiC with 0.5%C, 1.0%C, 1.5%C, 2.0%C, and 2.5%C

Table 83. Rietveld refinement analyses of 70% B_4C-unetched SiC with 0.5%C, 1.0%C, 1.5%C, 2.0%C, and 2.5%C

Nominal (wt. %)			**Rietveld Refinement of the XRD Patterns**		
B_4C	**SiC**	**C**	**B_4C**	**SiC**	**C**
70	29.5	0.5	70.7±0.3	29.0±0.2	0.3±0.2
70	29.0	1.0	70.5±0.4	28.7±0.2	0.8±0.2
70	28.5	1.5	70.8±0.3	28.4±0.2	0.8±0.1
70	28.0	2.0	71.0±0.4	27.2±0.2	1.8±0.1
70	27.5	2.5	70.4±0.4	27.6±0.2	2.0±0.1

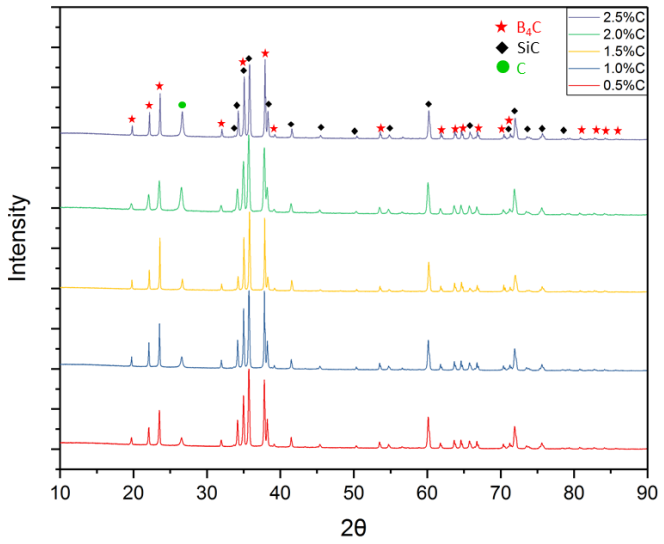

Figure 140. X-ray diffraction patterns of 80% B_4C-unetched SiC with 0.5%C, 1.0%C, 1.5%C, 2.0%C, and 2.5%C

Table 84. Rietveld refinement analyses of 80% B_4C-unetched SiC with 0.5%C, 1.0%C, 1.5%C, 2.0%C, and 2.5%C

Nominal (wt. %)			**Rietveld Refinement of the XRD Patterns**		
B_4C	**SiC**	**C**	**B_4C**	**SiC**	**C**
80	19.5	0.5	80.5±0.3	18.9±0.2	0.6±0.3
80	19.0	1.0	80.5±0.4	18.6±0.2	0.9±0.2
80	18.5	1.5	80.4±0.6	18.7±0.1	0.9±0.2
80	18.0	2.0	80.9±0.4	17.1±0.2	2.0±0.2
80	17.5	2.5	80.5±0.4	17.3±0.2	2.2±0.1

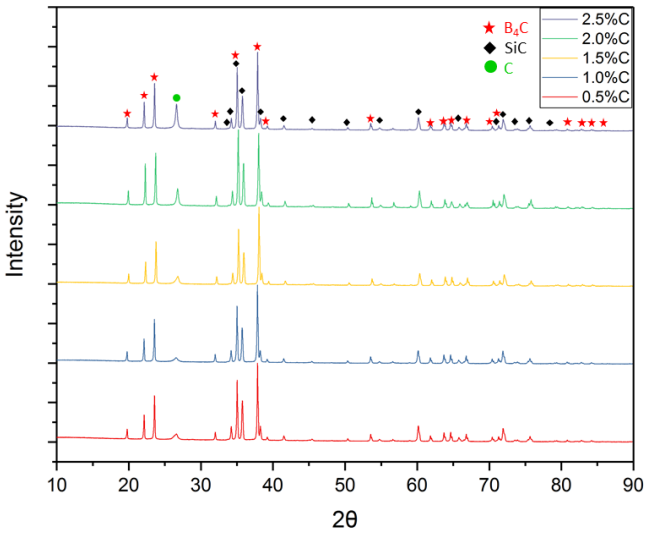

Figure 141. X-ray diffraction patterns of 90% B_4C-unetched SiC with 0.5%C, 1.0%C, 1.5%C, 2.0%C, and 2.5%C

Table 85. Rietveld refinement analyses of 90% B_4C-unetched SiC with 0.5%C, 1.0%C, 1.5%C, 2.0%C, and 2.5%C

Nominal (wt. %)			**Rietveld Refinement of the XRD Patterns**		
B_4C	**SiC**	**C**	**B_4C**	**SiC**	**C**
90	9.5	0.5	90.7±0.3	8.7±0.2	0.6±0.2
90	9.0	1.0	90.8±0.3	8.2±0.2	1.0±0.3
90	8.5	1.5	90.5±0.6	8.1±0.1	1.4±0.1
90	8.0	2.0	90.8±0.4	7.2±0.1	2.0±0.1
90	7.5	2.5	90.5±0.4	7.0±0.2	2.5±0.1

5.3.2.3. Mechanical Properties

5.3.2.3.1. Ultrasound Analysis

The samples' elastic properties were measured using ultrasound analysis. c_L (longitudinal sound speed), c_S (shear sound speed), Poisson's ratio, Young's modulus (E),

shear modulus (G), and bulk modulus (K) values were calculated from equations 22, 23, 24, 25, 26, and 27 respectively as described in section 4.5.3. The density values of the SPS samples were determined using the Archimedes method as described in section 4.5.1. The theoretical density of the samples was determined by the rule of mixture. All sintered samples reached more than 98.26% relative density. These results matched up with the literatures [114, 125].

The oxygen was managed so the carbon addition also played a role as well as the oxygen because the oxygen content was modifying by adding varying amounts of carbon resulted in surplus carbon. Since carbon had mass, it did not affect density, however residual carbon could affect mechanical properties like porosity and decrease the mechanical properties of composites.

The elastic modulus of ceramics is an important property since it can tell how easily the material bended or stretched, and when the material will deform. When increasing the elastic modulus, the materials become stiffer and the material will require greater force to deform.

Looking at the density and elastic properties of all the samples, 1.5% added carbon was enough to remove oxygen. When the addition of carbon was more than 1.5% carbon, it remained in the structure as excess carbon. The precense of carbon is similar to porosity being present and will lead to similar affects on hardness and elastic properties. When compared with the etched samples series, unetched samples showed higher elastic properties values. This might be due to the excess carbon effect.

Also, increasing the boron carbide content from 10% to 90% in the matrix decreased the relative density of samples. Yoshida et al. found similar results processing silicon carbide boron carbide composites with pressureless sintering method [129].

The results of 10% B_4C-SiC composites can be seen in Table 86 and Figure 142. Each value represents the mean of five analyses. The relative density reached ≥99.99% for samples with 0.5%, 1.0%,and 1.5% carbon theneduced to 99.36 % when the carbon content increased to 2.0%, and 99.04% when carbon addition was 2.5%. The Poisson's ratio value increased from 0.158 to 0.168 when the carbon content changed from 0.5% to 1.5% then decreased from 0.168 to 0.159 when the carbon increased from 1.5% to 2.5%. The Young's modulus showed an increase from 443 GPa to 451 GPa when the carbon increased from 0.5% to 1.5%, then decreased from 451 GPa to 400 GPa.The shear modulus changed from 191 GPa to 193 GPa with an increasing carbon content from 0.5% to 1.5% then it decreased from 193 GPa to 173 GPa while the carbon content increased from 1.5% to 2.5%. The bulk modulus increased from 216 GPa to 226 GPa when carbon increased from 0.5% to 1.5%, then declined from 226 GPa to 195 GPa when carbon continued to be added from 1.5% to 2.5%.

Table 86. Elastic properties of 10%B_4C- unetched SiC composites

Sample	**c_L (m/s)**	**c_S(m/s)**	**Poisson's Ratio**	**Bulk Density (g/cm^3)**	**Porosity (%)**	**E (GPa)**	**G (GPa)**	**K (GPa)**
$10B_4C$-SiC-0.5C	12274	7825	0.158±0.003	3.12±0.001	<0.01	443±9	191±4	216±4
$10B_4C$-SiC-1.0C	12435	7866	0.167±0.003	3.12±0.001	<0.01	451±9	193±4	226±5
$10B_4C$-SiC-1.5C	12447	7864	0.168±0.003	3.11±0.001	<0.01	451±9	193±4	226±5
$10B_4C$-SiC-2.0C	11951	7617	0.158±0.003	3.10±0.001	0.64	422±8	181±4	211±4
$10B_4C$-SiC-2.5C	11746	7480	0.159±0.003	3.08±0.001	0.96	400±8	173±4	195±4

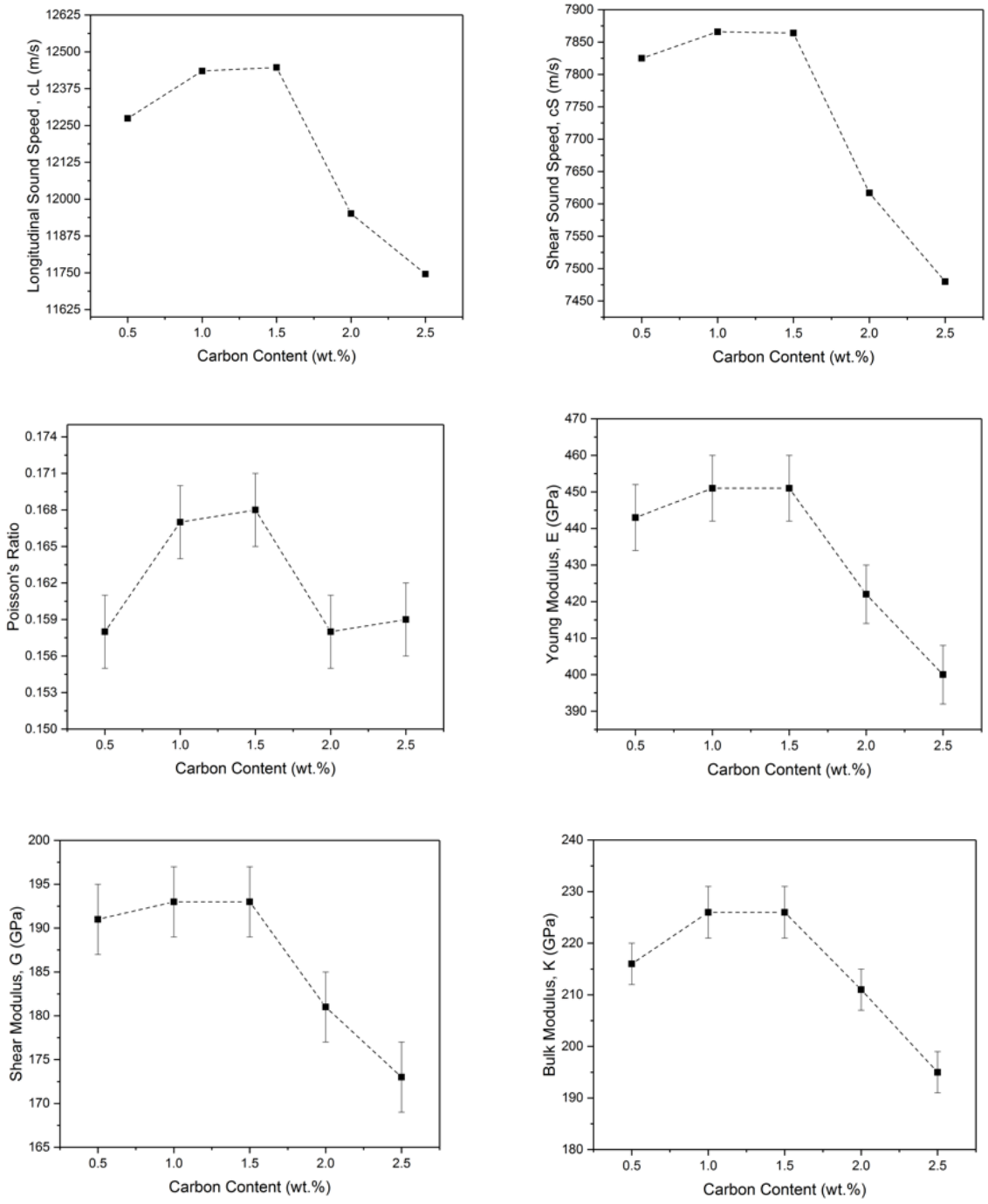

Figure 142. Effect of carbon content on elastic properties of 10%B_4C- unetched SiC composites

The results of 20% B_4C-SiC composites can be seen in Table 87 and Figure 143. Each value represents the mean of five analyses. Samples reached relative density 99.67%

for samples with 0.5%, 1.0%, 1.5%, and 2.0% carbon, and then reduced to 99.01% when the carbon content increased to 2.5%. The Poisson's ratio value increased from 0.156 to 0.166 when the addition of carbon changed from 0.5% to 1.5, then decreased from 0.166 to 0.154 when the carbon addition increased from 1.5% to 2.5%. The Young's modulus showed an increase from 429 GPa to 448 GPa when carbon increased from 0.5% to 1.5%, then decreased from 448 GPa to 400 GPa. The shear modulus changed from 186 GPa to 192 GPa with increasing carbon content from 0.5% to 1.5%, then it decreased from 192 GPa to 173 GPa while the carbon content increased from 1.5% to 2.5%. The bulk modulus increased from 207 GPa to 224 GPa when carbon increased from 0.5% to 1.5%, then declined from 224 GPa to 193 GPa when the carbon increased from 1.5% to 2.5%.

Table 87. Elastic properties of 20%B_4C- unetched SiC composites

Sample	**c_L (m/s)**	**c_S(m/s)**	**Poisson's Ratio**	**Bulk Density (g/cm^3)**	**Porosity (%)**	**E (GPa)**	**G (GPa)**	**K (GPa)**
20B_4C-SiC-0.5C	12228	7809	0.156±0.003	3.03±0.001	0.33	429±9	186±4	207±4
20B_4C-SiC-1.0C	12438	7861	0.167±0.003	3.03±0.001	0.33	438±9	187±4	219±4
20B_4C-SiC-1.5C	12562	7948	0.166±0.003	3.03±0.001	0.33	448±9	192±4	224±5
20B_4C-SiC-2.0C	11932	7600	0.159±0.003	3.02±0.001	0.33	405±8	175±4	198±4
20B_4C-SiC-2.5C	11897	7607	0.154±0.003	2.99±0.001	0.99	400±8	173±4	193±4

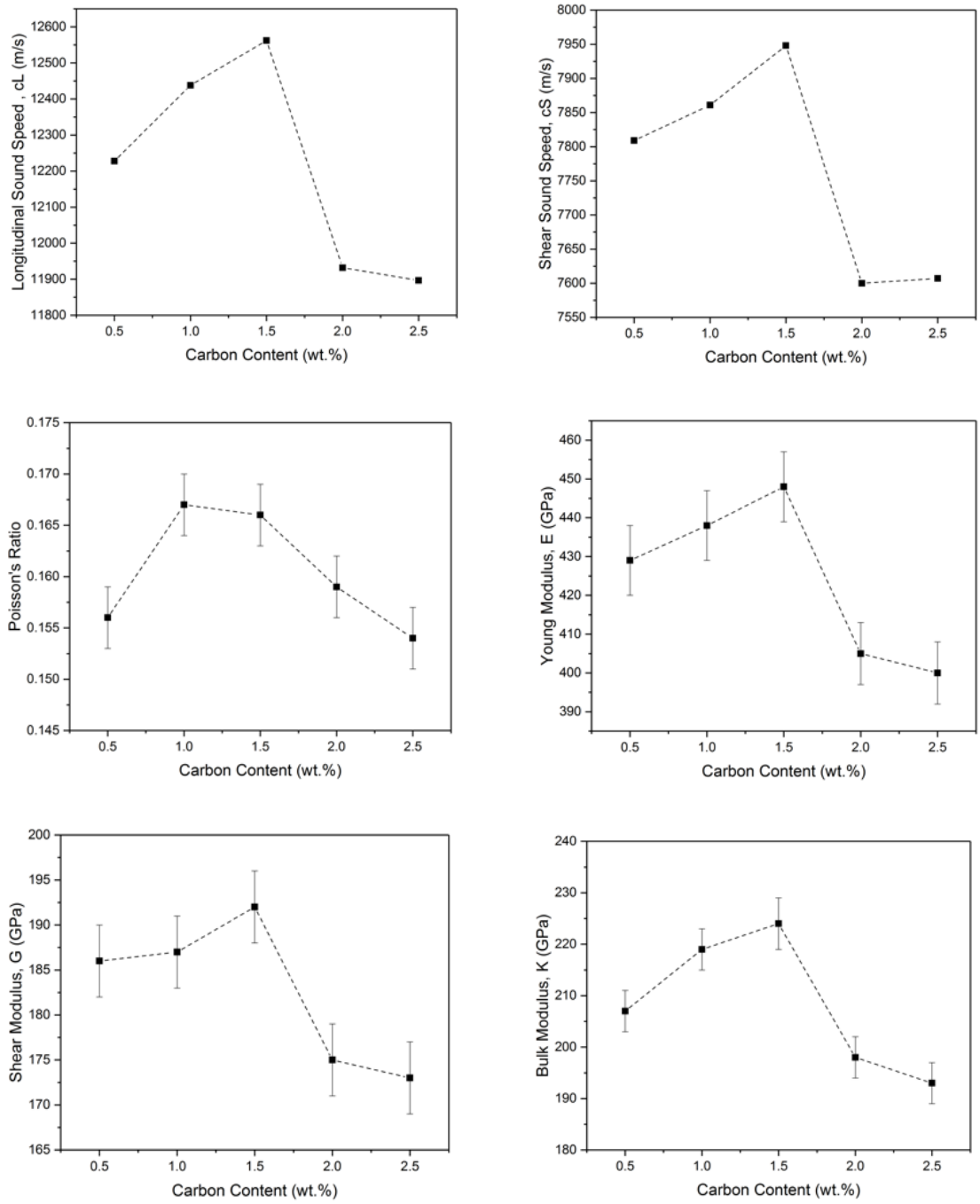

Figure 143. Effect of carbon content on elastic properties of 20%B_4C- unetched SiC composites

The results of 30% B_4C-SiC composites can be seen in Table 88 and Figure 144. Each value represents the mean of five analyses. Relative density reached 99.66% for

samples with 0.5%, 1.0%, 1.5%, and 2.0% carbon, and then reduced to 99.32% when the carbon content increased to 2.5%. The Poisson's ratio value increased from 0.157 to 0.168 when the carbon changed from 0.5% to 1.5%, then decreased from 0.168 to 0.155 when the carbon increased from 1.5% to 2.5%. The Young's modulus showed an increase from 419 GPa to 420 GPa when the carbon increased from 0.5% to 1.5%, then decreased from 420 GPa to 386 GPa. The shear modulus changed from 181 GPa to 180 GPa with an increasing carbon content from 0.5% to 1.5%, then it decreased from 180 GPa to 167 GPa while the carbon content increased from 1.5% to 2.5%. The bulk modulus increased from 204 GPa to 211 GPa when the carbon increased from 0.5% to 1.5%, then declined from 211 GPa to 186 GPa when the carbon further increased from 1.5% to 2.5%.

Table 88. Elastic properties of 30%B_4C- unetched SiC composites

Sample	**c_L (m/s)**	**c_S(m/s)**	**Poisson's Ratio**	**Bulk Density (g/cm^3)**	**Porosity (%)**	**E (GPa)**	**G (GPa)**	**K (GPa)**
30B_4C-SiC-0.5C	12238	7806	0.157±0.003	2.95±0.001	0.34	419±8	181±4	204±4
30B_4C-SiC-1.0C	12374	7821	0.167±0.003	2.95±0.001	0.34	419±8	179±4	210±4
30B_4C-SiC-1.5C	12354	7802	0.168±0.003	2.95±0.001	0.34	420±8	180±4	211±4
30B_4C-SiC-2.0C	11896	7602	0.155±0.003	2.94±0.001	0.34	395±8	171±3	191±4
30B_4C-SiC-2.5C	11851	7574	0.155±0.003	2.92±0.001	0.68	386±8	167±3	186±4

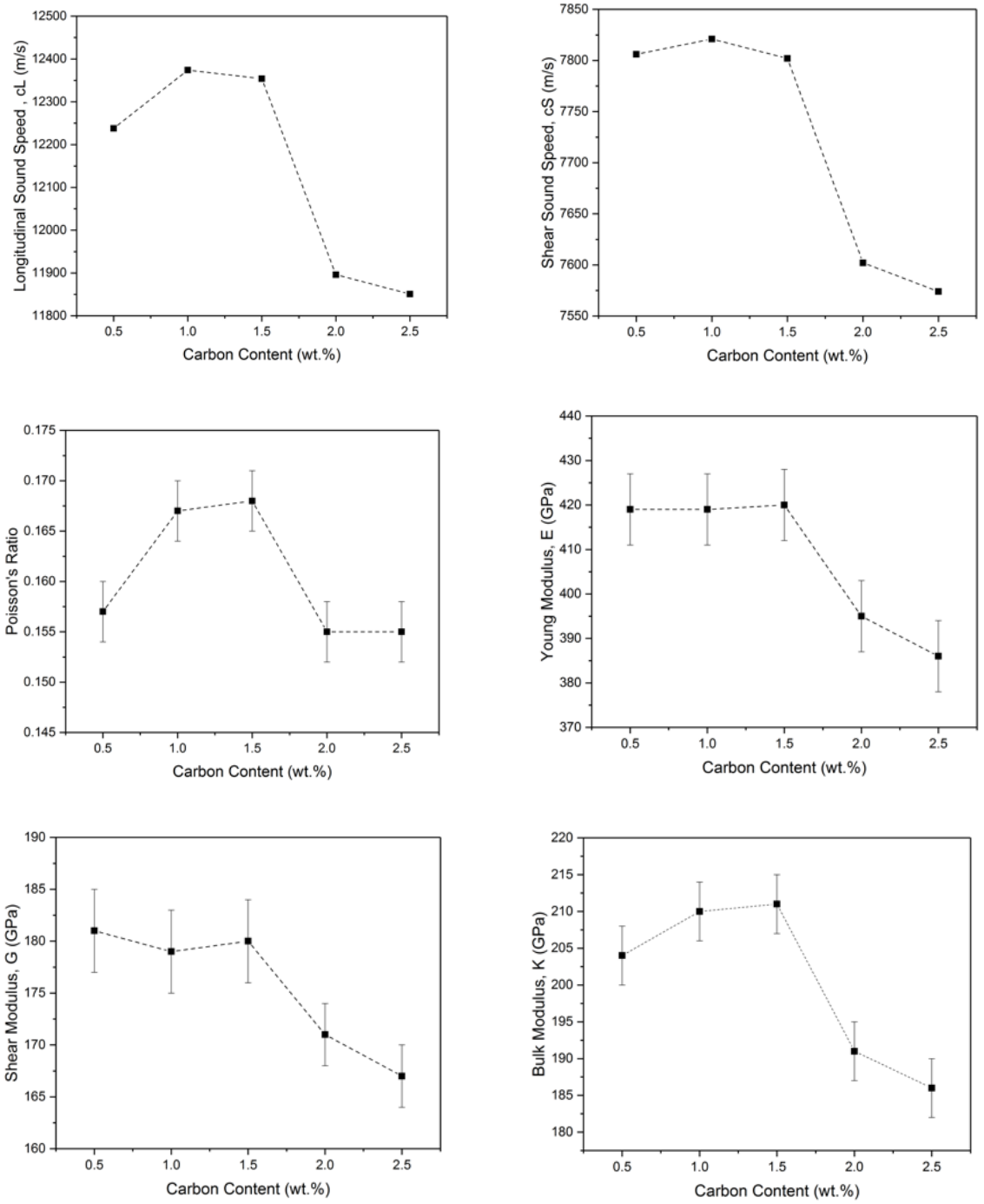

Figure 144. Effect of carbon content on elastic properties of 30%B_4C- unetched SiC composites

The results of 40% B_4C-SiC composites can be seen in Table 89 and Figure 145. Each value represents the mean of five analyses. A 98.97% relative density was obtained with 0.5% and 99.31% 1.0% carbon. The highest relative density was 99.65% and reached with 1.5% carbon. After 1.5% carbon, the relative density of samples decreased to 98.95% at 2.0% carbon and to 98.26% at 2.5% carbon. The Poisson's ratio value increased from 0.155 to 0.167 when the carbon changed from 0.5% to 1.5%, then decreased from 0.167 to 0.155 when the carbon increased from 1.5% to 2.5%. The Young's modulus showed an increase from 407 GPa to 414 GPa when the carbon increased from 0.5% to 1.5%, then decreased from 414 GPa to 380 GPa. The shear modulus changed from 176 GPa to 177 GPa when the carbon content increased from 0.5% to 1.5%, then it decreased from 177 GPa to 164 GPa while the carbon content increased from 1.5% to 2.5%. The bulk modulus increased from 197 GPa to 207 GPa when the carbon contetn increased from 0.5% to 1.5%, then declined from 207 GPa to 183 GPa when the carbon increased from 1.5% to 2.5%. Since high temperatures are needed to densify SiC-B_4C composites Sahani et. al. achieved only 94% relative density with composition of 60%SiC and 40%B4C composites [112].

Table 89. Elastic properties of 40%B_4C- unetched SiC composites

Sample	**c_L (m/s)**	**c_S(m/s)**	**Poisson's Ratio**	**Bulk Density (g/cm^3)**	**Porosity (%)**	**E (GPa)**	**G (GPa)**	**K (GPa)**
40B_4C-SiC-0.5C	12248	7825	0.155±0.003	2.86±0.001	1.03	407±8	176±4	197±4
40B_4C-SiC-1.0C	12441	7871	0.166±0.003	2.86±0.001	0.69	412±8	177±4	206±4
40B_4C-SiC-1.5C	12430	7856	0.167±0.003	2.87±0.002	0.35	414±8	177±4	207±4
40B_4C-SiC-2.0C	12154	7739	0.159±0.003	2.84±0.001	1.05	394±8	170±3	193±4
40B_4C-SiC-2.5C	11946	7634	0.155±0.003	2.82±0.001	1.74	380±8	164±3	183±4

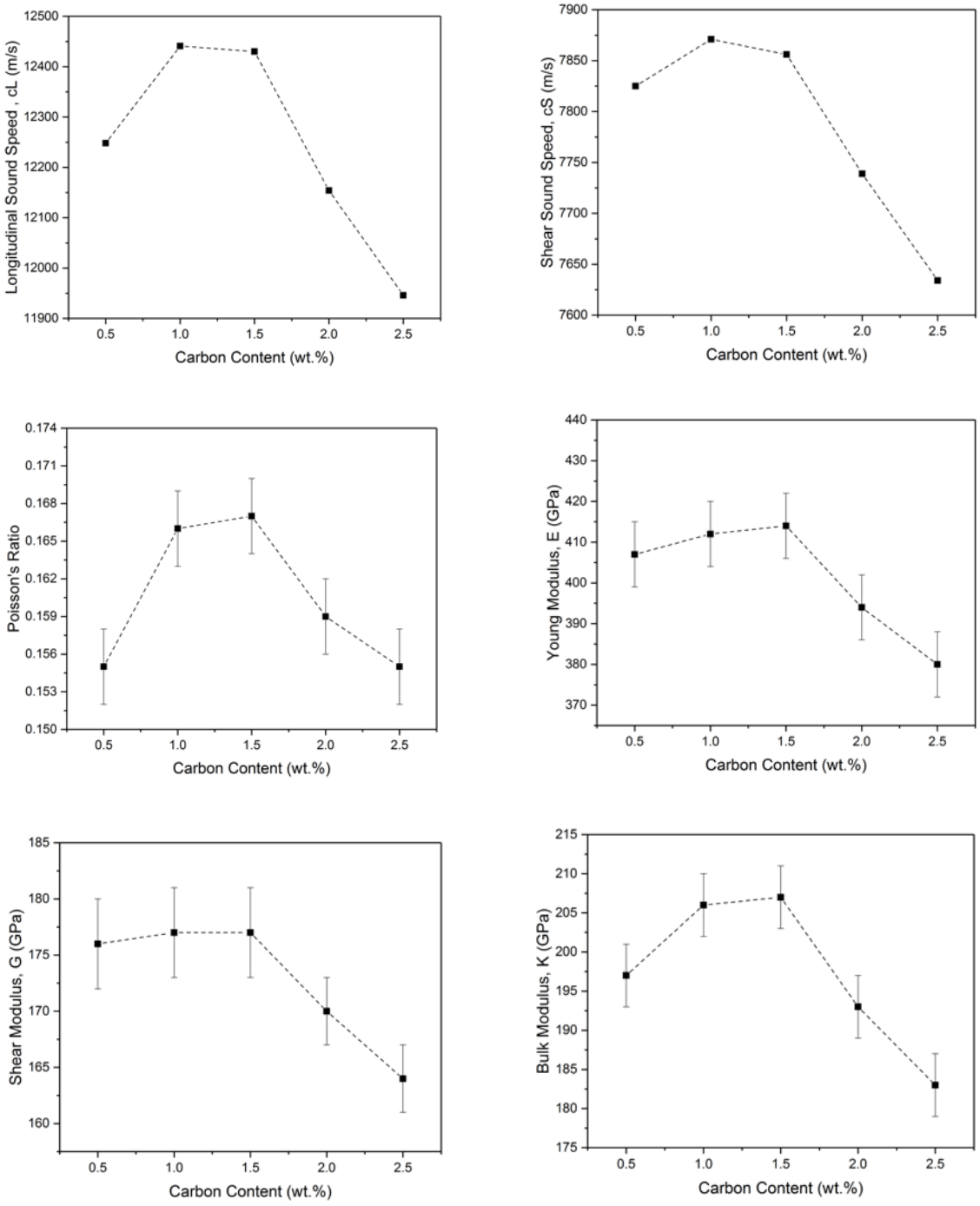

Figure 145. Effect of carbon content on elastic properties of 40%B_4C- unetched SiC composites

The results of 50% B_4C-SiC composites can be seen in Table 90 and Figure 146. Each value represents the mean of five analyses. A 99.29% relative density was achieved with 0.5%. At 1.0% carbon, the sample's relative density was slightly lower than the 0.5% sample, which was 98.99%, but the value was within standard error. The highest relative density was achived 99.65% with 1.5% carbon. The relative density of the samples decreased to 98.93% at 2.0% carbon and 98.21% at 2.5% carbon. The Poisson's ratio value increased from 0.157 to 0.165 when the carbon changed from 0.5% to 1.5%, then decreased from 0.165 to 0.154 when the carbon increased from 1.5% to 2.5%. The Young's modulus showed an increase from 401 GPa to 409 GPa when the carbon increased from 0.5% to 1.5%, then decreased from 409 GPa to 379 GPa. The shear modulus changed from 173 GPa to 176 GPa with an increasing carbon content from 0.5% to 1.5%, then it decreased from 176 GPa to 164 GPa while the carbon content increased from 1.5% to 2.5%. The bulk modulus increased from 195 GPa to 203 GPa when the carbon increased from 0.5% to 1.5% then declined from 203 GPa to 183 GPa when the carbon further increased from 1.5% to 2.5%.

Table 90. Elastic properties of 50%B_4C- unetched SiC composites

Sample	**c_L (m/s)**	**c_S(m/s)**	**Poisson's Ratio**	**Bulk Density (g/cm^3)**	**Porosity (%)**	**E (GPa)**	**G (GPa)**	**K (GPa)**
50B_4C-SiC-0.5C	12319	7858	0.157±0.003	2.80±0.001	0.71	401±8	173±4	195±4
50B_4C-SiC-1.0C	12451	7888	0.165±0.003	2.79±0.001	1.01	404±8	174±4	201±4
50B_4C-SiC-1.5C	12506	7921	0.165±0.003	2.80±0.002	0.35	409±8	176±4	203±4
50B_4C-SiC-2.0C	12286	7851	0.155±0.003	2.77±0.001	1.07	394±8	171±3	190±4
50B_4C-SiC-2.5C	12101	7737	0.154±0.003	2.74±0.001	1.79	379±8	164±3	183±4

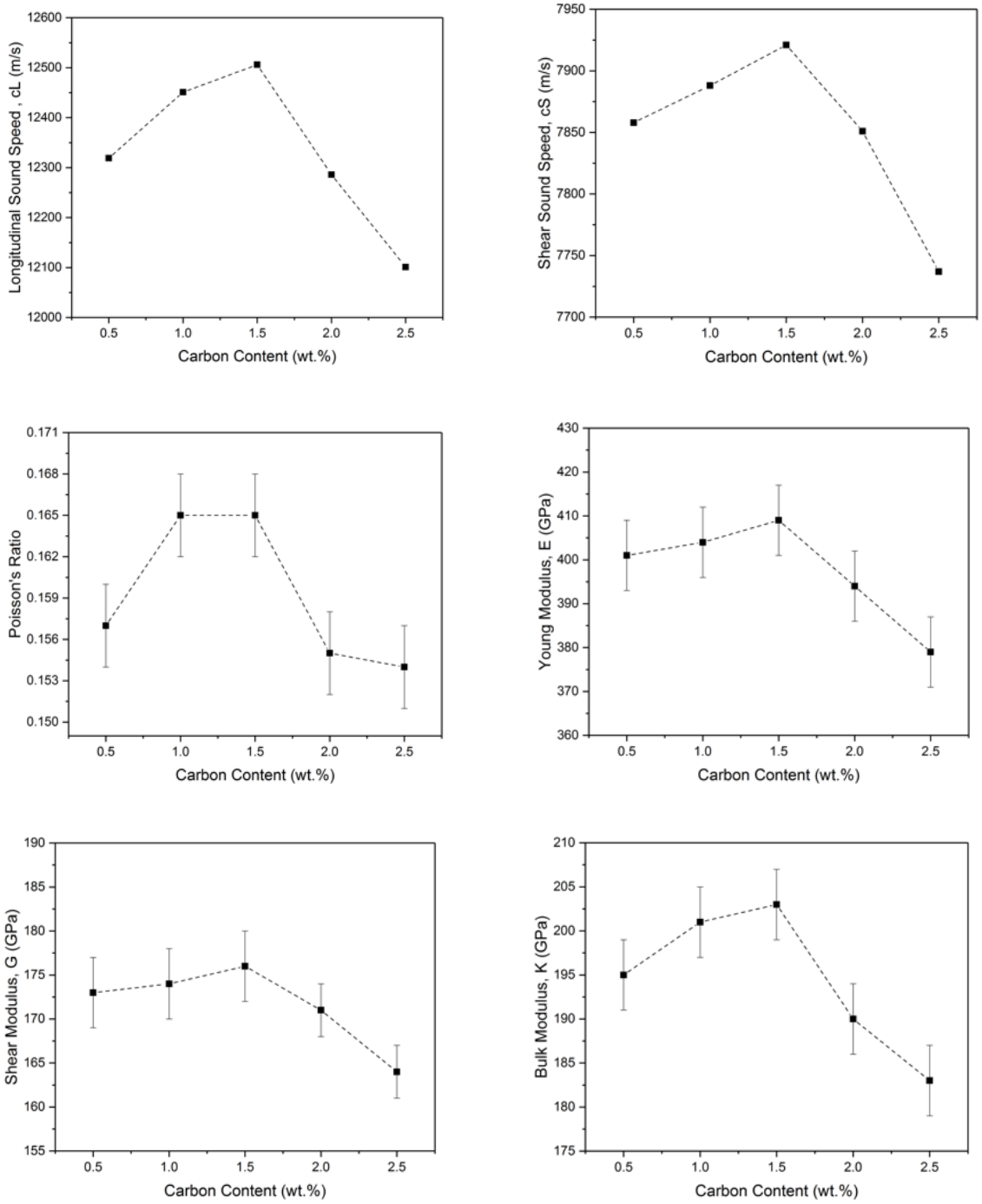

Figure 146. Effect of carbon content on elastic properties of 50%B_4C- unetched SiC composites

The results of 60% B_4C-SiC composites can be seen in Table 91 and Figure 147. Each value represents the mean of five analyses. A 98.91% relative density was obtained with the 0.5% carbon samples. The relative density of the sample decreased to 98.55% at 1.0%, and 1.5% carbon however it was still in standart error. 98.80% and 98.53% relative density was achieved for samples with 2.0% and 2.5% carbon. The Poisson's ratio value increased from 0.154 to 0.164 while the carbon changed from 0.5% to 1.5%, then decreased from 0.164 to 0.154 when the carbon increased from 1.5% to 2.5%. The Young's modulus showed an increase from 400 GPa to 405 GPa when the carbon content increased from 0.5% to 1.5%, then decreased from 405 GPa to 376 GPa. The shear modulus changed from 173 GPa to 174 GPa with an increasing carbon content from 0.5% to 1.5% then it decreased from 174 GPa to 163 GPa when the carbon content increased from 1.5% to 2.5%. The bulk modulus increased from 193 GPa to 201 GPa when the carbon content increased from 0.5% to 1.5%, then decreased from 201 GPa to 181 GPa when the carbon content increased further from 1.5% to 2.5%. Thuault et. al. worked on reaction bonded B_4C-SiC composites, with a composition of 56 wt.% B_4C,32.5 wt.%SiC, and 11.5wt.%Si Young's modulus only reached to 309 GPa which is ~31% lower than the Young's modulus that was obtained in this research.This low elastic modulus was caused by the presence of silicon [96].

Table 91. Elastic properties of 60%B_4C- unetched SiC composites

Sample	**c_L (m/s)**	**c_S(m/s)**	**Poisson's Ratio**	**Bulk Density (g/cm^3)**	**Porosity (%)**	**E (GPa)**	**G (GPa)**	**K (GPa)**
$60B_4C$-SiC-0.5C	12487	7984	0.154±0.003	2.71±0.001	1.09	400±8	173±4	193±4
$60B_4C$-SiC-1.0C	12596	7984	0.164±0.003	2.71±0.002	1.45	405±8	174±4	201±4
$60B_4C$-SiC-1.5C	12665	8031	0.164±0.003	2.70±0.002	1.45	405±8	174±4	201±4
$60B_4C$-SiC-2.0C	12432	7931	0.157±0.003	2.69±0.001	1.2	391±8	169±3	190±4
$60B_4C$-SiC-2.5C	12166	7778	0.154±0.003	2.68±0.001	1.47	376±8	163±3	181±4

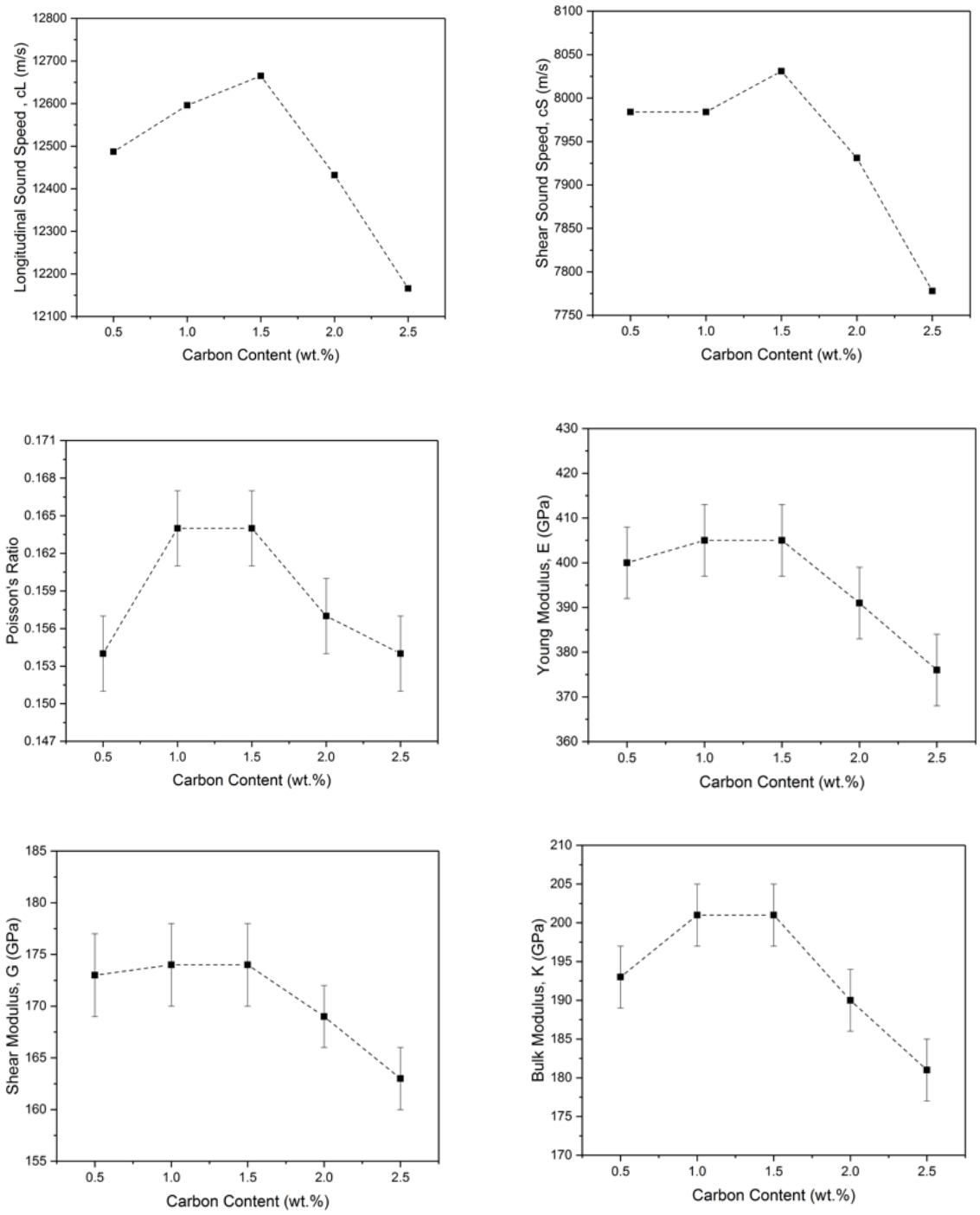

Figure 147. Effect of carbon content on elastic properties of 60%B_4C- unetched SiC composites

The results of 70% B_4C-SiC composites can be seen in Table 92 and Figure 148. Each value represents the mean of five analyses. The relative density of samples increased from 98.14% to 99.26% when the carbon increased from 0.5% to 1.5% carbon. Then the relative density declined from 99.26% to 98.50% when the carbon addition increased from 1.5% to 2.5% carbon. The Poisson's ratio value increased from 0.155 to 0.165 while the addition of carbon changed from 0.5% to 1.5%, then decreased from 0.165 to 0.155 when the carbon addition increased from 1.5% to 2.5%. The Young's modulus showed an increase from 396 GPa to 402 GPa when the carbon increased from 0.5% to 1.5%, then decreased from 402 GPa to 376 GPa. The shear modulus changed from 171 GPa to 172 GPa when carbon content increased from 0.5% to 1.5%, then it decreased from 172 GPa to 163 GPa when the carbon content increased from 1.5% to 2.5%. The bulk modulus increased from 191 GPa to 200 GPa when the carbon increased from 0.5% to 1.5%, then declined from 200 GPa to 181 GPa when the carbon increased from 1.5% to 2.5%.

Table 92. Elastic properties of 70%B_4C- unetched SiC composites

Sample	**c_L (m/s)**	**c_S(m/s)**	**Poisson's Ratio**	**Bulk Density (g/cm^3)**	**Porosity (%)**	**E (GPa)**	**G (GPa)**	**K (GPa)**
70B_4C-SiC-0.5C	12630	8070	0.155±0.003	2.63±0.001	1.86	396±8	171±3	191±4
70B_4C-SiC-1.0C	12789	8103	0.165±0.003	2.64±0.002	1.49	403±8	173±4	200±4
70B_4C-SiC-1.5C	12730	8066	0.165±0.003	2.65±0.002	0.74	402±8	172±3	200±4
70B_4C-SiC-2.0C	12342	7849	0.160±0.003	2.64±0.001	0.76	379±8	163±3	186±4
70B_4C-SiC-2.5C	12341	7886	0.155±0.003	2.62±0.001	1.50	376±8	163±3	181±4

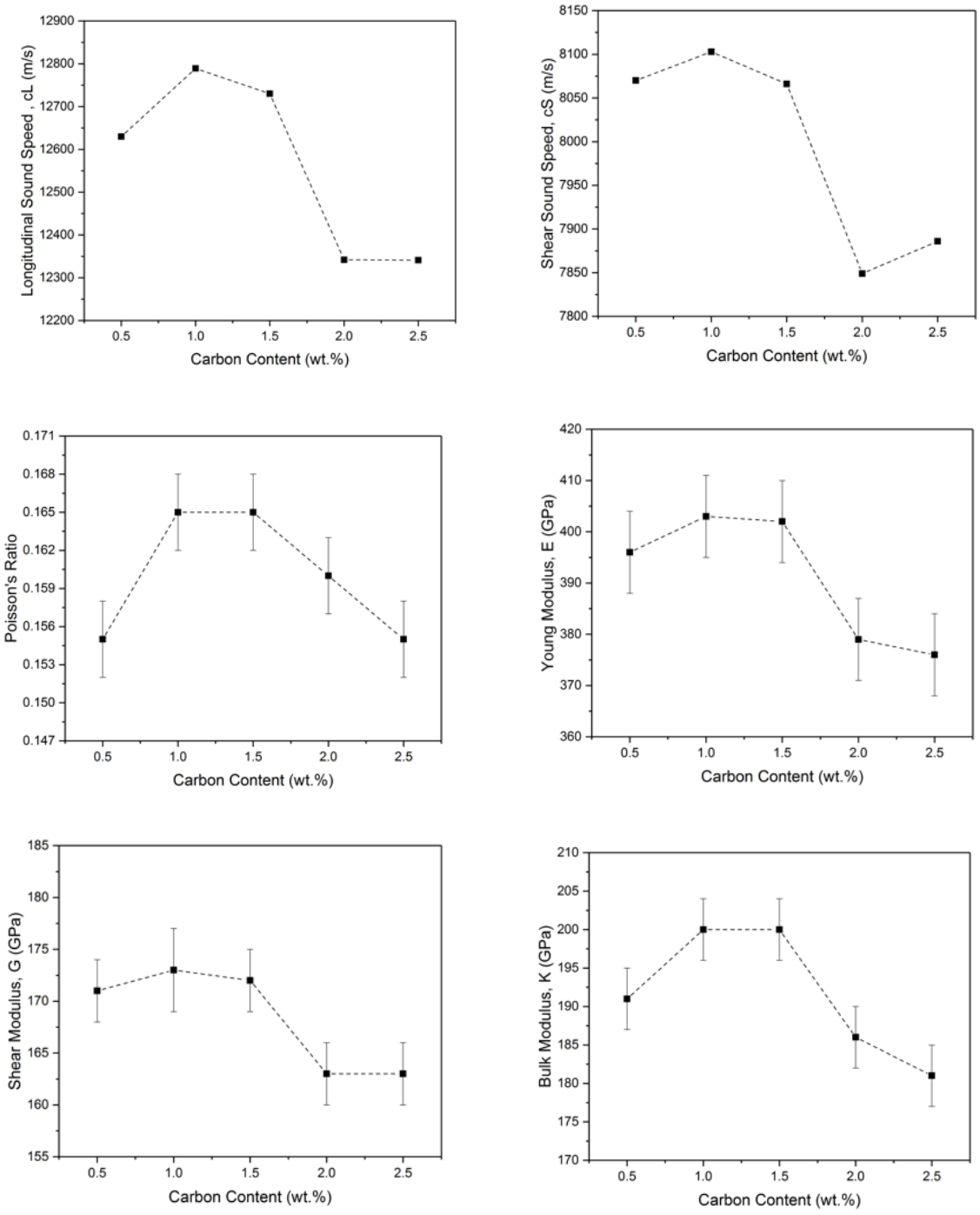

Figure 148. Effect of carbon content on elastic properties of 70%B_4C- unetched SiC composites

The results of 80% B_4C-SiC composites can be seen in Table 93 and Figure 149. Each value represents the mean of five analyses. A 98.48% relative density was obtained with the 0.5%,1.0%, and 1.5% carbon samples. The relative density of the samples was 99.60% at 2.0% and 98.99% at 2.5% carbon. The Poisson's ratio value increased from 0.157 to 0.164 when the carbon changed from 0.5% to 1.5%, then decreased from 0.164 to 0.153 when the carbon addition from 1.5% to 2.5%. The Young's modulus showed an increase from 387 GPa to 402 GPa when the carbon increased from 0.5% to 1.5%, then decreased from 402 GPa to 370 GPa. The shear modulus changed from 167 GPa to 173 GPa when the carbon content increased from 0.5% to 1.5%, then it decreased from 173 GPa to 160 GPa while the carbon content increased from 1.5% to 2.5%. The bulk modulus increased from 188 GPa to 200 GPa when the carbon increased from 0.5% to 1.5%, then declined from 200 GPa to 178 GPa when the carbon increased further from 1.5% to 2.5%.

Table 93. Elastic properties of 80%B_4C- unetched SiC composites

Sample	**c_L (m/s)**	**c_S(m/s)**	**Poisson's Ratio**	**Bulk Density (g/cm^3)**	**Porosity (%)**	**E (GPa)**	**G (GPa)**	**K (GPa)**
$80B_4C$-SiC-0.5C	12593	8031	0.157±0.003	2.58±0.001	1.52	387±8	167±3	188±4
$80B_4C$-SiC-1.0C	12873	8169	0.163±0.003	2.58±0.002	1.52	401±8	173±4	198±4
$80B_4C$-SiC-1.5C	12912	8183	0.164±0.003	2.58±0.002	1.52	402±8	173±4	200±4
$80B_4C$-SiC-2.0C	12358	7871	0.159±0.003	2.58±0.001	0.40	371±7	160±3	181±4
$80B_4C$-SiC-2.5C	12298	7869	0.153±0.003	2.57±0.001	1.01	370±7	160±3	178±4

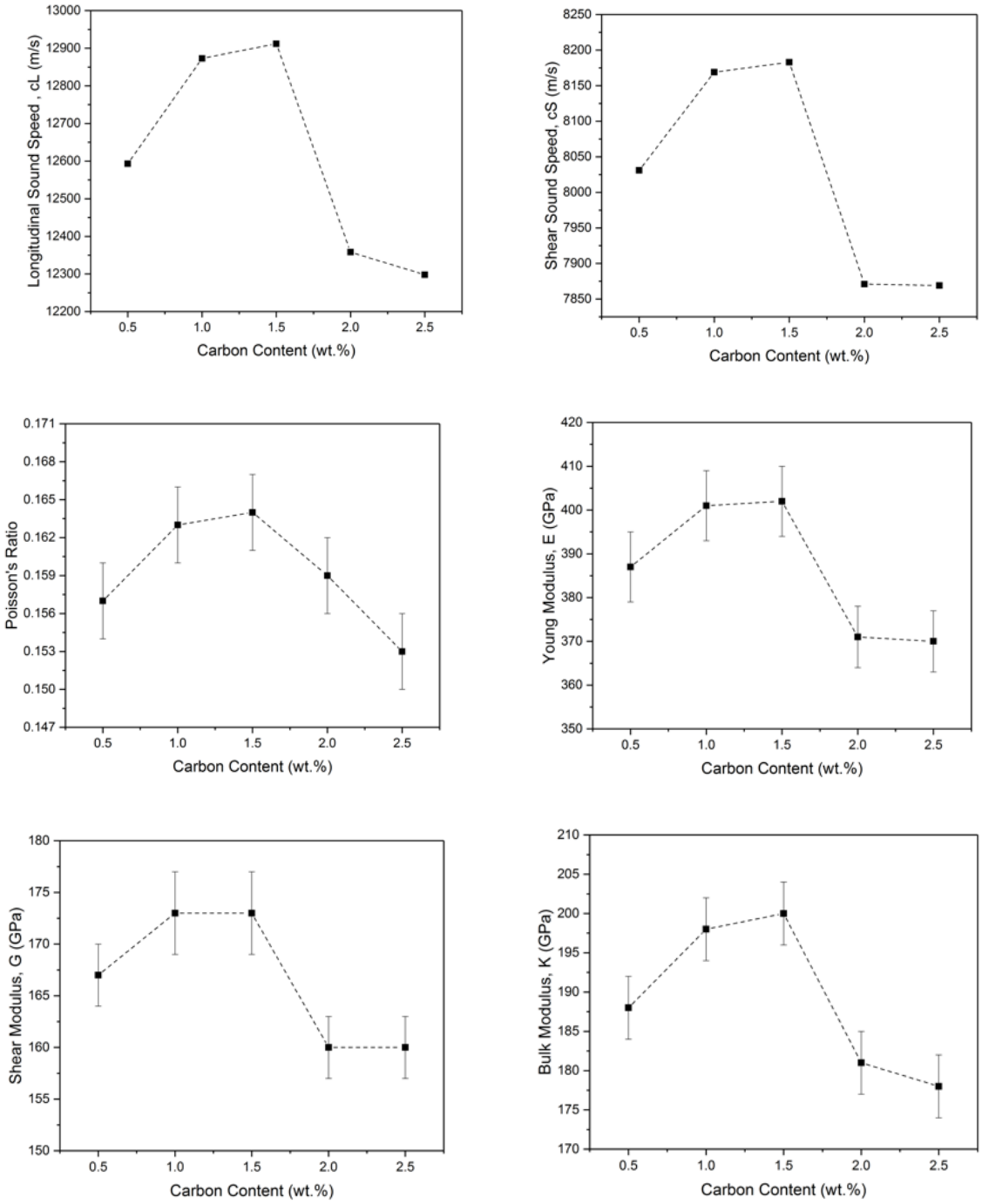

Figure 149. Effect of carbon content on elastic properties of 80%B_4C- unetched SiC composites

The results of 90% B_4C-SiC composites can be seen in Table 94 and Figure 150. Each value represents the mean of five analyses. The relative density was increased from 98.83% to 99.61% when the carbon content changed from 0.5% to 1.5%. However, it decreased from 99.22% to 99.20% when the carbon content increased from 1.5% to 2.5%. The Poisson's ratio value increased from 0.157 to 0.162 when the addition of carbon changed from 0.5% to 1.5%, then decreased from 0.162 to 0.154 when the carbon addition increased from 1.5% to 2.5%. The Young's modulus showed an increase from 380 GPa to 401 GPa when the carbon content increased from 0.5% to 1.5%, then decreased from 401 GPa to 365 GPa. The shear modulus changed from 164 GPa to 173 GPa when the carbon content increased from 0.5% to 1.5%, then it decreased from 173 GPa to 158 GPa when the carbon content increased from 1.5% to 2.5%. The bulk modulus increased from 185 GPa to 197 GPa when the carbon increased from 0.5% to 1.5%, then declined from 197 GPa to 176 GPa when the carbon content increased from 1.5% to 2.5%.

Table 94. Elastic properties of 90%B_4C- unetched SiC composites

Sample	**c_L (m/s)**	**c_S(m/s)**	**Poisson's Ratio**	**Bulk Density (g/cm^3)**	**Porosity (%)**	**E (GPa)**	**G (GPa)**	**K (GPa)**
90B_4C-SiC-0.5C	12614	8043	0.157±0.003	2.53±0.002	1.17	380±8	164±3	185±4
90B_4C-SiC-1.0C	12812	8141	0.161±0.003	2.54±0.001	0.39	391±8	168±3	192±4
90B_4C-SiC-1.5C	12977	8244	0.162±0.003	2.54±0.001	0.39	401±8	173±4	197±4
90B_4C-SiC-2.0C	12379	7887	0.158±0.003	2.53±0.001	0.39	365±7	158±3	178±4
90B_4C-SiC-2.5C	12400	7931	0.154±0.003	2.51±0.001	0.80	365±7	158±3	176±4

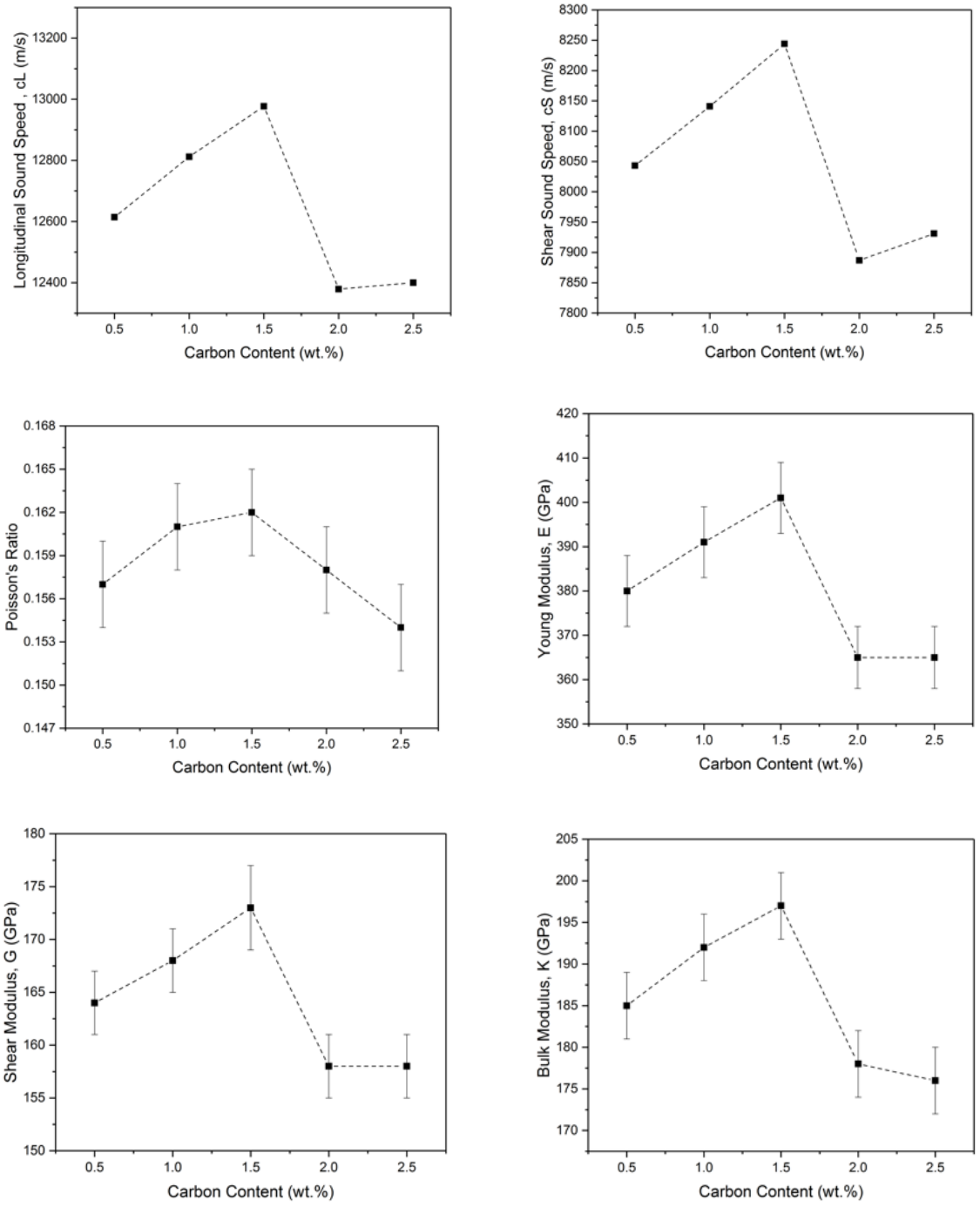

Figure 150. Effect of carbon content on elastic properties of 90%B_4C- unetched SiC composites

5.3.2.3.2. Vickers Microhardness and Indentation Fracture Toughness

The samples' hardness values were measured using Vickers diamond intentation and the fracture toughness values were calculated by measuring Vickers indenter crack length, as described in section 4.5.5. using equations 28 and 29.

The hardness of a material is an important property since it tells how much the material can resist plastic deformation when a load is applied. Materials that have higher hardness can resist more to deformation.

For all boron carbide content, the 1.5% carbon addition series obtained higher hardness values than other carbon series. The 1.5% carbon addition was enough to remove excess oxygen in the powders, so the 2.0% and 2.5% carbon had surplus carbon remaining in the samples, and that excess carbon caused the relative density to decrease. Since the density affects the hardness, decreasing the density decreased the hardness [123]. As mention above the precense of excess carbon is similar to porosity and will lead to similar affects on hardness.

Boron carbide has a higher hardness than silicon carbide, so increasing the boron carbide content in the composites increased the hardness of samples. The highest hardness value was 32.85 GPa reached at 90%B_4C-1.5%C-SiC.

Except for the 10% B_4C-SiC samples SiC grain size, all the grain sizes for both SiC and B_4C had submicron grain sizes. Even though the grain size values were close to each other, slightly larger grain sizes can be observed when the oxygen content was reduced by

adding carbon up to 1.5% carbon. Then grain size would again be decreased due to the effect of additional carbon.

Fracture toughness is an important property since it is related to the materials resistance to brittle fracture when a crack is present. Fracture toughness has an inverse relation with hardness. Even though both silicon carbide and boron carbide are hard ceramics and have a low fracture toughness, since boron carbide is harder than silicon carbide, boron carbide fracture toughness values are lower than silicon carbide. So increasing the boron carbide content in the composites decreased the fracture toughness of samples.The best indentation fracture toughness value was 2.87 $MPa.m^{1/2}$ and gained at the 10%B_4C-2.5%C-SiC. Since the 2.5% C series had some pores, it obtained a slightly higher fracture toughness value as the discussion in the literature stated [66]. Also, as mentioned above, the thermal expansion coefficients of silicon carbide and boron carbide are similar, so this difference does not affect the fracture mode, but it can influence fracture toughness value.

The Vickers hardness and indentation fracture toughness results can be seen in Tables 95 through 104 and in Figures 151 through 159. Each value represents the mean of ten calculated hardness and indentation fracture toughness.

Table 95. Hardness and fracture toughness of 10%B_4C-unetched SiC composites

Sample	Hardness (GPa)	Fracture Toughness ($MPa.m^{1/2}$)
10B_4C-SiC-0.5C	28.42±0.84	2.85±0.12
10B_4C-SiC-1.0C	28.75±0.63	2.82±0.13
10B_4C-SiC-1.5C	28.79±0.49	2.84±0.17
10B_4C-SiC-2.0C	28.57±1.32	2.85±0.18
10B_4C-SiC-2.5C	27.49±0.92	2.87±0.09

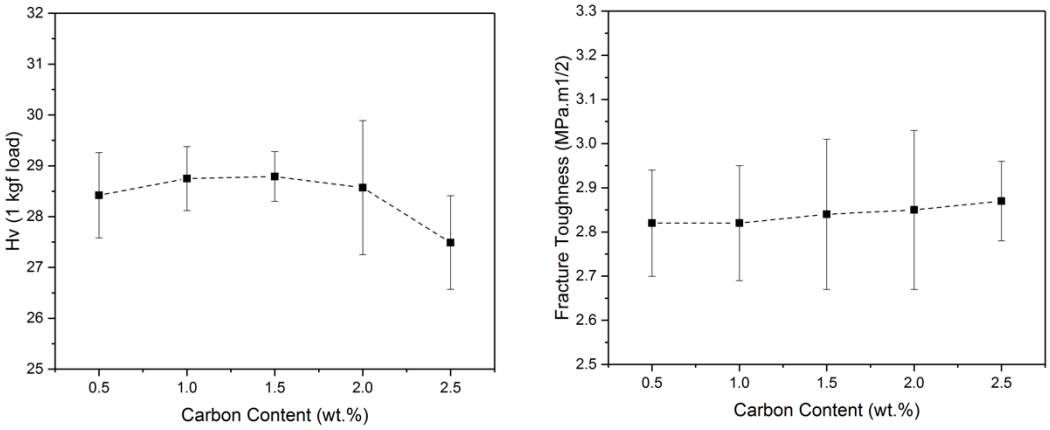

Figure 151. Effect of carbon content on hardness and fracture toughness of 10%B_4C-unetched SiC composites

Table 96. Hardness and fracture toughness of 20%B_4C-unetched SiC composites

Sample	Hardness (GPa)	Fracture Toughness ($MPa.m^{1/2}$)
20B_4C-SiC-0.5C	28.45±0.89	2.81±0.11
20B_4C-SiC-1.0C	29.19±0.67	2.80±0.11
20B_4C-SiC-1.5C	29.35±0.68	2.79±0.17
20B_4C-SiC-2.0C	28.61±0.43	2.81±0.19
20B_4C-SiC-2.5C	27.96±1.01	2.83±0.13

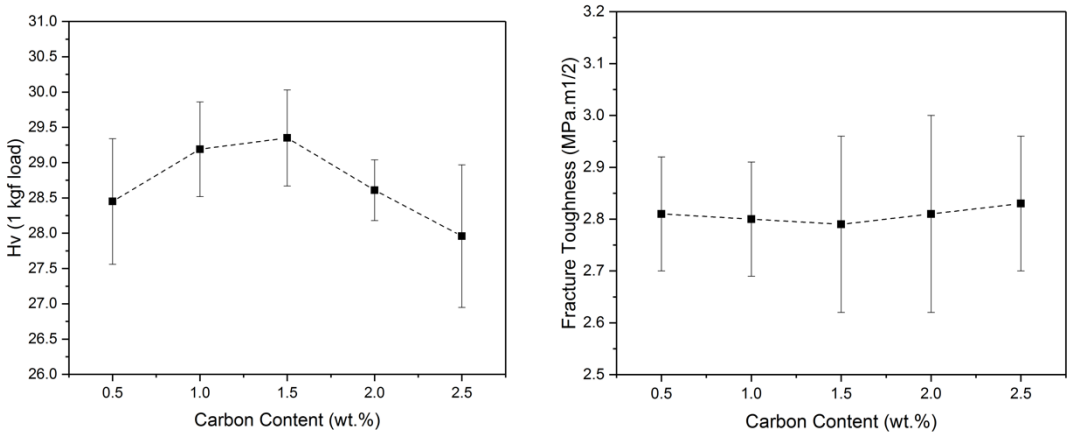

Figure 152. Effect of carbon content on hardness and fracture toughness of 20%B_4C-unetched SiC composites

Table 97. Hardness and fracture toughness of 30%B_4C-unetched SiC composites

Sample	Hardness (GPa)	Fracture Toughness ($MPa.m^{1/2}$)
30B_4C-SiC-0.5C	29.10±0.49	2.74±0.09
30B_4C-SiC-1.0C	29.21±0.73	2.74±0.08
30B_4C-SiC-1.5C	29.70±1.19	2.74±0.19
30B_4C-SiC-2.0C	28.86±0.92	2.76±0.11
30B_4C-SiC-2.5C	28.47±0.94	2.78±0.13

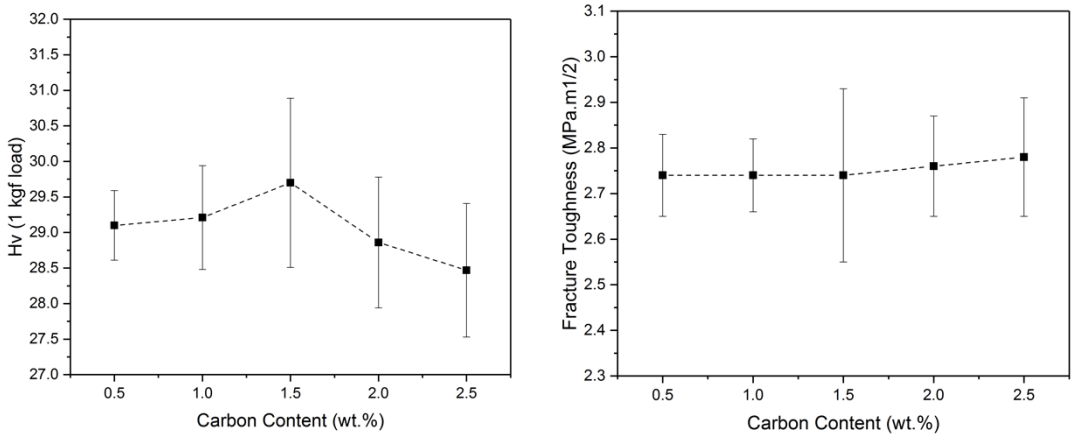

Figure 153. Effect of carbon content on hardness and fracture toughness of 30%B_4C-unetched SiC composites

Table 98. Hardness and fracture toughness of 40%B_4C-unetched SiC composites

Sample	Hardness (GPa)	Fracture Toughness ($MPa.m^{1/2}$)
40B_4C-SiC-0.5C	29.22±0.62	2.68±0.15
40B_4C-SiC-1.0C	29.31±0.30	2.68±0.09
40B_4C-SiC-1.5C	29.87±0.66	2.67±0.13
40B_4C-SiC-2.0C	29.67±0.42	2.67±0.15
40B_4C-SiC-2.5C	29.69±0.89	2.68±0.11

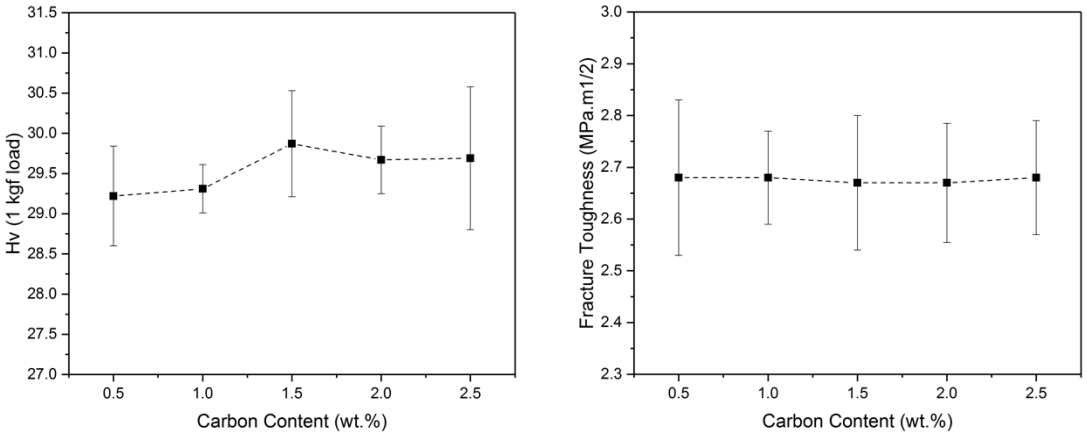

Figure 154. Effect of carbon content on hardness and fracture toughness of 40%B_4C-unetched SiC composites

Table 99. Hardness and fracture toughness of 50%B_4C-unetched SiC composites

Sample	Hardness (GPa)	Fracture Toughness ($MPa.m^{1/2}$)
50B_4C-SiC-0.5C	30.65±1.11	2.64±0.05
50B_4C-SiC-1.0C	30.73±0.41	2.63±0.09
50B_4C-SiC-1.5C	30.79±1.79	2.63±0.24
50B_4C-SiC-2.0C	30.46±0.46	2.65±0.15
50B_4C-SiC-2.5C	29.74±0.97	2.65±0.09

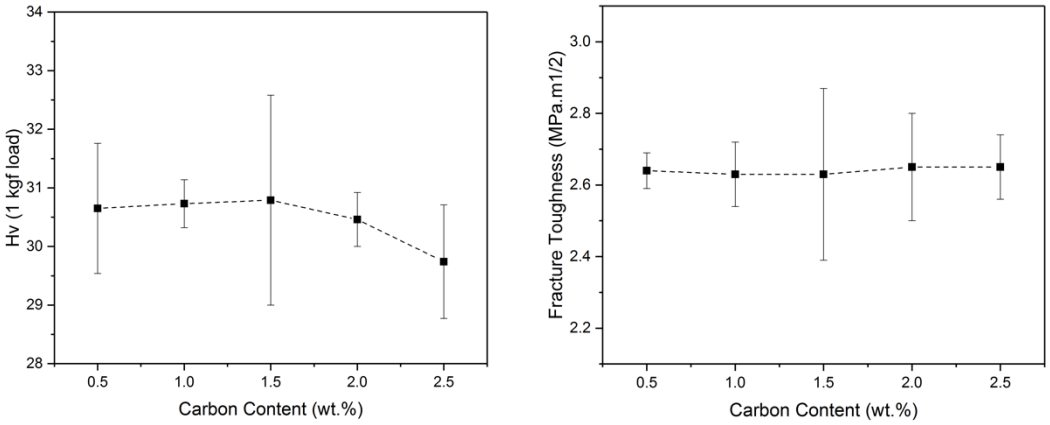

Figure 155. Effect of carbon content on hardness and fracture toughness of 50%B_4C-unetched SiC composites

As mention previously Sahani et. al. achieved only 94% relative density at 60%SiC-40% B4C, due to the porosity the hardness was only 28 GPa. The hardness achieved was ~ 11% higher than Sahani results in this research.

Table 100. Hardness and fracture toughness of 60%B_4C-unetched SiC composites

Sample	Hardness (GPa)	Fracture Toughness ($MPa.m^{1/2}$)
60B_4C-SiC-0.5C	30.75±0.73	2.60±0.07
60B_4C-SiC-1.0C	30.95±0.75	2.60±0.06
60B_4C-SiC-1.5C	31.05±0.60	2.60±0.09
60B_4C-SiC-2.0C	30.10±0.30	2.61±0.09
60B_4C-SiC-2.5C	30.03±1.00	2.62±0.07

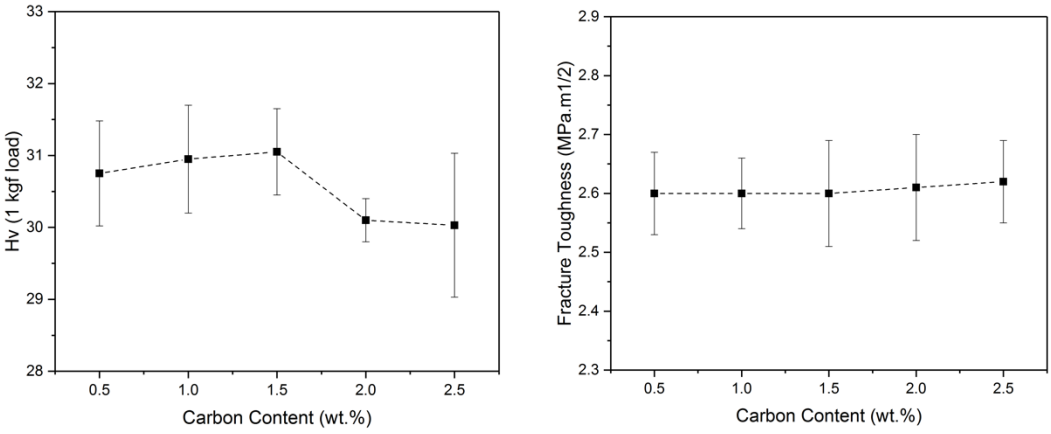

Figure 156. Effect of carbon content on hardness and fracture toughness of 60%B_4C-unetched SiC composites

Table 101. Hardness and fracture toughness of 70%B_4C-unetched SiC composites

Sample	Hardness (GPa)	Fracture Toughness ($MPa.m^{1/2}$)
70B_4C-SiC-0.5C	30.79±1.66	2.56±0.17
70B_4C-SiC-1.0C	31.30±1.17	2.55±0.10
70B_4C-SiC-1.5C	32.20±1.28	2.54±0.10
70B_4C-SiC-2.0C	30.98±0.94	2.58±0.17
70B_4C-SiC-2.5C	30.07±1.00	2.61±0.16

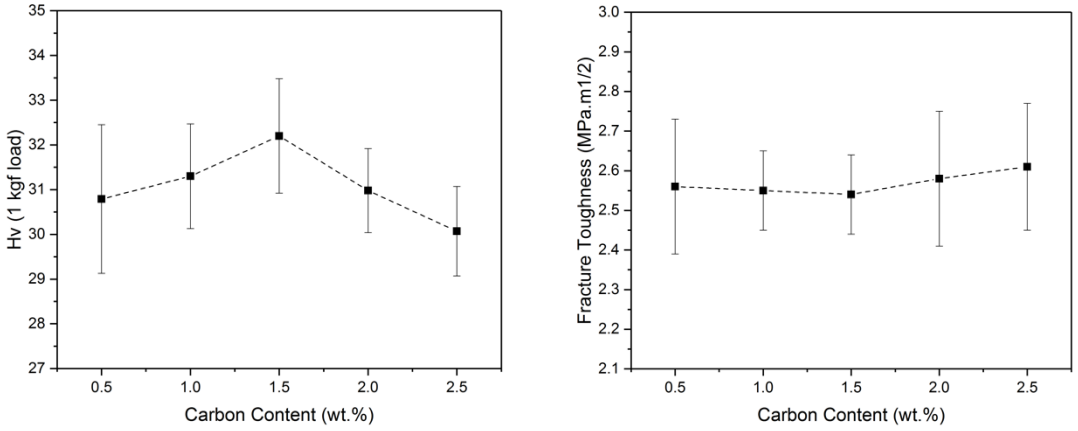

Figure 157. Effect of carbon content on hardness and fracture toughness of 70%B_4C-unetched SiC composites

Table 102. Hardness and fracture toughness of 80%B_4C-unetched SiC composites

Sample	Hardness (GPa)	Fracture Toughness ($MPa.m^{1/2}$)
80B_4C-SiC-0.5C	32.01±0.82	2.55±0.07
80B_4C-SiC-1.0C	32.04±0.87	2.55±0.08
80B_4C-SiC-1.5C	32.64±1.03	2.54±0.10
80B_4C-SiC-2.0C	31.68±0.75	2.55±0.14
80B_4C-SiC-2.5C	31.54±0.94	2.58±0.16

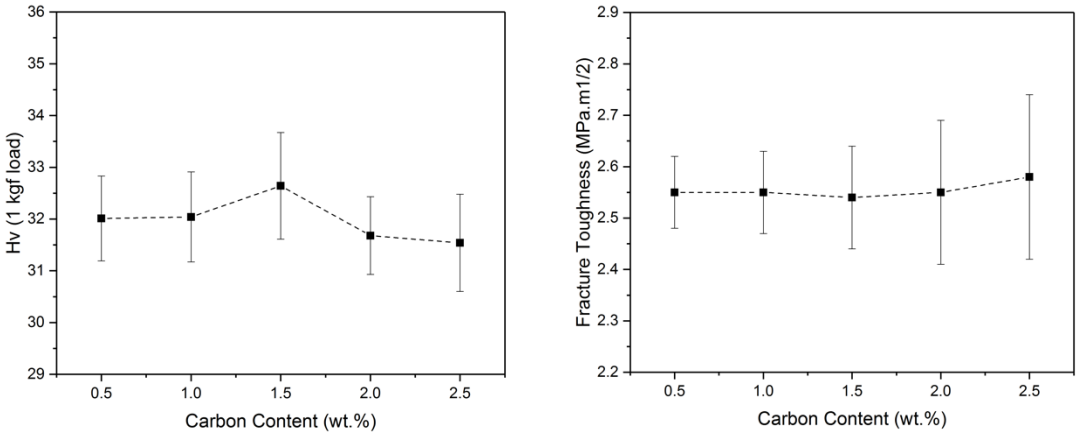

Figure 158. Effect of carbon content on hardness and fracture toughness of 80%B_4C-unetched SiC composites

Table 103. Hardness and fracture toughness of 90%B_4C-unetched SiC composites

Sample	Hardness (GPa)	Fracture Toughness ($MPa.m^{1/2}$)
90B_4C-SiC-0.5C	32.63±1.44	2.53±0.10
90B_4C-SiC-1.0C	32.73±1.02	2.53±0.15
90B_4C-SiC-1.5C	32.85±1.28	2.51±0.17
90B_4C-SiC-2.0C	32.52±0.96	2.54±0.20
90B_4C-SiC-2.5C	31.68±1.94	2.57±0.17

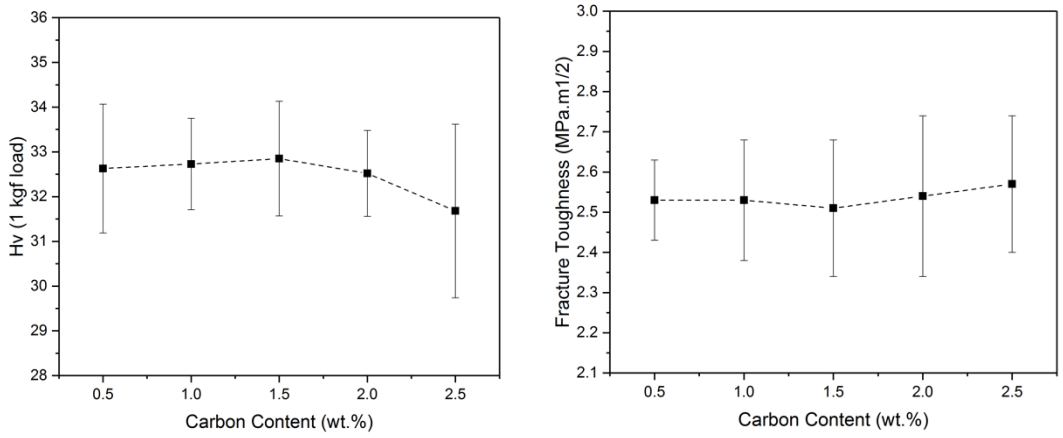

Figure 159. Effect of carbon content on hardness and fracture toughness of 90%B_4C-unetched SiC composites

5.3.2.3.3. Berkovich Hardness and Reduced Modulus

The Berkovich hardness and reduced modulus were measured as described in section 4.5.6. Unlike microhardness, nanoindentation had the advantage of smaller indents to be analyzed since it had low load ability. These smaller indents could determine the effect of homogeneity in the material on the nanoindentation hardness and reduced modulus.

For this test, twenty indents were made for each load at 100Mn, 300mN, and 500mN to polished sample surfaces. The MicroMaterials software was used to calculate the hardness values of samples using the indenter load and the depth of penetration. Each result represented the average of twenty indents (abnormal shaped indents were not include in the analysis), and these results are shown in Tables 104 through 112. Load versus hardness and reduced modulus curves can be seen in Figures 160 through 168. The plots showed that both hardness and reduced modulus values decreased with increasing applied load. Even if the values were close to each other, a slight decrease can still be seen. For each series, 1.5% carbon showed higher results because 2.0% and 2.5% carbon series had residual carbon. The 1.5% carbon addition was enough to remove the oxide layer, so increasing the carbon content further caused the excess carbon.

Table 104. Berkovich hardness and reduced modulus of 10%B_4C-unetched SiC composites

100mN (10g)	**H (GPa)**	**Std. Dev.**	**Reduced Modulus (GPa)**	**Std. Dev.**
10B_4C-SiC-0.5C	33.47	1.06	320.49	10.44
10B_4C-SiC-1.0C	33.79	1.21	332.12	10.33
10B_4C-SiC-1.5C	34.15	0.87	341.57	09.72
10B_4C-SiC-2.0C	33.94	1.06	325.29	10.88
10B_4C-SiC-2.5C	33.62	1.02	325.35	10.00
300mN (30g)	**H (GPa)**	**Std. Dev.**	**Reduced Modulus (GPa)**	**Std. Dev.**
10B_4C-SiC-0.5C	33.75	1.16	320.25	07.59
10B_4C-SiC-1.0C	33.38	1.03	327.58	09.85
10B_4C-SiC-1.5C	33.80	0.71	336.99	08.51
10B_4C-SiC-2.0C	33.16	1.69	324.33	10.05
10B_4C-SiC-2.5C	32.49	1.10	308.92	10.29
500mN (50g)	**H (GPa)**	**Std. Dev.**	**Reduced Modulus (GPa)**	**Std. Dev.**
10B_4C-SiC-0.5C	32.10	0.78	311.63	10.93
10B_4C-SiC-1.0C	32.82	1.53	320.26	09.88
10B_4C-SiC-1.5C	33.29	1.57	331.30	06.81
10B_4C-SiC-2.0C	31.73	1.46	311.69	10.53
10B_4C-SiC-2.5C	31.17	1.13	310.84	10.74

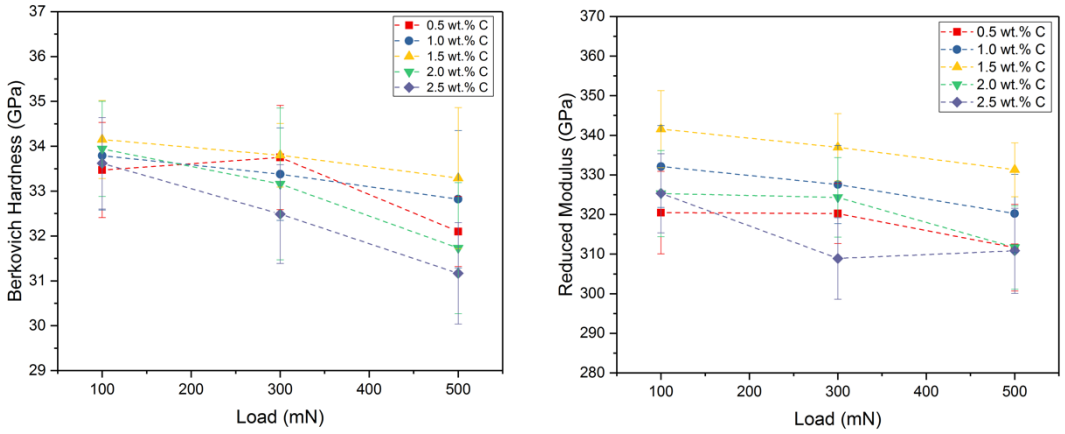

Figure 160. Load- hardness and load- reduced modulus curves for 10%B_4C-unetched SiC composites

Table 105. Berkovich hardness and reduced modulus of 20%B_4C-unetched SiC composites

100mN (10g)	**H (GPa)**	**Std. Dev.**	**Reduced Modulus (GPa)**	**Std. Dev.**
20B_4C-SiC-0.5C	34.79	1.80	331.26	07.98
20B_4C-SiC-1.0C	34.76	1.33	333.75	10.74
20B_4C-SiC-1.5C	36.25	1.52	341.86	10.23
20B_4C-SiC-2.0C	33.67	1.81	335.67	10.11
20B_4C-SiC-2.5C	33.33	1.85	315.14	10.39
300mN (30g)	**H (GPa)**	**Std. Dev.**	**Reduced Modulus (GPa)**	**Std. Dev.**
20B_4C-SiC-0.5C	33.66	1.60	324.67	10.65
20B_4C-SiC-1.0C	34.04	1.07	330.64	10.78
20B_4C-SiC-1.5C	34.11	1.30	335.33	10.02
20B_4C-SiC-2.0C	33.75	1.70	324.72	06.70
20B_4C-SiC-2.5C	33.46	1.57	317.51	10.96
500mN (50g)	**H (GPa)**	**Std. Dev.**	**Reduced Modulus (GPa)**	**Std. Dev.**
20B_4C-SiC-0.5C	33.40	1.11	330.10	10.08
20B_4C-SiC-1.0C	33.57	1.49	325.61	07.56
20B_4C-SiC-1.5C	33.62	1.13	333.33	10.68
20B_4C-SiC-2.0C	33.38	1.92	322.25	05.47
20B_4C-SiC-2.5C	33.35	1.16	315.45	10.06

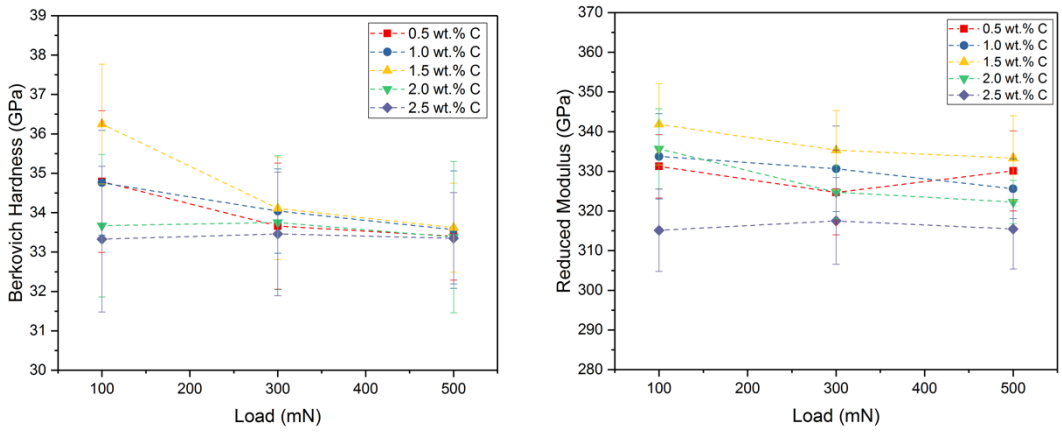

Figure 161. Load- hardness and load- reduced modulus curves for 20%B_4C-unetched SiC composites

Table 106. Berkovich hardness and reduced modulus of 30%B_4C-unetched SiC composites

100mN (10g)	**H (GPa)**	**Std. Dev.**	**Reduced Modulus (GPa)**	**Std. Dev.**
30B_4C-SiC-0.5C	36.23	1.32	328.69	07.04
30B_4C-SiC-1.0C	35.01	1.56	336.65	06.13
30B_4C-SiC-1.5C	35.64	1.04	342.84	10.95
30B_4C-SiC-2.0C	35.22	1.35	334.01	07.99
30B_4C-SiC-2.5C	32.98	1.23	329.56	10.08
300mN (30g)	**H (GPa)**	**Std. Dev.**	**Reduced Modulus (GPa)**	**Std. Dev.**
30B_4C-SiC-0.5C	34.57	1.40	322.55	10.89
30B_4C-SiC-1.0C	35.20	1.58	337.76	06.74
30B_4C-SiC-1.5C	35.69	1.72	343.41	10.33
30B_4C-SiC-2.0C	35.08	1.17	331.48	05.69
30B_4C-SiC-2.5C	34.57	1.09	331.56	10.44
500mN (50g)	**H (GPa)**	**Std. Dev.**	**Reduced Modulus (GPa)**	**Std. Dev.**
30B_4C-SiC-0.5C	34.55	1.00	321.25	07.16
30B_4C-SiC-1.0C	34.55	1.10	329.49	10.37
30B_4C-SiC-1.5C	34.67	1.84	339.87	10.38
30B_4C-SiC-2.0C	34.41	1.09	330.14	10.23
30B_4C-SiC-2.5C	34.35	1.26	333.93	05.06

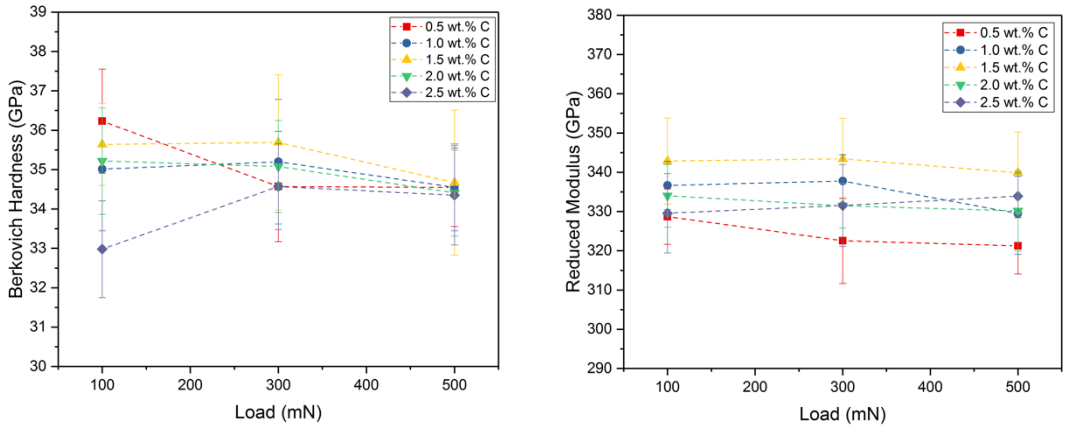

Figure 162. Load- hardness and load- reduced modulus curves for 30%B_4C-unetched SiC composites

Table 107. Berkovich hardness and reduced modulus of 40%B_4C-unetched SiC composites

100mN (10g)	**H (GPa)**	**Std. Dev.**	**Reduced Modulus (GPa)**	**Std. Dev.**
40B_4C-SiC-0.5C	36.21	1.14	328.71	10.14
40B_4C-SiC-1.0C	32.63	1.92	328.44	10.81
40B_4C-SiC-1.5C	35.17	1.00	338.73	10.70
40B_4C-SiC-2.0C	34.00	1.99	332.72	10.32
40B_4C-SiC-2.5C	34.38	1.67	333.67	08.88
300mN (30g)	**H (GPa)**	**Std. Dev.**	**Reduced Modulus (GPa)**	**Std. Dev.**
40B_4C-SiC-0.5C	35.67	1.14	337.73	07.86
40B_4C-SiC-1.0C	36.18	1.89	336.97	08.16
40B_4C-SiC-1.5C	35.88	1.83	345.41	10.84
40B_4C-SiC-2.0C	35.35	1.51	330.63	10.22
40B_4C-SiC-2.5C	35.54	1.53	324.37	09.05
500mN (50g)	**H (GPa)**	**Std. Dev.**	**Reduced Modulus (GPa)**	**Std. Dev.**
40B_4C-SiC-0.5C	34.95	1.83	320.13	07.65
40B_4C-SiC-1.0C	35.00	1.81	334.03	07.67
40B_4C-SiC-1.5C	35.03	1.26	338.20	10.61
40B_4C-SiC-2.0C	34.94	1.34	334.95	10.49
40B_4C-SiC-2.5C	34.79	1.96	334.38	07.57

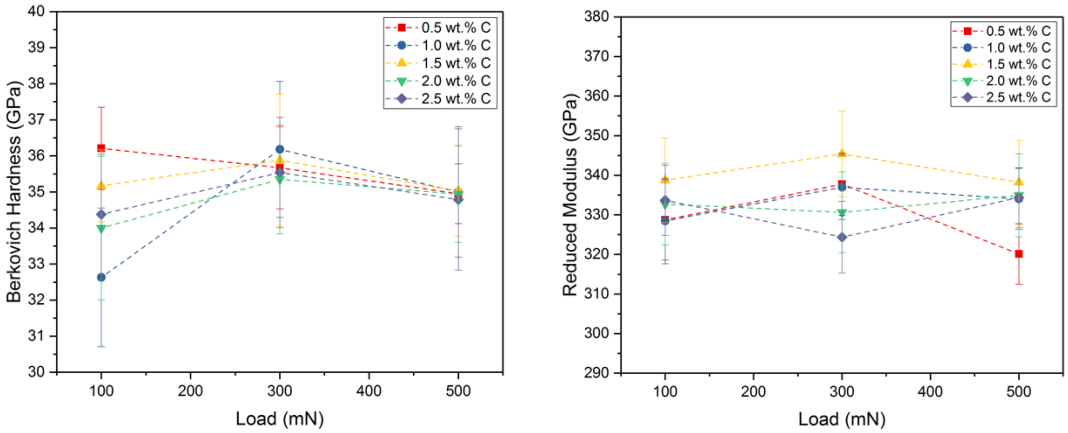

Figure 163. Load- hardness and load- reduced modulus curves for 40%B_4C-unetched SiC composites

Table 108. Berkovich hardness and reduced modulus of 50%B_4C-unetched SiC composites

100mN (10g)	**H (GPa)**	**Std. Dev.**	**Reduced Modulus (GPa)**	**Std. Dev.**
50B_4C-SiC-0.5C	34.25	1.81	338.76	10.33
50B_4C-SiC-1.0C	35.13	1.97	337.46	10.15
50B_4C-SiC-1.5C	35.23	1.20	338.08	10.65
50B_4C-SiC-2.0C	32.71	1.54	330.53	10.49
50B_4C-SiC-2.5C	34.51	1.22	333.72	08.89
300mN (30g)	**H (GPa)**	**Std. Dev.**	**Reduced Modulus (GPa)**	**Std. Dev.**
50B_4C-SiC-0.5C	35.65	1.86	338.85	10.56
50B_4C-SiC-1.0C	35.75	1.90	340.57	08.08
50B_4C-SiC-1.5C	35.87	1.91	344.86	10.64
50B_4C-SiC-2.0C	35.34	1.10	334.75	10.74
50B_4C-SiC-2.5C	35.17	1.37	331.95	09.81
500mN (50g)	**H (GPa)**	**Std. Dev.**	**Reduced Modulus (GPa)**	**Std. Dev.**
50B_4C-SiC-0.5C	35.33	1.41	336.21	08.44
50B_4C-SiC-1.0C	35.35	1.80	341.16	10.14
50B_4C-SiC-1.5C	35.74	1.39	343.91	09.77
50B_4C-SiC-2.0C	35.31	1.93	334.45	08.47
50B_4C-SiC-2.5C	35.29	1.11	334.31	09.97

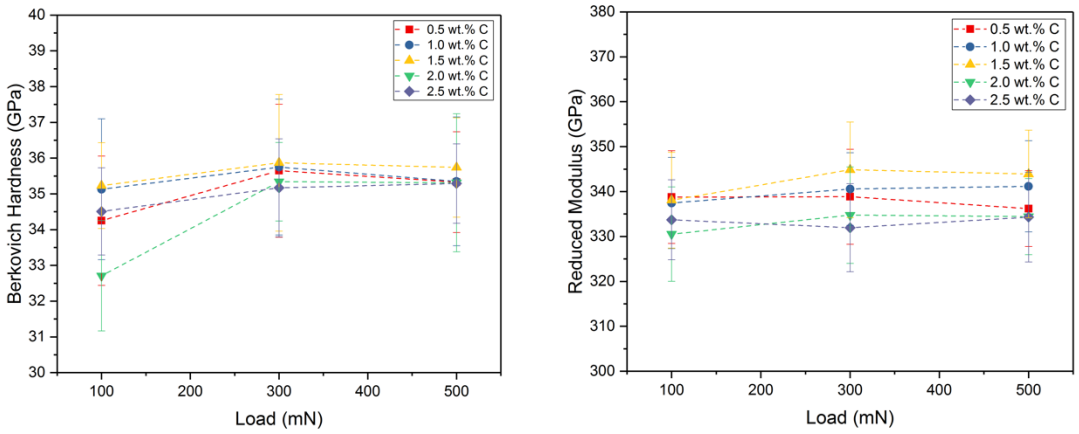

Figure 164. Load- hardness and load- reduced modulus curves for 50%B_4C-unetched SiC composites

Table 109. Berkovich hardness and reduced modulus of 60%B_4C-unetched SiC composites

100mN (10g)	**H (GPa)**	**Std. Dev.**	**Reduced Modulus (GPa)**	**Std. Dev.**
60B_4C-SiC-0.5C	36.09	1.88	335.40	10.26
60B_4C-SiC-1.0C	37.47	1.22	344.41	10.31
60B_4C-SiC-1.5C	38.07	1.47	347.86	10.05
60B_4C-SiC-2.0C	35.50	1.03	344.12	10.73
60B_4C-SiC-2.5C	34.75	1.96	333.53	10.81
300mN (30g)	**H (GPa)**	**Std. Dev.**	**Reduced Modulus (GPa)**	**Std. Dev.**
60B_4C-SiC-0.5C	36.85	1.44	334.04	10.59
60B_4C-SiC-1.0C	36.29	1.92	343.05	05.32
60B_4C-SiC-1.5C	36.90	1.20	347.59	10.99
60B_4C-SiC-2.0C	35.17	1.72	336.91	07.22
60B_4C-SiC-2.5C	35.92	1.00	332.86	09.65
500mN (50g)	**H (GPa)**	**Std. Dev.**	**Reduced Modulus (GPa)**	**Std. Dev.**
60B_4C-SiC-0.5C	35.60	1.96	336.15	10.75
60B_4C-SiC-1.0C	35.63	1.03	336.73	06.09
60B_4C-SiC-1.5C	35.73	1.30	346.50	06.28
60B_4C-SiC-2.0C	35.53	1.47	331.26	10.75
60B_4C-SiC-2.5C	35.37	1.28	329.26	09.97

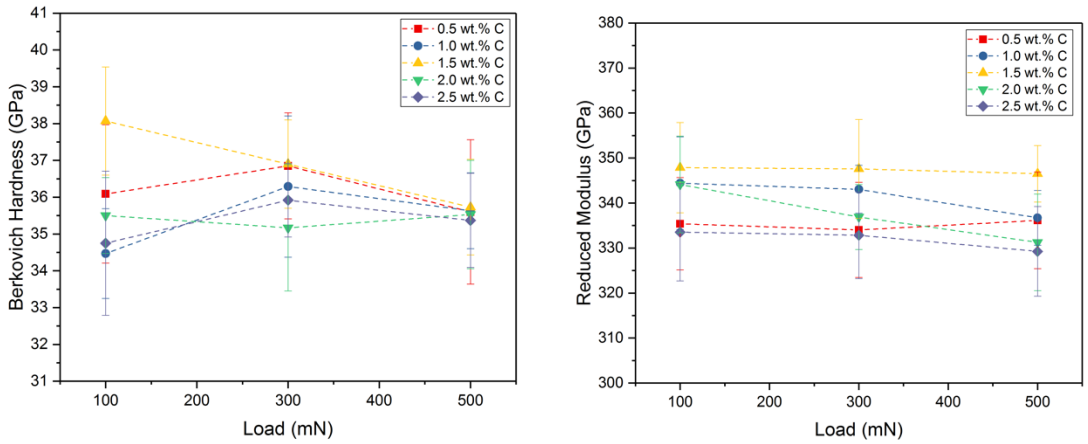

Figure 165. Load- hardness and load- reduced modulus curves for 60%B_4C-unetched SiC composites

Table 110. Berkovich hardness and reduced modulus of 70%B_4C-unetched SiC composites

100mN (10g)	**H (GPa)**	**Std. Dev.**	**Reduced Modulus (GPa)**	**Std. Dev.**
70B_4C-SiC-0.5C	35.09	1.83	337.94	07.92
70B_4C-SiC-1.0C	36.45	1.31	331.46	10.97
70B_4C-SiC-1.5C	37.79	1.46	346.48	10.24
70B_4C-SiC-2.0C	36.25	1.36	335.07	10.52
70B_4C-SiC-2.5C	35.90	1.24	329.12	08.10
300mN (30g)	**H (GPa)**	**Std. Dev.**	**Reduced Modulus (GPa)**	**Std. Dev.**
70B_4C-SiC-0.5C	35.97	1.26	339.61	05.89
70B_4C-SiC-1.0C	36.07	1.42	340.47	10.32
70B_4C-SiC-1.5C	36.43	1.35	343.72	08.53
70B_4C-SiC-2.0C	36.40	1.23	332.66	10.16
70B_4C-SiC-2.5C	35.81	1.02	328.08	09.45
500mN (50g)	**H (GPa)**	**Std. Dev.**	**Reduced Modulus (GPa)**	**Std. Dev.**
70B_4C-SiC-0.5C	35.95	1.43	337.74	05.72
70B_4C-SiC-1.0C	36.01	1.47	330.39	06.63
70B_4C-SiC-1.5C	36.07	1.67	342.72	08.18
70B_4C-SiC-2.0C	35.86	1.92	336.42	09.64
70B_4C-SiC-2.5C	35.84	1.89	335.84	10.24

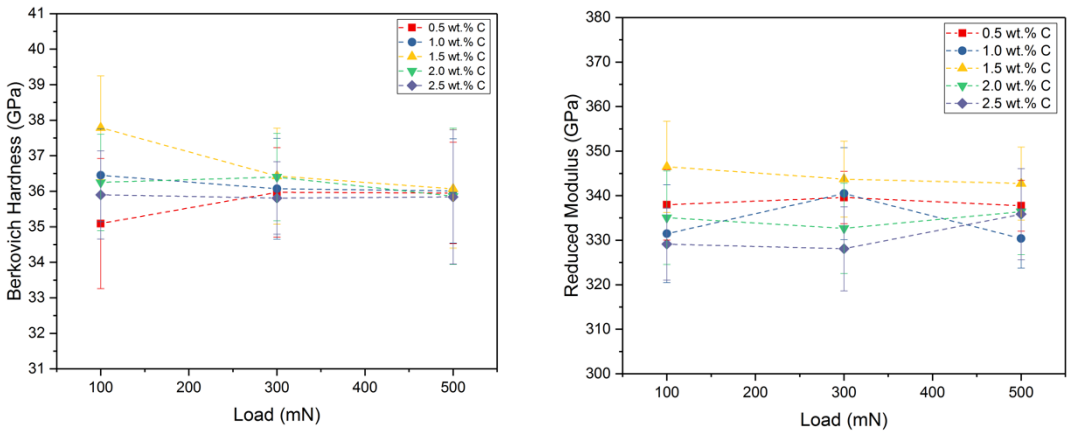

Figure 166. Load- hardness and load- reduced modulus curves for 70%B_4C-unetched SiC composites

Table 111. Berkovich hardness and reduced modulus of 80%B_4C-unetched SiC composites

100mN (10g)	**H (GPa)**	**Std. Dev.**	**Reduced Modulus (GPa)**	**Std. Dev.**
80B_4C-SiC-0.5C	37.55	1.29	342.57	10.33
80B_4C-SiC-1.0C	38.73	1.07	347.33	10.79
80B_4C-SiC-1.5C	38.73	1.08	357.16	10.19
80B_4C-SiC-2.0C	36.23	1.49	337.30	10.52
80B_4C-SiC-2.5C	34.83	1.35	331.57	09.22
300mN (30g)	**H (GPa)**	**Std. Dev.**	**Reduced Modulus (GPa)**	**Std. Dev.**
80B_4C-SiC-0.5C	36.83	1.21	339.98	10.79
80B_4C-SiC-1.0C	38.66	1.43	347.19	07.38
80B_4C-SiC-1.5C	38.81	1.76	347.61	06.64
80B_4C-SiC-2.0C	36.91	1.54	336.21	10.04
80B_4C-SiC-2.5C	36.18	1.79	332.14	10.00
500mN (50g)	**H (GPa)**	**Std. Dev.**	**Reduced Modulus (GPa)**	**Std. Dev.**
80B_4C-SiC-0.5C	36.39	1.15	336.71	08.84
80B_4C-SiC-1.0C	36.64	1.06	330.59	06.97
80B_4C-SiC-1.5C	36.86	1.99	349.11	08.85
80B_4C-SiC-2.0C	36.33	1.64	335.21	10.21
80B_4C-SiC-2.5C	36.00	1.37	339.24	10.81

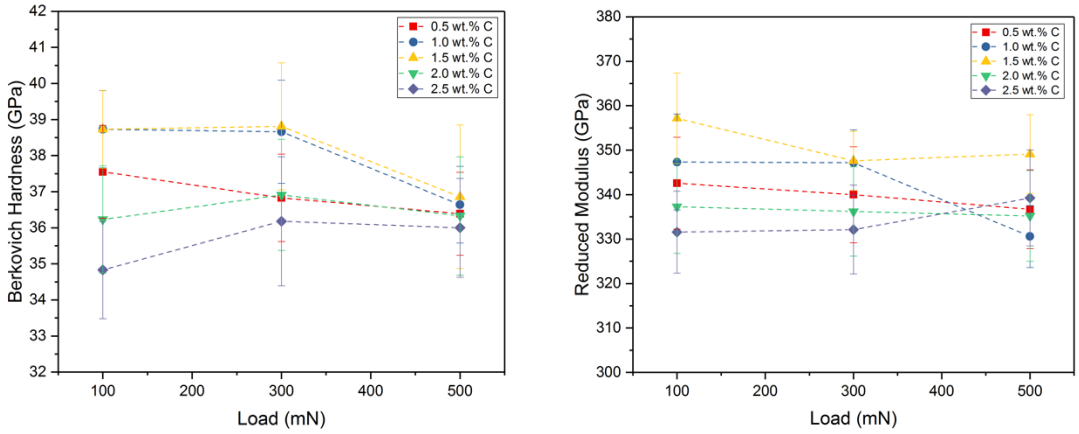

Figure 167. Load- hardness and load- reduced modulus curves for 80%B_4C-unetched SiC composites

Table 112. Berkovich hardness and reduced modulus of 90%B_4C-unetched SiC composites

100mN (10g)	**H (GPa)**	**Std. Dev.**	**Reduced Modulus (GPa)**	**Std. Dev.**
90B_4C-SiC-0.5C	36.69	1.97	339.02	08.96
90B_4C-SiC-1.0C	38.25	1.35	342.02	06.44
90B_4C-SiC-1.5C	38.67	1.90	357.11	10.59
90B_4C-SiC-2.0C	35.62	1.46	336.98	10.31
90B_4C-SiC-2.5C	35.91	1.67	336.66	08.38
300mN (30g)	**H (GPa)**	**Std. Dev.**	**Reduced Modulus (GPa)**	**Std. Dev.**
90B_4C-SiC-0.5C	37.49	1.55	345.00	08.42
90B_4C-SiC-1.0C	37.69	1.02	350.25	09.29
90B_4C-SiC-1.5C	38.16	1.24	352.61	10.53
90B_4C-SiC-2.0C	37.40	1.97	336.85	07.37
90B_4C-SiC-2.5C	35.74	1.72	332.84	06.99
500mN (50g)	**H (GPa)**	**Std. Dev.**	**Reduced Modulus (GPa)**	**Std. Dev.**
90B_4C-SiC-0.5C	37.10	1.18	333.97	08.47
90B_4C-SiC-1.0C	37.79	1.27	350.60	10.07
90B_4C-SiC-1.5C	37.42	1.87	350.75	07.95
90B_4C-SiC-2.0C	37.09	1.66	341.54	10.85
90B_4C-SiC-2.5C	36.87	1.09	341.37	10.02

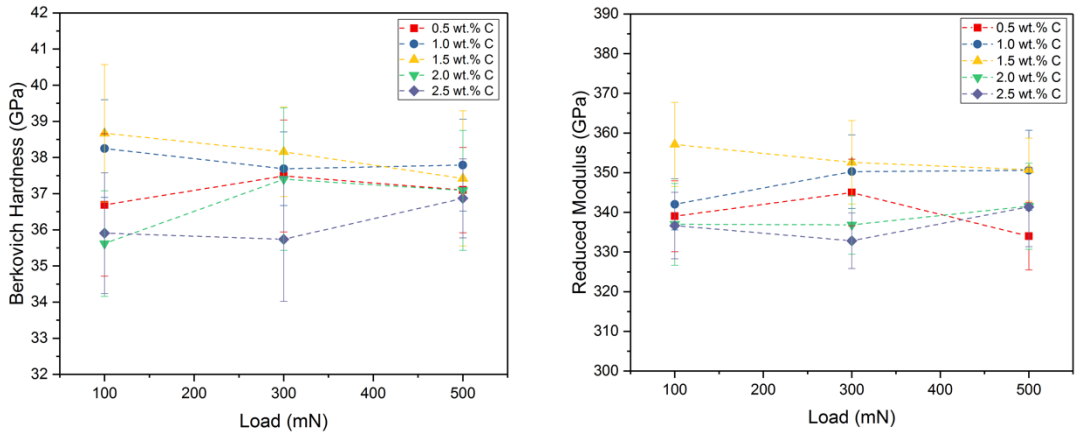

Figure 168. Load- hardness and load- reduced modulus curves for 90%B_4C-unetched SiC composites

By using equation 35 in section 4.5.6., the reduced modulus can be converted to Young's modulus. In this equation, the measured Poisson's ratio from ultrasound analysis was used to measure Young's modulus. The Young's modulus from Berkovich and from ultrasound analysis followed the same trend, however, they have some difference in values. The results can be seen in Tables 113 through 121. For both the ultrasound and nanoindentation methods, with increasing the carbon content from 0.5% to 1.5% carbon, the Young's modulus values increased. With a rise of carbon content from 1.5% to 2.5%, the Young's modulus decreased. However, the nanoindentation method provided higher Young's modulus values. Oliver et al. experimented with one phase materials and ignored the reverse plasticity because they supposed that reverse plasticity was insignificant [118, 127]. On the other hand, Shuman's mentioned that using nanoindentation unload curves to measure elastic modulus can cause the samples to have a higher elastic modulus since reverse plasticity added to the elastic recovery. Reverse plasticity is brought by dislocations

or grain boundary adjustment because of the indentation experiments. They have even found a 100 GPa difference between literature and experimental elastic modulus values from unloading curves [128]. For this experiment, Shuman's assumption might be acceptable, since composite materials were analyzed.

The Young's modulus decreased with increasing the boron carbide content when measured with ultrasound analysis. This was expected since there was an increase in the boron carbide, residual carbon occurred, and porosity increased. Carbon's Young's modulus was low, so it reduced the Young's modulus of samples. However, with the Berkovich indentation method, the Young's modulus increased with an increase in boron carbide content. This might be due to the size effect of the indenter tip since it is too small. The indenter tip might hit mostly boron carbide grains and again reverse plasticity.

Table 113. Comparison of 10%B_4C-unetched SiC of Young's modulus measured by ultrasound and nanoindentation

Sample	**E (GPa)**	**500 mN Elastic Modulus**	**% Difference**
10B_4C-SiC-0.5C	443	417	-05
10B_4C-SiC-1.0C	451	431	-05
10B_4C-SiC-1.5C	451	453	01
10B_4C-SiC-2.0C	422	417	-01
10B_4C-SiC-2.5C	400	415	03

Table 114. Comparison of 20%B_4C-unetched SiC of Young's modulus measured by ultrasound and nanoindentation

Sample	E (GPa)	500 mN Elastic Modulus	% Difference
20B_4C-SiC-0.5C	429	452	05
20B_4C-SiC-1.0C	438	442	01
20B_4C-SiC-1.5C	448	456	02
20B_4C-SiC-2.0C	405	437	07
20B_4C-SiC-2.5C	400	425	06

Table 115. Comparison of 30%B_4C-unetched SiC of Young's modulus measured by ultrasound and nanoindentation

Sample	E (GPa)	500 mN Elastic Modulus	% Difference
30B_4C-SiC-0.5C	419	435	03
30B_4C-SiC-1.0C	419	449	07
30B_4C-SiC-1.5C	420	469	11
30B_4C-SiC-2.0C	395	452	14
30B_4C-SiC-2.5C	386	459	19

Table 116. Comparison of 40%B_4C-unetched SiC of Young's modulus measured by ultrasound and nanoindentation

Sample	E (GPa)	500 mN Elastic Modulus	% Difference
40B_4C-SiC-0.5C	407	433	06
40B_4C-SiC-1.0C	412	458	11
40B_4C-SiC-1.5C	414	466	13
40B_4C-SiC-2.0C	394	461	12
40B_4C-SiC-2.5C	380	460	21

Table 117. Comparison of 50%B_4C-unetched SiC of Young's modulus measured by ultrasound and nanoindentation

Sample	E (GPa)	500 mN Elastic Modulus	% Difference
50B_4C-SiC-0.5C	401	463	15
50B_4C-SiC-1.0C	404	472	17
50B_4C-SiC-1.5C	409	472	15
50B_4C-SiC-2.0C	394	460	17
50B_4C-SiC-2.5C	379	460	21

Table 118. Comparison of 60%B_4C-unetched SiC of Young's modulus measured by ultrasound and nanoindentation

Sample	E (GPa)	500 mN Elastic Modulus	% Difference
60B_4C-SiC-0.5C	400	464	16
60B_4C-SiC-1.0C	405	464	14
60B_4C-SiC-1.5C	405	483	19
60B_4C-SiC-2.0C	391	454	16
60B_4C-SiC-2.5C	376	450	19

Table 119. Comparison of 70%B_4C-unetched SiC of Young's modulus measured by ultrasound and nanoindentation

Sample	E (GPa)	500 mN Elastic Modulus	% Difference
70B_4C-SiC-0.5C	396	467	18
70B_4C-SiC-1.0C	403	451	12
70B_4C-SiC-1.5C	402	475	18
70B_4C-SiC-2.0C	379	463	22
70B_4C-SiC-2.5C	376	463	23

Table 120. Comparison of 80%B_4C-unetched SiC of Young's modulus measured by ultrasound and nanoindentation

Sample	E (GPa)	500 mN Elastic Modulus	% Difference
80B_4C-SiC-0.5C	387	464	19
80B_4C-SiC-1.0C	401	452	13
80B_4C-SiC-1.5C	402	488	21
80B_4C-SiC-2.0C	371	461	24
80B_4C-SiC-2.5C	370	470	27

Table 121. Comparison of 90%B_4C-unetched SiC of Young's modulus measured by ultrasound and nanoindentation

Sample	E (GPa)	500 mN Elastic Modulus	% Difference
90B_4C-SiC-0.5C	380	459	20
90B_4C-SiC-1.0C	391	491	32
90B_4C-SiC-1.5C	401	492	22
90B_4C-SiC-2.0C	365	474	30
90B_4C-SiC-2.5C	365	474	30

5.3.3. Correlation of Mechanical Properties

Microsoft Excel was used to analyze data and correlate a meaningful relationship between free carbon and mechanical properties. Results all samples (etched and unetched samples with all different boron carbide percentage) were analyzed together. The correlation coefficient of parameters and free carbon can be seen in Table 122. The correlation coefficient can be between -1 and +1. When the correlation coefficient is -1.0, it is perfect negative and has a negative correlation. When the correlation coefficient is 1.0, it is perfect positive and has a positive correlation. The significance p-value should be

lower than 0.05 to be considered significant with 95% confidence level. All parameters, the significance was found to be <0.001, so that means all parameters had a meaningful correlation with free carbon and was highly significant. Relative density, grain size, elastic modulus, and fracture toughness all had a negative correlation with free carbon as shown in Table 122.

Table 122. Correlation between parameters and free carbon

	Parameters	**Free Carbon**
Pearsons Correlation Coefficient	Relative Density	-0.645
	Grain Size	-0.569
	Elastic Modulus	-0.793
	Fracture Toughness	-0.535
Significance	Relative Density	<0.001
	Grain Size	<0.001
	Elastic Modulus	<0.001
	Fracture Toughness	<0.001

6. Conclusions

In this work, H.C. Starck UF 25 Silicon Carbide, Saint Gobain Silicon Carbide, HD-20 Boron Carbide, and Carbon Lamp black from Fisher Scientific were used. The oxygen content of the starting materials were modified by acid etching and adding different amounts of carbon.

To reduce the oxygen content, H.C. Starck UF25 Silicon Carbide was etched with 20%, 40%, 50% HF and HF-HNO_3 for 1hour, 4 hour, and 24 hour. It showed that when the concentration of hydrofluoric acid increased, the efficiency of acid etching also increased to remove the oxide layer. Also, with increasing the etching time, the oxygen content of the etched powder decreased. The silicon carbide powder etched for 1 hour with 50%HF was chosen since the 1 hour etching process was more effective in the time frame. Etching silicon carbide powder with HF and HNO_3 did not reduce the oxygen content, it instead increased the oxygen content of powder since HNO_3 was a strong oxidizing agent.

Etched H.C. Starck UF 25 Silicon Carbide was mixed with 1.5 wt. % Carbon Lampblack and 0.5 wt. % H.C. Starck HD20 Boron Carbide and densified by spark plasma sintering at 1950°C for 5 min. Overall H.C. Starck Silicon Carbide mainly had elongated grains. Also SEM images showed that increasing the etching time decreased the grain size, it means the high oxygen content caused grain coarsened. The high oxygen content also affected the mechanical properties and the density. When the samples had high oxygen content, they had a lower Young's modulus, shear modulus and bulk modulus, and they could not reach full density due to the oxide layer.

Saint Gobain powder was etched only for 1 hour with 50% HF, and the powders were sintered at different times to see the effect of oxygen content of powder. All samples

showed equiaxed grain shape, however the grain sizes changed by day. Sample made with fresh powder had smaller grain sizes while higher oxygen content powder (day 9) showed bigger grain sizes. Fresh powder also had higher density and mechanical properties (Young's modulus, shear modulus, and bulk modulus) than higher oxygen content powders. It was clear that increasing the oxygen content decreased the density and elastic properties.

H.C. Starck UF25 Silicon Carbide, HD20 Boron carbide, and Carbon Lamp black from Fisher Scientific were used to produce SiC-B_4C composites by Spark Plasma Sintering. Samples were characterized using SEM, XRD, and ultrasound analysis. Density, hardness, and fracture toughness were evaluated.

To find the optimal sintering temperature, 50%B_4C-1.5%C-48.5%SiC sample was sintered under four different temperatures: 1800°C, 1850°C, 1900°C, 1950°C. The sinterability of the composite was increased by increasing the sintering temperature. After increasing the sintering temperature, the diffusion increased and the bonding between particles increased. Therefore, the amount of porosity in the samples decreased, and the properties were affected positively by that. While increasing the sintering temperature decreased the B_4C grain in composite, it increased the SiC grains. Ultrasound analysis showed that increasing sintering temperature increased the elastic, shear, and bulk modulus. Hardness and fracture toughness values also increased by increasing the sintering temperature.

To find the optimal applied pressure, 50%B_4C-1.5%C-48.5%SiC sample was sintered at 1950°C at four different applied pressures: 20, 30, 40 and 50MPa. Increasing the applied pressure showed a positive effect on the composites' density. By increasing the

applied pressure the B_4C and SiC grains get smaller. Ultrasound analysis showed that increasing the applied pressure increased the elastic modulus, shear, and bulk modulus of composites. Once again increasing the applied pressure, hardness, and fracture toughness of composites.

Two different mixing methods were tried: dry mixing and wet mixing (ball milling). Dry mixing did not provide uniform mixing. Large pockets of individual components were clearly observed. Increasing the B_4C amount caused bigger B_4C islands. On the other hand, ball milling provided a well homogeneous distribution. There were no pockets of individual components. It can be seen that ball milling provided higher density than dry mixing. However, in both mixing methods, the density decreased with increasing B_4C content in the composites. Dry mixing samples did not show consistent ultrasound analyses and hardness values since they had an agglomerate problem. Increasing the B_4C content increased the hardness values, and decreased the Young's modulus, shear modulus, and bulk modulus for ball milling samples.

Based on experiment, etched/ unetched SiC- B_4C composite powders were mixed with ball milling and sintered at 1950°C for 5 min under 50 MPa applied pressure.

The oxygen managed using two methods: acid etching and carbon addition. However, carbon also played a role as well as the oxygen since the oxygen content was modified by adding varying amounts of carbon and causing surplus carbon. Residual carbon could affect the mechanical properties of composites like porosity.

The etched SiC- B_4C series, ball milling provided homogeneous distribution and SEM images did not show visible porosity. Increasing the boron carbide content in the

composites increased the average grain size of boron carbide. On the contrary, decreasing the silicon carbide content in the composites decreased the average grain size of silicon carbide. Increasing the amount of carbon decreased the grain size of both silicon carbide and boron carbide. Since acid etching processing reduced the oxygen content of powders, the composites needed less additional carbon to remove the remaining oxide layer. Rietveld refinement analysis results showed that all the samples had residual carbon, and the amount of excess carbon increased with increasing boron carbide content. Even if all the etched series samples were almost fully dense, the elastic, shear, and bulk modulus values decreased with increasing additional carbon. Again, because of the etching process, less carbon was needed to remove the remaining oxide layer. The best results were obtained with the addition of 0.5% carbon. Hardness results showed that increasing the carbon content decreased the hardness values for all samples. Fracture toughness values were close to each other. When comparing elastic modulus values from ultrasound analysis and Berkovich indentation, it was clear to see the effect of excess carbon on Young's modulus with the Berkovich nanoindentation calculated Young’s modulus values since 1% and 1.5% carbon samples showed drastically decreased Young’s modulus values.

In the unetched SiC- B_4C series, microstructure images showed that ball milling delivered an even distribution of both components and high densities were achieved. Rietveld refinement analysis results showed that samples that had a 2.5% carbon addition had residual carbon for all boron carbide content samples. The amount of excess carbon increased with increasing boron carbide content. The results showed that the addition of carbon from 0.5% to 1.5% increased the mechanical properties. However, after a 1.5%

carbon addition, increasing the amount of carbon had negative effects on the composites' properties due to the presence of residual carbon.

Grain sizes were measured using the lince intercept method. The grain size of dense SiC-B_4C composites measured less than a μm. The grain size of samples increased when the carbon increased from 0.5% to 1.5%, then decreased when the carbon content further increased from 1.5% to 2.5%. It showed that there was no grain coarsening with the spark plasma sintering method, and excess carbon caused grain size reduction.

Vickers hardness values showed that the hardness was increased slightly when the amount of carbon increased from 0.5% to 1.5%. After 1.5% addition carbon, the hardness results dropped. This showed that excess carbon has reduced hardness values.

Contrary to the hardness, the 2.5% carbon series composites have higher fracture toughness values. This showed that increasing the fracture toughness decreased the hardness value.

All of the SiC- B_4C composites showed transgranular fracture behavior.

To compare the elastic modulus using the ultrasound analysis results, the Berkovich nanoindentation reduced modulus values was used to convert the elastic modulus. The Young's modulus from Berkovich and from the ultrasound analysis followed the same trend, however, they showed some difference in value. The elastic modulus from Berkovich indentation showed higher values than the ultrasound analysis results. Since the modulus measured using nanoindentation unload curves, the samples may have a higher elastic modulus since reverse plasticity added to the elastic recovery.

Comparing etched and unetched samples based on residual carbon showed that at higher SiC content composites etching had preferable values than unetched samples. However increasing the B_4C content, etched and unetched composites showed similar values.

For all samples results, Microsoft Excel was used to analyze data and correlate a meaningful relationship between free carbon and mechanical properties. Significance p-values were found to be <0.001 for all parameters that had a meaningful correlation with free carbon.

7. Future Work

1. To see if differences in mixing time have an effect on the microstructure and mechanical properties, shorter ball milling time can be tried.

2. The advantage of high energy mixing can be used with ethanol and SiC media with Spectromill.

3. Less than 0.5% carbon can be added to etched samples to avoid residual carbon.

4. Since freshly etched SiC powder oxidized when it exposed to air, to avoid this problem, acid etching procedure can be done in glove box to reduce the oxygen content powder 0%.

5. To optimized composites properties, some parameters can be limited and working only some percentage of B_4C compositions.

6. Longer mid dwell time can be tried to see if it has any benefit on allowing carbon to react with the oxide layer when held longer.

7. Since commercially it is hard to make bigger samples with an SPS and the samples were fairly small, a hot press can be utilized to make larger samples 4”x4” or 6” round and tested to see if the results will be same or not. Also, different temperature studies can be done to produce fully dense samples with hot press.

8. Similar experiments can be done using pressureless sintering to make larger and more complicated samples. Again, it is widely used commercially.

9. TEM analysis can be done to look at the grain boundaries closely and discover where the excess oxygen or carbon goes.

8. References

[1] V. Ekinci, Alümina Takviyeli Alüminyum Matriksli Kompozit Malzeme Üretimi ve Mekanik Özelliklerinin Araştırılması, Yüksek Lisans Tezi, Gazi Üniversitesi, Fen Bilimleri Enstitüsü, (2007).
[2] T. Koçer, Basınçlı İnfiltrasyon Yöntemiyle Üretilen Al2o3 Ve Sic Partikül Takviyeli, Al-mg Metal Matriksli Kompozitlerin Aşınma Davranışlarının İncelenmesi, Fen Bilimleri Enstitüsü, 2002.
[3] C. Zweben, Composire Materials, Mechanical Engineers' Handbook, Volume 1: Materials and Engineering Mechanics, John Wiley & Sons2015.
[4] P. Feinle, H. Knoch, Product Development with SiC and B4C Ceramics, 3rd European Symposium on Engineering Ceramics, Springer, 1991, pp. 51-67.
[5] P. Sahani, S. Karak, B. Mishra, D. Chakravarty, D. Chaira, A Comparative Study on SiC-B 4 C-Si Cermet Prepared by Pressureless Sintering and Spark Plasma Sintering Methods, Metallurgical and Materials Transactions A, 47 (2016) 3065-3076.
[6] J. Roy, S. Chandra, S. Das, S. Maitra, Oxidation behaviour of silicon carbide-a review, Rev. Adv. Mater. Sci, 38 (2014) 29-39.
[7] J. Quanli, Z. Haijun, L. Suping, J. Xiaolin, Effect of particle size on oxidation of silicon carbide powders, Ceramics international, 33 (2007) 309-313.
[8] J. Evans, Pressureless Sintering of Boron Carbide, Imperial College London Department of Materials Science and Engineering, London, (2014).
[9] V. Izhevskyi, L. Genova, J. Bressiani, A. Bressiani, silicon carbide. Structure, properties and processing, Cerâmica, 46 (2000) 4-13.
[10] K.A. Schwetz, Silicon carbide based hard materials, in: R. Riedel (Ed.) Handbook of Ceramics Hard Materials, WILEY-VCH, Germany, 2000, pp. 683-748.
[11] S.E. Saddow, A.K. Agarwal, Advances in silicon carbide processing and applications, Artech House2004.
[12] C. Schmalzried, K.A. Schwetz, Silicon Carbide-and Boron Carbide-Based Hard Materials, Ceramics Science and Technology, Set, (2010) 131-227.
[13] W.J. MoberlyChan, J. Cao, C. Gilbert, R. Ritchie, L. De Jonghe, The cubic-to-hexagonal transformation to toughen SiC, Ceramic Microstructures, (1998) 177-190.
[14] H. Abderrazak, E.S.B.H. Hmida, Silicon carbide: synthesis and properties, Properties and applications of Silicon Carbide, InTech2011.
[15] D. Ahmoye, Pressureless Sintering and Mechanical Properties of Silicon Carbon Composites with in-situ Converted Titanium Dioxide to Titanium Carbon, 2010.
[16] J. Tan, Mechanical properties characterisation of silicon carbide layers in simulated coated particles, University of Manchester, 2010.
[17] R. Rurali, E.R. Hernández, P. Godignon, Theoretical studies of defects in silicon carbide, Universitat Autònoma de Barcelona2004.
[18] F. Fabbri, 4H silicon carbide particle detectors: study of the defects induced by high energy neutron irradiation, alma, 2008.
[19] S. Somiya, Y. Inomata, Silicon carbide ceramics. 1. Fundamental and solid reaction, Springer1991.
[20] B. Basu, K. Balani, Advanced structural ceramics, John Wiley & Sons2011.
[21] G. Liu, 4H-silicon carbide MOSFET interface structure, defect states and inversion layer mobility, Rutgers The State University of New Jersey-New Brunswick2014.
[22] Y. Xu, Sturcture and chemistry of defect passivation at the interface between silicon dioxide and silicon carbide, Rutgers The State University of New Jersey-New Brunswick2014.

[23] P. Shaffer, A review of the structure of silicon carbide, Acta Crystallographica Section B: Structural Crystallography and Crystal Chemistry, 25 (1969) 477-488.
[24] A. Rashed, Properties and characteristics of silicon carbide, POCO Graphite Inc., Decatur, (2002).
[25] L. Silvestroni, Development and characterization of non-oxide ceramic composites for mechanical and tribological applications, alma, 2009.
[26] H.J. Seifert, F. Aldinger, Phase equilibria in the Si-BCN system, High Performance Non-Oxide Ceramics I, Springer2002, pp. 1-58.
[27] B.P. Groth, On the use of Raman spectroscopy and instrumented indentation for characterizing damage in machined carbide ceramics, Rutgers The State University of New Jersey-New Brunswick2013.
[28] D.M. Slusark, The effect of microstructural variation on the mechanical and acoustic properties of silicon carbide, Rutgers The State University of New Jersey-New Brunswick2012.
[29] K.K. Saxena, S. Agarwal, S.K. Khare, Surface characterization, material removal mechanism and material migration study of micro EDM process on conductive SiC, Procedia CIRP, 42 (2016) 179-184.
[30] B. Lanfant, Y. Leconte, G. Bonnefont, V. Garnier, Y. Jorand, S. Le Gallet, M. Pinault, N. Herlin-Boime, F. Bernard, G. Fantozzi, Effects of carbon and oxygen on the spark plasma sintering additive-free densification and on the mechanical properties of nanostructured SiC ceramics, Journal of the European Ceramic Society, 35 (2015) 3369-3379.
[31] J.R. McDermid, A thermodynamic approach to the brazing of silicon carbide, (1994).
[32] P.J. Guichelaar, Acheson process, Carbide, Nitride and Boride Materials Synthesis and Processing, Springer1997, pp. 115-129.
[33] K. Yamada, M. Mohri, Properties and applications of silicon carbide ceramics, in: Y.I. S. Somiya (Ed.) Silicon Carbide Ceramics—1, Elsevier Applied Science, England, 1991, pp. 13-44.
[34] K. Biswas, Liquid phase sintering of SiC ceramics with rare earth sesquioxides, (2002).
[35] W. Wesch, Silicon carbide: synthesis and processing, Nuclear Instruments and Methods in Physics Research Section B: Beam interactions with materials and atoms, 116 (1996) 305-321.
[36] M. Karaman, Chemical Vapor Deposition of Boron Carbide, Doktora Tezi, Middle East Technical University, The Graduate School Of Natural And Applied Sciences, (2007).
[37] N. Cho, Processing of boron carbide, Georgia Institute of Technology, 2006.
[38] M. Zhang, W. Zhang, Y. Zhang, L. Gao, Fabrication, microstructure and mechanical behavior of SiCw-B4C–Si composite, Materials Science and Engineering: A, 552 (2012) 410-414.
[39] F. Thévenot, Boron carbide—a comprehensive review, Journal of the European Ceramic society, 6 (1990) 205-225.
[40] D. Emin, Structure and single-phase regime of boron carbides, Physical Review B, 38 (1988) 6041.
[41] S. Reynaud, Fabrication and characterization of carbon and boron carbide nanostructured materials, Rutgers The State University of New Jersey-New Brunswick2010.
[42] M.M. Balakrishnarajan, P.D. Pancharatna, R. Hoffmann, Structure and bonding in boron carbide: The invincibility of imperfections, New Journal of Chemistry, 31 (2007) 473-485.
[43] A. Suri, C. Subramanian, J. Sonber, T.C. Murthy, Synthesis and consolidation of boron carbide: a review, International Materials Reviews, 55 (2010) 4-40.
[44] D.W. Maiorano, The evolution and implication of boron carbide microstructural variations and transformations during powder processing, Rutgers The State University of New Jersey-New Brunswick2011.
[45] T. Tavşanoğlu, Deposition and Characterization of Single and Multilayered Boron Carbide and Boron Carbonitride Thin Films Different Sputtering Configurations, 2009.
[46] H. Clark, J. Hoard, The crystal structure of boron carbide, Journal of the American Chemical Society, 65 (1943) 2115-2119.

[47] V. Domnich, S. Reynaud, R.A. Haber, M. Chhowalla, Boron carbide: structure, properties, and stability under stress, Journal of the American Ceramic Society, 94 (2011) 3605-3628.
[48] D. Tallant, T. Aselage, A. Campbell, D. Emin, Boron carbide structure by Raman spectroscopy, Physical review B, 40 (1989) 5649.
[49] G. Fanchini, J.W. McCauley, M. Chhowalla, Behavior of disordered boron carbide under stress, Physical review letters, 97 (2006) 035502.
[50] H. Lee, R.F. Speyer, Pressureless sintering of boron carbide, Journal of the American Ceramic Society, 86 (2003) 1468-1473.
[51] L.S.S.a.K.T. R.Telle, Boride-Based Hard Materials, in: R. Riedel (Ed.) Handbook of Ceramics Hard Materials, Wiley-vch, Germany, 2000, pp. 802-945.
[52] V. Ponomarev, I. Kovalev, S. Konovalikhin, V. Vershinnikov, Ordering of carbon atoms in boron carbide structure, Crystallography Reports, 58 (2013) 422-426.
[53] N. Orlovskaya, J. Adams, J. Sankar, S. Yarmolenko, M. Lugovy, V. Subbotin, O. Rachenko, M. Chheda, J. Shih, Design and Manufacturing B4C-SiC Layered Ceramics for Armor Applications, Ceramic Armor and Armor Systems, Volume 151, (2003) 59-70.
[54] R.M. da Rocha, F.C. de Melo, Pressureless Sintering of B4C-SiC Composites for Armor Applications, Advances in Ceramic Armor V, (2010) 113-119.
[55] V.V. Skorokhod, Processing, Microstructure, and Mechanical Properties of B4C—TiB2 Particulate Sintered Composites. Part II. Fracture and Mechanical Properties, Powder Metallurgy and Metal Ceramics, 39 (2000) 504-513.
[56] Y.-j. WANG, H.-x. PENG, Y. Feng, Z. Yu, Effect of TiB2 content on microstructure and mechanical properties of in-situ fabricated TiB2/B4C composites, Transactions of Nonferrous Metals Society of China, 21 (2011) s369-s373.
[57] J. Sun, C. Liu, C. Duan, Effect of Al and TiO 2 on sinterability and mechanical properties of boron carbide, Materials Science and Engineering: A, 509 (2009) 89-93.
[58] M. Mashhadi, E. Taheri-Nassaj, V.M. Sglavo, Pressureless sintering of boron carbide, Ceramics International, 36 (2010) 151-159.
[59] W.S. Wilson, P.J. Guichelaar, Electric arc furnace processes, Carbide, nitride and boride materials synthesis and processing, Springer1997, pp. 131-136.
[60] M. Kakiage, Y. Tominaga, I. Yanase, H. Kobayashi, Synthesis of boron carbide powder in relation to composition and structural homogeneity of precursor using condensed boric acid–polyol product, Powder technology, 221 (2012) 257-263.
[61] A. Alizadeh, E. Taheri-Nassaj, N. Ehsani, Synthesis of boron carbide powder by a carbothermic reduction method, Journal of the European Ceramic Society, 24 (2004) 3227-3234.
[62] A. Vogt, F. Schroll, Electrothermic production of boron carbide, Google Patents, 1939.
[63] W. Rafaniello, W.G. Moore, Producing boron carbide, Google Patents, 1989.
[64] S. Miller, F. Toksoy, W. Rafaniello, R. Haber, Submicron boron carbide synthesis through rapid carbothermal reduction, Advances in Ceramic Armor VIII: Ceramic Engineering and Science Proceedings, Volume 33, (2012) 195.
[65] A. W.Weimer, Thermochemistry and Kinetics, in: A.W.Weimer (Ed.) Carbide,Nitride and Boride Materials Synthesis and Processing, CHAPMAN&HALL, England, 1997, pp. 79-113.
[66] Z. Zhang, X. Du, W. Wang, Z. Fu, H. Wang, Preparation of B 4 C–SiC composite ceramics through hot pressing assisted by mechanical alloying, International journal of refractory metals and hard materials, 41 (2013) 270-275.
[67] S. Hayun, V. Paris, M. Dariel, N. Frage, E. Zaretzky, Static and dynamic mechanical properties of boron carbide processed by spark plasma sintering, Journal of the European Ceramic Society, 29 (2009) 3395-3400.
[68] L. Vargas-Gonzalez, R.F. Speyer, J. Campbell, Flexural strength, fracture toughness, and hardness of silicon carbide and boron carbide armor ceramics, International Journal of Applied Ceramic Technology, 7 (2010) 643-651.

[69] T. Narushima, T. Goto, M. Maruyama, H. Arashi, Y. Iguchi, Oxidation of boron carbide-silicon carbide composite at 1073 to 1773 K, Materials Transactions, 44 (2003) 401-406.
[70] W. Li, R. Tu, T. Goto, Preparation of directionally solidified B4C–TiB2–SiC ternary eutectic composites by a floating zone method and their properties, Materials transactions, 46 (2005) 2067-2072.
[71] Z. Xia, Effect Of Neutron Radiation On The Mechanical Properties Of B4c, (2011).
[72] J. Yin, Z. Huang, X. Liu, Z. Zhang, D. Jiang, Microstructure, mechanical and thermal properties of in situ toughened boron carbide-based ceramic composites co-doped with tungsten carbide and pyrolytic carbon, Journal of the European Ceramic Society, 33 (2013) 1647-1654.
[73] D.-H. Riu, R. Choi, H.-E. Kim, E.-S. Kang, Oxidation behaviour and strength of B4C-30 wt% SiC composite materials, Journal of materials science, 30 (1995) 3897-3902.
[74] X. Du, Z. Zhang, W. Wang, H. Wang, Z. Fu, Microstructure and properties of B4C-SiC composites prepared by polycarbosilane-coating/B4C powder route, Journal of the European Ceramic Society, 34 (2014) 1123-1129.
[75] D. Das, J. Farjas, P. Roura, Passive-Oxidation Kinetics of SiC Microparticles, Journal of the American Ceramic Society, 87 (2004) 1301-1305.
[76] S. Baik, P.F. Becher, Effect of oxygen contamination on densification of TiB2, Journal of the American Ceramic Society, 70 (1987) 527-530.
[77] L. Stobierski, A. Gubernat, Sintering of silicon carbideI. Effect of carbon, Ceramics international, 29 (2003) 287-292.
[78] W.J. Clegg, Role of Carbon in the Sintering of Boron-Doped Silicon Carbide, Journal of the American Ceramic Society, 83 (2000) 1039-1043.
[79] M. Wilhelm, S. Werdenich, W. Wruss, Influence of resin content and compaction pressure on the mechanical properties of SiC–Si composites with sub-micron SiC microstructures, Journal of the European Ceramic Society, 21 (2001) 981-990.
[80] D. Bucevac, Microstructure-mechanical properties relations in pressureless sintered silicon carbide-titanium diboride composite ceramics, 2010.
[81] V. Lankau, H.-P. Martin, R. Hempel-Weber, N. Oeschler, A. Michaelis, Preparation and Thermoelectric Characterization of SiC-B 4 C Composites, Journal of electronic materials, 39 (2010) 1809-1813.
[82] J.S. Reed, Principles of ceramics processing, (1995).
[83] L.C. De Jonghe, M.N. Rahaman, Sintering of ceramics, Elsevier, England, 2003.
[84] S.R. Mercurio Jr, Effect of coprecipitation of sintering aids on the microstructure and grain boundary development of sintered silicon carbide, Rutgers The State University of New Jersey-New Brunswick2011.
[85] M.N. Rahaman, Ceramics Processing and Sintering 2005.
[86] M. Barsoum, Fundamentals of ceramics, McGraw Hill Companies, New York, NY, 1997.
[87] D.L. Johnson, Solid-State Sintering, Springer Science & Business Media, New York, 1970.
[88] R.M. German, Liquid phase sintering, Springer Science & Business Media2013.
[89] P. Sahani, S. Karak, B. Mishra, D. Chakravarty, D. Chaira, Effect of Al addition on SiC–B4C cermet prepared by pressureless sintering and spark plasma sintering methods, International Journal of Refractory Metals and Hard Materials, 57 (2016) 31-41.
[90] X.-J. GAO, J.-W. CAO, L.-F. CHENG, D.-M. YAN, C. ZHANG, P. MAN, Effect of carbon content on mechanical properties of SiC/B4C prepared by reaction sintering, 无机材料学报, 30 (2015).
[91] D. Nesmelov, S. Perevislov, Reaction sintered materials based on boron carbide and silicon carbide, Glass and Ceramics, 71 (2015) 313-319.
[92] S. Song, C. Bao, B. Wang, Effect of the addition of carbon fibres on the microstructure and mechanical properties of reaction bonded B4C/SiC composites, Journal of the European Ceramic Society, 36 (2016) 1905-1913.

[93] Y. Zhou, D. Ni, Y. Kan, P. He, S. Dong, X. Zhang, Microstructure and mechanical properties of reaction bonded B4C-SiC composites: The effect of polycarbosilane addition, Ceramics International, 43 (2017) 5887-5895.
[94] P. Chhillar, M. Aghajanian, D. Marchant, R. Haber, M. Sennett, The Effect of Si Content on the Properties of B4C-SiC-Si Composites, Advances in Ceramic Armor III: Ceramic and Engineering Science Proceedings, Volume 28, Issue 5, (2009) 161-167.
[95] S. Hayun, N. Frage, M. Dariel, The morphology of ceramic phases in BxC–SiC–Si infiltrated composites, Journal of Solid State Chemistry, 179 (2006) 2875-2879.
[96] A. Thuault, S. Marinel, E. Savary, R. Heuguet, S. Saunier, D. Goeuriot, D. Agrawal, Processing of reaction-bonded B4C–SiC composites in a single-mode microwave cavity, Ceramics International, 39 (2013) 1215-1219.
[97] I.-M. Low, Advances in ceramic matrix composites, Woodhead Publishing2014.
[98] R. German, Sintering: from empirical observations to scientific principles, Butterworth-Heinemann2014.
[99] M.F. Toksoy, Densification of rapid carbothermal synthesized and commercial boron carbide by spark plasma sintering, Rutgers University-Graduate School-New Brunswick, 2014.
[100] M. Uehara, R. Shiraishi, A. Nogami, N. Enomoto, J. Hojo, SiC–B 4 C composites for synergistic enhancement of thermoelectric property, Journal of the European Ceramic Society, 24 (2004) 409-412.
[101] M. Suárez, A. Fernández, J. Menéndez, R. Torrecillas, H. Kessel, J. Hennicke, R. Kirchner, T. Kessel, Challenges and opportunities for spark plasma sintering: a key technology for a new generation of materials, Sintering Applications, InTech2013.
[102] S.E. Bagienski, Effect of sintering time and composition of sintering aids on the core-rim microstructure and material properties of spark plasma sintered silicon carbide, Rutgers The State University of New Jersey-New Brunswick2013.
[103] D.M. Hulbert, D. Jiang, D.V. Dudina, A.K. Mukherjee, The synthesis and consolidation of hard materials by spark plasma sintering, International Journal of Refractory Metals and Hard Materials, 27 (2009) 367-375.
[104] H.D. Gençkan, Reaktif spark plazma sinterleme yöntemi ile B4C/SiC kompoziti eldesi, Fen Bilimleri Enstitüsü, 2009.
[105] D. Secrist, Phase equilibria in the system boron carbide-silicon carbide, Journal of the American Ceramic Society, 47 (1964) 127-130.
[106] W. Tomlinson, J. Whitney, Strength of lapped and oxidized SiC□ B4C composites, Ceramics international, 18 (1992) 207-211.
[107] V. Paris, N. Frage, M. Dariel, E. Zaretsky, The spall strength of silicon carbide and boron carbide ceramics processed by spark plasma sintering, International Journal of Impact Engineering, 37 (2010) 1092-1099.
[108] I. Ogawa, K. Nishikubo, T. Imamura, Growth of graphite particles in carbons/SiC/B4C composites, Carbon, 37 (1999) 1000-1002.
[109] S. Prochazka, W.S. Coblenz, Silicon carbide-boron carbide sintered body, Google Patents, 1978.
[110] F. Thevenot, Sintering of boron carbide and boron carbide-silicon carbide two-phase materials and their properties, Journal of Nuclear Materials, 152 (1988) 154-162.
[111] G. Magnani, G. Beltrami, G.L. Minoccari, L. Pilotti, Pressureless sintering and properties of αSiC–B 4 C composite, Journal of the European Ceramic Society, 21 (2001) 633-638.
[112] P. Sahani, D. Chaira, Nonlubricated Sliding Wear Behavior Study of SiC–B4C–Si Cermet Against a Diamond Indenter, Journal of Tribology, 139 (2017) 051601.
[113] B.M. Moshtaghioun, A.L. Ortiz, D. Gómez-García, A. Domínguez-Rodríguez, Toughening of super-hard ultra-fine grained B 4 C densified by spark-plasma sintering via SiC addition, Journal of the european ceramic society, 33 (2013) 1395-1401.

[114] F.C. Sahin, B. Apak, I. Akin, H.E. Kanbur, D.H. Genckan, A. Turan, G. Goller, O. Yucel, Spark plasma sintering of B 4 C–SiC composites, Solid state sciences, 14 (2012) 1660-1663.
[115] K.A. Kuwelkar, Chemical and structural characterization of boron carbide powders and ceramics, 2016.
[116] G.D. Quinn, J. Salem, I. Bar-On, K. Cho, M. Foley, H. Fang, Fracture toughness of advanced ceramics at room temperature, Journal of research of the National Institute of Standards and Technology, 97 (1992) 579.
[117] A.C. Fischer-Cripps, Nanoindentation Testing, Nanoindentation, Springer2011, pp. 21-37.
[118] W.C. Oliver, G.M. Pharr, An improved technique for determining hardness and elastic modulus using load and displacement sensing indentation experiments, Journal of materials research, 7 (1992) 1564-1583.
[119] S. Sagadevan, P. Murugasen, Novel Analysis on the Influence of Tip Radius and Shape of the Nanoindenter on the Hardness of Materials, Procedia Materials Science, 6 (2014) 1871-1878.
[120] M. Wilhelm, M. Kornfeld, W. Wruss, Development of SiC–Si composites with fine-grained SiC microstructures, Journal of the European Ceramic Society, 19 (1999) 2155-2163.
[121] R. Vassen, D. Stöver, Processing and properties of nanograin silicon carbide, Journal of the American Ceramic Society, 82 (1999) 2585-2593.
[122] X. Zhang, Z. Zhang, W. Wang, H. Che, X. Zhang, Y. Bai, L. Zhang, Z. Fu, Densification behaviour and mechanical properties of B4C–SiC intergranular/intragranular nanocomposites fabricated through spark plasma sintering assisted by mechanochemistry, Ceramics International, 43 (2017) 1904-1910.
[123] Z. Zhang, X. Du, Z. Li, W. Wang, J. Zhang, Z. Fu, Microstructures and mechanical properties of B4C–SiC intergranular/intragranular nanocomposite ceramics fabricated from B4C, Si, and graphite powders, Journal of the European Ceramic Society, 34 (2014) 2153-2161.
[124] T. Williams, Development of pressureless sintered silicon carbide-boron carbide composites for armour applications, University of Surrey (United Kingdom), 2016.
[125] D. Hallam, Understanding the deformation of ceramic materials at high strain rates, University of Surrey (United Kingdom), 2015.
[126] C.J. Engberg, E.H. Zehms, Thermal Expansion of Al2O3, BeO, MgO, B4C, SiC, and TiC Above 1000° C, Journal of the American Ceramic Society, 42 (1959) 300-305.
[127] W.C. Oliver, G.M. Pharr, Measurement of hardness and elastic modulus by instrumented indentation: Advances in understanding and refinements to methodology, Journal of materials research, 19 (2004) 3-20.
[128] D.J. Shuman, A.L. Costa, M.S. Andrade, Calculating the elastic modulus from nanoindentation and microindentation reload curves, Materials characterization, 58 (2007) 380-389.
[129] T. Yoshida, A. Nakahira, K. Kijima, Y.-H. Choa, K. Niihara, Fabrication by Prssureless Sintering and Evaluation of SiC/B4C Composites, Journal of the Japan Society of Powder and Powder Metallurgy, 44 (1997) 1078-1082.